Vol. 278, No. 2, June 22, 1993
Completing Volume 278

ISSN 0003-2670

ANALYTICA CHIMICA ACTA

An international journal devoted to all branches of analytical chemistry

ELSEVIER

ANALYTICA CHIMICA ACTA

Scope. *Analytica Chimica Acta* publishes original papers, preliminary communications and reviews dealing with every aspect of modern analytical chemistry. Reviews are normally written by invitation of the editors, who welcome suggestions for subjects. Preliminary communications of important urgent work can be printed within four months of submission, if the authors are prepared to forego proofs.

Submission of Papers

Americas

Prof. Harry L. Pardue
Department of Chemistry
1393 BRWN Bldg, Purdue University
West Lafayette, IN 47907-1393
USA
Tel:(+1-317) 494 5320
Fax:(+1-317) 496 1200

Computer Techniques

Prof. J.T. Clerc
Universität Bern
Pharmazeutisches Institut
Baltzerstrasse 5, CH-3012 Bern
Switzerland
Tel:(+41-31) 654171
Fax:(+41-31) 654198

Other Papers

Prof. Alan Townshend
Department of Chemistry
The University
Hull HU6 7RX
Great Britain

Tel:(+44-482) 465027
Fax:(+44-482) 466410

Prof. Willem E. van der Linden
Laboratory for Chemical Analysis
Department of Chemical Technology
Twente University of Technology
P.O. Box 217, 7500 AE Enschede
The Netherlands
Tel:(+31-53) 892629
Fax:(+31-53) 356024

Prof. Paul Worsfold
Dept. of Environmental Sciences
University of Plymouth
Plymouth PL4 8AA
Great Britain

Tel:(+44-752) 233006
Fax:(+44-752) 233009

Submission of an article is understood to imply that the article is original and unpublished and is not being considered for publication elsewhere. *Anal. Chim. Acta* accepts papers in English only. There are no page charges. Manuscripts should conform in layout and style to the papers published in this issue. See inside back cover for "Information for Authors".

Publication. *Analytica Chimica Acta* appears in 14 volumes in 1993. The subscription price for 1993 (Vols. 267–280) is Dfl. 4214.00 plus Dfl. 462.00 (p.p.h.) (total approx. US$ 2597.75). *Vibrational Spectroscopy* appears in 2 volumes in 1993. The subscription price for *Vibrational Spectroscopy* (Vols. 4 and 5) is Dfl. 700.00 plus Dfl. 66.00 (p.p.h.) (total approx. US$ 407.50). The price of a combined subscription (*Anal. Chim. Acta* and *Vib. Spectrosc.*) is Dfl. 4592.00 plus Dfl. 528.00 (p.p.h.) (total approx. US$ 2844.50). All earlier volumes (Vols. 1–266) except Vols. 23 and 28 are available at Dfl. 259.50 (US$ 144.00), plus Dfl. 18.00 (US$ 10.00) p.p.h., per volume. The Dutch guilder price is definitive. The U.S. dollar price is subject to exchange-rate fluctuations and is given only as a guide. Subscriptions are accepted on a prepaid basis only, unless different terms have been previously agreed upon.
Our p.p.h. (postage, packing and handling) charge includes surface delivery of all issues, except to subscribers in the U.S.A., Canada, Australia, New Zealand, China, India, Israel, South Africa, Malaysia, Thailand, Singapore, South Korea, Taiwan, Pakistan, Hong Kong, Brazil, Argentina and Mexico, who receive all issues by air delivery (S.A.L.-Surface Air Lifted) at no extra cost. For Japan, air delivery requires 25% additional charge of the normal postage and handling charge; for all other countries airmail and S.A.L. charges are available upon request.

Subscription orders. Subscription orders can be entered only by calendar year and should be sent to: Elsevier Science Publishers B.V., Journals Department, P.O. Box 211, 1000 AE Amsterdam, The Netherlands. Tel: (+31-20) 5803 642, Telex: 18582, Telefax: (+31-20) 5803598, to which requests for sample copies can also be sent. Claims for issues not received should be made within six months of publication of the issues. If not they cannot be honoured free of charge. Readers in the U.S.A. and Canada can contact the following address: Elsevier Science Publishing Co. Inc., Journal Information Center, 655 Avenue of the Americas, New York, NY 10010, U.S.A. Tel: (+1-212) 6333750, Telefax: (+1-212) 6333990, for further information, or a free sample copy of this or any other Elsevier Science Publishers journal.
Advertisements. Advertisement rates are available from the publisher on request.

Detailed "Instructions to Authors" for *Analytica Chimica Acta* was published in Volume 256, No. 2, pp. 373–376. Free reprints of the "Instructions to Authors" of *Analytica Chimica Acta* and *Vibrational Spectroscopy* are available from the Editors or from: Elsevier Science Publishers B.V., P.O. Box 330, 1000 AH Amsterdam, The Netherlands. Telefax: (+31-20) 5862845.

US mailing notice - Analytica Chimica Acta (ISSN 0003-2670) is published biweekly by Elsevier Science Publishers (Molenwerf 1, Postbus 211, 1000 AE Amsterdam). Annual subscription price in the USA US$ 2597.75 (subject to change), including air speed delivery. Second class postage paid at Jamaica, NY 11431. *USA Postmasters*: Send address changes to Anal. Chim. Acta, Publications Expediting, Inc., 200 Meacham Av., Elmont, NY 11003. Airfreight and mailing in the USA by Publication Expediting.

ANALYTICA CHIMICA ACTA

An international journal devoted to all branches of analytical chemistry

(Full texts are incorporated in CJELSEVIER, a file in the Chemical Journals Online database available on STN International; Abstracted, indexed in: Aluminum Abstracts; Anal. Abstr.; Biol. Abstr.; BIOSIS; Chem. Abstr.; Curr. Contents Phys. Chem. Earth Sci.; Engineered Materials Abstracts; Excerpta Medica; Index Med.; Life Sci.; Mass Spectrom. Bull.; Material Business Alerts; Metals Abstracts; Sci. Citation Index)

VOL. 278 NO. 2 CONTENTS JUNE 22, 1993

(Continued overleaf)

Contents (continued)

Analytica Chimica Acta, 278 (1993) 211–225
Elsevier Science Publishers B.V., Amsterdam

Synthesis and characterization of neutral hydrogen ion-selective chromoionophores for use in bulk optodes

Eric Bakker, Markus Lerchi, Thomas Rosatzin, Bruno Rusterholz and Wilhelm Simon [1]

Swiss Federal Institute of Technology (ETH), Department of Organic Chemistry, Universitätstrasse 16, CH-8092 Zürich (Switzerland)

(Received 17th November 1992; revised manuscript received 14th January 1993)

Abstract

The type of ion-selective sensors discussed is based on a solvent polymeric membrane with optical transduction (bulk optode), and requires a reversible mass transfer of analyte ions into and from the bulk of the organic phase. Apart from the ion to be analysed, such sensors simultaneously measure a reference ion. For analytical purposes, an H^+-selective carrier absorbing light in the visible range (chromoionophore) is incorporated in the membrane together with an ionophore as known from ion-selective electrodes. A series of neutral H^+-selective chromoionophores, synthesized with a view to their possible use in bulk optodes, are described. The results of various studies on the basicity in different solvents, lipophilicity, chemical stability, selectivity, molar absorption coefficients and absorbance maxima are given and, in part, discussed theoretically. It is shown that the chromoionophores described are highly selective and offer a wide range of basicities. Their lipophilicity usually guarantees a long lifetime for applications in both aqueous solutions and diluted blood and serum, but for measurements in undiluted blood samples they should be covalently immobilized to the polymer of the optode membrane. Their chemical stability is usually sufficient, only direct sunlight causing rapid decomposition.

Keywords: Ion selective electrodes; Sensors; Chromoionophores; Ion-selective optodes

About a decade ago, an irreversibly working test strip based on solvent polymeric membranes and an incorporated ionophore, as known from ion-selective electrodes (ISEs), was presented [1]. An anionic dye, erythrosin B, is added to the sample solution and its concentration retained in the membrane is detected as a function of the analyte ion concentration in the solution. Some years later, a novel device that measures alkali and alkaline earth metal ions was patented [2]. In the latter system, a neutral cation-selective ionophore and an H^+-selective chromoionophore are trapped in a solvent polymeric membrane. The chromoionophore involved is neutral in its protonated form and negatively charged in its unprotonated form (charged chromoionophore). By constant buffering of the sample pH, the device measures specific cation activities.

A different type of H^+-selective chromoionophore is positively charged in its protonated form and neutral in its unprotonated form (neutral chromoionophore). With both charged and neutral chromoionophores, ion-selective optodes are realizable. A detailed theoretical description of such sensors was not given until Morf and co-workers showed that the response of such optodes is based on a reversible mass transfer of analyte ions or electrically neutral molecules from the sample solution into the organic phase [3,4] (see also [5,6]). Ion-selective optodes were found to respond to activity products or ratios of two

Correspondence to: E. Bakker, Swiss Federal Institute of Technology (ETH), Department of Organic Chemistry, Universitätstrasse 16, CH-8092 Zürich (Switzerland).

[1] Deceased, 17th November 1992.

analyte ions, one of them serving as a reference ion. As H^+-sensitive chromoionophores are highly selective carriers, H^+ was chosen as the most suitable reference ion for all the cases described so far. By making lipophilic derivatives of conventional pH indicators, their properties have been adapted to fulfil different analytical needs.

In combination with neutral ionophores, the charged chromoionophores need the incorporation of cationic additives for anionic analytes and the neutral chromoionophores need anionic additives for cations, whereas the charged chromoionophores for cations and the neutral chromoionophores for anions do not require ionic additives. However, optodes with ionic additives are much better to describe theoretically [6]. Charged chromoionophores are therefore suited in anion-selective optodes and, to this end, a range of indonaphthol and eosin derivatives with different basicities have been described [2,7]. On the other hand, neutral chromoionophores have been successfully used in cation-selective optodes, e.g., for the determination of Ca^{2+} [8], NH_4^+ [9], K^+ [10], Na^+ [11], chiral ammonium derivatives [12,13] and Pb^{2+} [14]. The optodes were shown to meet the requirements for clinical analyses of diluted blood and serum samples [8,10,11], and their applicability for monitoring environmental processes is being investigated [14,15].

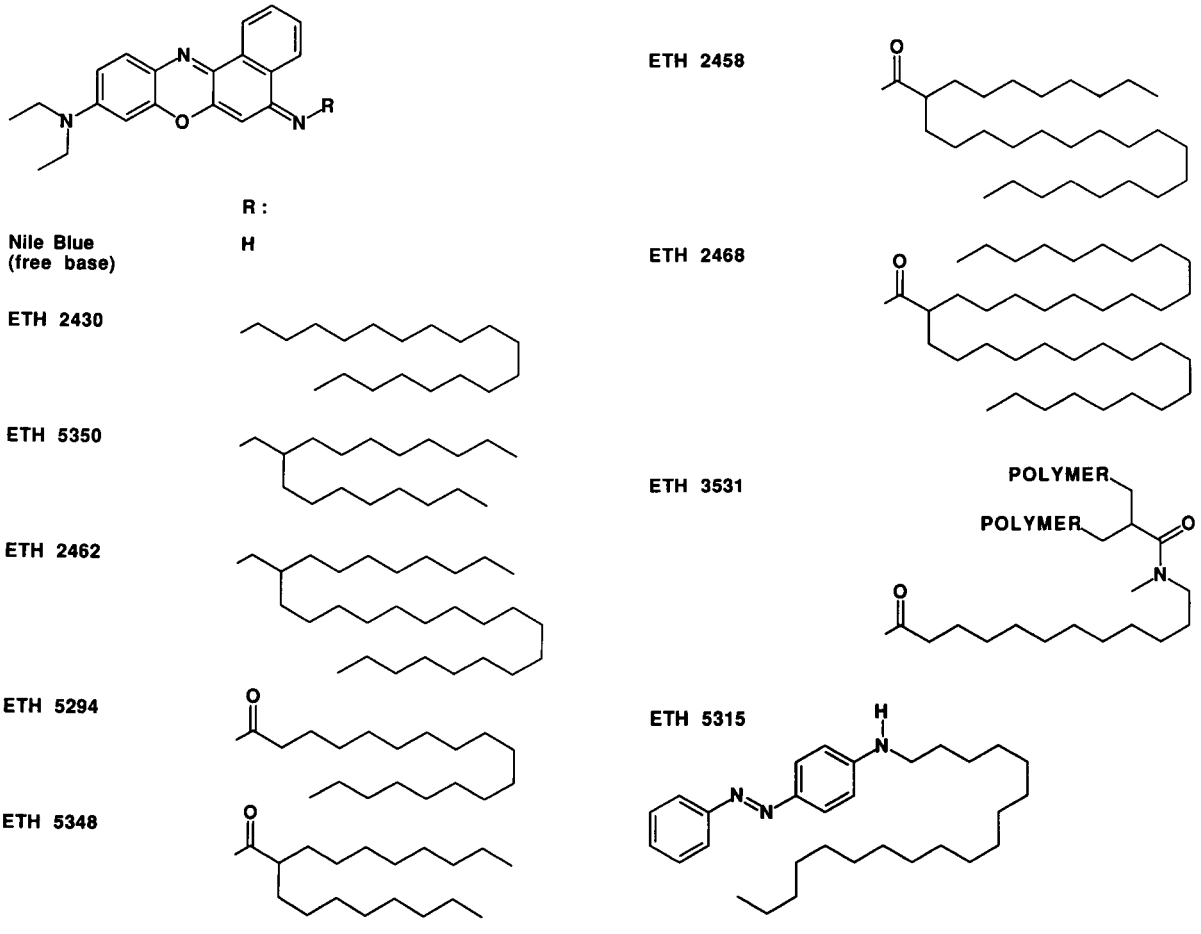

Fig. 1. Structural formulae of chromoionophores.

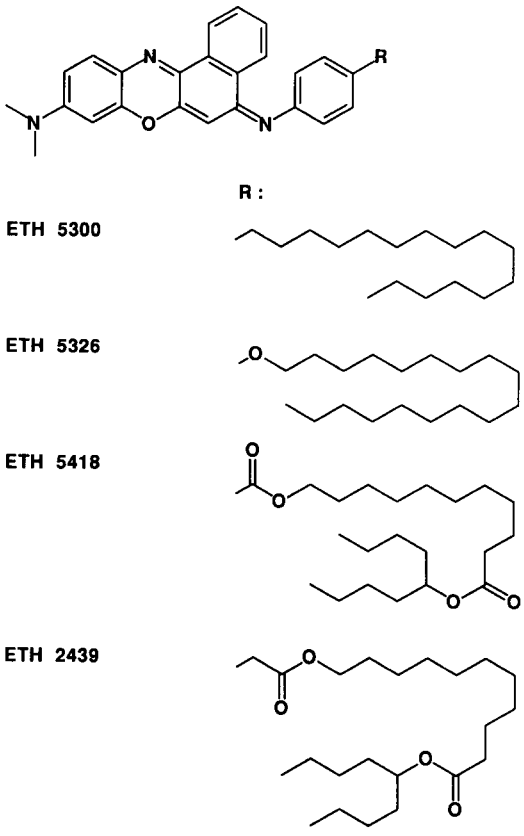

Fig. 1 (continued).

This paper reports on a series of neutral chromoionophores, i.e., several lipophilic Nile Blue derivatives and an azo compound, some synthesized in the laboratory and others commercially available [16]. They are characterized with respect to basicity in different solvents, lipophilicity, chemical stability and spectral properties, and are discussed in view of their possible use in optical sensors. However, they are equally suited as H^+ carriers in ISEs [17], as their characteristics are also valid for sensors with electrical transduction.

EXPERIMENTAL

All aqueous solutions were prepared with doubly quartz-distilled water and with reagents of the highest purity available. For membrane preparation, poly(vinyl chloride) (PVC, high molecular weight), potassium or sodium tetrakis[3,5-bis(trifluoromethyl)phenyl]borate (KTFPB or NaTFPB), bis(2-ethylhexyl) sebacate (DOS) and tetrahydrofuran (THF, freshly distilled prior to use) were obtained from Fluka (Buchs, Switzerland).

Apparatus

pH values were determined with a glass electrode (Orion Ross Model 81–02) and pH meter (Orion Model 920A) (Orion Research, Uetikon am See, Switzerland). Spectrophotometric studies on optode membranes were performed with a specially designed measuring cell [8] mounted in a Uvikon 810 conventional double-beam spectrophotometer (constant band width 2 nm) (Kontron, Zürich, Switzerland). Absorption spectra were usually recorded between 800 and 400 nm at 25 ± 1°C. In general, equilibrium was assumed to be reached when no detectable change in the absorption value was observed.

Buffers

Aqueous buffers. All activities were calculated according to the Debye–Hückel theory with parameters given in [18]. For the determination of K_{chrom} values in the membrane phase, dilute KOH solutions were used for the more basic chromoionophores, whereas potassium phosphate and acetate buffers [19] were chosen for membranes with the less basic chromoionophores (ETH 2439, ETH 5418, see Fig. 1; for chemical names, see *Syntheses of chromoionophores*) and with the azo compound (ETH 5315), respectively.

Methanol buffers. pH buffers in methanol were prepared according to [19].

Membrane preparation

Four types of solvent polymeric membranes were prepared, all of which contained DOS–PVC (2:1) and either a chromoionophore or a borate salt, or both:

Type 1: chromoionophore and NaTFPB (each 9.0 mmol kg^{-1})
Type 2: chromoionophore (8.5 mmol kg^{-1})
Type 3: NaTFPB (8.5 mmol kg^{-1})
Type 4: chromoionophore (1–10 mmol kg^{-1})

Membrane types 1 and 2 (1–5 μm thick, optode membranes) were prepared on glass plates with a specially designed spin-on device [5] and types 3 and 4 (ISE membranes) as described [20]. For membrane types 1, 2 and 4, the thickness and chromoionophore concentration were chosen so that the absorbance followed the Lambert–Beer law.

pK_a of chromoionophores

In methanol buffers. With a GC syringe (ITO, Fuji, Japan), 10 μl of 1×10^{-4} M chromoionophore in THF were injected into 2 ml of methanol buffer solutions (see *Buffers*) and the spectra were recorded immediately. From the absorption spectra taken at different pH values, the pK_a of the chromoionophore was determined at the point of half-protonation.

In the membrane phase. The overall equilibrium constant, K_{chrom}, of the chromoionophore in the membrane phase was determined by exposing membranes of type 1 to different buffers (see *Buffers* and Eqn. 3). The distribution coefficient of H^+ and K^+ between the organic and aqueous phases was estimated from the potentiometric selectivity coefficient k_{HK}^{pot} determined with ISEs on a membrane of type 3 using the following cell: $Hg \mid Hg_2Cl_2 \mid KCl$ (sat.) ¦ 1 M LiOAc ¦¦ sample ‖ membrane ‖0.1 M KCl | AgCl | Ag, with a calomel reference electrode of the free-flowing free-diffusion type [21]. The ISE assembly and measuring equipment have been described [20]. Membranes were conditioned in 0.1 M KCl overnight. Selectivity coefficients were determined by the separate solution method (SSM) [22] in 0.01 M HCl and KCl at 23 ± 1°C and calculated on the basis of the average e.m.f. values from three ISEs.

Lipophilicity of chromoionophores

Nile Blue. The free base of Nile Blue (0.20 mg) in DOS–PVC (2:1) (30.5 mg) and THF (1 ml) were mixed in a 7-ml glass vial (with screw-cap) (Müller & Krempel, Bülach, Switzerland). By rotating the open vial overnight, the THF was evaporated. The homogeneous membrane phase in the vial was then equilibrated with 5 ml of 0.01 or 0.001 M NaOH for 48 h in the dark. The concentration of Nile Blue in the aqueous phase was determined spectrophotometrically with the molar absorption coefficient, ϵ, of the protonated form in water as 7.2×10^4 l mol^{-1} cm^{-1}. The partition coefficient, log K (see Eqn. 6), of Nile Blue in a DOS–PVC (2:1) membrane was evaluated using $pK_a = 11.6$ (in water) [23].

ETH 5350. Membranes of type 1 containing ETH 5350 but only half the amount of borate (see *Membrane preparation*) were equilibrated with 0.01 M HCl, and the loss of chromoionophore was monitored spectrophotometrically using the flow-through cell described in [8]. The partition coefficient, log K, of ETH 5350 was calculated with $pK_a = 11.4$ (in water, see Table 1) and the co-extraction constant for the corresponding chloride, log $K_{coex} = 3.8$. For the definition of log K_{coex}, see [6].

Chemical stability of chromoionophores

The chemical stability of the protonated and unprotonated chromoionophores ETH 2439, ETH 5294, ETH 5315 and ETH 5350 was studied spectrophotometrically on membranes exposed to N_2, O_2, humidity or light and to combinations of these parameters. To protonate the chromoionophores, membranes of type 1 were conditioned in 0.01 M HCl for a few minutes. The unprotonated form was examined on unconditioned membranes of type 2, except with ETH 5315, where membranes of type 1 were equilibrated with 0.01 M KOH. The influence of gas phases and humidity was studied by flushing the cell with N_2 or O_2 that had been dried by passing through wash bottles containing molecular sieve and silica gel (with humidity indicator), or humidified by bubbling through water. Spectra were recorded every few hours at 25 ± 1°C without interrupting the gas flow. To investigate the effect of light, membranes on quartz plates were exposed to a halogen lamp (50 W, type 6462000E; Philips) placed 18 cm in front of the measuring cell, thus resulting in a temperature of ca. 28 ± 2°C. For comparing the results, the half-life of the chromoionophore under study was calculated assuming a first-order decomposition rate and, for each

membrane, normalizing the absorbance at the recording time $t = 0$ as 100%.

Molar absorption coefficients of chromoionophores

In methanol. In a 1-cm quartz cell, 5 μl (GC syringe) of 1×10^{-4} M chromoionophore in THF were dissolved in MeOH (2 ml). The absorption spectrum was recorded after first adding 3 μl of 1 M NaOH and then 10 μl of 1 M HCl to obtain the unprotonated and protonated form of the chromoionophore, respectively.

In membranes of type 1. After equilibrating membranes of type 1 with dilute HCl, absorption spectra were recorded. The thickness of the membranes was determined by spectrometric interferometry as described [24]. With these data and the concentration of the chromoionophore in the membrane phase, the molar absorption coefficient was calculated from the Lambert–Beer law, assuming the membrane density to be 1 kg l^{-1}.

In membranes of type 4. The molar absorption coefficients of ETH 5350, ETH 5294, ETH 2439 and ETH 5315 were determined at concentrations of 0.901, 9.72, 0.822 and 2.14 mmol kg^{-1}, respectively, on membranes of type 4. After marking the membranes on the top and bottom sides, their thickness was obtained by focusing the two marks under a light microscope (BH-2 Olympus). By calibration with a 2-mm glass plate, the exact thickness of which had been ascertained with a 25-mm micrometer screw, 1 scale unit of the fine focus adjustment knob of the microscope was found to correspond to 1.6 μm.

Syntheses of chromoionophores

The preparation of the following chromoionophores has been published already: free base of Nile Blue (*N,N*-diethyl-5-imino-5*H*-benzo[*a*]phenoxazin-9-amine), *N,N*-diethyl-5-(octadecanoylimino)-5*H*-benzo[*a*]phenoxazin-9-amine (ETH 5294) [8]; Nile Blue bound to carboxylated PVC by means of 12-(methylamino)dodecanoyl as spacer (ETH 3531), *N,N*-(diethyl)-5-[(2-octyldecanoyl)imino]-5*H*-benzo[*a*]phenoxazin-9-amine (ETH 5348), *N,N*-(diethyl)-5-[(2-octyldecyl)imino]-5*H*-benzo[*a*]phenoxazin-9-amine (ETH 5350) [24]; 11-[(-butylpentyl)oxy]-11-oxoundecyl 4-{[9-(dimethylamino)-5*H*-benzo[*a*]phenoxazin-5-ylidene]amino}benzoate (ETH 5418), 4-(octadecylamino)azobenzene (ETH 5315) [14].

Synthesis of N,N-Diethyl-5-(octadecylimino)-5H-benzo[a]phenoxazin-9-amine (ETH 2430)

This was prepared and purified as described for ETH 5350 [24], obtaining a 7.7% yield. Analysis: calculated for $C_{38}H_{55}N_3O$ (569.87), C 80.09, H 9.73, N 7.37; found, C 79.99, H 9.89, N 7.09%.

Synthesis of 11-[(1-butylpentyl)oxyl]-11-oxoundecyl 4-{[9-(dimethylamino)-5H-benzo[a]phenoxazin-5-ylidene]amino}benzeneacetate (ETH 2439)

11-Bromoundecanoyl chloride. To a solution of 11-bromoundecanoic acid (5.0 g, 19 mmol) (Fluka, pract.) in toluene (80 ml), thionyl chloride (10 ml, 138 mmol) in toluene (20 ml) was added dropwise at room temperature. After stirring the reaction mixture at room temperature for 18 h and at 80°C for 2 h, the solvent was evaporated and the residue purified by bulb-to-bulb distillation (150–160°C, 0.09 Torr), obtaining the product (4.2 g, 14.8 mmol, 77.9%).

11-Bromo-(1-butylpentyl) undecanoate. To a solution of triethylamine (1.1 g, 11 mmol) (Fluka, puriss. p.a.) and nonan-5-ol (1.4 g, 10 mmol) (Fluka, puriss.) in diethyl ether (40 ml), 11-bromoundecanoyl chloride (2.8 g, 10 mmol) in diethyl ether (10 ml) was added dropwise at 0–5°C and the reaction mixture stirred at room temperature for 4 h. The precipitate was filtered off and the filtrate evaporated. The crude product was purified by flash chromatography [silica gel, hexane–ethyl acetate (9 + 1)] and bulb-to-bulb distillation (190°C, 0.04 Torr) to yield the product (1.6 g, 4.1 mmol, 41%).

11-[(1-Butylpentyl)oxy]-11-oxoundecyl 4-aminobenzeneacetate. A solution of 4-aminobenzeneacetic acid (1.51 g, 10 mmol) (Fluka, purum), 11-bromo-(1-butylpentyl) undecanoate (3.91 g, 10 mmol) and 1,8-diazabicyclo[5.4.0]undec-7-ene (1.52 g, 10 mmol) (Fluka, purum) in toluene (80 ml) was refluxed for 3 h. The reaction mixture was washed twice with water and the organic phase was dried over Na_2SO_4. After evaporating the solvent, the residue was purified by flash

chromatography [silica gel, hexane–ethyl acetate (7 + 3)] to give the product (2.13 g, 4.6 mmol, 46%).

9-(Dimethylamino)-5H-benzo[a]phenoxazonium nitrate (Meldola Blue nitrate). 9-(Dimethylamino)-5*H*-benzo[*a*]phenoxazine hemi(zinc chloride) (600 mg, 1.6 mmol) (Sigma) was dissolved in distilled water (40 ml) at 50–60°C. The solution was filtered and HNO_3 (65%, 1.5 ml) added to the filtrate. After leaving it at 5°C overnight, the resulting precipitate was filtered off and dissolved in ethanol (15 ml). Hexane (150 ml) was added and the precipitate was filtered, washed with hexane (50 ml) and dried under high vacuum, yielding Meldola Blue nitrate (405 mg, 1.2 mmol, 76%).

ETH 2439. A solution of Meldola Blue nitrate (168 mg, 0.5 mmol) and 11-[(1-butylpentyl)oxy]-11-oxoundecyl 4-aminobenzeneacetate (230 mg, 0.5 mmol) in ethanol (10 ml) was stirred in an open flask overnight. The reaction mixture was then diluted with CH_2Cl_2 (60 ml) and washed with 0.1 M NaOH (80 ml). After filtering the organic phase and evaporating the solvent, the residue was purified by flash chromatography [silica gel, hexane–ethyl acetate (7 + 3)] and three recrystallizations from hexane, obtaining pure ETH 2439 (125 mg, 0.17 mmol, 34%). Analysis: calculated for $C_{46}H_{59}N_3O_5$ (734.0), C 75.27, H 8.10, N 5.72; found, C 75.26, H 8.32, N 5.51%.

Synthesis of N,N-Diethyl-5-[(2-octyleicosanoyl) imino]-5H-benzo[a]phenoxazin-9-amine (ETH 2458)

This was synthesized as described for ETH 5348 [24], but instead of 2-octyldecanoic acid chloride using 2-octyleicosanoic acid chloride prepared accordingly [24]. The crude product was recrystallized from hexane to give pure ETH 2458 (54% yield). Analysis: calculated for $C_{48}H_{73}N_3O_2$ (724.13), C 79.62, H 10.16, N 5.80; found, C 79.45, H 10.38, N 5.85%.

Synthesis of N,N-Diethyl-5-[(2-octyleicosyl)]imino-5H-benzo[a]phenoxazin-9-amine (ETH 2462)

This was prepared as described for ETH 5350 [24]. The crude product was purified by flash chromatography [silica gel, CH_2Cl_2–acetone (1 + 1)], obtaining ETH 2462 (9.3% yield). Analysis: calculated for $C_{48}H_{75}N_3O$ (710.14), C 81.18, H 10.65, N 5.92; found, C 81.24, H 10.38, N 5.69%.

Synthesis of N,N-Diethyl-5-[(2-octadecyleicosanoyl)imino]-5H-benzo[a]phenoxazin-9-amine (ETH 2468)

This was prepared as described for ETH 5348 [24], but instead of 2-octyldecanoic acid chloride using 2-octadecyleicosanoic acid chloride which had been obtained accordingly [24]. The crude product was recrystallized three times from hexane to give pure ETH 2468 (6.4% yield). Analysis: calculated for $C_{58}H_{93}N_3O_2$ (864.40), C 80.59, H 10.84, N 4.86; found, C 80.67, H 10.78, N 4.86%.

Synthesis of 9-(Dimethylamino)-5-[(4-hexadecyl)phenylimino]-5H-benzo[a]phenoxazine (ETH 5300)

This was prepared as described for ETH 2439, but in the last step using 4-hexadecylaniline (Aldrich) instead of the 4-aminobenzeneacetate. The crude product was purified by flash chromatography [basic alumina, hexane–ethyl acetate (9 + 1)] and recrystallized from ethyl acetate to give ETH 5300 (11% yield). Analysis: calculated for $C_{40}H_{51}N_3O$ (589.87), C 81.45, H 8.71, N 7.12; found, C 81.47, H 8.82, N 7.03%.

Synthesis of 9-(Dimethylamino)-5-[(4-octadecyloxy)phenylimino]-5H-benzo[a]phenoxazine (ETH 5326)

This was prepared as described for ETH 2439, but in the last step using 4-octadecyloxyaniline (Alfred Bader Chemicals) instead of the 4-aminobenzeneacetate. The crude product was purified by flash chromatography [basic alumina, CH_2Cl_2–ethanol (99 + 1)] and dissolved in a small amount of CH_2Cl_2. Hexane was added and the precipitate filtered off to give pure ETH 5326 (13% yield). Analysis: calculated for $C_{42}H_{55}N_3O_2$ (633.92), C 79.58, H 8.75, N 6.63; found: C 79.47, H 8.89, N 6.32%.

The constitutions of all the chromoionophores synthesized were confirmed by ^1H NMR (300 MHz, $CDCl_3$), IR ($CHCl_3$) and fast atom bombardment mass spectrometry.

RESULTS AND DISCUSSION

The chromoionophores presented (see Fig. 1) are mainly derivatives of Nile Blue, a common basic pH indicator. In addition, a lipophilized azo compound of weaker basicity is shown in membrane phases to behave similar to the more basic chromoionophores. As components in optodes, they all serve for determining specific cation activities. Optode membranes were prepared with PVC as matrix and bis(ethylhexyl) sebacate (DOS) as lipophilic plasticizer [25], although not all chromoionophores were sufficiently soluble in this system. As ETH 5300 slowly crystallized in the membrane, it was replaced with the much better soluble ETH 2439. Membranes with the highly lipophilic ETH 2468 showed good performance during short-time experiments, but after several days a slight decrease in the signal of the protonated form was observed, probably owing to insufficient solubility. Nevertheless, the two chromoionophores were included in the study, as solubility problems could be overcome by altering the membrane composition.

Basicity

By knowing the relative basicity of different chromoionophores in the membrane phase, it is possible to compare the response curves of the respective bulk optodes, to predict their relevant analytical range and determine very high selectivities, i.e., of more than ten orders of magnitude [14]. On the other hand, the absolute basicity of these compounds in water is important for determining their lipophilicity (see *Lifetime*).

Basicity in amphiprotic media. As the lipophilic chromoionophores are not sufficiently soluble in water, their pK_a values were measured in methanol buffers. The titration of ETH 5418 with HCl in Fig. 2 demonstrates the suitability of methanol as solvent. The pK_a(MeOH) of all the chromoionophores could thus be determined, only the experimental data of the less soluble ones (ETH 2468, ETH 5326) not completely agreeing with the theoretical curves.

For compounds of comparable chemical structure, the pK_a in water and methanol can be correlated in a first approximation [26]:

$$pK_a(H_2O) = pK_a(MeOH) + c \quad (1)$$

From the pK_a of Nile Blue in water and methanol, c was determined as -0.7, and on this basis the pK_a values of the other chromoionophores measured in methanol were estimated in water (see Table 1).

Basicity in the membrane phase. In addition to

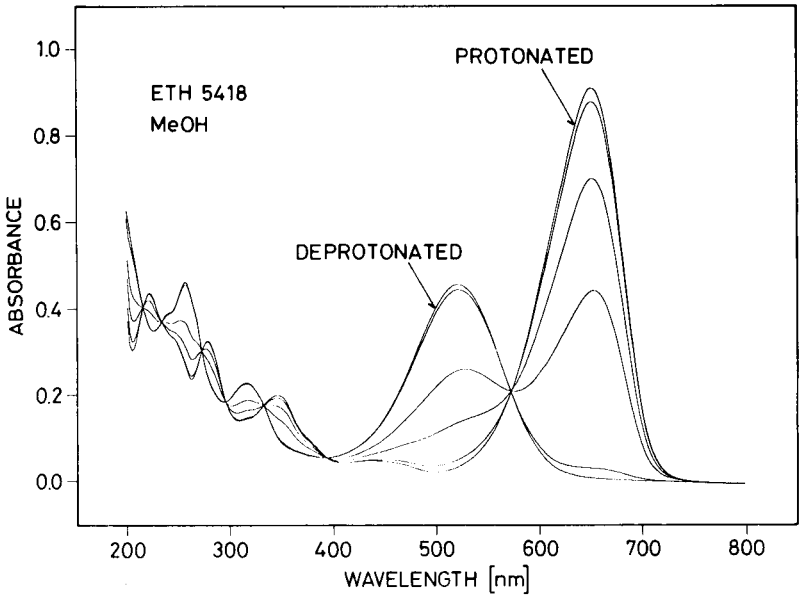

Fig. 2. Spectra in the course of a typical titration of the chromoionophore ETH 5418 in methanol with HCl.

TABLE 1

pK_a values of chromoionophores in different solvent phases at 25 ± 1°C

Compound	pK_a(MeOH) [a]	$pK_a(H_2O)$ [b]	$-\text{Log } K_{chrom}$ [a]	pK_a(membr) [c]
Nile Blue	12.2 (0.05; 6)	11.6 [d]	13.8 [e] (0.03; 3)	14.0
ETH 2430	12.1 (0.03; 6)	11.5	13.5 (0.04; 4)	13.7
ETH 2439	8.3 (0.05; 6)	7.7	10.0 (0.14; 4)	10.2
ETH 2458	10.5 (0.04; 7)	9.9	11.9 (0.02; 5)	12.1
ETH 2462	12.1 (0.04; 7)	11.5		
ETH 2468	10.4 (0.14; 6)	9.8	12.0 (0.01; 4)	12.2
ETH 3531			11.5 [f]	11.7
ETH 5294	10.6 (0.07; 6)	10.0	11.8 (0.06; 5)	12.0
ETH 5300	8.1 (0.09; 5)	7.5		
ETH 5315	3.6 (0.06; 6)	3.0	5.0 (0.06; 6)	5.2
ETH 5326	8.5 (0.23; 5)	7.9		
ETH 5348	10.5 (0.07; 6)	9.9	11.7 (0.10; 5)	11.9
ETH 5350	12.0 (0.07; 6)	11.4	13.2 (0.03; 4)	13.4
ETH 5418	7.4 (0.03; 5)	6.8	8.8 (0.02; 4)	9.0

[a] Experimental values; in parentheses: S.D. and number of data points. [b] Estimated from Eqn. 1. [c] Estimated on the basis of potentiometric measurements with cation-exchange membranes and from Eqn. 3. [d] Experimental value [23]. [e] Experimental value [28]. [f] Extrapolated from measurements with Ca^{2+}-selective optodes (cf. [24]).

the pK_a determination in methanol, the relative basicity of the chromoionophores in the membrane phase was evaluated. As absolute pK_a values in aprotic media are not easily accessible, phase-transfer equilibria for H^+ and the relatively lipophilic K^+ were studied on optode membranes containing the chromoionophore C and lipophilic anionic sites R^-. On the assumption that no ion pairs are formed and no specific interaction occurs between K^+ and C, the cation-exchange equilibrium, which depends on the basicity of C, corresponds to

$$K^+(aq) + CH^+(org) \rightleftharpoons K^+(org) + C(org) + H^+(aq) \quad (2)$$

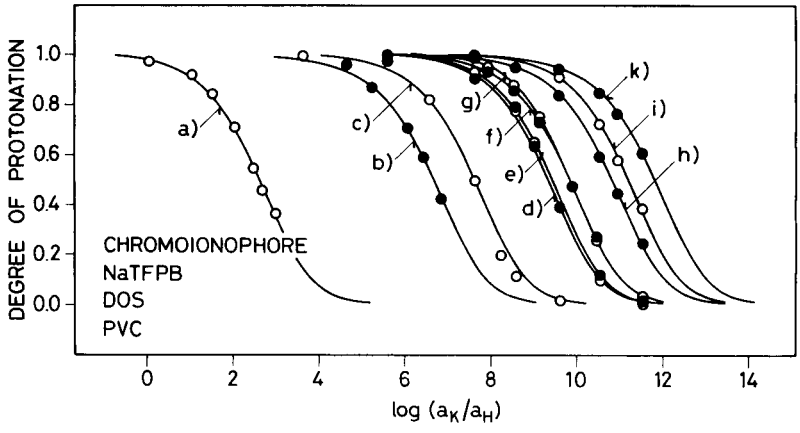

Fig. 3. Determination of the relative basicity of chromoionophores in the membrane phase [DOS–PVC (2:1)] in a cation-exchange system with K^+ as the exchanger cation [14]. (a) ETH 5315; (b) ETH 5418; (c) ETH 2439; (d) ETH 5348; (e) ETH 5294; (f) ETH 2458; (g) ETH 2468; (h) ETH 5350; (i) ETH 2430; (k) Nile Blue. On the first contact of the membranes with water, Na^+ of the lipophilic additive NaTFPB is completely exchanged by H^+. Solid curves were calculated according to Eqn. 3, using the overall equilibrium constants log K_{chrom} given in Table 1.

with the overall equilibrium constant K_{chrom} given by

$$K_{chrom} = \frac{[K^+]_{org}[C]_{org}(H^+)_{aq}}{(K^+)_{aq}[CH^+]_{org}} = \frac{k_K}{k_H} \cdot K_a \qquad (3)$$

where brackets refer to concentrations and parentheses to activities. The ratio of the activity coefficients of K^+ and CH^+ in the organic phase is assumed to be 1. The value of K_{chrom} depends on the pK_a of C and on the distribution coefficients k_K and k_H of the uncomplexed K^+ and H^+ between the aqueous and organic phases. With different chromoionophores, k_H and k_K are assumed to be constant and expected to be influenced only by varying the membrane solvent and/or matrix. On the other hand, on replacing K^+ with another cation, the corresponding distribution coefficient, and hence K_{chrom}, will change.

The results of the spectrophotometric determination [14] of the overall equilibrium constant K_{chrom} are presented in Fig. 3 and Table 1. The ratio of the K_{chrom} values for two chromoionophores gives the difference in their basicities. This also holds for optode membranes sensitive to cations other than K^+ and in addition containing an ionophore [14].

The relative basicities (log K_{chrom}) in the membrane phase [DOS–PVC (2:1)] and the absolute pK_a values in methanol are compared in Fig. 4. A good correlation is obtained, which in analogy to Eqn. 1 corresponds to

$$-\log K_{chrom} = pK_a(MeOH) + \Delta \qquad (4)$$

with $\Delta = 1.43$ and S.D. = 0.19. Obviously, the relative pK_a values of the chromoionophores in the membrane phase can be determined by this approach.

For estimating the absolute pK_a values in the membrane phase (see Eqn. 3), the ratio of the distribution coefficients, k_K/k_H, was approximated by determining the potentiometric selectivity coefficient k_{KH}^{pot} for the same cation-exchange membrane as above but without chromoionophore, and with the assumptions discussed elsewhere [27]. With $\log k_{KH}^{pot} = -0.2$, $\log(k_K/k_H)$ was estimated as 0.2. In Table 1, the approximate pK_a of the chromoionophores in the membrane

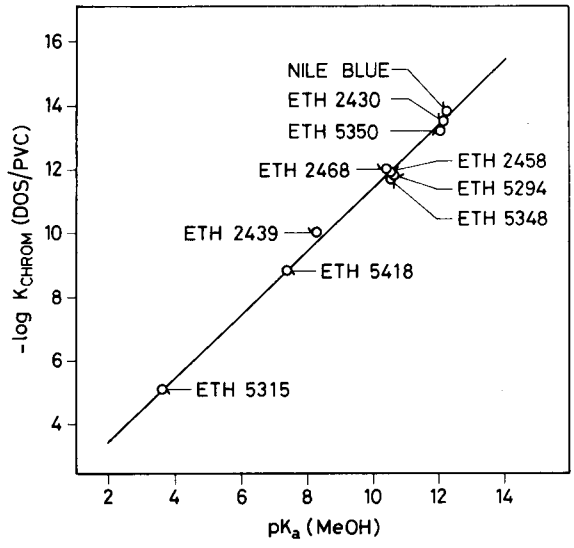

Fig. 4. Correlation of overall equilibrium constants $-\log K_{chrom}$ of chromoionophores in the membrane phase [DOS–PVC (2:1)] with pK_a values determined in methanol buffers. Solid line according to Eqn. 4 with slope of unity.

phase [DOS–PVC (2:1)] as calculated from Eqn. 3 is given. A comparison of the pK_a values obtained for the different solvent systems shows that the chromoionophores are more basic in the membrane phase than in amphiprotic media. This may be due to stronger solvation of H^+ in methanol and water [26].

Lifetime

As the signal of optical sensors depends strongly on the membrane composition, the lifetime of these devices is primarily governed by the chemical stability of the compounds involved and their leaching rate from the membrane. As discussed elsewhere [29], the latter is mainly determined by the lipophilicity of the membrane components, which is defined as the partition coefficient k of a compound between organic and aqueous phases. For compounds of relatively high lipophilicity, the concentration decrease with time follows the relationship [30]

$$\ln\left[\frac{c_{tot}(org, 0)}{c_{tot}(org, t)}\right] = \frac{D_{aq}}{kd\delta} \cdot t \qquad (5)$$

where $c_{tot}(org, 0)$ and $c_{tot}(org, t)$ represent the

total concentration of the compound in the organic phase at time $t = 0$ and $t > 0$, respectively, D_{aq} is the diffusion coefficient of the compound in the aqueous phase, δ the thickness of the Nernstian boundary layer of the aqueous phase and d that of the organic phase.

The diffusion coefficient of most compounds in aqueous phase lies in the narrow range of $(2\text{–}5) \times 10^{-6}$ cm^2 s^{-1} [25]. The thickness of the Nernstian boundary layer depends on the viscosity and convection of the aqueous phase and the geometry of the measuring cell [30]. As optode membranes of the type described in this paper normally have a thickness of a few μm and their signal is directly proportional to the amount of membrane components, they suffer much more from leaching than ISE membranes, where the amount of ionophore may decrease considerably before a dramatic change in the response properties is observed. The leaching from optode membranes can be corrected to some extent, however, by recording the isosbestic point in the absorbance spectrum.

For an electrically neutral species (e.g., a chromoionophore C) with no complexing capabilities, the thermodynamic partition coefficient

$$K = [C]_{org}/[C]_{aq} \tag{6}$$

is assumed to be equal to k. This only holds for membrane components such as plasticizers and electrically neutral ionophores, which do not, or only very weakly, form complexes in the aqueous phase [31]. For basic chromoionophores, however, the lipophilicity k is not generally a constant, but depends on the sample pH because of C being protonated in the aqueous and organic phase [32]:

$$k = \frac{[C]_{org} + [CH^+]_{org}}{[C]_{aq} + [CH^+]_{aq}} \tag{7}$$

Equation 5 is valid if the diffusion coefficients of the protonated and unprotonated chromoionophore in the aqueous phase are comparable. As measurements with optodes are usually performed around half-protonation of the chromoionophore ($[C]_{org} = [CH^+]_{org}$), Eqn. 7 can be rewritten with Eqn. 6 and the acidity constant K_a of the chromoionophore in the aqueous phase:

$$k = 2 \cdot \frac{[C]_{org}}{[C]_{aq}} \cdot \frac{K_a}{K_a + (H^+)_{aq}} = 2K \cdot \frac{K_a}{K_a + (H^+)_{aq}} \tag{8}$$

where $(H^+)_{aq}$ is the hydrogen ion activity in the aqueous sample solution. Evidently, if $(H^+)_{aq} \gg K_a$, the lipophilicity k is significantly reduced. For its evaluation, K and K_a must be determined separately. The former can be obtained by different approaches: calculation of the Hansch partition coefficient P_H in the system octanol–water by adding up structural parameters [33]; determination of the retention time by thin-layer chromatography (TLC) which can be referred to the partition coefficient P_{TLC} in octanol–water by using standard compounds of known lipophilicity [30]; experimental evaluation of the partition coefficient K between the membrane phase and aqueous sample solution by means of leaching experiments with optode membranes [30].

Thermodynamic partition coefficients for the solvent systems octanol–water (P) and membrane phase–aqueous sample solution (K) follow a linear relationship [29]:

$$\log K = a \log P + b \tag{9}$$

The values of a and b were found to be 0.4 and 0.8, respectively, for the extraction system membrane phase–water and 0.48 and 0.33, respectively, for the system membrane phase–undiluted serum [29,30]. Owing to the strong basicity of the chromoionophores, their P_{TLC} could not be measured. The lipophilicity increment of the conjugated system common to all but ETH 5315 being difficult to calculate [33], log K of Nile Blue was determined from leaching experiments as 4.6. Additional increments for the side-chains were then calculated according to Hansch [33]. In Table 2, log P_H for octanol–water is given together with log K for the systems (DOS–PVC)–water and (DOS–PVC)–undiluted serum.

Figure 5 shows the partition coefficient log k for the system (DOS–PVC)–water calculated from Eqn. 8 with log K from Table 2 and pK_a(H_2O) from Table 1 as a function of the

TABLE 2

Lipophilicity constants of chromoionophores in different extraction systems

Compound	Log P_H [a]	Log K		
		(DOS–PVC)–water		(DOS–PVC)–serum: calc. [b]
		Exp.	Calc.	
Nile Blue	5.2	4.6 [c]		
ETH 2430	15.1		12.5	5.5
ETH 2439	13.1		10.9	4.8
ETH 2458	18.4		15.1	6.6
ETH 2462	20.3		16.6	7.2
ETH 2468	23.8		19.4	8.3
ETH 5294	13.1	10.6 [d]	10.9	4.8
ETH 5300	14.5		12.0	5.3
ETH 5326	14.9		13.3	5.4
ETH 5348	13.0		10.8	4.8
ETH 5350	14.9	13.6 [c]	12.3	5.4
ETH 5418	13.5		11.2	4.9
ETH 5315	11.1		9.3	4.1

[a] Calculated for the extraction system octanol–water according to Hansch [33], with the lipophilicity increment for the conjugated system of Nile Blue estimated from experimental data using Eqn. 9 (see text). [b] Calculated from Eqn. 9 for the extraction systems membrane phase–water (with $a = 0.4$, $b = 0.8$) and membrane phase–undiluted serum (with $a = 0.48$, $b = 0.33$) [29]. [c] At 23 ± 1°C. [d] From experimental data given in [24].

sample pH. According to Eqn. 5, the required log k value for a typical optode membrane is 9.3, with $D_{aq} = 5 \times 10^{-6}$ cm^2 s^{-1}, $\delta = 30$ μm [25], $d = 2$ μm and assuming a concentration decrease of 1% within 30 days. Obviously, the most basic chromoionophores are the least lipophilic, but few of them do not meet the required log k value in aqueous solution and in diluted serum at moderate and higher pH. For acidic samples, only the highly lipophilized derivatives of the most basic chromoionophores are adequate. From Table 2 and Eqn. 8, it can be deduced that in the system membrane phase–undiluted serum, log k is smaller than 9.3 for all chromoionophores (except for the covalently immobilized derivative ETH 3531 of theoretically infinite lipophilicity), which therefore are unsuitable, even at higher pH. Further lipophilization of the compounds may lead to solubility problems and, therefore, the chemical immobilization of pH indicators seems to be the most promising way to prolong the lifetime of optode membranes for the clinical analysis of biological fluids [24,34].

Chemical stability

Light, oxygen, humidity and their possible combinations are the most important deteriorating factors when handling optode membranes in the laboratory and in routine work. Their influence on four chromoionophores of different basicity (ETH 2439, ETH 5294, ETH 5315 and ETH 5350) was therefore examined in the membrane phase. To exclude leaching effects, the measuring cell in these experiments contained no solution. In Table 3, the long-term stabilities of the species investigated are summarized. As typical example, Fig. 6 shows the results obtained for the unprotonated form of ETH 5350. The combined effects of light and O_2 evidently caused light-induced

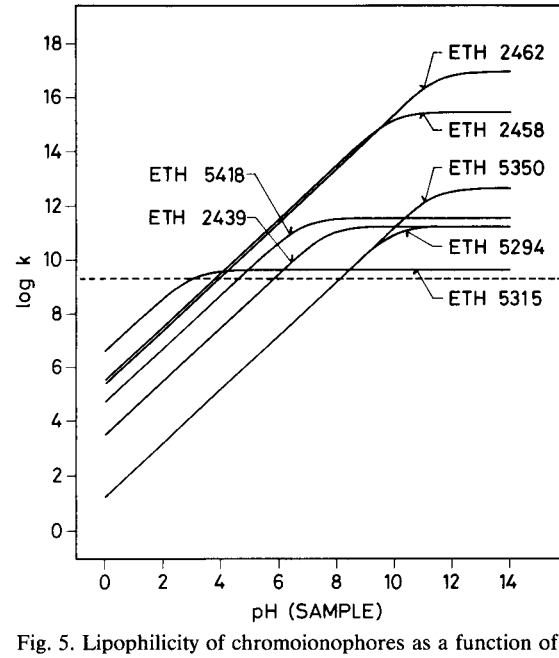

Fig. 5. Lipophilicity of chromoionophores as a function of the pH of aqueous sample solutions, calculated with Eqn. 8, assuming half-protonation of the chromoionophore. Lipophilicity increments were determined according to Hansch [33] and pK_a values in water were extrapolated from measurements in methanol buffers (Eqn. 1). Dashed line: required minimum lipophilicity (log $k \geq 9.3$) for a membrane of thickness 2 μm and a decrease in chromoionophore concentration of 1% within 1 month (see text).

TABLE 3

Half-lives (h) of protonated (prot.) and unprotonated (unprot.) chromoionophores in DOS–PVC (2:1) membranes assuming first-order decomposition (25 ± 1°C; for exposure to light: ca. 28 ± 2°C) [a]

Exposures [b]	ETH 2439		ETH 5294		ETH 5315 [c]: unprot.	ETH 5350	
	Prot.	Unprot.	Prot.	Unprot.		Prot.	Unprot.
N_2	+	+	+	+	+	+	+
O_2	+	+	+	+	+	(+)	+
H_2O, N_2	+	+	+	+	+	+	+
H_2O, O_2	+	+	(+)	+	+	+	+
$h\nu$, N_2	+	+	35	6.1	+	(+)	51
$h\nu$, O_2	+	+	46	3.9	+	6.1	4.7
$h\nu$, H_2O, N_2	76	+	25	9.5	+	72	24
$h\nu$, H_2O, O_2	+	+	39	3.3	+	24	10
Conclusion: sensitive to	–		Light		–	Light-induced oxidation	

[a] + = Stable absorbance at λ_{max} within 22–50 h of exposure; (+) = half-life (> 100 h) could not be evaluated from experimental results. [b] H_2O, humidity; $h\nu$, 50-W halogen lamp (see Experimental). [c] No measurements possible for the protonated form (see text).

oxidation, but in a humid atmosphere the process slowed (see Table 3). With ETH 5294, the influence of light was dominant, the other parameters having little impact. The less basic Nile Blue derivative ETH 2439 was found to be more stable than the other two. Only when its protonated form was exposed to light and humidity did the absorbance decrease by about 8% within 10 h. In borate-free membranes, the unprotonated diazo compound ETH 5315 proved to be stable in all these experiments, but in membranes containing borate, rapid decomposition of NaTFPB was observed [35]. From Table 3, it can be concluded that the electrically neutral chromoionophores

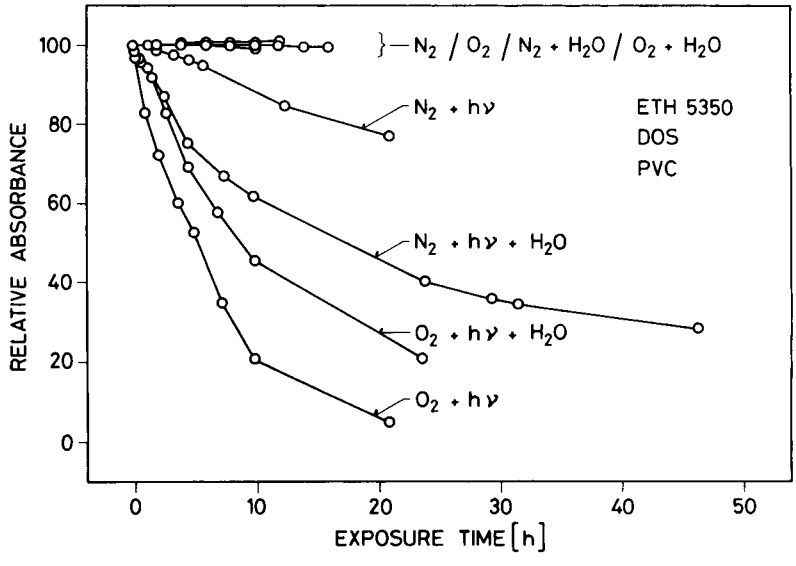

Fig. 6. Decomposition of the unprotonated chromoionophore ETH 5350 in the membrane phase [DOS–PVC (2:1)] when exposed to N_2, O_2, humidity (H_2O), or light ($h\nu$), or to combinations of these parameters (see Experimental). For comparison purposes, the initial absorbance of the unprotonated chromoionophore at λ_{max} was set to 100%.

TABLE 4

Exposure of the unprotonated form of ETH 5294 in DOS–PVC (2:1) membranes to different light sources

Light source	Exposure time (h)	Relative absorbance [a] after exposure (%)
Daylight [b]	3.0	94
50-W halogen lamp	4.0	30
Direct sunlight [c]	0.5	47
Sunlight [d]	4.0	10

[a] Measured at $\lambda_{max} = 536$ nm with $A(t = 0) = 100\%$ (see Experimental). [b] In laboratory with additional neon light. [c] Membrane on top of glass plate. [d] Membrane under glass plate.

studied are more stable in the protonated than in the unprotonated form.

As light is a major deteriorating factor, membranes containing unprotonated ETH 5294 (having the shortest half-life) on their glass supports were exposed to different light sources (see Table 4). Under the usual laboratory conditions, the decomposition was found to be very slow, whereas direct sunlight, owing to its higher UV content had a strong influence. It is therefore recommended that optodes with such chromoionophores be stored in the dark when not in use. As the absorption is in the visible range (see Table 5), the observed UV sensitivity is no obstacle during long-time experiments as long as other light sources are excluded. In all experiments, decomposition products absorbing in the visible range were absent.

Selectivity

In optode membranes, H^+-selective chromoionophores should exhibit no affinity to other cations, as this would result in a decreased selectivity compared with analogous ISE membranes. Maximum affinity is observed when no additional ionophore is present [6]. If strong complexation occurs, e.g., with K^+, the exchange equilibrium for H^+ and K^+ can be formulated as

$$K^+(aq) + CH^+(org) \rightleftharpoons CK^+(org) + H^+(aq) \quad (10)$$

whose exchange constant, taking into account Eqn. 3, corresponds to

$$K_{exch} = \frac{[CK^+]_{org}(H^+)_{aq}}{(K^+)_{aq}[CH^+]_{org}} = \frac{k_K}{k_H} \cdot K_a \beta_{CK} = K_{chrom} \beta_{CK} \quad (11)$$

TABLE 5

Wavelength maxima (λ_{max}) and molar absorption coefficients (ϵ) of chromoionophores in methanol and DOS-PVC (2:1) membranes [a]

Compound	Protonated				Unprotonated			
	λ_{max} (nm)		$\epsilon(10^4$ l mol^{-1} cm^{-1})		λ_{max} (nm)		$\epsilon(10^4$ l mol^{-1} cm^{-1})	
	MeOH	Membrane	MeOH	Membrane	MeOH	Membrane	MeOH	Membrane
Nile Blue	625	638	2.5		511	510	1.3	
ETH 2430	634	644	8.0	6.0 [a]	510	498	4.1	3.0 [b]
ETH 2439	648	656	7.2	7.1 [c]	518	512	3.4	3.2 [c]
ETH 2458	639	658	3.8	5.0 [b]	552	536	3.1	2.4 [b]
ETH 2462	614	642	1.8	4.6 [b]	514	505	1.1	2.2 [b]
ETH 2468	640	658	3.8		552	542	3.2	
ETH 3531		660				545		
ETH 5294	640	658	3.1	2.0 [b]; 6.9 [c]	540	536	2.3	1.6 [b]; 5.4 [c]
ETH 5300	646	659	7.7		514	445	1.9	
ETH 5315	507	514		4.5 [c]	403	404		2.6 [c]
ETH 5326	646	656	7.7		454	444	1.3	
ETH 5348	638	658	3.6		552	538	2.9	
ETH 5350	637	645	8.1	8.2 [b]; 8.5 [c]	508	498	3.9	3.3 [b]; 3.4 [c]
ETH 5418	656	664	7.9		524	522	3.9	

[a] The density of membranes was assumed to be 1 kg l^{-1}. The protonated forms of ETH 2458, ETH 2468, ETH 5294 and ETH 5348 have a second λ_{max} around 600 nm, which was not used. [b] Based on membrane thickness determined by the interference method [24]. [c] Based on measurements of membrane thickness with a light microscope (see Experimental).

The stability constant β_{CK} refers to the chromoionophore–K^+ complex in the membrane phase and is assumed to be different for chromoionophores of different basicity. Hence, no linear correlation would be expected between the overall equilibrium constant K_{chrom} and the acidity constant K_a(MeOH). In contrast, the correlation in Fig. 4 shows that the cation-exchange equilibria discussed seem to follow Eqn 2. It can therefore be assumed that the chromoionophores do not appreciably form complexes with K^+. The affinity to other cations is studied in the same way or by determining the potentiometric selectivity coefficient in ISE membranes [17].

Spectral properties

Generally, to obtain optical sensors with maximum sensitivity, sufficient chromoionophore must be present in the membrane. For bulk optodes, however, the mass transfer of ions from the aqueous into the organic phase is essential, and the smaller the amount of chromoionophore, the less is the depletion of measuring ions in the sample solution [5]. Hence, when using thin membranes exhibiting good sensitivity and short response times, they should contain a chromoionophore of high molar absorption coefficient ϵ. The value of ϵ, in turn, may be utilized for estimating the average membrane thickness d, provided that the concentration of the chromoionophore in the membrane phase is known, its distribution is uniform and ϵ is not influenced by additives. In contrast, for the determination of d by the more exact interference method [24], the chromoionophore must be destroyed.

Three methods were used for evaluating ϵ: spectrophotometrically in methanol; by measuring the absorbance in optode membranes of type 1 and, after photolytic degradation of the chromoionophore, determining the membrane thickness by the interference method [24]; and by measuring the absorbance in ISE membranes (type 4) and determining the membrane thickness with a light microscope.

Table 5 shows the molar absorption coefficients obtained in methanol and in the membrane phase. The S.D. of the measurements was ca. 10%, so that membrane thicknesses cannot be accurately determined by these methods. The inaccuracy observed might also be due to water uptake by the membrane.

With increasing lipophilicity, a slight peak broadening was observed but, on the whole, the influence of different side-chains on the spectral properties of the chromoionophores was found to be small. Even chemical immobilization of the chromoionophore on the polymer matrix, as in ETH 3531, leads to optodes with adequate optical properties. With a typical ϵ of 6×10^4 l mol^{-1} cm^{-1} and a membrane thickness of 2 μm, a chromoionophore concentration of 8.3 mmol l^{-1} is required for an absorbance of 0.1 according to the Lambert–Beer law. This is a reasonable value for many applications.

Conclusions

Lipophilic neutral H^+-selective chromoionophores of different basicities are presented which, in combination with neutral cation-selective ionophores, make it possible to design bulk optodes for different measuring ranges and to adapt them to particular analytical needs. When the membrane, in addition, contains a tetraphenylborate derivative, the chromoionophore must have a minimum basicity because the additive decomposes in acidic media. Except for the more basic chromoionophores in acidic solutions, the lipophilicity was usually found to be sufficient. For general applications, the most lipophilized derivatives ETH 2458, ETH 2468, ETH 2462 and the less basic compounds ETH 2439 and ETH 5418 are most suitable. However, to meet the lifetime requirements in lipophilic samples such as undiluted serum, they should be immobilized on the polymer, although this leads to longer response times. Under the usual laboratory conditions, the chromoionophores proved to be chemically stable. After photochemical treatment, no decomposition products absorbing in the visible range could be detected, so that certain deteriorating influences should not severely impair the calibration of optodes. By making the chromoionophores more lipophilic, their molar absorption coefficients, which also serve for determining the average membrane thickness, were not significantly influenced.

This work was supported by the Swiss National Science Foundation. The authors thank D. Wegmann and E. Pretsch for careful reading of the manuscript. The first four authors acknowledge the late Professor Wilhelm Simon as a great personality, who initiated this work with enthusiasm.

REFERENCES

1 S.C. Charlton, R.L. Fleming and A. Zipp, Clin. Chem., 28 (1982) 1857
2 M.L. Gantzer, P.R. Hemmes and D. Wong, Eur. Pat. Appl., EP 153.641 (1985).
3 W.E. Morf, K. Seiler, B. Lehmann, Ch. Behringer, S.S.S. Tan, K. Hartman, P.R. Sørensen and W. Simon, in E. Pungor (Ed.), Ion-Selective Electrodes, Vol. 5, Akadémiai Kiadó, Budapest, 1989, p. 115.
4 W.E. Morf, K. Seiler, P.R. Sørensen and W. Simon, in E. Pungor (Ed.), Ion-Selective Electrodes, Vol. 5, Akadémiai Kiadó, Budapest, 1989, p. 141.
5 K. Seiler and W. Simon, Anal. Chim. Acta, 266 (1992) 73.
6 E. Bakker and W. Simon, Anal. Chem., 64 (1992) 1805.
7 S.S.S. Tan, Dissertation, ETH, Zürich, No. 9552, 1991.
8 W.E. Morf, K. Seiler, B. Rusterholz and W. Simon, Anal. Chem., 62 (1990) 738.
9 K. Seiler, W.E. Morf, B. Rusterholz and W. Simon, Anal. Sci., 5 (1989) 557.
10 K. Wang, K. Seiler, W.E. Morf, U.E. Spichiger, W. Simon, E. Lindner and E. Pungor, Anal. Sci., 6 (1990) 715.
11 K. Seiler, K. Wang, E. Bakker, W.E. Morf, B. Rusterholz, U.E. Spichiger and W. Simon, Clin. Chem., 37 (1991) 1350.
12 P. Holý, W.E. Morf, K. Seiler, W. Simon and J.-P. Vigneron, Helv. Chim. Acta, 73 (1990) 1171.
13 H. He, G. Uray and O.S. Wolfbeis, Anal. Chim. Acta, 246 (1991) 251.
14 M. Lerchi, E. Bakker, B. Rusterholz and W. Simon, Anal. Chem., 64 (1992), 1534.
15 M. Lerchi and W. Simon, Proc. SPIE Int. Soc. Opt. Eng., 1716 (1992) 336.
16 Selectophore, Ionophores for Ion-Selective Electrodes and Optodes, Fluka, Buchs, Switzerland, 1991.
17 V.V. Cosofret, T.M. Nahir, E. Lindner and R.P. Buck, J. Electroanal. Chem. Interfacial Electrochem., 327 (1992) 137.
18 P.C. Meier, Anal. Chim. Acta, 136 (1982) 363.
19 D.D. Perrin and B. Dempsey, Buffers for pH and Metal Ion Control, Chapman and Hall, London, New York, 1983.
20 C. Behringer, B. Lehmann, J.-P. Haug, K. Seiler, W.E. Morf, K. Hartman and W. Simon, Anal. Chim. Acta, 233 (1990) 41.
21 R.E. Dohner, D. Wegmann, W.E. Morf and W. Simon, Anal. Chem., 58 (1986) 2585.
22 IUPAC Recommendations for Nomenclature of Ion-Selective Electrodes, Pure Appl. Chem., 48 (1976) 127.
23 F.E. Ray and M.L. Jung, Br. J. Cancer, 5 (1951) 358.
24 T. Rosatzin, P. Holý, K. Seiler, B. Rusterholz and W. Simon, Anal. Chem., 64 (1992) 2029.
25 O. Dinten, Dissertation, ETH, Zürich, No. 8591, 1988.
26 R.G. Bates, in J.J. Lagowsky (Ed.), The Chemistry of Non-Aqueous Solvents, Vol. I, Academic, New York, London, 1966, Chap. 3.
27 W.E. Morf, The Principles of Ion-Selective Electrodes and of Membrane Transport, Akadémiai Kiadó, Budapest, 1981, Ch. 11.
28 J. Jeney, Dissertation, Technical University, Budapest, in preparation.
29 U. Oesch and W. Simon, Anal. Chem., 52 (1980) 692.
30 O. Dinten, U.E. Spichiger, N. Chaniotakis, P. Gehrig, B. Rusterholz, W.E. Morf and W. Simon, Anal. Chem., 63 (1991) 596.
31 P. Oggenfuss, Dissertation, ETH, Zürich, No. 7619, 1984.
32 Y. Marcus and A.S. Kertes, Ion Exchange and Solvent Extraction of Metal Complexes, Wiley, London, 1969.
33 C. Hansch and A. Leo, Substituent Constants for Correlation Analysis in Chemistry and Biology, Wiley, New York, 1979.
34 Th. Rosatzin, Dissertation, ETH, Zürich, No. 9829, 1992.
35 Th. Rosatzin, E. Bakker, K. Suzuki and W. Simon, Anal. Chim. Acta, in press.

Analytica Chimica Acta, 278 (1993) 227–232
Elsevier Science Publishers B.V., Amsterdam

Trioctyltin chloride as carrier for a chloride-selective electrode in flow-injection potentiometry

Peter C. Hauser

University of Auckland, Department of Chemistry, Private Bag 92019, Auckland (New Zealand)

(Received 24th November 1992; revised manuscript received 12th January 1993)

Abstract

Trioctyltin chloride was incorporated into a poly(vinyl chloride) membrane and its potentiometric response to different anions in flow-injection analysis tested. It was found that by using the membrane in this mode inherent instabilities can be overcome and reproducible measurements obtained.

Keywords: Ion selective electrodes; Flow injection; Potentiometry; Chloride-sensitive electrode; Trioctyltin chloride

Trialkyltin chlorides or acetates have been suggested as carriers for anion selective electrodes [1–7]. These compounds invoke a selectivity pattern that is different to that obtained when lipophilic cations such as quaternary amines are incorporated into poly(vinyl chloride) (PVC) membranes. The selectivities of the latter are governed by the lipophilicity of the anions which is related to their hydration energy and follows the Hofmeister series: $ClO_4^- > SCN^- > I^- > NO_3^- > Br^- > Cl^- > HCO_3^-$ > acetate > SO_4^{2-} [8,9]. Ion-selective electrodes with this selectivity sequence are used for the determination of the more lipophilic ions such as nitrate. For certain applications, however, this selectivity pattern is not suitable. An example is the determination of chloride in clinical samples where Hofmeister-type membranes are used, but problems caused by insufficient selectivity for chloride have been reported [10,11]. ISEs based on trialkyltin chlorides show a different selectivity pattern that in principle makes them much better suited for chloride determinations. However, unduly long response times, unstable potentials and non-Nernstian response have been reported [3,12]. This precludes practical applications. The shortcomings were attributed to an exchange of the anionic substituent on the tin centre with interfering anions (X^-) according to a nucleophilic substitution reaction (SN_2) [3,7]:

$$R_3SnCl_{mem} + X^-_{aq} \rightleftharpoons R_3SnClX^-_{mem} \rightleftharpoons R_3SnX_{mem} + Cl^-_{aq} \quad (1)$$

This would lead to a constantly changing composition of the carrier in the membrane according to the affinity to and concentration of the interfering anion X^-, the response of the electrode then being dependent on its history.

The above scheme is valid if trialkyltin chloride compounds act as neutral carriers, i.e., they are present in the membrane as electrically neutral species when not complexed by analyte chloride. The charged intermediate will then be responsible for the electrode response. This view is supported by NMR and electrical field transport studies under conditions similar to that in a PVC

Correspondence to: P.C. Hauser, University of Auckland, Department of Chemistry, Private Bag 92019, Auckland (New Zealand)

membrane as used in ion-selective electrodes [6,7]. It is also possible however, that the compounds are partially dissociated in the membrane and then act as charged carriers according to the scheme below:

$$R_3Sn^+_{mem} + Cl^-_{aq} \rightleftharpoons R_3SnCl_{mem} \quad (2)$$

One successful approach to overcome the above mentioned limitations has been reported recently [13]. Trioctyltin chloride (TOTCl) was combined with a lipophilic pH indicator and both ion carriers dissolved in a thin PVC membrane. This leads to a coextraction of chloride and protons and for pH-buffered samples the extent of protonation of the pH indicator is dependent on the chloride concentration only. The colour change of the membrane rather than the potential is measured in this case. Both neutral and charged carrier mechanisms can explain the observed coextraction scheme.

A different approach to improve the performance of the carrier is presented here. Potential measurements using a membrane in the flow-injection analysis (FIA) mode promises to overcome instabilites in two ways. Firstly, peak heights are measured in FIA rather than absolute potentials. Drifts in potential are then not relevant if the sensitivity remains constant. Secondly, the ion-selective membrane can be conditioned between each sample measurement by the carrier solution. The membrane should thus be in the same state before each sample injection.

EXPERIMENTAL

Apparatus

The FIA manifold incorporated a Gilson Minipuls 2 peristaltic pump and a Rheodyne 5020 injection valve. PTFE tubings of 0.5 mm inner diameter and $1/4 \times 28$ type fittings were used for the connections.

Data acquisition

The operational amplifiers used were of type TL074CN. The analog-to-digital converter board (ADC) was from National Instruments (NB-MIO-16XL-42) and located in a Macintosh IIci personal computer. The data acquisition software was written in LabVIEW 2 (National Instruments) and gives a display of the measured potential vs. time on the computer screen and a readout of peak heights. In some instances a Philips PM 8251 chart-recorder was employed concurrently with the computer-based system.

Procedures

All aqueous solutions were made up from analytical reagent grade chemicals. The anion solutions were made up from potassium salts except in the case of perchlorate, acetate and salicylate were sodium salts were used. The carrier, buffer and reference solutions for the FIA system were degassed prior to usage by briefly stirring them under vacuum in order to prevent the build-up of air bubbles in the manifold. Membrane solutions were prepared by dissolving 1.5 mg trioctyltin chloride (TOTCl), 65.5 mg bis(1-butylpentyl) adipate (BBPA) and 33 mg poly(vinyl chloride) (PVC) in approximately 1 ml of freshly distilled tetrahydrofuran. The membrane ingredients were purchased from Fluka (Selectophore) and used as obtained.

The chromatographic chloride determinations were carried out on a Dionex ion chromatograph, using a HPIC-AS4A column with bicarbonate–carbonate buffer as eluent, a micromembrane suppressor and a conductivity detector.

Selectivity coefficients for the flow-injection potentiometry system were obtained according to the Nicolsky formalism by comparing the peak heights for the solutions 1×10^{-1} mol l^{-1} in the interfering species with that of a solution 1×10^{-1} mol l^{-1} in chloride and using the experimentally determined slope for chloride.

RESULTS AND DISCUSSION

FIA system

The ion-selective electrode is essentially of a coated wire configuration in which the membrane is in direct contact with a silver wire. A drop of the membrane solution is placed onto the top of a silver wire of 0.8 mm diameter which is glued into a perspex block. The resulting membrane is

about 0.1 mm thick and extends about 0.3 mm over the edge of the wire and is thus well sealed. A reference electrode is formed by anodizing a second silver wire in the perspex block in a solution of 1×10^{-1} mol l^{-1} HCl. Two merging flow channels are defined by a Y-shaped slot cut into a PTFE sheet of 1 mm thickness which is placed onto the block containing the electrodes. The assembly is completed with a second perspex block that contains the fluid in- and outlets and held together with screws. A platinum wire contacts the flow channel after the confluence of the two arms and allows grounding of the solution. A similar flow-through cell has been described previously [14,15].

A schematic of the manifold is shown in Fig. 1. The carrier stream consists of a 1×10^{-4} mol l^{-1} KCl solution. The chloride background is included for two reasons. Firstly it defines the baseline potential of the electrode. Secondly it conditions the electrode between sample injections. The exposure to chloride solutions between measurements is presumed to reverse any structural changes that may have occurred on injection of a sample such as an exchange of chloride on the tin centre with interfering ions according to a S_{N_2}-mechanism. The membrane therefore would always be in the same condition on exposure to samples and thus reproducible results obtained.

Downstream from the sample injection valve an ionic strength adjustment buffer is merged into the carrier. This also serves dual purposes. Firstly, it suppresses streaming potentials which are measurable under the conditions employed here when solutions with low electrolyte concentrations are used. Secondly, differences in ionic strength between solutions are eliminated and the direct measurement of concentrations is possible.

The reference stream contains a concentration of potassium chloride to define the reference potential and the ionic strength buffer at the same concentration as that of the carrier stream to reduce liquid junction potentials. Both electrodes were connected to operational amplifiers in the voltage follower configuration to lower the impedance before passing the signals to the measuring instruments. These amplifiers were mounted as close a possible to the silver pins forming the electrodes in order to minimize any noise pick-up. A three-electrode setup was used with the platinum wire located in the flow-cell serving as the common electrode. The peak heights were acquired with a 16-bit analog-to-digital converter rather than the usual chart recorder in order to be able to measure the values with acceptable resolution.

Response of the system

The response of the system to the injection of KCl solutions of different concentration is illustrated in Fig. 2. A linear response to the loga-

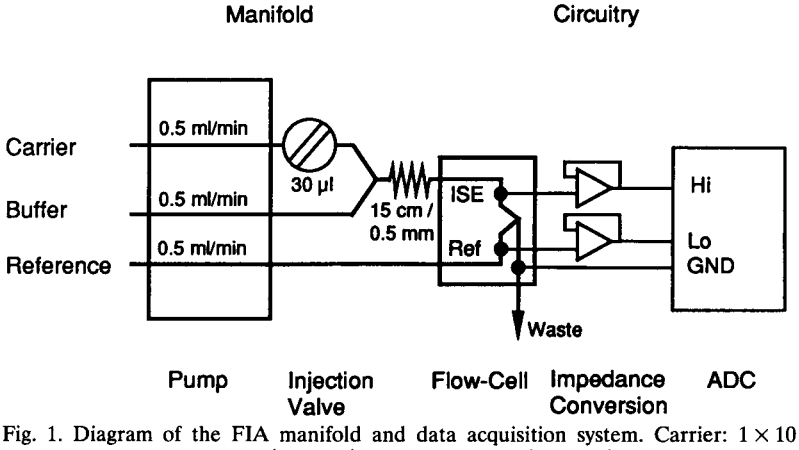

Fig. 1. Diagram of the FIA manifold and data acquisition system. Carrier: 1×10^{-4} mol l^{-1} KCl. Buffer: 2×10^{-1} mol l^{-1} Na_2SO_4. Reference: 1×10^{-1} mol l^{-1} Na_2SO_4, 1×10^{-1} mol l^{-1} KCl. ADC denotes the analog-to-digital converter located in the microcomputer.

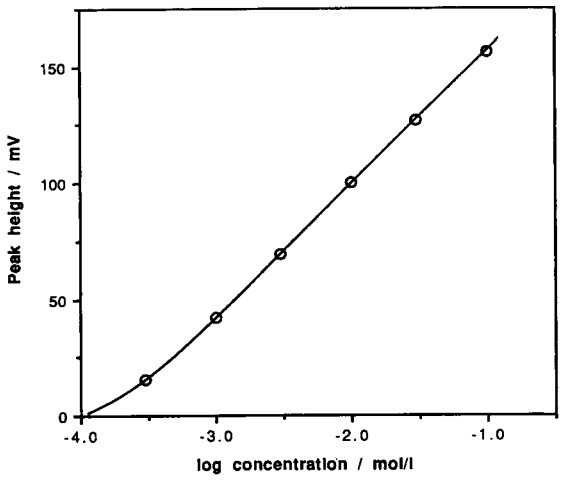

Fig. 2. Calibration curve for the injection of various concentrations of chloride solutions.

rithm of concentration was obtained between about 1×10^{-1} mol l^{-1} and 1×10^{-3} mol l^{-1} of chloride. The lower limit of detection of about 1×10^{-4} mol l^{-1} is comparable to that found with conventional electrodes based on TOTCl [1]. The gradient in the linear region is slightly sub-Nernstian with 57.3 mV per decade. The peak maxima were attained within about 15 s. This is comparable with response times found for other PVC based membranes (for K^+, Ca^{2+} and NO_3^-) in a similar system [14,15] and clearly shows that the rate of response is not a limitation for this ionophore. The precision for repeated injections was found to be good with a typical standard deviation of 0.3 mV for 5 consecutive injections. This also compares well with values obtained for other PVC-based electrodes in such a configuration [14,15]. The baseline potential was often found to be subject to drift (typically 5 mV h^{-1}), which, however, did not affect the measured peak heights. Drift is often associated with the coated wire configuration used here because the interface between the membrane and the metal is ill defined. This is generally not a problem in flow-injection potentiometry as has been demonstrated before because peak heights rather than absolute potentials are measured [14,15].

Effect of secondary anions

The selectivity coefficients obtained for several anions with the present flow-injection potentiometry system are given in Fig. 3. These values are in agreement with literature data for conventional measurements with conventional ISEs based on TOTCl [4,6]. However, a peculiar behaviour was observed in the course of these studies. The return to baseline was found to be delayed after the injection of certain secondary anions.

This effect is illustrated in Fig. 4. The first three peaks shown are due to the injection of chloride solutions of increasing concentration. Subsequently identical concentrations of other anions were injected. The order followed was that of increasing interference viz. peak height. Clearly, the time taken for baseline recovery is not directly correlated with peak height. Fluoride solutions even cause a temporary deviation from the baseline in the opposite direction. The delay in baseline recovery appears to be most pro-

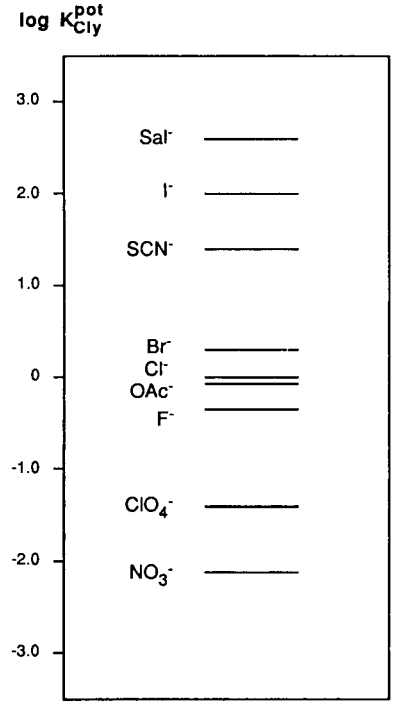

Fig. 3. Potentiometric selectivity coefficients for the flow-injection system.

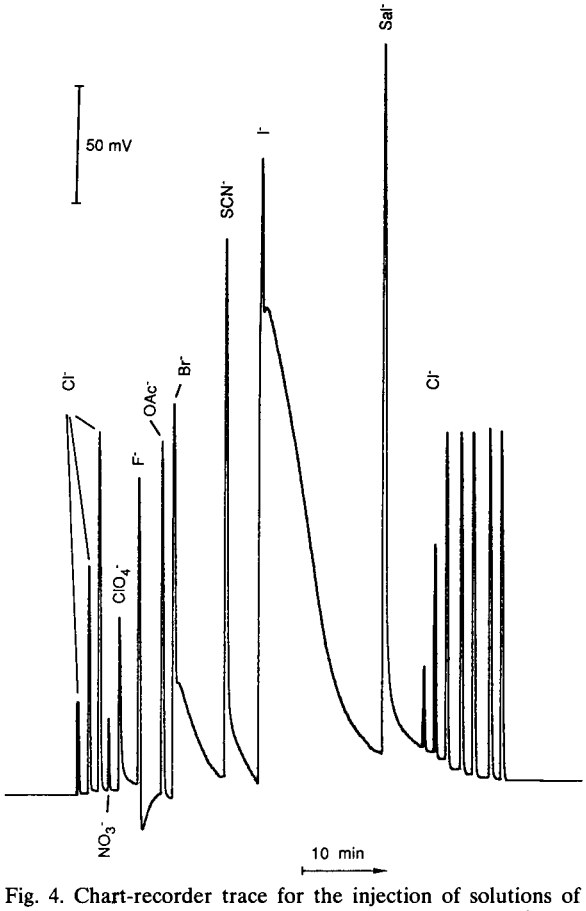

Fig. 4. Chart-recorder trace for the injection of solutions of different anions. The chloride solutions were 1×10^{-1}, 1×10^{-2} and 1×10^{-3} mol l^{-1} in concentrations. The solutions for the interfering ions were all 1×10^{-1} mol l^{-1} in the anion concentration.

nounced for the halides and the pseudohalide SCN^-. It is possible that the effect is caused by a ligand exchange on the tin centre according to the mechanism of Eqn. 1 discussed above and related to the reaction rate of the nucleophilic substitution for the different anions. Another explanation may be that TOTCl in the membrane is partially dissociated and acts both as a neutral and a charged carrier at the same time. The two reactions may have different reversibilities and be dependent on the anion species.

On completion of the measurements of the different anions, chloride solutions were again injected. It was found that the sensitivity on the shoulder of the salicylate peak was slightly reduced but regained its previous value after return to the original baseline. The effect of the secondary anions can thus indeed be reversed in the FIA system.

It was attempted to increase the speed of return to baseline on injection of interfering anions by optimising the flow-injection parameters. Reducing the sample loop volume, in order to limit the time of exposure to interferants, however was found to yield a sub-Nernstian slope. The time of exposure to the analyte was shorter than the response time in that case. Using a higher concentration of chloride in the carrier solution (10^{-1} mol l^{-1}) was thought to increase the rate of reconditioning after sample injection. The results in terms of baseline recovery were however very similar to those obtained with the low chloride concentration in the carrier.

It was found that this interference effect is not a problem in an analytically relevant situation as long as the secondary ions are present in mixed solutions at levels that do not cause a measurable signal in terms of peak height.

Determination of chloride in atmospheric aerosol samples

The system was applied to the determination of chloride in atmospheric aerosol samples (sea spray) that had been analysed previously by anion chromatography. The results are given in Table 1. A resonable agreement between the two sets of data was obtained considering that single determinations only had been carried out by ion-chromatography.

Conclusions

It was found possible to overcome the reported limitations for the trioctyltin chloride ionophore by using it in a flow-injection mode. The membrane was found to respond Nernstian and the response time was short and allowed sample volumes as small as 30 μl to be used. Some secondary ions caused a slow return to baseline after injection, an effect which is not

TABLE 1

Chloride concentrations (mg l^{-1}) in atmospheric aerosol samples determined with the flow-injection potentiometry system (FIP) and by ion-chromatography (IC) [a]

Sample No.	FIP	IC
1	59.3 ± 0.9	58
2	77.5 ± 1.3	96
3	70.8 ± 0.8	82
4	40.0 ± 0.4	49
5	35.5 ± 0.7	34
6	177.1 ± 0.7	180

[a] The mean values of five determinations with confidence intervals for confidence levels of 95% are given for the FIP data. Single determinations only were carried out for the ion chromatographic determinations. The correlation coefficient (r) for the two sets of data is 0.9887.

directly related to the potentiometric interference of the ions. However, the adverse effect of this behaviour on the analytical performance could be overcome by conditioning the electrode between sample measurements by including chloride in the carrier stream.

The author thanks D. Wylie for the analysed aerosol samples and S.S. Tan for useful discussions. The work was mainly funded by University of Auckland grant number A18/XXXXX/61890/F3391087 and a special Vice Chancellor's grant.

REFERENCES

1 U. Wuthier, H.V. Pham, R. Zünd, D. Welti, R.I.J. Funck, A. Bezegh, D. Ammann, E. Pretsch and W. Simon, Anal. Chem., 56 (1984) 535.
2 U. Wuthier, H.V. Pham, E. Pretsch, A.K. Beck, D. Seebach and W. Simon, Helv. Chim. Acta, 68 (1985) 1822.
3 U. Wuthier and W. Simon, Mikrochim. Acta, III (1986) 225.
4 U. Oesch, D. Ammann, H.V. Pham, U. Wuthier, R. Zünd and W. Simon, J. Chem. Soc., Faraday Trans. 1, 82 (1986) 1179.
5 U. Wuthier, H.V. Pham, B. Rusterholz and W. Simon, Helv. Chim. Acta, 69 (1986) 1435.
6 H.-V. Pham, E. Pretsch, K. Fluri, A. Bezegh and W. Simon, Helv. Chim. Acta, 73 (1990) 1894.
7 K. Fluri, J. Koudelka and W. Simon, Helv. Chim. Acta, 75 (1992) 1012.
8 F. Hofmeister, Arch. Exp. Pathol. Pharmakol., 24 (1888) 247.
9 D. Wegmann, H. Weiss, D. Ammann, W.E. Morf, E. Pretsch, K. Sugahara and W. Simon, Mikrochim. Acta, III (1984) 1.
10 R. Lewandowski, T. Sokalski and A. Hulanicki, Clin. Chem., 35 (1989) 2146.
11 K. Emancipator and M.H. Kroll, Clin. Chem., 36 (1990) 1470.
12 U. Oesch, D. Ammann and W. Simon, Clin. Chem., 32 (1986) 1448.
13 S.S.S. Tan, P.C. Hauser, K. Wang, K. Fluri, K. Seiler, B. Rusterholz, G. Suter, M. Krüttli, U.E. Spichiger and W. Simon, Anal. Chim. Acta, 255 (1991) 35.
14 T.J. Cardwell, R.W. Cattrall, P.C. Hauser and I.C. Hamilton, Anal. Chim. Acta, 214 (1988) 359.
15 P.C. Hauser, S.S. Tan, T.J. Cardwell, R.W. Cattrall and I.C. Hamilton, Analyst, 113 (1988) 1551.

Analytica Chimica Acta, 278 (1993) 233–236
Elsevier Science Publishers B.V., Amsterdam

Removing the influence of buffer concentration on the response of enzyme field effect transistors by using additional membranes

A.A. Shul'ga and V.I. Strikha

Semiconductor Department, Kiev University, Vladimirskaya St. 64, Kiev 252017 (Ukraine)

A.P. Soldatkin and A.V. El'skaya

Institute of Molecular Biology and Genetics of the Ukrainian Academy of Science, Kiev (Ukraine)

H. Maupas, C. Martelet [1] and P. Clechet

LPCI, URA CNRS 404, Ecole Centrale de Lyon, B.P. 163, 69131 Ecully Cedex (France)

(Received 17th December 1992)

Abstract

Urea- and glucose-sensitive enzyme field effect transistors (ENFETs) were prepared by cross-linking urease and glucose oxidase, respectively, with bovine serum albumin (BSA) in saturated glutaraldehyde vapour on the gate area of the ISFETs. Additional BSA and polyvinylbutyral membranes were formed by a dip-coating procedure from the appropriate solutions on the top of the enzyme layer. In case of the urea ENFET the additional albumin membrane led to complete elimination of the influence of the buffer concentration on the sensor response. For the glucose ENFET additional BSA membranes resulted in an extension of the dynamic range of the sensor up to a glucose concentration of 25 mM while not affecting substantially the buffer effect on the sensor response. However, after the formation of one more additional polyvinylbutyral membrane more than a fivefold decrease in the influence of the buffer concentration on the biosensor response was observed.

Keywords: Enzymatic methods; Biosensors; Enzyme field effect transistors; Glucose; Ion-sensitive field effect transistors; Urea

Since the first reported enzyme biosensor (ENFET) based on ion-selective field effect transistors (ISFETs) [1], substantial research efforts were undertaken to improve the performance characteristics of the ENFETs developed. From the beginning it was recognized that one of the most serious problems arising in practical applications of this kind of biosensor was a dramatic decrease of the biosensor response with an increase in the buffer concentration in the sample. The reason for this phenomenon is a kind of carrier-mediated transport of protons inside the membrane with immobilized enzyme in the presence of mobile buffer species [2]. In fact, the best assay conditions would be those when the substrate

Correspondence to: A.A. Shul'ga, LCPI, URA CNRS 404, Ecole Centrale de Lyon, B.P. 163, 69131 Ecully Cedex (France).

[1] LTDS URA CNRS 855.

concentration is comparable to that of the buffer, but unfortunately this is not the case in many real situations.

This paper proposes a practical approach in order to remove or at least substantially reduce the influence of the buffer concentration on the ENFET response. This objective is achieved by the formation of additional permselective membranes on the top of the enzymatic membrane.

EXPERIMENTAL

Materials

Glucose oxidase (GOD) (EC 1.1.3.4) from *Penicillium vitale* having an activity of 168 U mg^{-1} was obtained from the Cosarsky alcohol plant (Cherkasy, Ukraine), urease (EC 3.5.1.5) from jack beans with an activity of 628 U mg^{-1} from Sigma, bovine serum albumin (BSA) from Serva and glutaraldehyde (GA) (25% aqueous solution) from Merck. As a material for additional membranes, polyvinylbutyral (PVB) was also used, consisting of a linear copolymer of vinylbutyral, vinyl alcohol and vinyl acetate in the approximate proportions 75 + 22 + 3. All other reagents were of analytical-reagent grade.

Enzyme immobilization

Enzymes were immobilized using a modified procedure described earlier [3]. Solutions of GOD, BSA and urease (10%) were prepared in 20 mM phosphate buffer (KH_2PO_4–NaOH) (pH 7.4). Prior to the deposition on the gate area of the ISFETs, these solutions were mixed in defined proportions and glycerol was added. The mixture compositions used were as follows: for the urea ENFET, 1% urease, 5% BSA, 5% glycerol, and for the glucose ENFET, 5% GOD, 5% BSA and 10% glycerol. With the differential experimental set-up used, one drop of enzyme-containing mixture was deposited on one of the measuring ENFETs while only a mixture containing BSA and glycerol was deposited on the reference ISFET. Then the sensor chips were placed in the saturated GA vapour and were kept there for 30 min. After exposure to GA vapour, the membranes were dried at room temperature for 10–15 min. Before use the membranes were soaked in 20 mM phosphate buffer (pH 7.4) for at least 30 min.

Formation of additional membranes

An additional BSA membrane was formed by a dip-coating procedure using 10% BSA solution and subsequent exposure of the membrane to saturated GA vapour for 30 min. The PVB membrane was formed by dip-coating of the sensor using a 5% solution of the polymer in ethanol. After deposition, the membranes were dried at room temperature. Before use the sensors were soaked in 20 mM phosphate buffer (pH 7.4) for 30 min.

Sensor design and measurements

n-Channel depletion-mode ISFETs were fabricated at the Research Institute of Microdevices (Kiev, Ukraine) on a p-Si wafer with orientation (100) and resistivity 7.5 Ω cm. After scribing, sensor chips (3 mm × 10 mm) containing two identical ISFETs were formed. A channel (7 μm × 250 μm) was made by ion implantation of phosphorus with a dose depending on the threshold voltage required. In these experiments IS-

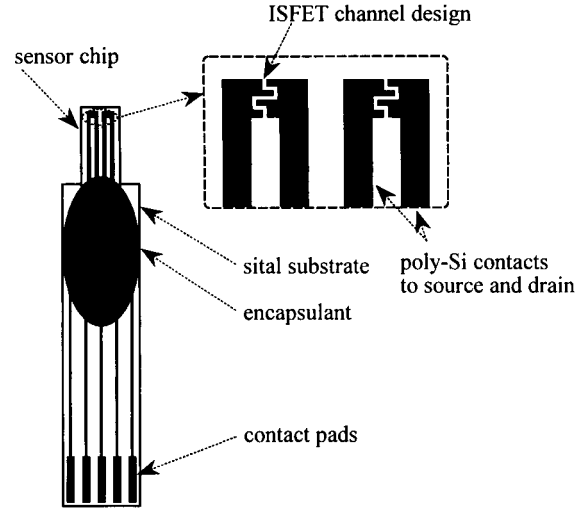

Fig. 1. General view of the ISFET chip (3 mm × 10 mm) containing two identical ISFETs mounted on a Sital (fused alumina ceramic) substrate (6 mm × 28 mm) with separately shown ISFET channel design (channel dimensions are 7 μm × 250 μm).

FETs with threshold voltages of about −4 V were employed.

Sensor chips were glued on to a Sital (fused Al_2O_3 ceramic) support with dimensions 6 mm × 28 mm having thickness 0.5 or 1.0 mm and sensor contact pads were electrically bonded by ultrasonic wiring to aluminium conductors photolithographically patterned on Sital. After wiring, the contact pads and wires were encapsulated with epoxy resin as shown in Fig. 1. The sensor design and mode of operation allowed them to be used when the substrate is in direct contact with the solution. Detailed information about the construction and mode of operation of the ISFETs is given elswhere [4].

The sensor chip and Ag/AgCl reference electrode were immersed in the measurement cell filled with about 3 ml of buffer solution and the differential output between the measuring and reference ISFETs recorded. Experiments were carried out under ambient conditions. Illumination was of no importance for the ISFETs used because they displayed no light sensitivity.

RESULTS AND DISCUSSION

Fabricated ENFETs without additional membranes demonstrated a fast (15–30 s), reproducible response to the addition of the corresponding substrates and the dynamic range of the biosensors extended up to 2–3 mM for both urea and glucose. The limited dynamic range of the urea ENFET is due to the low retained activity of immobilized urease [5] whereas for glucose the reason is the oxygen limitation of the biocatalytic glucose oxidation [3].

Calibration graphs for the urea ENFET without additional membranes are presented in Fig. 2. There was a more than 20-fold decrease in the sensor output signal amplitude when the buffer concentration was changed from 2 to 20 mM. However, the same measurements performed with the ENFET covered with an additional BSA membrane (the formation of the BSA membrane did not change the sensor's response time) showed no influence of the buffer concentration on the sensor response. The latter corresponds to a more

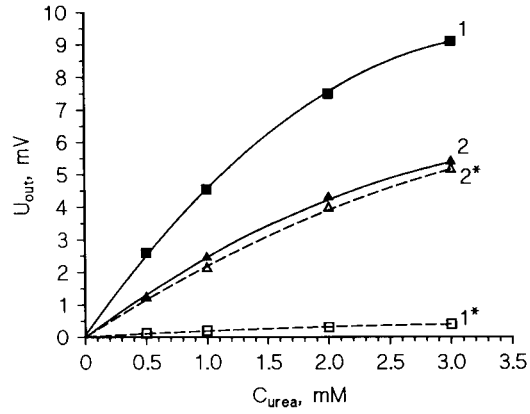

Fig. 2. Calibration graphs for urea ENFET without [(1) in 2 mM and (1*) in 20 mM phosphate buffer (pH 7.4)] and with an additional BSA membrane [(2) in 2 mM and (2*) in 20 mM phosphate buffer (pH 7.4)].

than tenfold increase in the sensor signal amplitude in 20 mM buffer.

With the glucose ENFET, the formation of an additional BSA membrane did not reduce the influence of the buffer concentration on the sensor response, so a further additional membrane of PVB was formed on the top of the initial BSA membrane. While preserving such characteristics as the response time (about 20 s), the presence of the BSA membrane resulted in a substantial extension of the sensor's dynamic range up to 25 mM glucose, probably owing to limitation of the diffusion of glucose into the membrane in comparison with oxygen. The observed extension of the dynamic range correlates well with the results of Saito and co-workers [6,7], where an additional membrane was formed on top of a glucose ENFET by spin-coating from BSA and GA solution.

The deposition conditions (speed of withdrawal of the chip from the PVB solution) allowed the deposition of, roughly speaking, "thin" and "thick" PVB membranes, that are different in thickness and probably in morphology because of the different conditions of the solvent evaporation. The behaviour of the ENFETs with "thin" and "thick" PVB membranes was very different. In the former instance no substantial changes in the sensor characteristics took place whereas in the latter a dramatic decrease in the influence of

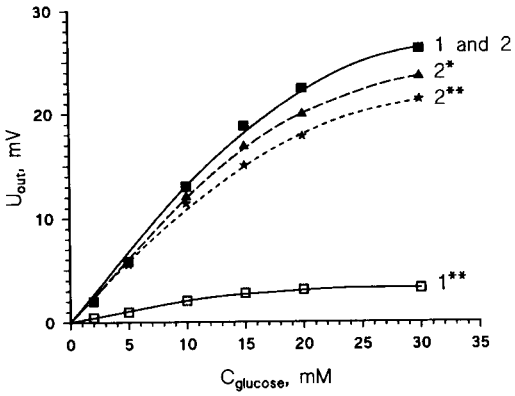

Fig. 3. Calibration graphs for glucose ENFET with additional BSA membrane and with a "thin" [(1) in 2 mM and (1**) in 20 mM phosphate buffer (pH 7.4)] and "thick" additional PVB membrane [(2) in 2 mM, (2*) in 10 mM and (2**) in 20 mM phosphate buffer (pH 7.4)].

the buffer capacity on the sensor response was observed (Fig. 3). Also, the presence of the "thick" PVB membrane led to an almost tenfold increase in the sensor's response time, which reflects the diffusion barrier properties of this membrane.

Under the assay conditions used (pH 7.4), a membrane made of cross-linked BSA should have a negative net charge as the isolelectric point of BSA lies between pH 4 and 5. The results obtained for a urea ENFET with a BSA membrane might then be explained by assuming that a negatively charged additional membrane possesses permselective properties as for charged buffer species diffusing in and out of the membrane, thus blocking the channel for facilitated transport of OH^- ions and thereby eliminating the effect of mobile buffer species present in the sample on the sensor response. The effect of the additional PVB membrane with the glucose ENFET may also be interpreted in the same way, taking into account the barrier properties of the predominantly hydrophobic PVB layer for the diffusion of hydrophilic species. However, no satisfactory explanation can be given for why an additional BSA membrane did not lead to the elimination of the influence of the buffer on the glucose ENFET response. For a better understanding of the observed phenomena, more detailed analysis of the membrane properties of the cross-linked BSA membranes containing or not containing enzymes is required. Such a study is in progress.

Conclusion

It was shown that formation of additional permselective membranes (cross-linked BSA for the urea ENFET and cross-linked BSA plus an additional PVB membrane for the glucose ENFET) leads to almost disappearance of the influence of the buffer concentration on the response of ENFETs. The latter influence was traditionally considered to be a generic feature of the enzyme sensors based on pH electrodes and pH-sensitive ISFETs. The results obtained are interpreted in terms of permselective properties of the additional membranes formed. These membranes block the carrier-mediated transport of protons and hydroxy ions inside the membrane in the presence of mobile buffer species, thus eliminating their effect on the output signal amplitude of the biosensors.

REFERENCES

1 S. Caras and J. Janata, Anal. Chem., 52 (1980) 1935.
2 S. Varansi, S.O. Ogundiran and E. Ruckenstein, Biosensors, 3 (1988) 269.
3 A.A. Shul'ga, A.P. Soldatkin, A.K. Sandrovski, N.F. Starodub, V.I. Strikha and A.V. El'skaya, Sensors Actuators, in press.
4 A.A. Shul'ga, L.I. Nechiporuk, A.K. Sandrovski, V.I. Strikha, A.A. Abalov, O.S. Frolov, Yu. G. Kononenko, H. Maupas, C. Martelet and N. Jaffrezic, Sensors Actuators, submitted for publication.
5 P. Clechet, N. Jaffrezic, C. Martelet, C. Valet, A.V. El'skaya, A.P. Soldatkin, V.I. Strikha and A.A. Shul'ga, in Proceedings of the Second World Congress, BIOSENSORS'92, 20–22 May 1992, Geneva, Switzerland, Elsevier, Amsterdam, 1992, p. 220.
6 A. Saito, K. Shionoya, J. Kimura and T. Kuriyama, in Proceedings of the Second World Congress, BIOSENSORS'92, 20–22 May 1992, Geneva, Switzerland, Elsevier, Amsterdam, 1992, p. 71.
7 A. Saito, S. Miyamoto, J. Kimura and T. Kuriyama, Sensors Actuators, B5 (1991) 237.

Analytica Chimica Acta, 278 (1993) 237–242
Elsevier Science Publishers B.V., Amsterdam

Rapid method for the determination of copper(II) and lead(II) in tap water using a portable potentiometric stripping analyser

D. Jagner, E. Sahlin and B. Axelsson

Department of Analytical and Marine Chemistry, University of Göteborg and Chalmers University of Technology, S-412 96 Gothenburg (Sweden)

R. Ratana-Ohpas

Chemistry Department, Prince of Songkla University, Hat Yai, Songkla 90112 (Thailand)

(Received 14th December 1992)

Abstract

Tap water samples of 400 μl were added to 200 μl of matrix-modifying solution consisting of hydrochloric acid, calcium chloride, mercury(II), ethanol, Triton X-100 and bismuth(III) as internal standard and contained in disposable 2-ml Eppendorff sample tubes. The mixture was analysed for copper(II) and lead(II) using a commercial computerized potentiometric stripping analyser in combination with a laboratory-made electrode system and rotating sample holder. Copper(II) in the range 0.10–5 mg l^{-1} was determined in less than 1 min and lead(II) in the range 1–50 μg l^{-1} in 3 min, the precisions being ca. 15%.

Keywords: Potentiometry; Stripping voltammetry; Copper; Lead; Water

The two most frequently investigated trace elements in tap water are copper(II) and lead(II). Copper(II) concentrations above ca. 0.5 mg l^{-1} are suspected to cause diarrhoea in bottle-fed children and there are indications that lead(II) concentrations above ca. 50 μg l^{-1} might affect the intellectual development of these children [1].

Elevated copper(II) and lead(II) tap water concentrations normally emanate from the household distribution net rather than from the water supply [2]. Thus, when monitoring for elevated concentrations of these elements it is necessary to sample each tap in the individual households. In order to optimize the sampling strategy and to obtain a rapid analytical result, it is consequently desirable to be able to perform the determination on-site.

Many methods have been proposed for the determination of lead(II) and copper(II) in tap water, most of them being based on flame or graphite furnace atomic absorption spectrometry [3–8]. Owing to the bulkiness of these instruments and to their special installation requirements with respect to ventilation and power supply, they are unsuitable for on-site analysis. In this respect, electroanalytical methods are attractive alternatives. This is particularly true for methods based on stripping potentiometry as

Correspondence to: D. Jagner, Department of Analytical and Marine Chemistry, University of Göteborg and Chalmers University of Technology, S-412 96 Gothenburg (Sweden).

these normally do not require deaeration of the samples, thus simplifying the experimental procedure [9,10].

This paper describes a method suitable for on-site monitoring of elevated copper(II) and lead(II) tap water concentrations using a commercial potentiometric stripping analyser in combination with a portable personal computer and a laboratory-constructed electrode system and rotating sample holder. Microlitre amounts of tap water sample are added to a matrix modifying solution contained in disposable sample containers, after which the analytical procedure, including result evaluation and presentation of the results, is performed under computer control. Copper(II) is determined in less than 1 min and, if desired, the analyser continues with the determination of lead(II), the latter determination taking ca. 3 min.

EXPERIMENTAL

Instrumentation

The electroanalytical measurements were performed with a potentiometric stripping unit (Tracelab, PSU 20; Radiometer, Copenhagen) connected to a portable IBM-compatible personal computer and controlled by the TAP2 Trace Talk Method Builder and Commander software package (Radiometer). The total weight of the stripping analyser was 7 kg and the overall dimensions 22 × 16 × 47 cm.

Flame atomic absorption measurements were made with a Perkin-Elmer Model 301 instrument.

Electrodes and rotating sample vessel

A 2-mm diameter glassy carbon disc was used as the working electrode and two 1-mm diameter Ag/AgCl rods as reference and counter electrodes, respectively. The three electrodes were built into one unit. The electrically isolated glassy carbon cylinder was glued into the middle of a 6-mm diameter porous ceramic frit which was then glued into a glass tube, the frit thus separating the inner solution of 0.50 M hydrochloric acid, containing the other two electrodes, from the sample solution mechanically, but not conductively. A detailed description of the electrode has been given elsewhere [11]. During preparation the electrode was polished with diamond particles with diameters of 10, 3 and 0.5 μm. After preparation the electrode was never repolished. All potentials given below are vs. Ag/AgCl in 0.50 M hydrochloric acid. When not in use the electrode was stored in 0.10 M hydrochloric acid. The first measurement after storage sometimes yielded erroneous results and for this reason the result from the first measurement was always disregarded.

Eppendorff tubes with a total volume of 2 ml were used as disposable sample containers. During analysis the tubes were inserted into a sample holder which could be rotated at a computer controlled rate between 800 and 2300 rpm [12].

Composition of the matrix-modifying solution

The matrix-modifying solution consisted of 2 M hydrochloric acid, 7.5 mM EDTA, 10 mM calcium chloride, 2 mg l^{-1} bismuth(III), 375 mg l^{-1} mercury(II) in 0.5% (v/v) Triton X-100 and 30% (v/v) ethanol. All chemicals were of analytical-reagent grade.

Sample pretreatment

Tap water samples of 400 μl were added to 200 μl of matrix-modifying solution pre-pipetted into Eppendorff sample tubes.

Electroanalytical procedure for the determination of copper(II)

The electrode was wiped with a tissue soaked in ethanol and the mercury film from the previous analysis or calibration was removed. The electrode was slid into the sample, rotation was started at a constant rate of 1500 rpm and a potential of −0.95 V was applied. Rotation was stopped after 5 s and, after a wait of 20 s, stripping was performed with a constant current of 0.2 μA until a potential of −0.05 V was reached. The copper and bismuth signals were integrated and the copper(II) concentration was calculated from a previously constructed calibration graph (see below) using bismuth as internal standard.

Electroanalytical procedure for the determination of lead(II)

Prior to the determination of lead(II), the copper (II) concentration of the sample was always determined according to the procedure described above. If the copper(II) concentration was not sought, the result from this determination was not presented. Based on the results from the copper(II) determination, either of two methods for the determination of lead(II) was used. If the copper(II) concentration was found to be less than 0.5 mg l^{-1}, the lead(II) determination was started by applying a potential of -1.10 V for 3 min at a rotation rate of 1500 rpm. Rotation was then stopped and 20 s later stripping was performed with a constant current of 0.2 μA until a potential of -0.05 V was reached. If the copper concentration was found to be higher than 0.5 mg l^{-1}, a multi-scanning procedure [10] was applied for the determination of lead(II). Three stripping scans were accumulated in the analyser, each scan involving electrolysis at -1.10 V with stirring for 40 s followed by no stirring for 20 s and stripping with 0.2 μA. The lead and bismuth signals were integrated and the lead(II) concentration was evaluated from either of the two calibration plots recorded separately (see below) using bismuth as internal standard. The reason for dividing the electrolysis period into three 1-min periods instead of one 3-min period was that at high copper(II) concentrations the copper and bismuth stripping peaks might otherwise overlap.

Calibration

The instrument was calibrated using four different solutions prepared by adding the appropriate amounts of copper(II) and lead(II) to doubly distilled water samples, the copper(II) and lead(II) concentrations in the four samples being 0.0 and 5.0, 500 and 15, 2000 and 5.0 and 4000 and 15 μg l^{-1}, respectively. The measurements were performed according to the electroanalytical procedures described above using the bismuth signal as internal standard. The four different copper(II) concentrations were used for the calibration graph for copper(II) and the two lead(II) concentrations were used for the two different calibration graphs for lead(II) at high and low copper(II). Normally the same calibration was used for a great number of measurements, the accuracy of the calibration being checked by intermittent analyses of the four calibration solutions. If the results thus obtained deviated by more than 20% from the correct values the instrument was re-calibrated.

RESULTS AND DISCUSSION

Determination of copper(II)

Figure 1 shows the stripping curves obtained in the analysis of doubly distilled water samples spiked with 0, 0.10, 0.50, 2.0 and 5.0 mg l^{-1} of copper(II). Table 1 summarizes the results obtained by five consecutive analyses of doubly distilled water samples spiked with eight different concentrations of copper(II). The same calibration was used for all measurements.

In order to compare the proposed method with flame atomic absorption spectrometric analysis, samples from 62 households in an acidified area of southern Sweden were analysed by both methods. The results are shown in Fig. 2; the slope of the regression line was 0.985 with a correlation coefficient of 0.989 and an intercept on the abscissa of 0.007 mg l^{-1}.

Determination of lead(II)

Figure 3 shows the lead stripping curves obtained in the analysis of doubly distilled water

TABLE 1

Results obtained by five consecutive analyses of eight doubly distilled water samples to which varying concentrations of copper(II) and lead(II) had been added

Copper(II) added (mg l^{-1})	Copper(II) found ±S.D. ($n = 5$) (mg l^{-1})	Lead(II) added (μg l^{-1})	Lead(II) found ±S.D. ($n = 5$) (μg l^{-1})
0.10	0.09 ± 0.02	2.5	3.1 ± 0.6
0.15	0.13 ± 0.03	5.0	5.3 ± 0.6
0.35	0.35 ± 0.04	7.5	7.1 ± 0.5
0.50	0.47 ± 0.06	10.0	9.6 ± 0.8
1.00	1.01 ± 0.09	12.5	12.4 ± 1.2
2.50	2.31 ± 0.13	20.0	17.8 ± 2.1
3.00	2.79 ± 0.37	37.5	35.2 ± 3.1
4.00	3.75 ± 0.31	50.0	46.8 ± 3.2

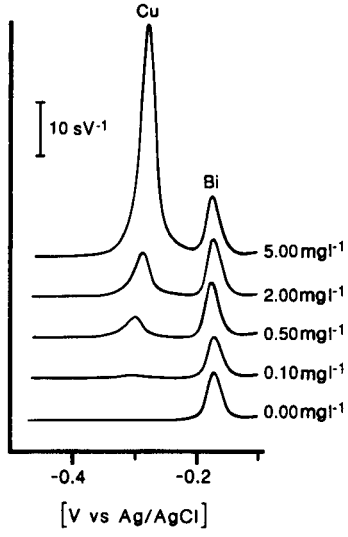

Fig. 1. Stripping curves obtained in the analysis of doubly distilled water samples containing 0, 0.10, 0.50, 2.0 and 5 mg l^{-1} of copper(II) using bismuth as internal standard.

samples spiked with 0, 5, 15, 25 and 50 μg l^{-1} lead(II). The samples containing 25 and 50 μg l^{-1} were also spiked with 2.0 mg l^{-1} of copper(II) and the others with 0.10 mg l^{-1} of copper(II). Table 1 summarizes the results obtained from five consecutive analyses of doubly distilled water samples spiked with eight different concentrations of lead(II).

The samples from the 62 different households mentioned above were also analysed for lead(II).

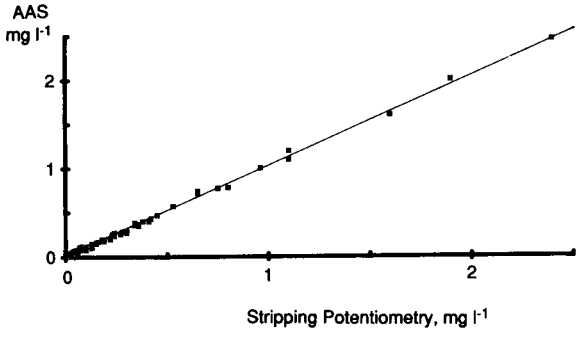

Fig. 2. Comparison of the results obtained by stripping potentiometry and flame atomic absorption spectrometry (AAS) in the analysis of tap water samples from 62 different households in an acidified area of southern Sweden. The slope of the regression line shown is 0.985 with a correlation coefficient of 0.989 and an intercept on the abscissa of 0.007 mg l^{-1}.

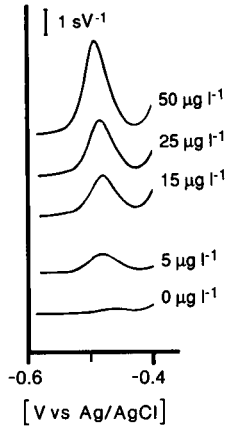

Fig. 3. Stripping curves obtained in the analysis of doubly distilled water samples containing 0.0, 5.0, 15, 25 and 50 μg l^{-1} of lead(II).

None of the samples had lead(II) concentrations above the estimated detection limit of 1 μg l^{-1}.

Accuracy. Matrix-modifying solution

The results presented in Fig. 2 clearly indicate that there is no systematic difference between the results obtained by flame atomic absorption spectrometry and by stripping potentiometry in the analysis for copper(II) in tap water samples. As no tap water samples with elevated lead(II) concentrations were available it was not possible to compare the results obtained by the proposed method with those obtained by another analytical technique, e.g., graphite furnace atomic absorption spectrometry. It does, however, seem reasonable to assume that even large variations in the chemical composition of different tap water samples will be rendered negligible by the matrix-modifying solution. Variations in water hardness and chloride concentration cannot affect the sensitivity for lead(II) owing to the high concentration of calcium chloride in the matrix-modifying solution. Variations in the content of organic constituents and surface-active compounds are made negligible by the high content of Triton X-100 and ethanol in the modifying solution. In the unlikely case of tap water containing sulphide, lead(II) and copper(II) will be rapidly released into electroactive forms owing to ion exchange with the excess mercury(II) in the matrix-

modifying solution, as was confirmed by experiment.

Precision

As seen from Table 1, the precision of the proposed method is in the range 10–15%, i.e., fairly low. The main reason for this is that each analytical value is based on the measurement of two stripping signals, i.e., the bismuth signal and the copper or lead signals. Further, the calibration plots are based on only two calibration points. In stripping potentiometry the typical precision in the measurement of a stripping peak is 5% provided that the signal is at least five time the detection limit. Consequently, precisions better than 10–15% cannot be expected with the proposed procedure. An improved precision could, of course, be obtained either by including more points on the calibration plots or by analysing the same sample several times.

Detection limit

The detection limits in stripping potentiometry are set either by the purity of the reagents used or by the magnitude of the stripping signal, the typical stripping signal at the detection limit for a 30-kHz instrument being 1–2 ms. In the present method the detection limit for both lead and copper is governed by impurities in the matrix-modifying solution and by contamination from the surroundings, the small sample volumes used making the latter aspect more important than is usually the case in electroanalysis. The detection limits for copper(II) and lead(II) when using the proposed method were estimated to be 100 and 1 $\mu g\ l^{-1}$, respectively. Below these values the results obtained were found to be unreliable, the relative standard deviations often exceeding 25%.

Electrode-to-electrode reproducibility. Calibration stability

Five laboratory-made electrodes were tested on a sample containing 1 $mg\ l^{-1}$ of copper(II) and 10 $\mu g\ l^{-1}$ of lead(II) according to the proposed electroanalytical procedure. The relative standard deviations of the copper and lead signals obtained with the five electrodes were 45 and 38%, respectively. The relative standard deviations of the copper to bismuth and lead to bismuth signal ratios were 16 and 14%, respectively. From this it was concluded that each electrode must be calibrated separately. The reason for the sensitivity variations from one electrode to another is not understood. The main reason, however, seems to be due to the inherent inhomogeneities in the glassy carbon material rather than to variations in the electrode manufacturing procedure.

Once calibrated, an individual electrode can be used for a large number of determinations without having to be re-calibrated. All measurements reported here were made with the same electrode during a period of 2 months and using the same calibration.

Conclusions

The proposed method based on the dilution of the sample in a concentrated matrix-modifier containing an internal standard (colloquially referred to as "dip-and-strip") provides a robust method for the determination of elevated concentrations of copper(II) and lead(II) in tap water, although with a modest precision. Attractive features of the technique compared with other electroanalytical techniques are simple handling of the samples and that there is no need for deoxygenation. Further, the extensive and flexible software supporting the instrumentation makes it possible not only to automate the analysis fully but also to present the results digitally and graphically and to store them for possible future processing and statistical treatment. The software could also be used for checking the reliability of each analysis, e.g., by ascertaining that the bismuth internal standard signal is within specified limits.

Compared with atomic absorption spectrometry, an additional advantage is the portability of the instrument, the total weight of the instrument and electrode system being ca. 7 kg. Also, the only installation requirement is access to line power.

This work was supported by the Swedish Natural Science Research Council.

REFERENCES

1 T. Lyngbye, Dissertation, Odense University, Denmark, 1987.
2 I. Singh and D.S. Mavinic, Can. J. Civ. Eng., 18 (1991) 893.
3 R.P. Mitcham, Analyst, 105 (1980) 43.
4 H. Berndt, G. Schaldach and R. Klockenkämper, Anal. Chim. Acta, 200 (1987) 573.
5 A. Alegria, R. Barberá, R. Farré, M.J. Lagarda, M.J. Roig and I. Romero, Int. J. Anal. Chem., 38 (1990) 65.
6 W.F. Davis, Am. Ind. Hyg. Assoc. J., 51 (1990) 620.
7 S.R. Bysouth, J.F. Tyson and P.B. Stockwell, Analyst, 115 (1990) 571.
8 U. Koklu and S. Akman, Anal. Lett., 23 (1990) 569.
9 A. Granéli, D. Jagner and M. Josefson, Anal. Chem., 52 (1980) 2220.
10 L. Renman, D. Jagner and R. Berglund, Anal. Chim. Acta, 188 (1986) 137.
11 D. Jagner, L. Renman and Y. Wang, Electroanalysis, 4 (1992) 267.
12 D. Jagner, L. Renman and Y. Wang, Electroanalysis, 5 (1992) in press.

Analytica Chimica Acta, 278 (1993) 243–247
Elsevier Science Publishers B.V., Amsterdam

Titrations in non-aqueous media: potentiometric investigation of the basicity of *meso*-porphyrins in nitrobenzene solvent

Turgut Gündüz, Neclâ Gündüz and Mustafa Hayvalı

Department of Chemistry, Faculty of Science, University of Ankara, Ankara (Turkey)

(Received 23rd December 1992)

Abstract

The basicity of the *meso*-porphyrins, namely *meso*-tetraphenylporphyrin (**I**), *meso*-tetrakis(4-methylphenyl)-porphyrin (**II**), *meso*-tetrakis(4-methoxyphenyl)porphyrin (**III**), *meso*-tetrakis(4-aminophenyl)porphyrin (**IV**), *meso*-tetrakis(4-chlorophenyl)porphyrin (**V**) and *meso*-tetrakis(4-nitrophenyl)porphyrin (**VI**), was investigated potentiometrically in nitrobenzene solvent. This investigation showed that these compounds are basic, rather than acidic. Whereas they cannot be titrated even with tetrabutylammonium hydroxide, they can readily be titrated with perchloric acid to give well shaped and stoichiometric end-points. In addition, they undergo two proton reactions per porphyrin molecule. However, **IV** shows a second end-point corresponding to a six-proton reaction per porphyrin molecule. Half-neutralization potentials (measures of their basicity) of these compounds are **I** = 321, **II** = 270, **III** = 255, **IV** = 155, **V** = 395 and **VI** = 480 mV. These values clearly indicate that, if *para*-hydrogen with respect to the bond found to be between the phenyl group and porphyrin core of *meso*-tetraphenylporphyrin (**I**) is replaced with basifying methyl, methoxy and amino groups, the basicity of **I** increases (270, 255 and 155 mV, respectively); if the same hydrogen atom is replaced with acidifying chlorine and nitro groups, the basicity of **I** decreases (395 and 480 mV, respectively). These observations show that the nitrogen atoms at the centre of the prophyrin molecules are strongly influenced by changes even at the perifery of the molecules, which is a good indication that porphyrin molecules are flat.

Keywords: Potentiometry; Titrimetry; Basicity; Porphyrins

Porphyrins are very important natural and synthetic compounds. Naturally occurring porphyrins play a vital role in the maintenance of both animal and plant bodies [1], because they constitute the basis of the respiratory systems. Haemoglobins, cytochromes and chlorophylls are the best known porphyrin pigments [2,3]. Haemoglobins and cytochromes contain iron(II) and chlorophylls contain magnesium ion [4–6]. Another naturally occurring porphyrin is vitamin B_{12}, which contains cobalt(II) ion [7].

Correspondence to: T. Gündüz, Department of Chemistry, Faculty of Science, University of Ankara, Ankara (Turkey).

Synthetic porphyrins are numerous. These compounds also form complexes with cations like their naturally occurring congeners [8]. Synthetic porphyrins are used for diverse industrial and scientific purposes, e.g., for protection of paints against ultraviolet light, as coloring pigments in paints, especially in automobile paints, as ingredients in plastics, for the identification of carcinogenic tissues in the human body [9] and ^{57}Co porphyrin complexes in chemotherapy [9].

Although the various properties of synthetic porphyrins have been well studied, no reports of their basicities in non-aqueous media have appeared so far. This work was aimed at establish-

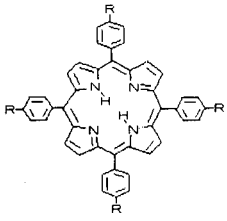

R=H I
R=CH_3 II
R=OCH_3 III
R=NH_2 IV
R=Cl V
R=NO_2 VI

Fig. 1. Structures of *para*-substituted-phenyl *meso*-porphyrins.

ing these properties. In order to do this, six *meso*-porphyrins were synthesized, namely *meso*-tetraphenylporphyrin (**I**) (taken as a standard), *meso*-tetrakis(4-methylphenyl)porphyrin (**II**), *meso*-tetrakis(4-methoxyphenyl)porphyrin (**III**), *meso*-tetrakis(4-aminophenyl)porphyrin (**IV**), *meso*-tetrakis(4-chlorophenyl)porphyrin (**V**) and *meso*-tetrakis(4-nitrophenyl)porphyrin (**VI**) [10–15]. Their structures are shown in Fig. 1.

These porphyrins were obtained from pyrrole and benzaldehyde, or pyrrole and *para*-substituted benzaldehydes, in dry dichloromethane or propionic acid as solvent. The raw materials were purified by column chromatographic techniques. Compounds obtained chromatographically were tested for purity by different methods and found to be sufficiently pure to study their basicity in non-aqueous media. Solubility studies of these compounds indicated that they are sufficiently soluble in nitrobenzene to carry out the planned basicity study.

EXPERIMENTAL

Apparatus

An Orion Model 720 potentiometer equipped with a combined glass electrode and a modified Ag/AgCl electrode was used for potentiometric titrations. The Ag/AgCl electrode was modified by emptying out the aqueous KCl solution and replacing it with a saturated solution of KCl in dry methanol. All titrations were carried out in a specially designed cell which is illustrated in Fig. 2. The cell was connected to a water-circulating thermostat, which kept the temperature of the cell and its contents at 25 ± 1°C. The cell had a capacity of about 50 ml and was connected to the combined glass electrode via inlet A, to a thin-tipped semi-micro burette via inlet B and to a nitrogen cylinder via inlet C. The semi-micro burette enabled the titrant solution to be read to within 0.01 ml.

Chemicals

Dichloromethane was purchased from Merck (99% purity) and was used after further purification. It was first shaken with concentrated sulphuric acid until it becomes colourless, then the sulphuric acid layer was separated using a separating funnel. The dichloromethane layer was shaken first with a 5% Na_2CO_3 solution and then shaken vigorously with distilled water, and subsequently dried with CaH_2 and distilled at normal pressure. The constant-boiling distillate was placed in a dark-coloured glass-stoppered flask and was kept over molecular sieve (4 Å) in the dark.

Chloroform was purchased from Merck (99% purity) and used after further purification. It was first shaken vigorously with distilled water and the chloroform layer was separated with a separating funnel. The chloroform was then dried with $CaCl_2$ and distilled with a tall distillation column.

Pyrrole was purchased from Merck (99% purity) and purified by distillation under high vacuum over zinc dust.

Benzaldehyde as purchased from Merck (98% purity) and used after distillation under vacuum.

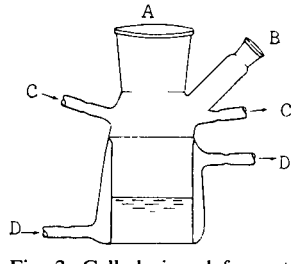

Fig. 2. Cell designed for potentiometric titrations of *meso*-porphyrins under a nitrogen atmosphere, at 25°C. The cell is equipped with a combined glass and Ag/AgCl electrode through A, with a curved thin-tipped semi-micro burette through B, nitrogen through C and constant-temperature water through D.

Silica gel was purchased from Merck (70–230 mesh) and used after activation at 150°C.

4-Nitrobenzaldehyde, 4-chlorobenzaldehyde, 4-methoxybenzaldehyde and 4-methylbenzaldehyde were purchased from Fluka (puriss grade) and used as received.

Boron trifluoride ethyl etherate complex was purchased from Fluka as a 48% solution in diethyl ether and used as received.

Nitrobenzene was purchased from Merck (98% purity) and was used after purification as described previously [16].

Tetrabutylammonium hydroxide was purchased from Merck as a 0.10 M stock solution in 2-propanol and was diluted to 0.02 M with 2-propanol. The solution was diluted as described previously [17].

Perchloric acid was purchased from Merck (70%) and a 0.02 M solution in nitrobenzene was prepared as described previously [18].

meso-Tetraphenylporphyrins **I–III** and **V** were prepared by the method of Lindsey and coworkers [12,13] and **IV** and **VI** by the method of Bettelheim et al. [14].

RESULTS AND DISCUSSION

Solutions (1×10^{-3} M) of the *meso*-tetraphenylporphyrins in nitrobenzene were first titrated potentiometrically with a 0.02 M solution of tetrabutylammonium hydroxide in isobutanol, but no end-points or meaningful curves in nitrobenzene or pyridine solvent were observed. This indicates that these compounds are not sufficiently acidic to be titrated even in one of the strongest non-aqueous bases. Such observations suggest the formation of metal complexes of the porphyrins. It is generally believed that the formation of such porphyrin complexes proceeds through the replacement of two protons on the nitrogen atoms of the porphyrin molecule with a cation, but the present observations imply that this is unlikely.

On the other hand, the titration of these com-

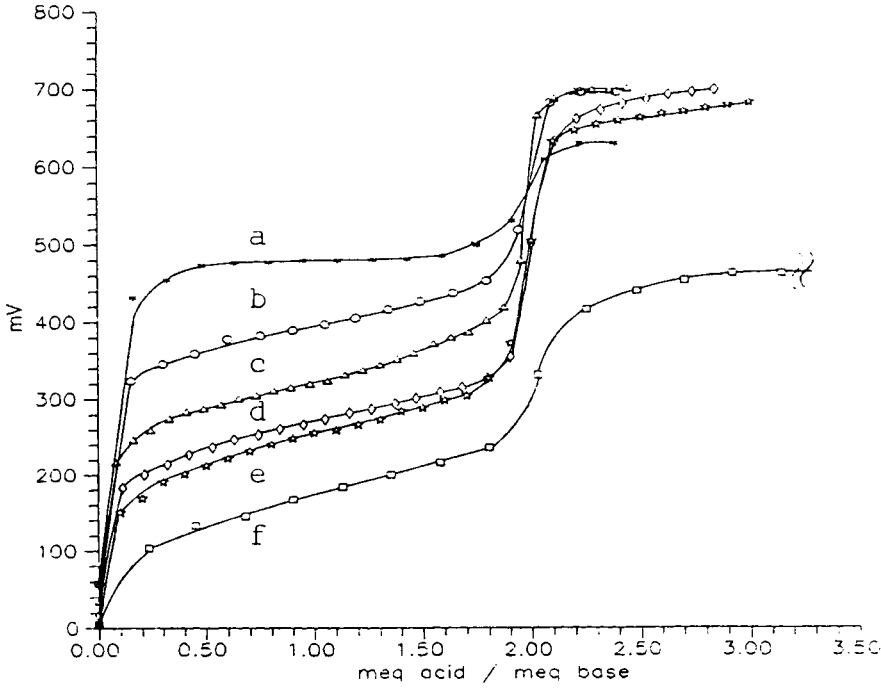

Fig. 3. Potentiometric titration curves of the *para*-substituted-phenyl *meso*-porphyrins with perchloric acid in nitrobenzene under a nitrogen atmosphere at 25°C. (a) **VI**; (b) **V**; (c) **I**; (d) **II**; (e) **III**; (f) **IV**.

pounds with 0.02 M perchloric acid gave well shaped and stoichiometric end-points with potential jumps ranging from 150 to 250 mV (Figure 3). Such potential jumps are considered to be very good for non-aqueous medium titrations.

Closer inspection of the potential jumps at the end-points and the half-neutralization potentials revealed that the *meso*-porphyrins studied are highly basic. The half-neutralization potentials are 480, 395, 321, 270, 255 and 153 mV for the nitro, chloro, hydro, methyl, methoxy and amino derivatives, respectively (higher values indicate a decrease and lower values an increase in basicity).

Another important result obtained from these titration curves is the protonation route of the porphyrins. As can easily be seen, each porphyrin molecule reacts with two molecules of perchloric acid. This means that two of the nitrogen atoms in a porphyrin molecule are protonated together. This indicates that such porphyrin molecules have very extensive resonance systems. As a result of this resonance, positive charge in the core (centre) of the molecule is very effectively dissipated throughout the molecule. Otherwise, a deposit would be observed in the medium. Such deposits, however, were never observed during titrations.

Closer inspection of the half-neutralization potentials reveals that substituents such as methyl, methoxy and chlorine at the *para*-position of the phenyl group, influence the basicity of the *meso*-porphyrins dissolved in nitrobenzene solvent. This means that the benzene rings participate strongly in resonance of the porphyrin core. For instance, if the *para*-hydrogen atom in *meso*-tetraphenylporphyrin (**I**) is replaced with a methyl group, the half-neutralization potential of the compound decreases from 321 to 270 mV. This must be the result of the electron-releasing property of the methyl group. If the *para*-hydrogen atom of the phenyl group in **I** is replaced with methoxy and amino groups, the half-neutralization potential decreases from 321 mV to 255 and 155 mV, respectively. This must be due to the even stronger electron-releasing power of the methoxy and amino groups than the methyl group. On the other hand, if the *para*-hydrogen atom is re-

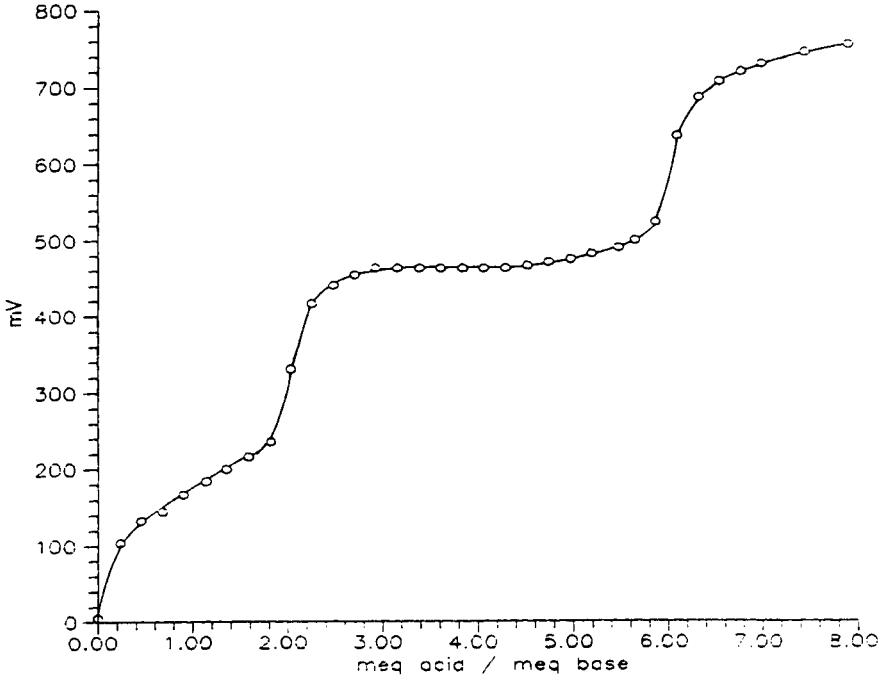

Fig. 4. Potentiometric titration curve of *meso*-tetrakis(4-aminophenyl)porphyrin (**IV**) with perchloric acid in nitrobenzene solvent under a nitrogen atmosphere at 25°C.

placed with a chlorine atom, the half-neutralization potential increases from 321 to 395 mV, owing to the electron-withdrawing power of the chlorine atom. If the *para*-hydrogen atom is replaced with a nitro group, the half-neutralization potential increases from 321 to 480 mV, owing to the even stronger electron-withdrawing power of the nitro group than the chlorine atom.

All the above results indicate that phenyl groups attached to the porphyrin core participate in the resonance structures of the *meso*-porphyrin molecules. This means that they are all in the same plane, and the whole system must be flat. Otherwise, minor changes on the phenyl group would not affect the basicity of the cores of the porphyrins. This result which shows that the substituted phenyl groups and the cores of the porphyrins are in the same plane, is in contrast to the conclusions of Gottwald and Ullman [19] and Burke et al. [20], who considered that the phenyl groups are either perpendicular or at least oblique to the plane of the porphyrin cores.

It is believed that the whole *meso*-porphyrin system is flat at least in nitrobenzene solvent, otherwise the cores of the porphyrins would not be influenced by minor changes at the periphery of these very large molecules.

Another important result obtained from these titrations is the behaviour of the *meso*-tetrakis(4-aminophenyl)porphyrin (**IV**). The titration curve for this compound shows two end-points. The mole ratios of acid to porphyrin at these points are 2:1 and 6:1 (Fig. 4). This is an unexpected observation, because in general at most two charged ions can be stabilized in a non-aqueous medium. This observation is also a very strong indication of the flatness of the *meso*-porphyrins at least in nitrobenzene.

Conclusions

From the potentiometric titration of six *meso*-porphyrins in nitrobenzene solvent, the following conclusions can be drawn. Two of the four nitrogen atoms in the core of the *meso*-porphyrins are very basic in character. They can be titrated together with perchloric acid to give one end-point in nitrobenzene solvent. The basicities of the *meso*-porphyrins are very sensitive to changes at the periphery. This sensitivity is a strong indication of the flatness of the whole *meso*-porphyrin molecule at least in nitrobenzene solvent. *meso*-Tetrakis(4-aminophenyl)porphyrin can undergo a six-proton reaction to give a hexacharged stable ion in nitrobenzene solvent. This is an unusual observation for non-aqueous media.

REFERENCES

1 L.R. Milgrom, J. Chem. Soc., Perkin Trans, 1 (1986) 1483.
2 R.G. Little, J. Heterocycl. Chem., 18 (1981) 129.
3 T. Mashiko, J.C. Marchon, D.T. Musser and C.A. Reed, J. Am. Chem. Soc., 101 (1979) 3653.
4 J. Almog, J.E. Baldwin, M.J. Crossley, J.F. Debernardis, R.L. Dyer, J.R. Huff and M.K. Peters, Tetrahedron, 37 (1981) 3589.
5 V. Thanabal and V. Krishnan, J. Am. Chem. Soc., 104 (1982) 3643.
6 J.L. Sessler, S.J. Weghorn, T. Morishima, M. Rosingana, V. Lynch and V. Lee, J. Am. Chem. Soc., 114 (1992) 8306.
7 M.K. Geno and J. Halpern, J. Am. Chem. Soc., 109 (1987) 1238.
8 A.D. Adler and F.R. Longo, J. Inorg. Nucl. Chem., 32 (1970) 2443.
9 N. Datta-Gupta and T.J. Bardos, J. Heterocycl. Chem., 3 (1966) 495.
10 A.D. Adler, F.R. Longo and J.D. Finarelli, J. Org. Chem., 23 (1967) 476.
11 J.S. Lindsey, I.C. Schreiman, H.C. Hsu, P.C. Kearney and A.M. Marguerettaz, J. Org. Chem., 52 (1987) 827.
12 J.S. Lindsey and R.W. Wagner, J. Org. Chem., 54 (1989) 828.
13 J.S. Lindsey and D.C. Mauzerall, J. Am. Chem. Soc., 104 (1982) 4498.
14 A. Bettelheim, B.A. White, S.A. Raybuck and R.W. Murray, Inorg. Chem., 26 (1987) 1009.
15 J.P. Collman, R.R. Gagne, C.A. Reed, T.R. Halbert, G. Lang and W.T. Robinson, J. Am. Chem. Soc., 97 (1975) 1427.
16 E. Kılıç and T. Gündüz, Analyst, 111 (1986) 949.
17 T. Gündüz, N. Gündüz, E. Kılıç, F. Köseoğlu and S.G. Öztas, Analyst, 113 (1988) 715.
18 T. Gündüz, N. Gündüz, E. Kılıç, A. Kenar and G. Çetinel, Analyst, 111 (1986) 1099.
19 L.K. Gottwald and E.F. Ullman, Tetrahedron Lett., 36 (1969) 3071.
20 J.M. Burke, J.R. Kincaid and T.G. Spiro, J. Am. Chem. Soc., 100 (1978) 6077.

Analytica Chimica Acta, 278 (1993) 249–257
Elsevier Science Publishers B.V., Amsterdam

Determination of aqueous aluminum with the fluorescent chelating ligand, 2-hydroxy-1-carbazole carboxylate

Part I. A model for speciation and stability constants

Todd A. Taylor [1] and Howard H. Patterson

Department of Chemistry, University of Maine, Orono, ME 04469 (USA)

(Received 8th November 1991; revised manuscript received 3rd December 1992)

Abstract

The compound 2-hydroxy-1-carbazole carboxylate (HCC^-) exhibits a shift in its fluorescence spectrum upon binding to aluminum in aqueous solution. Fluorescence studies at a variety of solution pHs and aluminum concentrations have been used to determine the most probable species in solution and binding constants of the complexes formed. The fluorescent chelating agent described in this paper can be used for the rapid determination of unperturbed free aluminum in aqueous solution.

Keywords: Fluorimetry; Aluminium; 2-Hydroxy-1-carbazole carboxylate

The interactions of simple bidentate ligands with aluminum in aqueous solutions where aluminum is extensively hydrolyzed are still not well characterized. Much of the uncertainty associated with aluminum–ligand speciation in these solutions results from the fact that few analytical methods are available to determine aluminum–ligand interactions at low concentrations.

Studies of aluminum complexes of bi- or tridentate oxygen coordinating ligands have suggested that these complexes can hydrolyze [1–6], form small oligomers [7–9], and polymerize [10,11]. Precipitates form at neutral pH under conditions used for potentiometric titrations of these complexes [7,10,12]. Few studies are available for solutions with low ionic strength [4,5] or solutions with high metal to ligand ratios [4–9]. Aluminum solutions that are supersaturated with respect to crystalline aluminum trihydroxide (gibbsite) are challenging to work with because they do not come to equilibrium immediately during acid–base titrations [13].

The bidentate chelating ligand described in this paper, 2-hydroxy-1-carbazole carboxylate (HCC^-),

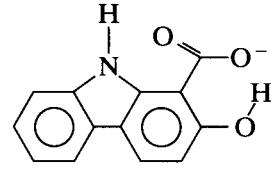

HCC^-

is fluorescent in both the free and aluminum bound forms. The fluorescence intensity of a solution containing HCC^- and aluminum has been measured at various pH and aluminum concen-

Correspondence to: H.H. Patterson, Department of Chemistry, University of Maine, Orono, ME 04469 (USA).
[1] Current address: Tufts University, Department of Chemistry, Medford, MA 02155 (USA).

trations. The total concentration of the ligand in solution was kept low to prevent it from significantly altering the aluminum speciation in solution, and a pH modulation technique was employed to study the species which form relatively rapidly in solution. A simple model has been constructed to determine the speciation and stability constants for the interaction of HCC^- with aluminum. In the accompanying paper, we use this model to develop a ratio fluorescence method to determine concentrations of free aluminum (i.e. $[Al(H_2O)_6^{3+}]$) with little perturbation to the solution [14].

EXPERIMENTAL

Apparatus

Fluorescence and absorption measurements were made with a Perkin-Elmer MPF-44A spectrofluorometer and a Cary 17D absorption spectrometer, respectively. The fluorometer employs a 150-W xenon lamp, single 1200 lines/mm excitation and emission gratings, and a Hamamatsu R928 PMT detector. Quartz cuvets of 1-cm pathlength were employed for fluorescence measurements. Right angle excitation/emission geometry was employed. Fluorescent solutions were thermostated at 25 ± 0.2°C, and 4 nm excitation and emission bandpasses were employed. Fluorescence spectra in this paper are not corrected for instumental characteristics.

An Altex Φ71 pH meter with an Orion 91-02 combination electrode was used for pH measurements following two point calibration. The term pH in this paper refers to $-\log[H^+]$ rather than what a "pH" meter measures, $-\log(a_{H^+})$, where a_{H^+} is the hydrogen ion activity. The activity coefficient of H^+ was obtained using the Guntelberg equation [15].

Reagents

Sodium 2-hydroxy-1-carbazole carboxylate (CCHNa, 97%) and 5-sulfosalicylic acid were obtained from Aldrich and used as obtained. All metals were analytical grade from Fisher, Al(III) as the nitrate and Ca(II), Mg(II) and Zn(II) as chlorides.

Metal binding

Metal solutions were prepared just prior to each experiment. Studies of the pH dependence of the interaction of CC with Al(III) were accomplished by adjusting the pH with acid and base alternately during the pH titration using 0.1 or 1.0 M HCl or NaOH. Solutions were vigorously stirred during pH adjustment. This procedure allowed rapid kinetic processes to approach equilibrium without letting the solutions sit for long periods between measurements. A similar procedure was employed by others [7–9] to test the reproducibility and reversibility of solution equilibria. The solutions remained clear and no precipitation was evident during the titrations for the aluminum concentrations employed in these experiments (0.1–1.0 mM).

Two fluorescence intensity measurements were obtained at each pH for each solution. The F^a intensity was obtained by exciting the solution at 330 nm and observing the fluorescence intensity at 450 nm. The F^b intensity was obtained by exciting at 355 nm and observing the emission at 400 nm. Daily calibration was accomplished by bringing a sample of 0.9 μM CC to pH 10–11 and measuring the fluorescence intensities F^a and F^b.

A complete pH titration of a CCAl solution of pH 4–12 could be done, along with spectroscopic measurements in ca. 6 h. Solutions were incubated until both the pH and the fluorescence intensity stabilized (2–15 min depending on the pH). Some solutions were incubated for 30 min after a pH change (between pH 3–7), and the observed fluorescence intensities did not differ significantly from the data obtained by the more rapid pH modulation results.

Solutions of CC were somewhat photosensitive and were shielded from exposure to ultraviolet light during storage or during pH titrations. Twenty to forty percent of the CC in solution had degraded by the time a pH titration of CCAl solution of pH 4–12 was completed under our experimental conditions. To account for this degradation, aliquots of the CCAl solution were periodically adjusted to pH 11 and the amount of CC remaining in solution was determined by measuring the fluorescence intensity of the solu-

tion. The excitation and emission spectra of these solutions indicated that the only fluorescent CC species present at pH 11 was HCC^-. Further studies indicated that degradation of CC was most rapid in aluminum solutions near neutral pH when exposed to room lights and when the solution contained dissolved oxygen.

Data analysis, binding curve studies, and modeling were accomplished using Lotus 1-2-3® on a Zenith ZF-248-81 microcomputer. The Guntelberg equation [15] was used to determine activity coefficients for ions and to convert ionic strength-dependent stability constants (Q values) to infinite dilution stability constants (K values) in this paper.

The abbreviation CC, with no charge specified, refers to the sum of all 2-hydroxy-1-carbazole carboxylate species in solution ($HCC^- + H_2CC + CCAl^+ + CCAlOH + \ldots$) in this paper. Similarly, the abbreviations Al and CCAl, with no charges specified, refer to all forms of aluminum and CC-bound forms of aluminum, respectively, in solution.

Aluminum hydrolysis

The aluminum species in solution are assumed to be restricted to monomeric aluminum when determining CCAl stability constants because low aluminum concentrations were employed and because the solutions were titrated rapidly [10]. Therefore, the monomeric hydrolysis constants of May et al. [16] were used for modeling different aluminum species in all solutions.

RESULTS

Spectroscopic properties of CC and CC–metal complexes

The absorption and fluorescence spectra of aqueous 2-hydroxy-1-carbazole carboxylate (HCC^-) and its low-pH aluminum complex, $CCAl^+$, are shown in Fig. 1. H_2CC was not fluorescent (pH ≈ 1) and its lowest energy absorption peak at 352 nm was broader than those of HCC^- and $CCAl^+$. The excitation and emission conditions for monitoring fluorescence intensities as a function of pH were chosen so that F^a was highly sensitive to HCC^- and F^b was highly sensitive to $CCAl^+$.

Figure 2 shows the fluorescence spectra of some CCAl complexes. At pH 4.4, only $CCAl^+$ fluorescence is observed (0.30 mM Al^{3+}). At pH 7.0, the solution fluorescence shows a 60% reduc-

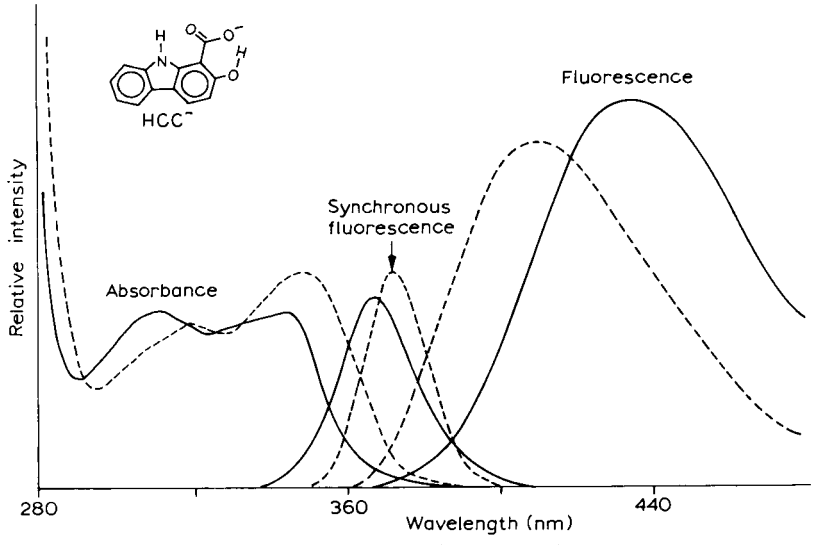

Fig. 1. Absorption, synchronous fluorescence ($\Delta\lambda = 20$ nm) and fluorescence spectra of HCC^- (———) and $CCAl^+$ (— — —). Spectral resolution was 1 nm, and λ_{ex} was 330 nm for the fluorescence spectra.

tion in intensity and a peak shifted to the red compared to the pH 4.4 case. When the pH is increased to 10 or greater, the fluorescence and absorption spectra of this solution are identical to that of HCC^- alone, and this indicates that hydroxide has displaced CC^{2-} from aluminum leaving HCC^- as the only CC species in solution.

The fluorescence of CCMg is also shown in Fig. 2. CCMg appears to form quantitatively at pH 10.5 (1.0 mM Mg^{2+}) and the fluorescence spectrum and intensity is nearly identical to that of $CCAl^+$. CC does not appear to bind to Ca^{2+} or Zn^{2+} because HCC^- fluorescence does not change between pH 2–12 in solutions containing 1.0 mM Ca^{2+} and Zn^{2+}.

The absorption and fluorescence spectra of solutions of CC in pure water were constant from pH 5.5 to 12 but exhibited changes at lower pH. The carboxylate pK_a measured by absorption (pK_{CH}) was 3.02 (370 nm, 10 μM CC), whereas the pK_a determined from the fluorescence data (pK^*_{CH}) was 3.28. Stability constants measured by fluorescence will be designated with an asterisk in this paper.

Determination of CCAl binding constants by fluorescence

The normalized fluorescence intensities of HCC^- and $CCAl^+$ upon addition of aluminum at pH 4 and 5 are shown in Fig. 3. The disappearance of HCC^- is indicated by the decline of F^a as the concentration of aluminum increases (i.e., as pAl decreases). Similarly, the appearance of $CCAl^+$ is indicated by the increase of F^b as the aluminum concentration increases. Figure 3 shows that a change in the fluorescence intensities of CC can be observed over 2.5 orders of magnitude of aluminum concentration at any pH.

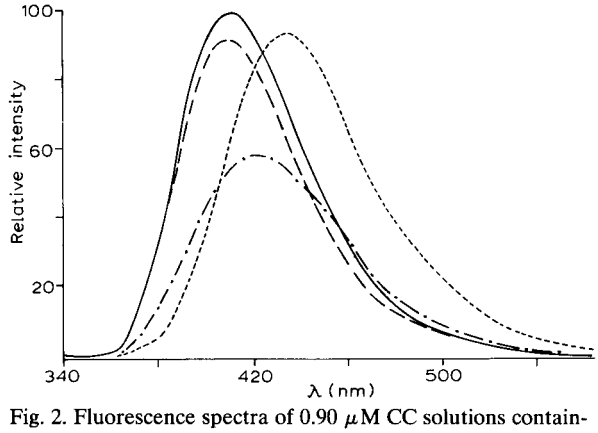

Fig. 2. Fluorescence spectra of 0.90 μM CC solutions containing aluminum or magnesium. Solutions containing 1 mM Mg at pH 11 (— — —); solutions containing 0.3 mM total aluminum at pH 4.4 (———), pH 7.0 (–·–·–·), and pH 10.5 (- - - - - -). Spectral resolution was 1 nm, and λ_{ex} was 330 nm for all spectra.

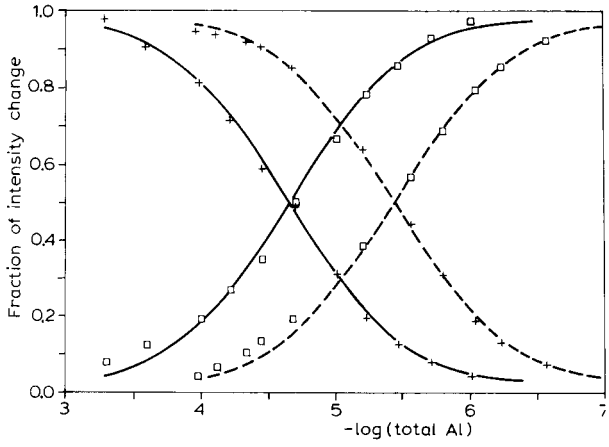

Fig. 3. Fluorescence intensities observed from CC solutions as a function of $-\log$(total aluminum) at pH 4 (———) and pH 5 (— — —); (□) F^a; (+) F^b.

The fluorescence intensities F^a and F^b are not purely from one form of CC when both forms are present. Data points shown in Fig. 3 represent relative fluorescence intensities observed after subtracting the fluorescence intensity from the other form. The curves in Fig. 3 show the fluorescence intensities expected if only one reaction occurs in solution: $HCC^- + Al^{3+} \rightleftharpoons CCAl^+ + H^+$. The data follow this simple binding model at low aluminum concentrations but deviate from the model at high aluminum concentrations. This indicates that a more complicated reaction than simple $CCAl^+$ formation is occurring, and more elaborate data and modeling are needed to describe the CC–Al interaction.

Figure 4 shows the CC fluorescence intensities as a function of pH for three solutions of different aluminum concentrations. $CCAl^+$ is formed as the pH is raised from 2.5 to 4.5 resulting in increases in both F^a and F^b. As the pH is increased further, F^a and F^b decrease in inten-

sity. These decreases in intensity indicate that hydrolysis of the $CCAl^+$ complex occurs because displacement of CC^{2-} from aluminum does not occur until pH ≈ 10. Other aluminum–organic complexes also exhibit their maximum fluorescence intensity between pH 4–5 under similar solution conditions [17,18].

BINDING MODEL

Twenty possible hydrolysis species of the form $CCAl_x(OH)_y$ with $4 > x > 0$ and $8 > y > 0$ were considered in an attempt to fit the fluorescence data. The solid line curves of Fig. 4 show the best fitting model of the CCAl fluorescence data. This model includes the fluorescent species HCC^-, $CCAl^+$, $CCAl_2(OH)_3^+$, $CCAl_3(OH)_4^{3+}$, CCAlOH and $CCAl(OH)_2^-$. The equilibria of these species are defined by the following stability constant expressions:

$$Q^*_{CH} = [H^+][HCC^-]/[H_2CC] \quad (1)$$

$$Q^*_{CA} = [H^+][CCAl^+]/([HCC^-][Al^{3+}]) \quad (2)$$

$$Q^*_{C23} = \left[CCAl_2(OH)_3^+\right][H^+]^3/([CCAl^+][Al^{3+}]) \quad (3)$$

$$Q^*_{C34} = \left[CCAl_3(OH)_4^{3+}\right][H^+]^4 / \left([CCAl^+][Al^{3+}]^2\right) \quad (4)$$

$$Q^*_{C11} = [CCAlOH][H^+]/[CCAl^+] \quad (5)$$

$$Q^*_{C12} = \left[CCAl(OH)_2^-\right][H^+]^2/[CCAl^+] \quad (6)$$

Fluorescence intensities at any given wavelength settings, e.g. F^a, result from the sum of the intrinsic fluorescence of each species present in solution times the concentrations of that species

$$F^a = a_1[HCC^-] + a_2[CCAl^+] + a_3\left[CCAl_2(OH)_3^+\right] + a_4\left[CCAl_3(OH)_4^{3+}\right] + a_5[CCAlOH] + a_6\left[CCAl(OH)_2^-\right] \quad (7)$$

The a_x values in this equation will depend upon the instrumental characteristics of the fluorometer used to obtain them, so only the ratio

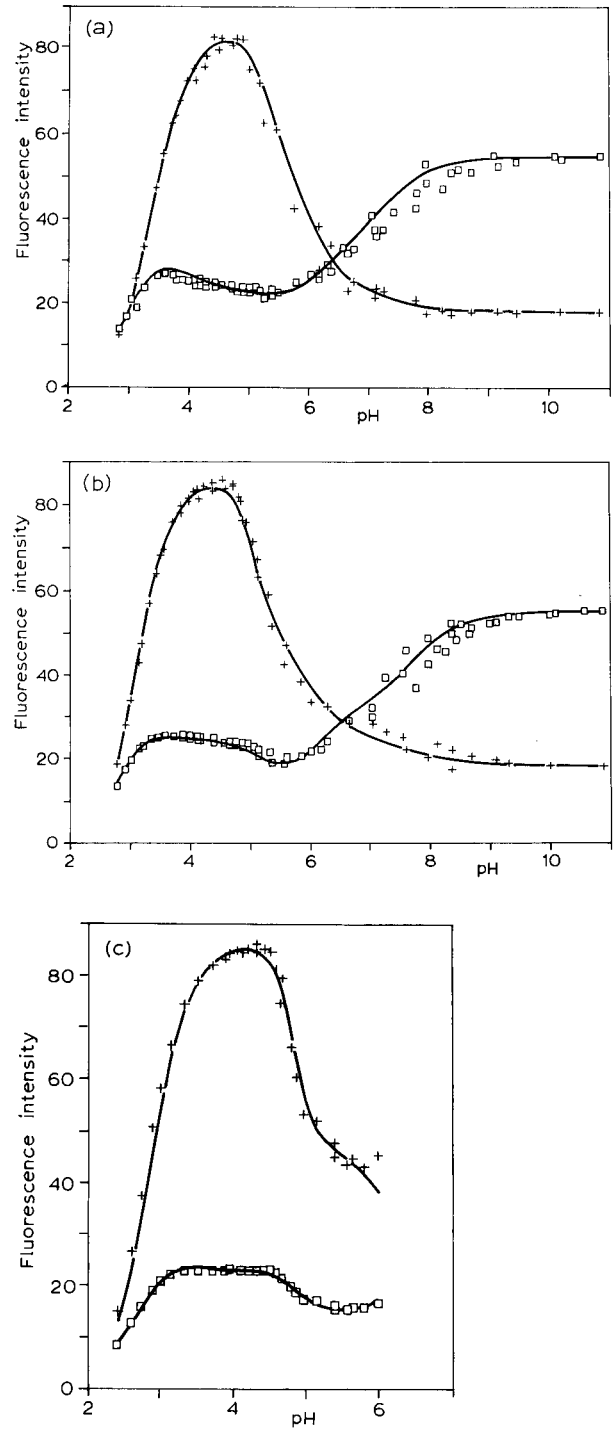

Fig. 4. Fluorescence intensities vs. pH for 0.90 μM CC solutions containing aluminum: (a) 0.10 mM Al at 4 mM ionic strength, (b) 0.30 mM Al at 5.5 mM ionic strength, (c) 1.0 mM Al at 10 mM ionic strength; (□) F^a; (+) F^b.

$a_1 : a_2 : a_3 : a_4 : a_5 : a_6$ will be independent of the fluorometer used. The total concentration of CC in solution, C_{cc}, is given by

$$C_{cc} = [HCC^-] \cdot \left([H^+]Q^*_{CH} + 1 + Q^{*a}_{CA}[Al^{3+}]/[H^+] + Q^{*a}_{CA}Q^{*a}_{C23}[Al^{3+}]^2/[H^+]^4 + Q^{*a}_{CA}Q^{*a}_{C34}[Al^{3+}]^3/[H^+]^5 + Q^{*a}_{CA}Q^{*a}_{C11}/[H^+] + Q^{*a}_{CA}Q^{*a}_{12}/[H^+]^2\right) \quad (8)$$

using Eqns. 1–6. By multiplying the right side of Eqn. 7 by C_{cc}/C_{cc}, an equation for F^a is obtained which is independent of $[HCC^-]$

$$F^a = C_{cc}\left\{a_1 + a_2Q^{*a}_{CA}[Al^{3+}]/[H^+] + a_3Q^{*a}_{CA}Q^{*a}_{C23}[Al^{3+}]^2/[H^+]^4 + a_4Q^{*a}_{CA}Q^{*a}_{C34}[Al^{3+}]^3/[H^+]^5 + a_5Q^{*a}_{CA}Q^{*a}_{C11}/[H^+] + a_6Q^{*a}_{CA}Q^{*a}_{C12}/[H^+]^2\right\} / \left\{[H^+]/Q^*_{CH} + Q^{*a}_{CA}[Al^{3+}]/[H^+] + Q^{*a}_{CA}Q^{*a}_{C23}[Al^{3+}]^2/[H^+]^4 + Q^{*a}_{CA}Q^{*a}_{C34}[Al^{3+}]^3/[H^+]^5 + Q^{*a}_{CA}Q^{*a}_{C11}/[H^+] + Q^{*a}_{CA}Q^{*a}_{C12}/[H^+]^2 + 1\right\} \quad (9)$$

where $[Al^{3+}] = C_{Al}/(1 + Q_{11}/[H^+] + Q_{12}/[H^+]^2 + Q_{13}/[H^+]^3 + Q_{14}/[H^+]^4)$ and C_{Al} is the total concentration of aluminum in solution. The model curves for F^b were obtained the same way by replacing the a_x and Q^{*a} values with b_x and Q^{*b} values in Eqn. 9.

The fluorescence model curves for all three solutions of Fig. 4 were obtained using the same K^*, a_x, and b_x values. The Q^* values were calculated for each of the three ionic strengths from the same K^* values and used in Eqn. 9 to obtain the model curves. The resulting relative fluorescence intensities of the CC–Al species are shown in Table 1. The resulting stability constants are given in Table 2.

The procedure used to model the fluorescence data and determine the CCA1 speciation is described below. The values of K^*_{CH}, a_1 and b_1 are known from CC solutions that are free of aluminum (previous sections). The values of K^*_{CA}, a_2, and b_2 can be determined accurately from the pH 3–4.5 fluorescence data. These low pH solutions are undersaturated with respect to gibbsite and give high precision fluorescence data when sufficient time is allowed for solution equilibration. The fluorescence data obtained at low aluminum concentrations (0.1 mM Al, Fig. 4a) can be fit by assuming only two additional CC species are present in solution other than HCC^-, H_2CC, and $CCAl^+$: CCAlOH and $CCAl(OH)_2^-$. The fluorescence intensities F^a and F^b level off at intensities characteristic of HCC^- when the solution pH > 10 (Fig. 4a).

TABLE 1

Relative fluorescence intensities of the CC–Al species determined from the F^a and F^b data

Compound	Relative fluorescence intensities	
	F^a	F^b
HCC^-	$a_1 = 55$	$b_1 = 18.4$
$CCAl^+$	$a_2 = 22.5$	$b_2 = 87.5$
$CCAl_2(OH)_3^+$	$a_3 = 18$	$b_3 = 22$
$CCAl_3(OH)_4^{3+}$	$a_4 = 15$	$b_4 = 48$
CCAlOH	$a_5 = 22$	$b_5 = 36$
$CCAl(OH)_2^-$	$a_6 = 29$	$b_6 = 26$

At higher aluminum concentrations (0.3 mM and 1.0 mM, Fig. 4b and c, respectively), the fluorescence data in the pH 5–8 region deviates from the above model, and polynuclear CCAl species must be invoked to describe the data. CCAl species having an Al : OH ratio close to 2 : 3 or 3 : 5 affect this pH region. Thus, the species investigated most carefully were $CCAl_2(OH)_{2,3,4}$, $CCAl_3(OH)_{3,4,5,6}$ and $CCAl_4(OH)_{4,5,6}$. Of these

TABLE 2

Stability constants obtained from the F^a and F^b data

F^a	F^b	Average
$pK^{*a}_{CH} = 3.35$	$pK^{*b}_{CH} = 3.30$	3.31 ± 0.06 [1]
$pK^{*a}_{CA} = -0.97$	$pK^{*b}_{CA} = -0.97$	-0.97 ± 0.06
$pK^{*a}_{C23} = 11.8$	$pK^{*b}_{C23} = 11.8$	11.8 ± 0.08
$pK^{*a}_{C34} = 12.7$	$pK^{*b}_{C34} = 12.7$	12.7 ± 0.08
$pK^{*a}_{C11} = 6.2$	$pK^{*b}_{C11} = 6.2$	6.2 ± 0.07
$pK^{*a}_{C12} = 11.9$	$pK^{*b}_{C12} = 11.9$	11.9 ± 0.11

[1] Including 3.28 measured directly.

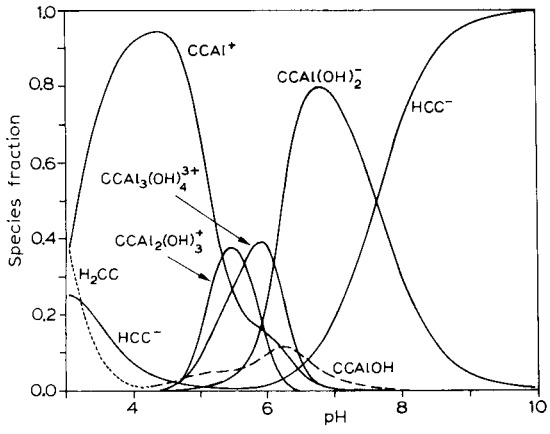

Fig. 5. CC speciation calculated for a 0.30 mM Al solution in 3 mM NaCl as a function of pH.

possibilities, no single species alone could explain the data, while the 2:3 + 3:4 pair gave the fit shown in Fig. 4b and c. No other pair gave as good a fit. A three component oligomer speciation should give a better fit, but the simplest speciation is preferred until evidence for more complex speciation is available.

The stability constants in Table 2 can be used to calculate the equilibrium speciation of CCAl solutions under various conditions. Figure 5 shows the CC speciation of a solution containing 3 mM total aluminum. Figure 6 shows the CC speciation

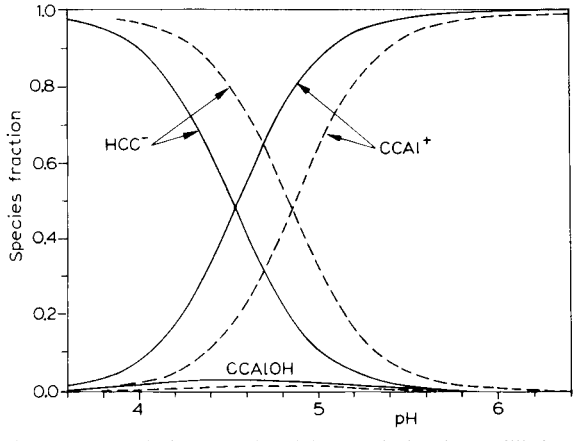

Fig. 6. CC speciation calculated for a solution in equilibrium with natural (— — —) and synthetic (———) gibbsite in 3 mM NaCl.

of solutions in equilibrium with natural or synthetic gibbsite.

DISCUSSION

The CCAl model described in this paper fits the fluorescence data over a wide range of solution conditions. The measurements in Fig. 4 span a 10-fold aluminum concentration range, a 2.5-fold ionic strength range and a pH range of 3–11, which supports the generality of this speciation model. Aluminum concentrations were chosen to keep the ionic strength low enough to obtain accurate infinite dilution calculations and high enough to keep CC bound to aluminum throughout the necessary pH range for stability constant determination.

Binding properties of CCAl species

The measured stability constant of HCC^- with Al^{3+} ($pK^*_{CA} = -0.97$, Table 2) is between that of the infinite dilution values estimated for salicylate (−0.48) and sulfosalicylate (−1.95) from the literature [19]. Aluminum(III) is a "hard" cation [20] and is expected to prefer the phenolate ligand over the amine ligand when binding with CC.

The hydrolysis constants of a metal bound by an organic ligand should be smaller than the hydrolysis constant of the bare metal [10]. Our results are consistent with this because the first two monomeric hydrolysis constants of $CCAl^+$ (pK^*_{C11}, pK^*_{C12}) determined in this paper are smaller than those of Al^{3+} ($pK_{11} = 4.99$, $pK_{12} = 10.13$, Ref. 16). However, our stability constants for $CCAl_3(OH)_4^{3+}$ and $CCAl_2(OH)_3^+$ are somewhat stronger than the aluminum hydrolysis constants for $Al_3(OH)_4^{5+}$ or $Al_2(OH)_3^{3+}$ [13] available in the literature. The fact that the same type of aluminum hydroxide clusters are found when aluminum hydrolysis is analyzed potentiometrically and fluorometrically supports the $CCAl_x(OH)_y$ speciation we derive in this paper. However, both potentiometry and fluorescence are only capable of estimating the speciation and formation constants of the dominent $Al_x(OH)_y$ species occurring in solution when many complicated equilibria are present.

Only CCAl complexes containing one CC molecule are assumed to form in these studies because CC is present at less than 1% of the total aluminum concentration. Furthermore, the stability constant for a second salicylate ligand binding to Al(III) or Ga(III) is more than two orders of magnitude smaller that the first [10,19]. Because CC_zAl_y species can be neglected, it is not necessary to solve high-order polynomials to test models for CCAl speciation in solution.

The accuracy of the CCAl constants determined in this paper is greatest for those constants determined in solutions undersaturated with respect to gibbsite (K^*_{CH}, K^*_{CA}, K^*_{C12}) and lowest for those species determined in supersaturated solutions [$CCAl_2(OH)_3^+$, $CCAl_3(OH)_4^{3+}$, CCAl(OH)]. This is because aluminum speciation and hydrolysis constants are not known with certainty in supersaturated solutions [13,16,21] and the formation of polymeric species can depend upon the solution conditions employed [22,23]. Previous studies of morin–aluminum complexes found only monomeric Al–morin hydrolysis products [4,5] because lower aluminum concentrations and pHs were employed. The difference between the pK^{*a} and pK^{*b} values in Table 2 are small in comparison to the range of aluminum hydrolysis constants in the literature [21]. The average of the values of pK^{*a} and pK^{*b}, shown in the last column of Table 2, are used for the speciation plots given in the last section.

Spectral properties of CCAl species

The similarities in the fluorescence intensities and electronic spectral shapes of HCC^-, $AlCC^+$, and MgCC (Figs. 1 and 2) suggest that the lowest energy electronic transition is the same for all species. The synchronous fluorescent spectra of these compounds indicate that the 0–0 energy is approximately the same for these compounds. The CCAl species in Table 1 having the highest positive charge, $CCAl^+$ and $CCAl_3(OH)_4^{3+}$, have the smallest Stokes shift and $b_x > a_x$. The more negatively charged species HCC^- and $CCAl(OH)_2^-$, have $a_x > b_x$, and a large Stokes shift. These results suggest that the more positively charged CCAl species are more rigid and have a smaller Stokes shift than the more negatively charged CCAl species. Rigid molecules exhibit a small Stokes shift because their excited state and ground state molecular configurations are more similar to each other [24]. By choosing instrumental conditions sensitive to species with a large Stokes shift (F^a) and then other conditions sensitive to species with a small Stokes shift (F^b), studies can be carried out of the different fluorescing CC species in solution.

Studies of the solution absorption spectra at 375 nm vs. pH for CCAl solutions (20 μM CC, 1 mM Al) showed absorption changes at pH values similar to those observed in the fluorescence spectra (Fig. 4c). Sulfosalicylate–aluminum solutions also exhibited similar absorption changes at 323 nm under the same experimental conditions. These results suggest that electronic absorption transitions of Al–salicylate complexes, like fluorescent transitions, are sensitive to the type of $CCAl_x(OH)_y$ complexes formed in solution.

Speciation modeling of CCAl solutions

The CC speciation of a 0.3 mM Al solution shown in Fig. 5 indicates that $CCAl(OH)_2^-$ is the predominant CC species in solution at pH 7.0. The fluorescence spectrum of this solution is shown in Fig. 2. The long wavelength of the fluorescence of this solution is consistent with the large Stokes shift expected for the negatively charged $CCAl(OH)_2^-$. A similar speciation curve for a 1.0 mM Al^{3+} solution indicates that the highly-fluorescent $CCAl^+$ species is formed almost quantitatively at pH 4.5. This is consistent with the high F^b values of CCAl solutions near pH 4.5 (Fig. 4c).

The CC speciation obtained for solutions in equilibrium with gibbsite indicate that the predominant CC species in solution are HCC^- and $CCAl^+$, with some (1–3%) CCAlOH present. The fraction of $CCAl_2(OH)_3^+$ never exceeds 0.002 and 0.0004 in the natural and synthetic gibbsite cases, respectively, and the fractions of $CCAl_3(OH)_4^{3+}$ and $CCAl(OH)_2^-$ are even lower. These results indicate that CC is a good fluorescent probe for measuring aluminum concentrations in gibbsite solutions in the pH range of 4.0–5.5.

This work was supported by the U.S. National Science Foundation (Grant BSR 8807826) and by the ALBIOS Project, EPRI (Contract RP-2365-01).

REFERENCES

1 V.A. Nazarenko and E.M. Nevskaya, Russ. J. Inorg. Chem, 14 (1969) 1696.
2 S.N. Dubey and R.C. Megrotra, J. Inorg. Nucl. Chem., 26 (1964) 1543.
3 T.R. Bhat, R.R. Das and I. Shanker, Indian J. Chem., 5 (1967) 324.
4 B.A. Browne, J.G. McColl and C.T. Driscoll, J. Environ. Qual., 19 (1990) 65.
5 B.A. Browne, J.G. McColl and C.T. Driscoll, J. Environ. Qual., 19 (1990) 73.
6 F.J. Sikora and M.B. McBride, Environ. Sci. Technol., 23 (1989) 349.
7 T. Hedlund, H. Bilinski, L. Horvath, N. Ingri and S. Sjoberg, Inorg. Chem., 27 (1988) 1370.
8 L.O. Ohman and S. Sjoberg, Tetrahedron, 2 (1983) 1329.
9 L.O. Ohman and S. Sjoberg, Acta Chem. Scand., 37 (1983) 875.
10 R.J. Motekaitis and A.E. Martell, Inorg. Chem., 23 (1984) 18.
11 J.D. Glickson, T.P. Pitner, J. Webb and R.A. Gams, J. Am. Chem. Soc., 97 (1975) 1679.
12 P. Letkaman, A.E. Martell and R.J. Motekaitis, J. Coord. Chem., 10 (1980) 47.
13 C.F. Baes and R.E. Mesmer, The Hydrolysis of Cations, Wiley, New York, 1976.
14 T.A. Taylor, H.H. Patterson, C.S. Cronan and C.L. Schofield, Anal. Chim. Acta, 278 (1993) 259.
15 W. Stumm and J.J. Morgan, Aquatic Chemistry, Wiley-Interscience, New York, 1981.
16 H.M. May, P.A. Helmke and M.L. Jackson, Geochim. Cosmochim. Acta, 43 (1979) 861.
17 Z. Zhujun and W.R. Sietz, Anal. Chim. Acta, 171 (1985) 251.
18 D.J. Hydes and P.S. Liss, Analyst, (1976) 922.
19 A.E. Martell and R.M. Smith, Critical Stability Constants, Vol. 3, Plenum Press, New York, 1977.
20 F. Basolo and R.G. Pearson, Mechanisms of Inorganic Reactions, Wiley, New York, 1967.
21 D.K. Nordstrom, S.D. Valentine, J.W. Ball, L.N. Plummber and B.F. Jones, U.S.G.S. Water-Resources Investigation Report 84-4186, 1984.
22 P.M. Bertsch, Soil Sci. Soc. Am. J., 51 (1987) 825.
23 S.J. Karlik, E. Tarien, G.A. Elgavish and G.L. Eichorn, Inorg. Chem., 22 (1983) 525.
24 I.B. Berlman, Handbook of Fluorescence Spectra of Aromatic Molecules, Academic Press, New York, 1971.

Analytica Chimica Acta, 278 (1993) 259–268
Elsevier Science Publishers B.V., Amsterdam

Determination of aqueous aluminum with the fluorescent chelating ligand, 2-hydroxy-1-carbazole carboxylate

Part II. Application of ratio fluorescence spectroscopy

Todd A. Taylor [1] and Howard H. Patterson
Department of Chemistry, University of Maine, Orono, ME 04469 (USA)

Christopher S. Cronan
Department of Botany and Plant Pathology, University of Maine, Orono, ME 04469 (USA)

Carl L. Schofield
Department of Natural Resources, Cornell University, Ithaca, NY 14853 (USA)

(Received 8th Novenber 1991; revised manuscript received 3rd December 1992)

Abstract

A ratio fluorescence (RF) technique is developed for the measurement of low aqueous concentrations of free aluminum ion ($[Al(H_2O)_6^{3+}]$) with little perturbation to the analyte solution. A small amount of the fluorescent aluminum-binding chelating agent 2-hydroxy-1-carbazole carboxylate (HCC^-) is added to an analyte solution and the solution fluorescence is measured at two different wavelength settings. The ratio of these two fluorescence intensities is used in conjunction with the solution pH and ionic strength to determine the aluminum concentration. The lower limit of measuring $[Al(H_2O)_6^{3+}]$ by this technique is 0.7 μM at pH 4 and 0.06 μM at pH 5. Effects of potential interferences present in natural water solutions are characterized, and the RF method is compared with a standard chemical extraction method of aluminum speciation in aged aluminum hydroxide solutions.

Keywords: Fluorimetry; Aluminium; 2-Hydroxy-1-carbazole carboxylate

Despite recent interest in the environmental chemistry and biotoxicity of aluminum [1–4] there is still considerable uncertainty regarding our ability to measure ambient concentrations of free inorganic aluminum in natural waters. Most chemical methods of aluminum speciation entail substantial modification of the analyte solution prior to aluminum measurement, such as pH and ionic strength adjustment and total complexation and extraction of all reactive iron and aluminum in solution [5–12]. Several methods have been employed to compensate for the shifts in equilibria imposed by the measurement process, among them measuring aluminum concentration as a function of time and extrapolating to time zero [5–7], or performing steps rapidly and assuming that solution equilibration with polymeric

Correspondence to: H.H. Patterson, Department of Chemistry, University of Maine, Orone, ME 04469 (USA).
[1] Current address: Tufts University, Department of Chemistry, Medford, MA 02155 (USA).

$Al_x(OH)_y$ species is kinetically slow [11]. Even recently developed methods of aluminum speciation require complete complexation of all reactive aluminum and substantial modification of the analyte solution before the measurement step [12–16]. One low-perburbation fluorescence method has been developed for aluminum analysis [17,18]; however, this is not a ratiometric method. Although ^{27}Al NMR is a non-perturbational method, the broad resonance peaks of the $Al_x(OH)_y^{3x-y}$ species in the pH range of 4–7 result in a high detection limit of 0.4 mM for monomeric aluminum [19].

The object of this study was to characterize the ability of the probe, 2-hydroxy-1-carbazole carboxylate (HCC^-) to determine aluminum concentrations in solutions similar to those found in natural waters. HCC^- is added to aqueous solutions at low concentrations and the ratio of two fluorescence intensity measurements is used to determine the concentration of free $Al(H_2O)_6^{3+}$ in solution using a chemical equilibrium model we have developed [20]. This ratio fluorescence technique (1) provides little perturbation to the solution being analyzed; (2) measures free aluminum ion over 2.5 orders of magnitude of concentrations in solutions of pH 6 or less; (3) is resistent to the potential interferences commonly found in natural water solutions, such as humic materials and other metals, and (4) does not foul as optrode sensors can, because new reagent is added to each solution. This ratio fluorescence chelating agent for determination of aluminum behaves in a manner similar to the wavelength-shifting ratio fluorescence agents employed for H^+, Ca^{2+} and Mg^{2+} determination in biological and cellular solutions [21–24].

EXPERIMENTAL

Apparatus and reagents

The instruments and reagents in this work have been described previously [20]. The fulvic acid employed in this study was characterized elsewhere [25]. A stock solution of 0.50 mM NaHCC was employed as the source of CC for these studies and was stored in the dark.

Ratio fluorescence measurements

Four fluorescence measurements, I_0^a, I_0^b, I^a, and I^b are required for aluminum determination. The I^a measurements are obtained using 330 nm excitation and 450 nm emission wavelengths, while the I^b measurements are obtained using 355 nm excitation and 400 nm emission wavelengths. I_0^a and I_0^b are measured before adding HCC^- to the solution. The ratio of F^b/F^a can then be calculated

$$r = \frac{F^b}{F^a} = \frac{I^b - I_0^b}{I^a - I_0^a} \quad (1)$$

Subtraction of the I_0 values from I values in Eqn. 1 accounts for any intensity arising from scattered light, stray light and endogenous fluorescence of the solution. The fluorescence intensities F^a and F^b arise only from the fluorescence of the CC species in solution. The concentration of $Al(H_2O)_6^{3+}$ is then calculated using r, the solution pH and ionic strength and either Eqn. 3 or Eqn. 4 (described in the theory section below).

The procedure employed to determine aluminum involved pipetting 10 ml of the sample solution thermostated at 25°C into a 50-ml Teflon bottle, obtaining I_0^a and I_0^b, adding approximately 18 μl of a 0.50 mM HCC^- solution, and obtaining I^a and I^b after mixing thoroughly and themostating at 25°C for 2–5 min. Equilibrium was assumed to be achieved if the fluorescence intensity of the solutions was stable for 1–2 min. Fluorescence intensities were checked periodically rather than irradiating the solution continuously over this time period in order to minimize photodegradation of CC. The absorbance of the CC-containing solution was determined at 330, 355, 400, and 450 nm for highly-absorbing solutions to allow correction for inner-filtering effects.

To calibrate the instrument from day to day, the F^a and F^b values of a solution of HCC^- in pure water at pH 10–11 are measured. Under these conditions, $F^a = a_1$ and $F^b = b_1$ [20]. The intensity of the fluorometer lamp at the excita-

tion wavelengths was found to vary from day to day, so this initial calibration was important for accurate results.

Inner-filtering correction

Inner-filtering is a common interference for quantitative fluorescence methods. Inner-filtering occurs when excitation or fluorescence light is absorbed or scattered by solution components.

A first order inner-filtering correction is used to correct the observed fluorescence intensities in this paper, i.e., $F_0 = F\ 10^{(A_{ex}+A_{em})/2}$, where F and F_0 are the observed and corrected fluorescence intensities, and A_{ex} and A_{em} are the solution absorbances (1 cm path length) at the excitation and emission wavelengths, respectively. More accurate methods to correct for inner-filtering when the solution absorption is high are available in the literature [26].

An inner-filtering error occurs in the ratio fluorescence method when there is a significant difference in the inner-filtering between the first and second set of fluorescence settings

$$\Delta A = A(F^a) - A(F^b)$$
$$= (A_{330} + A_{450}) - (A_{355} + A_{400}) \quad (2)$$

where A_x is the solution absorbance measured at a wavelength of x nm.

Metal binding studies

All metals were analytical grade from Fisher. Al(III) and Fe(III) were used as nitrates and Mn(II), Fe(II) and Cu(II) as chlorides. Metal solutions were prepared using water purged with nitrogen gas to remove dissolved carbon dioxide. The resistance of the distilled, deionized, and 0.2-μm filtered water used in these experiments were greater than 1 MΩ.

The monomeric aluminum hydrolysis constants and stability constants of the aluminum–CC interaction have been described previously [20]. The Guntelberg equation [27] was used to determine activity coefficients for ions and for converting to infinite dilution stability constants (K values) and ionic strength dependent stability constants (Q values). The log K values employed for the formation of $AlSO_4^+$ and $Al(SO_4)_2^-$ were 3.20 and 5.10 [28].

Gibbsite solutions

Gibbsite is a crystalline phase of $Al(OH)_3$. Synthetic gibbsite solutions were prepared in polyethylene bottles from $Al(NO_3)_3$ and NaOH. Sodium sulfate was added to these solutions for ionic strength adjustment because acidified natural water solutions frequently contain high sulfate concentrations. These aluminum solutions were allowed to sit for 1 year at room temperature and then thermostated at 25°C for >1 week before the aluminum determination was carried out. X-ray diffraction patterns of filtered samples showed the presence of gibbsite in these samples. Teflon bottles were found to give more reproducible results than polyethylene bottles for analyzing gibbsite samples, as others have found [6,29]. Aluminum concentrations in these solutions were also determined by the 8-hydroxyquinoline method described by Driscoll [9].

THEORY

We previously showed that the fluorescence intensities F^a and F^b were both dependent on aluminum concentration in aqueous solutions [20]. Thus, the concentration of free aluminum in solution, $[Al(H_2O)_6^{3+}]$, can be determined from either F^a and F^b if the solutions pH and ionic strength are known. The ratio F^b/F^a ($=r$) also defines a unique aluminum concentration, and the next two sections describe the relationship between r and $[Al(H_2O)_6^{3+}]$.

Free hydrated aluminum, $Al(H_2O)_6^{3+}$, will be abbreviated as Al^{3+} throughout this paper. CC and CCAl refer to all forms of CC and aluminum-bound CC in solution, respectively.

General relationship between r and Al

The relationship between r (from Eqn. 1) and the measured value of $[Al^{3+}]$, $C_{Al^{3+}}$, can be derived from the aluminum–CC speciation model previously described [20]. The CC species occurring in these solutions are HCC^-, $AlCC^+$,

$CCAl_2(OH)_3^+$, and $CCAl_3(OH)_4^{3+}$, CCAl(OH), and $CCAl(OH)_2^-$; thus, r can be written as:

$$r = \frac{F^b}{F^a} = \{b_1 + Q^*_{CA}C_{Al^{3+}}/[H^+] \cdot (b_2 + b_3Q^*_{C23}C_{Al^{3+}}/[H^+]^3 + b_4Q^*_{C34}(C_{Al^{3+}})^2/[H^+]^4 + b_5Q^*_{C11}/[H^+] + b_6Q^*_{C12}/[H^+]^2)\} / \{a_1 + Q^*_{CA}C_{Al^{3+}}/[H^+] \cdot (a_2 + a_3Q^*_{C23}C_{Al^{3+}}/[H^+]^3 + a_4Q^*_{C34}(C_{Al^{3+}})^2/[H^+]^4 + a_5Q^*_{C11}/[H^+] + a_6Q^*_{C12}/[H^+]^2)\} \quad (3)$$

This equation is cubic in $C_{Al^{3+}}$ and can be solved. Alternatively, a table or graph of r vs. $C_{Al^{3+}}$ can be generated from Eqn. 3 with a knowledge of the solution pH and ionic strength, and $C_{Al^{3+}}$ can be determined directly from r.

Curves of r vs. $pC_{Al^{3+}}$ using Eqn. 3 are shown by the solid lines in Fig. 1 at pH 4.5, 5.0 and 5.5. The $pC_{Al^{3+}}$ values of solutions in equilibrium with natural and synthetic gibbsite are represented on each curve by × and △ marks, respectively. Saturated and undersaturated solutions exhibit a unique relationship between r and $C_{Al^{3+}}$.

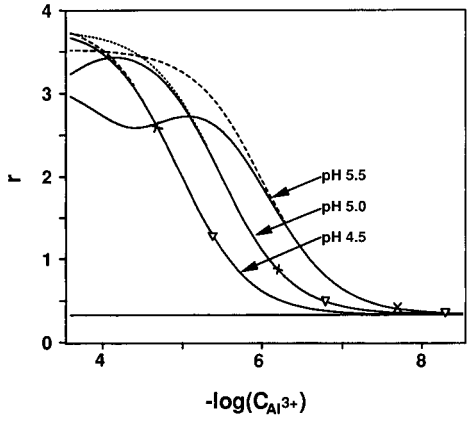

Fig. 1. Relationships between r and pAl^{3+} at pH 4.0, 4.5 and 5.0 at 1 mM ionic strength using Eqn. 3 are shown with the solid curves. The dashed curves show the relationship between r and $p[Al^{3+}]$ obtained using Eqn. 4.

However, at high $C_{Al^{3+}}$ (low $pC_{Al^{3+}}$), r comes to a maximum and starts to decline as a result of the formation of $CCAl_2(OH)_3^+$ and $CCAl_3(OH)_4^{3+}$ species having low b values. Thus, additional information must be acquired to assign a unique aluminum concentration to solutions highly oversaturated with respect to gibbsite using this method.

Relationship between r and Al for saturated and undersaturated solutions

The concentrations of $CCAl_2(OH)_3^+$, $CCAl_3(OH)_4^{3+}$ and $CCAl(OH)_2^-$ were previously shown to be very small for solutions that are undersaturated or in equilibrium with gibbsite below pH 7 [20]. Thus, assuming that HCC^-, $CCAl^+$ and CCAlOH are the only fluorescent CC species in these solutions, Eqn. 3 simplifies to:

$$C_{Al^{3+}} = \frac{[H^+] \cdot (b_1 - ra_1)}{Q^*_{CA} \cdot [(ra_2 - b_2) + Q^*_{C11}/[H^+](ra_5 - b_5)]} \quad (4)$$

The dashed lines in Fig. 1 show the predicted value of r vs. $pC_{Al^{3+}}$ using this equation. The dashed line curves diverge from the solid line curves only at high aluminum concentrations where the solutions are supersaturated.

Once $C_{Al^{3+}}$ is determined, the equilibrium speciation of aluminum and CC can be easily calculated in saturated and undersaturated solutions. Monomeric hydrolyzed aluminum, MHA, the fraction of CC bound to aluminum, $f_{CC}(Al)$, and the fraction of monomeric hydrolyzed aluminum bound by CC, $f_{MHA}(CC)$, are determined from

$$MHA = C_{Al^{3+}} \cdot (1 + Q_{11}/[H^+] + Q_{12}/[H^+]^2 + Q_{13}/[H^+]^3 + Q_{14}/[H^+]^4) \quad (5)$$

$$f_{CC}(Al) = \left[\frac{[H^+] + [H^+]^2/Q^*_{CH}}{Q^*_{CA} \cdot C_{Al^{3+}} \cdot (1 + Q^*_{C11}/[H^+])} + 1\right]^{-1} \quad (6)$$

$$f_{MHA}(CC) = \frac{[CC] \cdot f_{CC}(Al)}{MHA + [CC] \cdot f_{CC}(Al)} \quad (7)$$

where [CC] is the total concentration of CC added to the solution.

Table 1 shows the calculated perturbation of the aluminum equilibria in gibbsite solutions as a result of adding CC to the solution. The solution pH and the fraction of CC bound to aluminum in a synthetic gibbsite solution are given in columns 1 and 2. The fraction of the monomeric aluminum bound in a synthetic gibbsite solution by 0.90 μM CC and 0.40 μM CC calculated from Eqn. 7 are shown in the next two columns. The fraction of aluminum bound by CC never exceeds 20% for the higher CC concentration and 10% for the lower CC concentration. The last two columns give the fractions of aluminum bound for solutions in equilibrium with natural gibbsite solutions. The fraction of aluminum bound to CC in natural gibbsite solution is less than the quantity bound in synthetic gibbsite solution due to the higher solubility of aluminum in natural gibbsite solutions.

Figure 2 shows the range of Al^{3+} concentrations that can be determined fluorometrically as a function of pH (shaded region) as predicted by Eqn. 6. The upper line of the shaded region corresponds to CC being 5% bound to aluminum, and the lower line corresponds to CC being 95% bound. The solubility lines of natural and synthetic gibbsite are also shown for reference. The boxes in Fig. 2 represent the solution conditions of freshly prepared aluminum solutions employed to test the ratio fluorescence method, as described below.

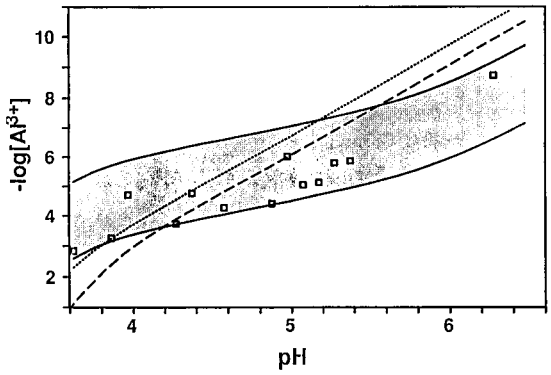

Fig. 2. Range of Al^{3+} concentrations which can be measured using CC (shaded region). The solubility of natural (— — —) and synthetic (· · · · · ·) gibbsites are also shown. The boxes shown correspond to solution conditions employed for the data shown in Fig. 3. The solution ionic strength was 1 mM.

RESULTS

Undersaturated aluminum solutions

Figure 3 shows the relationship between the total concentration of aluminum added to freshly

TABLE 1

Effect of CC on aluminum equilibria in gibbsite solutions

pH	Fraction of CC bound [1], $f_{CC}(Al)$	Fraction of soluble monomeric hydrolyzed aluminum bound to CC, f_{MHA} (CC)			
		Synthetic gibbsite solutions		Natural gibbsite solutions	
		9×10^{-7} M CC	4×10^{-7} M CC	9×10^{-7} M CC	4×10^{-7} M CC
3.8	0.951	0.001	0.000	0.000	0.000
4.0	0.910	0.004	0.002	0.001	0.000
4.2	0.810	0.015	0.006	0.004	0.002
4.4	0.639	0.041	0.017	0.013	0.007
4.6	0.420	0.087	0.039	0.037	0.017
4.8	0.226	0.139	0.067	0.083	0.039
5.0	0.105	0.180	0.088	0.137	0.066
5.2	0.045	0.191	0.095	0.167	0.082
5.4	0.019	0.174	0.085	0.161	0.080
5.6	0.007	0.134	0.068	0.130	0.063

[1] For Al^{3+} concentrations in equilibrium with synthetic gibbsite, from Eqn. 5.

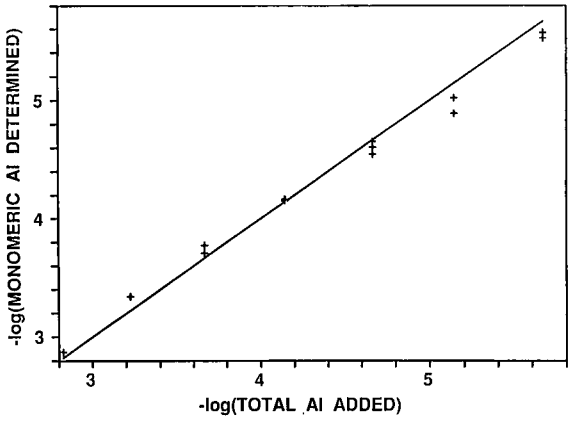

Fig. 3. Standard curve for the determination of monomeric aluminum by RF spectroscopy.

prepared solutions and the monomeric aluminum determined by ratio fluorescence. The measured r value is used to determine $C_{Al^{3+}}$ and monomeric aluminum concentrations from Eqn. 4 and 5. The correlation coefficient is 0.983 in Fig. 3 and the standard error is 0.10 pAl units. Aluminum solutions with Al concentrations near that of gibbsite equilibrium reacted immediately with CC, while solutions that were highly undersaturated or supersaturated required up to 15 min before the solution fluorescence intensity stabilized at a constant value.

Gibbsite solutions

Table 2 compares the aluminum concentrations determined by RF spectroscopy and a standard 8-hydroxyquinoline method of aluminum determination in aged aluminum hydroxide solutions. The solution number, pH, the total concentrations of aluminum and sulfate initially added to solution and the measured value of r are given in the first five columns. The concentration of monomeric aluminum of these solutions is given in the last three columns, as determined by either RF spectroscopy or the 8-hydroxyquinoline method, or as predicted to be in equilibrium with synthetic gibbsite. Monomeric aluminum is calculated from the observed $C_{Al^{3+}}$ value in the RF method, whereas it is measured directly by the 8-hydroxyquinoline method. Monomeric-aluminum is defined as $[Al^{3+}]+[AlOH^{2+}]+Al(OH)_2^+]+[Al(OH)_3]+[Al(OH)_4^-]+[AlSO_4^+]+Al(SO_4)_2^-]+[CCAl^+]+[CCAlOH]+[CCAl(OH)_2^-]$ in Table 2.

Effects of acetate

Acetate buffers had no measurable effect on the value of F^a, F^b or r up to concentrations of 2 mM at pH 4 (1.0 mM aluminum) and 1 mM at pH 5 (0.1 mM aluminum) when various amounts of acetate were added to solutions of constant aluminum concentration.

Effects of fulvic acid

The effect of solution absorption on the value of F^a is approximately the same as the absorption attenuating the value of F^b, thus the effect of inner-filtering on the ratio F^a/F^b largely can-

TABLE 2

Comparison of RF method with a standard method of aluminum speciation using synthetic gibbsite solutions

Solution	pH	Total aluminum added (mM)	Total sulfate added (mM)	r	Monomeric aluminum concentration (mM) [1]		
					RF	8-HQ	Syn. gibb. equilib.
1	3.96	6.000	0.192	3.60	1.360	1.546	0.522
2	4.27	0.600	4.50	3.12	0.420	0.401	0.133
3	4.10	1.500	0.447	3.46	0.442	0.530	0.159
4	4.35	0.150	2.181	2.53	0.0936	0.0868	0.0522
5	4.34	0.300	0.165	3.30	0.1239	0.1483	0.0233
6	4.75	0.0300	0.464	2.32	0.0180	0.0181	0.00203
7	4.94	0.0060	0.473	1.61	0.0064	0.00042	0.00068

[1] Monomeric aluminum determined by ratio fluorescence (RF), 8-hydroxyquinoline (8-HQ), or expected for solutions in equilibrium with synthetic gibbsite.

cels out. Table 3 shows that the solution absorbance contributing to F^a inner-filtering, $A(F^a)$, is much greater than the absorbance contributing to ratio fluorescence inner-filtering, ΔA (Eqn. 2). A 5% inner-filtering error occurs at less than 1 ppm FA for the F^a measurement, and 12 ppm FA for the ratio fluorescence measurement. The last two columns of Table 3 show how the value of r and the value of r corrected for inner-filtering change with fulvic acid concentration.

Effects of paramagnetic metals

No fluorescent complexes were observed when CC was mixed with the paramagnetic metals Fe^{+3}, Fe^{+2}, Mn^{+2} and Cu^{+2} in aqueous solution. The only fluorescence changes observed upon increasing the pH of 0.10 mM solutions of these metals in solution with CC was quenching of F^a and F^b; no changes in the ratio of F^b/F^a or in the fluorescence spectra from that of pure HCC^- were observed when 95% of the solution fluorescence had disappeared.

Table 4 shows the effect of Fe^{3+} on the ability of the RF method to determine the Al^{3+} concentration of a 40 μM Al solution at pH 4. The absorption spectrum of iron in the 300–500 nm spectral region is similar to that of fulvic acid solutions; thus, the values of $A(F^a)$ and ΔA in Table 4 are similar to those of Table 3. The values of F^a and F^b are lower than can be accounted for by inner-filtering effects alone, thus, significant concentrations of nonfluorescent Fe–CC complexes must have formed in solution.

TABLE 3

Effect of fulvic acid on CC fluorescence

[FA] (ppm)	$A(F^a)$ [1]	ΔA [1]	r	r_{corr} [2]
0.00	0.024	0.016	0.375	0.375
1.50	0.035	0.018	0.385	0.375
3.00	0.046	0.020	0.390	0.380
6.00	0.067	0.023	0.390	0.380
12.0	0.110	0.030	0.395	0.375
25.0	0.200	0.044	0.410	0.385
50.0	0.369	0.072	0.435	0.400
100.0	0.714	0.128	0.520	0.450

[1] Defined in Eqn. 7. [2] Value after correcting for solution inner-filtering.

TABLE 4

Effect of iron on aluminum analysis by RF

$[Fe^{3+}]$, $\times 0.1$ mM	$A(F^a)$ [1]	ΔA [1]	$[Al^{3+}]$, $\times 10$ μM	$[Al^{3+}]_{corr}$ [2], $\times 10$ μM
0.00	0.027	0.012	4.03	3.92
0.09	0.045	0.012	4.08	3.97
0.18	0.065	0.013	4.03	3.91
0.36	0.103	0.013	4.08	3.96
0.75	0.191	0.019	4.25	3.96
1.50	0.374	0.035	4.55	4.06
2.92	0.758	0.080	7.46	5.75

[1] Defined in Eqn. 7. [2] Value after correcting for solution inner-filtering.

The fourth column of Table 4 indicates that aluminum can be determined accurately by the RF method at concentrations of up to 36 μM Fe^{3+} without any corrections. The last column shows that aluminum can be determined in the presence of 150 μM Fe^{3+} if inner-filtering is corrected for. Iron is rarely present at concentrations greater than 10 μM in natural water solutions.

DISCUSSION

Undersaturated aluminum solutions

The ratio fluorescence method allows aluminum determination in aqueous solutions of pH 6 or less with little perturbation to the solution being analyzed. Free hexahydroaluminum, $C_{Al^{3+}}$, can be directly determined using Eqn. 4 as long as the solution is near saturation or undersaturated with respect to gibbsite. Concentrated aluminum solutions exhibiting a high r value (where the dashed line deviates from the solid line in the appropriate pH curve of Fig. 1) must employ Eqn. 3 for accurate aluminum determination, or the solution must be diluted prior to aluminum determination.

The concentration of indicator is kept small (< 1 μM) so that the fraction of aluminum bound to CC is always less than 20% (Table 1). The solution perturbation can be reduced to less than 10% if the CC concentration is reduced to 0.4 μM in solution (Table 1). In contrast to the 10–20% perturbation of aluminum concentration in this method of analysis, all widely used com-

pleximetric methods of aluminum determination involve binding all kinetically labile aluminum species occurring in solution prior to aluminum determination. These complexiметric methods are believed to determine monomeric aluminum rather than free hexahydroaluminum. Other labile metal concentrations in natural water solutions, such as iron and manganese, are also strongly perturbed in the widely-used complexiметric methods.

The range of aluminum concentrations that can be determined by CC depends upon the pH of the solution, as shown in Fig. 2. This range, which includes much of the gibbsite equilibrium region of acidic aluminum solutions, is the aluminum concentration range of greatest interest in natural water solution analysis [4]. Determination of higher or lower aluminum concentrations would require developing RF probes with different binding affinities for aluminum. Figure 3 shows that the amount of monomeric aluminum calculated from r using Eqn. 3 agrees with the total amount of aluminum added to the solution over 3 orders of magnitude concentration of pH 3.5–6.5. There is relatively little formation of solid $Al(OH)_3$ in these undersaturated or saturated solutions so Eqn. 4 was used to determine $C_{Al^{3+}}$ rather than the more complex Eqn. 3.

Gibbsite solutions

Both the RF method and the 8-hydroxyquinoline method of determining monomeric aluminum agree with each other to within 8% for gibbsite solutions 2, 4 and 6 (Table 2). These solutions were only moderately oversaturated with respect to gibbsite when initially prepared. Gibbsite solutions 1, 3 and 5 appear to have 10–20% higher aluminum concentrations when determined by 8-hydroxyquinoline than by ratio fluorescence. These solutions were initially prepared under highly supersaturated conditions. An ^{27}Al NMR study has shown that complexometric methods can determine some $Al_x(OH)_y$ polymers in addition to monomeric aluminum [7]. The reason for the discrepancy between the two measurement methods for solution 7 has not been determined.

Both the ratio fluorescence and the 8-hydroxyquinoline methods indicate that all aged aluminum hydroxide solutions were supersaturated with respect to synthetic gibbsite. Supersaturated solutions often come to equilibrium with gibbsite slowly, especially at low pH [6,30].

Fulvic acid effects

Fulvic acid fluoresces and contributes to inner-filtering in the analyte solution. The fluorescence contribution of fulvic acid is assumed to be independent of the fluorescence of CC and is subtracted off before r is calculated (Eqn. 1). Table 3 shows that the ratio fluorescence method is much less sensitive to fulvic acid inner-filtering errors than single fluorescence measurements are for determining aluminum concentrations.

The value of r_{corr} (i.e., r corrected for inner-filtering) from Table 3 remains constant up to a fulvic acid concentration of 25 ppm, which indicates that there is no interaction between CC and fulvic acid up to a fulvic acid concentration of at least 25 ppm. Solutions containing aluminum as well as fulvic acid and CC were not investigated in this study because the binding constants of aluminum with fulvic acid have not been well characterized in the literature. Further studies are planned to evaluate these solutions.

Iron interference

Aluminum determination methods which rely on optical absorption or fluorescence measurements usually exhibit interference from the presence of iron in solution [10,12–18]. This interference can be mitigated by performing extra steps to mask the effects of iron. Iron and other paramagnetic metals quench the fluorescence of organic compounds upon binding. However, the ratio fluorescence method should not be affected by formation of nonfluorescent complexes of the fluorescence probe because these complexes will not contribute to the value of F^b/F^a. Table 2 shows that iron complexation with CC and its contribution to inner-filtering does not compromise the RF method's ability to determine aluminum when iron is present at high concentrations.

Dynamic (collisional) quenching by paramagnetic ions or other fluorescence quenchers in

solution is a potential source of error in this method. We calculate that the dynamic quenching of fluorescence intensities is less than 2% as long as the total concentration of quenchers is less than 1 mM. The Stern–Volmer equation [31] was used for these calculations along with the following parameters: radius of CCAl species = 5 Å, radius of quencher = 2 Å, temperature = 25°C, diffusion coefficients estimated from the Stokes–Einstein equation, fluorescence lifetime of the CC species = 1 ns, and collisional quenching efficiency = 1. A smaller quenching error would occur if the quenching efficiency was less than unity or the concentration of quenchers in solution were lower. When r is used to determine $C_{Al^{3+}}$, this error will be smaller because all fluorescent CC species are quenched simultaneously.

Other interferences

The formation of fluorescent CC complexes other than the $CCAl_x(OH)_y$ species described in this paper could cause an interference to this method of aluminum analysis. The magnesium complex of HCC^- has a fluorescence spectrum very similar to that of $AlCC^+$ [20]. However, this complex forms only at high Mg^{2+} concentrations at high pH, thus, Mg^{2+} does not bind strongly enough to CC^{2-} to interfere with aluminum analysis in environmental solutions below pH 7. The diamagnetic cations Zn^{2+}, Ca^{2+}, Na^+ and K^+ showed no evidence of forming a fluorescent complex with CC [20].

The cations NO_3^- and Cl^- in the concentration range 0.5–10 mM and 1–9 mM, respectively, exhibited no evidence of altering CCAl speciation or CCAl fluorescence [20]. The results of Table 2 suggest that sulfate competes directly with CC^{2-} as a ligand rather than forming a CCAl complex, as also found in morin–Al studies [18]. Acetate and fulvic acid did not interfere with HCC^- fluorescence as long as concentrations were below 1 mM and 25 ppm, respectively. Additional competition studies would be necessary to evaluate other possible interferences.

Comparison with other fluorescence methods of aluminum determination

The currently available fluorescence probes for aluminum analysis are fluorescent in only the metal-bound state [12–18,32,33]. Analysis methods employing these probes involve solution preparation steps and exhibit matrix interferences from iron, various metal ions, and humic materials. These methods also involve complexing all free aluminum in solution, with the exception of the optrode aluminum sensors [12,32,33] and one recent study that employs low concentrations of morin as a fluorescent probe [17,18]. One optrode method uses the ratio of an Al-sensitive fluorescent with that of an Al-insensitive fluorescence to help compensate for inner-filtering, probe degradation, and other matrix effects [12]. However, this correction only works if both fluorescence signals respond the same way to the interference, whereas wavelength-shifting RF probes always respond in the same way because the same probe is involved in both measurements [22].

CC exhibits several desirable properties as a wavelength-shifting RF probe, including (1) a large change in the position of its fluorescence peaks upon aluminum binding, (2) a similar fluorescence quantum yield in both the free and Al-bound states, and (3) little change in its 0–0 energy upon metal binding. The first two properties allow both CC fluorescence measurements to be obtained sensitively, with equal precision, and with both measurements providing independent information. The small change in 0–0 energy allows the optimum wavelengths for the F^a measurements (330 and 450 nm) to flank the wavelengths of the F^b measurements (355 and 400 nm). This makes the ratio F^b/F^a less susceptible to inner-filtering errors than the non-flanking situation for solutions having an absorption spectrum that varies continuously with wavelength. Most wavelength-shifting RF probes currently available for pH or metal determination [21–24] lack these desirable characteristics.

Procedure for aluminum determination in natural water solutions

The following procedure is recommended for determining aluminum in unknown natural water solutions by the ratio fluorescence method: (1) measure a_1 and b_1 values for the instrument being used and calculate the other a and b val-

ues as described in the methods section; (2) determine the solution's pH and ionic strength; (3) determine the solution's F^a and F^b values and calculate r; (4) Measure the absorbance of the solution containing CC at 330, 355, 400, and 450 nm and determine if the absorbance is large enough to require an inner-filtering correction; and (5) calculate $C_{Al^{3+}}$ using Eqn. 4. If this result indicates that the solution is highly supersaturated, $C_{Al^{3+}}$ should be determined from the more accurate Eqn. 3. Also, if the aluminum concentration is high, it is necessary to recalculate the ionic strength and $C_{Al^{3+}}$ until the ionic strength and aluminum concentrations do not change any more. A Lotus123® program was written to calculate $C_{Al^{3+}}$, monomeric aluminum, and $f_{MA}(CC)$ directly from the solution pH, $[SO_4^{2-}]$. ionic strength, I^a, I^b, and A_x values. This program was designed to account for inner-filtering for maximum versatility and was used to obtain the RF results for the gibbsite solutions in Table 4.

This work was supported by the U.S. National Science Foundation (Grant BSR 8807826) and by the ALBIOS project, EPRI (Contract RP-2365-01).

REFERENCES

1 C.S. Cronan and C.L. Schofield, Science, 204 (1979) 304.
2 A. Huag, CRC Crit. Rev. Plant Sci., 1 (1984) 345.
3 W.C. Shortle and K.T. Smith, Science, 240 (1988) 1017.
4 C.S. Cronan, W.J. Walker and P.R. Bloom, Nature, 324 (1986) 140.
5 R.W. Smith, in R.F. Gould (Ed.), Relations Among Equilibrium and Nonequilibrium Species of Aluminum Hydroxy Complexes (Advances in Chemistry Series, Vol. 106), American Chemical Society, Washington, DC, 1971, Chap. 10.
6 H.M. May, P.A. Helmke and M.L. Jackson, Chem. Geol., 24 (1979) 259.
7 P.M. Bertsch, W.J. Layton and R.I. Barnhisel, Soil Sci. Soc. Am. J., 50 (1986) 1449.
8 P.G.C. Campbell, M. Bisson, R. Bougie, A. Tessier and J.P. Villeneuve, Anal. Chem., 55 (1983) 2248.
9 C.T. Driscoll, Int. J. Environ. Anal. Chem., 16 (1984) 267.
10 W.K. Dougan and A.L. Wilson, Analyst, 99 (1974) 413.
11 R.B. Barnes, Chem. Geol., 15 (1976) 177.
12 O.S. Wolfbeis, B.P.H. Schaffar and R.A. Chalmers, Talanta, 33 (1986) 867.
13 A.G. Howard, A.J. Coxhead, I.A. Potter and A.P. Watt, Analyst, 11 (1986) 1379.
14 E. Pastor, F. Pablos and J.L. Ariza, Analyst, 112 (1987) 1041.
15 G.L. Campi and J.D. Ingle, Anal. Chim. Acta, 224 (1989) 363.
16 F. Carrillo, C. Perez and C. Camara, Anal. Chim. Acta, 243 (1991) 121.
17 B.A. Browne, J.G. McColl and C.T. Driscoll, J. Environ. Qual., 19 (1990) 65.
18 B.A. Browne, J.G. McColl and C.T. Driscoll, J. Environ. Qual., 19 (1990) 73.
19 P.M. Bertsch, R.I. Barnhisel, G.W. Thomas, W.J. Layton and S.L. Smith, Anal. Chem., 58 (1986) 2583.
20 T.A. Taylor and H.H. Patterson, Anal. Chim. Acta, 278 (1993) 249.
21 I. Kurtz and R.S. Balaban, Biophys. J., 48 (1985) 499.
22 R.P. Hauglane, Handbook of Fluorescent Probes and Research Chemicals, Molecular Probes Inc., Eugene, OR, 5th edn., 1992, pp. 113–152.
23 M. Poenie, J. Alderton, R.Y. Tsien and R.A. Steinhardt, Nature, 315 (1985) 147.
24 D.W. Tank, M. Sugimore, J.A. Conner and R.R. Llimas, Science, 242 (1988) 773.
25 B.J. Plankey and H.H. Patterson, Environ. Sci. Technol., 21 (1987) 595.
26 F. Van Geel, E. Voigtman and J.D. Winefordner, Appl. Spectrosc. 38 (1984) 228.
27 W. Stumm and J.J. Morgan, Aquatic Chemistry, Wiley-Interscience, New York, 1981.
28 D.K. Nordstrom, S.D. Valentine, J.W. Ball, L.N. Plummer and B.F. Jones, U.S.G.S. Water-Resources Investigation Report 84-4186, 1984.
29 H.M. May, P.A. Helmke and M.L. Jackson, Chem. Geol., 24 (1979) 259.
30 C.F. Baes and R.E. Mesmer, The Hydrolysis of Cations, Wiley, New York, 1976.
31 J.R. Lakowicz, Principles of Fluorescence Spectroscopy, Plenum, New York, 1983, Chap. 9.
32 L.A. Saari and W.R. Seitz, Anal. Chem., 55 (1983) 667.
33 Z. Zhujun and W.R. Seitz, Anal. Chim. Acta, 171 (1985) 251.

Analytica Chimica Acta, 278 (1993) 269–274
Elsevier Science Publishers B.V., Amsterdam

Spectroscopic properties of polycyclic aromatic compounds

Part II. Fluorescence emission and quenching behavior of select acenaphthylene derivatives in organic nonelectrolyte solvents

Sheryl A. Tucker, Heather C. Bates, Vicki L. Amszi and William E. Acree, Jr.
Department of Chemistry, University of North Texas, Denton, TX 76203–5068 (USA)

Hongmee Lee, Pasquale Di Raddo and Ronald G. Harvey
Ben May Institute, University of Chicago, Chicago, IL 60637 (USA)

John C. Fetzer
Chevron Research and Technology Center, Richmond, CA 94802–0627 (USA)

Gerald Dyker
Institut für Organische Chemie der TU Braunschweig, Hagenring 30, 3300 Braunschweig (Germany)

(Received 22nd October 1992; revised manuscript received 11th January 1993)

Abstract

Fluorescence emission spectra have been measured for acenaphthylene, aceanthrylene, acephenanthrylene, benz[*e*]aceanthrylene, 3-methylbenz[*j*]aceanthrylene, 6-methylbenz[*j*]aceanthrylene, benzo[*def*]cyclopenta[*hi*]chrysene, cyclopenta[*cd*]pyrene (also called acepyrylene) and acenaphth[1,2*a*]acenaphthylene in organic nonelectrolyte solvents of varying polarity. Benz[*e*]aceanthrylene was found to exhibit probe character for many of the solvents considered; however, emission intensity ratios in benzene, toluene, *p*-xylene and *o*-xylene were too small compared against nonelectrolyte solvents of similar polarity. The effect of nitromethane as selective quenching agent was also examined. Results of these measurements show that nitromethane does quench the fluorescence emission of the nine solutes studied, which is contrary to what would be expected based upon the fact that all nine solutes are nonalternant polycyclic aromatic hydrocarbons.

Keywords: Fluorimetry; Acenaphthylene derivatives; PAHs

Identification and quantification of polycyclic aromatic hydrocarbons (PAHs) in unknown mixtures require accurate fluorescence emission intensity measurements and availability of a large spectral data file for comparing the unknown's spectrum against PAH standards. To prevent misidentification, the data file should include both polar and nonpolar solvents since electronic interactions between a solvent dipole and an excited PAH solute can lead to spectral distortions,

Correspondence to: W.E. Acree, Jr., Department of Chemistry, University of North Texas, P.O. Box 5068, Denton, TX 76203–5068 (USA).

wavelength shifts and/or intensity ratio variations, as was the case with many of the polycyclic aromatic compounds examined previously [1–12]. Solvent-induced fluorescence spectral changes can be rationalized qualitatively in a relatively straightforward manner. Excitation promotes the PAH solute from a ground state of low dipole moment to one of the vibrational levels of the first electronic excited state, S_{1v}, with an accompanying electron distribution in the surrounding solvent molecules. Insufficient time exists; however, for solvational-sphere molecules to physically reorient with the new PAH dipole moment. Relaxation from the vibronically excited S_{1v} level to the excited S_{1o} level occurs whenever solvent molecules rotationally reorient to a more stable dipole configuration during the excited state's lifetime. Emission of the fluorescence photon returns both the PAH molecule to the ground S_{0v} state and solvational molecules to their initial electronic configuration. Subsequent rotation of the solvent molecules to the ground-state dipole orientation restores the system to its original state. Transition probabilities and energy separation between the different energy levels vary with each solute/solvent pair, and give rise to observed intensity ration changes and emission wavelengths shifts [13,14].

Mixtures of environmental/industrial importance rarely contain a single component. The majority of mixtures commonly encountered contain several isomeric pairs or structurally similar polycyclic aromatic compounds (PACs), which emit in approximately the same spectral regions. Kalman filtering and Gaussian or other curve-fitting techniques [15–20], alone or in combination with phase-resolved [21–23] or synchronous scanning [24–26] fluorescence spectroscopy, theoretically allow uncoupling of overlapped spectra. Such methods become less reliable; however, as the number of mixture components increases. Liquid chromatographic (LC) separation prior to fluorimetric analysis affords a viable alternative, but again the method is extremely time-consuming whenever large numbers of isomeric compounds are present. Blümer and Zander [27] recommended that nitromethane and/or nitrobenzene could be added to a water–acetonitrile (20:80, v/v) binary mobile phase to selectively suppress fluorescence signals of alternant PAHs. Emission intensities of nonalternant PAHs would remain unchanged. Solutes are classified as alternant PAHs because every alternant carbon atom in the aromatic ring system can be "starred". Nonalternant PAHs, on the other hand, would have at least one pair of adjacent starred atoms [28,29].

Published studies [12,30–34] involving over 80 PAHs have identified dibenzo[*hi,wx*]heptacene, benzo[*k*]fluoranthene, fluoranthene, and naphtho[2,3*b*]fluoranthene as among the few exceptions to the so-called nitromethane selective quenching rule in the PAH6 benzenoid, fluorenoid, fluoranthenoid and "methylene-bridged" cyclopenta-PAH subclasses. Although a large data file now exists for several subclasses of PACs, we have not reported the fluorescence emission and quenching behavior of the subclass that contains the acenaphthylene-derivatives. As a continuation of our fluorescence studies we have measured the fluorescence behavior of acenaphthylene (AcNa), aceanthrylene (AcAn), acephenanthrylene (AcPh), benz[*e*]aceanthrylene (B[e]AA), 3-methylbenz[*j*]aceanthrylene (3-B[*j*]AA), 6-methylbenz[*j*]aceanthrylene (6-B[*j*]AA), benzo[*def*]cyclopenta[*hi*]chrysene (BCPC), cyclopenta[*cd*]pyrene (CPP) (also called acepyrylene) and acenaphth[1,2*a*]acenaphthylene (ANAN) (see Fig. 1 for molecular structures) dissolved in nonelectrolyte organic solvents of varying solvent polarity. Also included is an examination of the effect of nitromethane and 1,2,4-trimethoxybenzene on the fluorescence emission intensity of these nine solutes that are classified as nonalternant PAHs [35].

MATERIALS AND METHODS

Acenaphthylene was purchased commerically from Aldrich and purified by vacuum sublimation. Cyclopenta[*cd*]pyrene was used as received from CTC Organics. The remaining seven PAH solutes were synthesized and purified by procedures described in the chemical literature [36–39]. Stock solutions were prepared by dissolving solutes in dichloromethane. Small aliquots of the

stock solutions were transferred into test tubes, allowed to evaporate, and diluted with the solvent of interest. Final solute concentration of 10^{-5} M (or less) were sufficiently dilute to minimize inner-filtering artifacts. Solvents were of HPLC, spectroquality or AR grade, purchased commercially from either Aldrich or Fisher Scientific, and the resulting solutions were optically dilute (absorbances < 0.01 cm^{-1}) at all wavelengths, except for the nitromethane and 1,2,4-trimethoxybenzene quenching studies.

Absorption spectra were recorded on a Bausch and Lomb Spectronic 2000 and a Hewlett-Packard 8450A photodiode array spectrophotometer in the usual manner. The fluorescence spectra were run on a Shimadzu RF-5000U spectrofluorometer with the detector set at high sensitivity. Solutions were excited at 288 (AcNa), 360 (AcAn), 300 (AcPh), 360 (B[*e*]AA), 300 (3-B[*j*]AA), 300 (6-B[*j*]AA), 300 (BCPC), 336 (CPP) and 406 nm (ANAN). Fluorescence data were accumulated in a 1-cm^2 quartz cuvette at 19°C (ambient room temperature) with excitation and emission slit width settings of 15 and 3 nm, respectively. The acenaphthylene derivatives fluorescence spectra, depicted in Figs. 2 and 3, represent a single scan which was then solvent blank corrected and verified by repetitive measurements. Fluorescence emission spectra of acenaphthylene, aceanthrylene and acephenanthrylene are in excellent agreement with previously reported spectra [40–42].

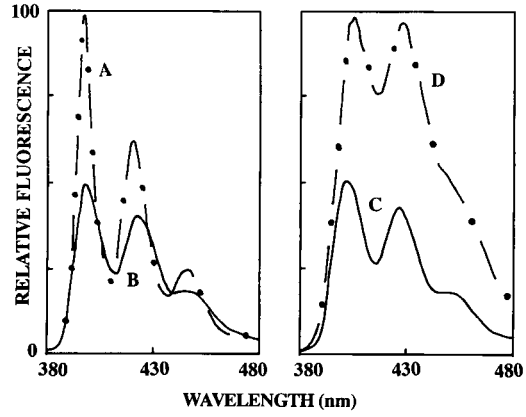

Fig. 2. Fluorescence emission spectra of benz[e]aceanthrylene dissolved in A (·–·–·), *n*-hexadecane; B (———), butyl acetate; C (———), dichloromethane; and D (·–·–·), dimethyl sulfoxide. In butyl acetate emission bands occur at about 398, 423 and 448 nm.

Emission intensities associated with the quenching study were corrected for primary inner-filtering artifacts arising from the absorption of excitation radiation. Several of the PACs have excitation wavelengths in the 300–320 nm spec-

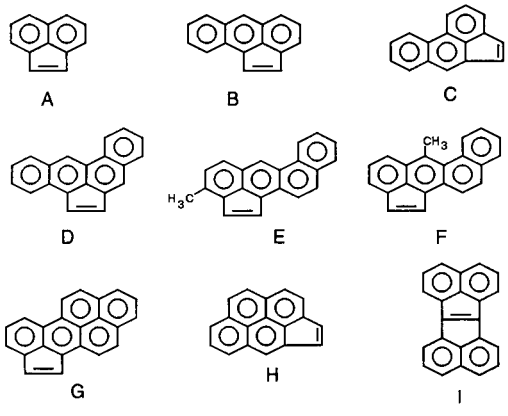

Fig. 1. Molecular structures of the acenaphthylene derivatives: (A) acenaphthylene; (B) aceanthrylene; (C) acephenanthrylene; (D) benz[e]aceanthrylene; (E) 3-methylbenz[*j*]aceanthrylene; (F) 6-methylbenz[*j*]aceanthrylene; (G) benzo[*def*]cyclopenta[*hi*]chrysene; (H) cyclopenta[*cd*]pyrene (also called acepyrylene); and (I) acenaphth[1,2*a*]acenaphthylene.

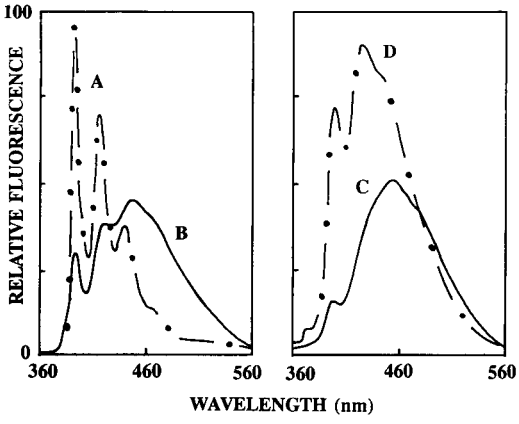

Fig. 3. Fluorescence emission spectra of 3-methylbenz[*j*]-aceanthrylene dissolved in A (·–·–·), *n*-hexadecane; B (———), butyl acetate; C (———), *N*,*N*-dimethyl formamide; and D (·–·–·), dimethyl sulfoxide. In butyl acetate emission bands occur at about 395, 421 and 448 nm.

tral region and a few drops of nitromethane or 1,2,4-trimethoxybenzene gave solutions having appreciable absorbances. Mathematical expressions, computational procedures and interrogation zone dimensions are given elsewhere [12,30,31,43,44]. Every effort was made to work at solution absorbances ≤ 0.95 cm^{-1} ($f_{prim} \leq 3.00$) where the inner-filtering correction equation is valid. Secondary inner-filtering corrections were not necessary in the present study since both nitromethane and 1,2,4-trimethoxybenzene are "optically transparent" in most of these PACs' emission ranges.

RESULTS AND DISCUSSION

Representative fluorescence emission spectra of benz[*e*]aceanthrylene dissolved in *n*-hexadecane, butyl acetate, dichloromethane and dimethyl sulfoxide is depicted in Fig. 2. These four nonelectrolyte solvents were judiciously selected so as to encompass the entire range of solvent polarity, from the nonpolar *n*-hexadecane hydrocarbon to the moderately polar butyl acetate and dichloromethane solvents to the very polar dimethyl sulfoxide, which is the most polar solvent considered in this present study. Examination of the spectral data reveals that benz[*e*]aceanthrylene shows signs of probe character as evidenced by variation of emission intensity ratios with solvent polarity. Calculated emission intensities for benz[*e*]aceanthrylene (B[*e*]AA; I/II) ranged from B[*e*]AA = 1.62 for cyclohexane to B[*e*]AA = 1.00 for dimethyl sulfoxide. Actual numerical values for the 14 solvents examined are tabulated in Table 1. Estimated uncertainties in the measured intensity ratios are believed to be on the order of ± 0.05 (or less) on the basis of replicate measurements. Although benz[*e*]aceanthrylene does show some signs of probe character, the emission intensity ratios do not vary systematically with solvent polarity as the numerical B[*e*]AA values for benzene, toluene, *p*-xylene and *o*-xylene (latter three not given) are far too small. Even if the benzene derivatives values are ignored, the dynamic range of 0.62 is significantly smaller than those of pyrene (1.37), benzo[*ghi*]perylene (0.98) and ovalene (2.08) [2,8]. To be consistent with our past classification scheme, benz[*e*]aceanthrylene is labelled as a solvent polarity nonprobe molecule because of the unexplained, abnormally low B[*e*]AA value measured for the benzene derivatives. 3-Methylbenz[*j*]aceanthrylene (see Fig. 3) initially appeared to exhibit solvent polarity behavior as evidence by a changing emission intensity ratio, but upon closer examination it was noted that there existed no correlation between the observed ratios and solvent polarities. For example, I/III band intensity ratios for dimethyl formamide and dimethyl sulfoxide were I/III = 0.31 and I/III = 0.79, respectively, despite the fact that these two solvents are approximately of equal solvent polarity. It was also found that a common set of emission bands cannot be assigned in all solvents, i.e., in dimethyl formamide two resolved bands were observed, the I and the III band, as opposed to two bands and a shoulder in dimethyl sulfoxide and three bands in *n*-hexadecane.

TABLE 1

Ratios of fluorescence emission intensities of benz[e]aceanthrylene in various organic solvents

Organic solvent	Py [a]	B[*e*]AA [b]
Cyclohexane	0.58	1.62
2,2,4-Trimethylpentane	0.59	1.60
n-Hexadecane	0.60	1.58
Carbon tetrachloride		Rxn [c]
Dibutyl ether	0.84	1.36
Benzene	1.05	1.16
2-Propanol	1.09	1.27
Chloroform	1.25	Rxn [c]
Butyl acetate	1.35	1.21
Methanol	1.35	1.20
Dichloromethane	1.35	1.17
Acetonitrile	1.79	1.11
Dimethyl formamide	1.81	1.06
Dimethyl sulfoxide	1.95	1.00
Dynamic range	1.37	0.62

[a] Experimental Py values are taken from Dong and Winnik [45] and are based upon the properties of pyrene. [b] Defined as the ratio of band I (at 394–406 nm)/band II (at 418–430 nm) for benz[*e*]aceanthrylene. [c] Photochemical reaction, ratios are not reproducible.

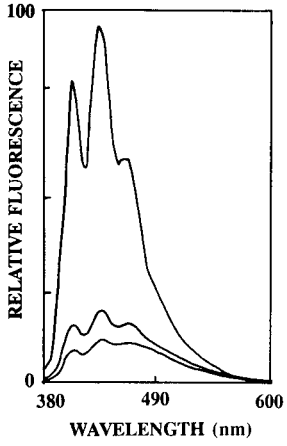

Fig. 4. Uncorrected fluorescence emission spectra of aceanthrylene dissolved in acetonitrile at various nitromethane concentrations. From top to bottom, the curves correspond to 0, 1 and 2 pasteur pipet drops of nitromethane. Emission intensities have not been corrected for inner-filtering artifacts resulting from absorption of the excitation radiation by nitromethane. Corrected fluorescence intensities (not shown) are larger; however, the values are still substantially below the original aceanthrylene spectra.

Fig. 4 shows the effect on nitromethane on aceanthrylene dissolved in acetonitrile. All the PAH solutes examined were quenched by nitromethane which was completely unexpected. Their behavior is indicative of alternant polycyclic aromatic hydrocarbons. This is the first subclass of PAHs in which all solutes examined behave as exceptions to the selective quenching rule. Quenching behavioral differences between alternant and nonalternant PAHs have been rationalized [33,46] in terms of processes originating from the vibrationally relaxed first electronic excited singlet state, ^{1}PAH*. Deactivation from the ^{1}PAH* state is governed by the competition between radiative and non-radiative processes. Rate constants of fluorescence decay, k_{fluores}, for PAH fluorophores are generally insensitive to molecular environment. Efficiencies of non-radiative processes, on the other hand, depend to a large extent upon external perturbations resulting from interactions involving PAH solutes with solvent/quenching molecules.

Breymann et al. [33] attributed nitromethane's selectivity to an electron/charge transfer reaction

$$^1\text{PAH}^* + {}^1\text{Quencher} \rightleftharpoons (\text{PAH}^{+/-}\text{---Quencher}^{-/+}) \rightarrow {}^2\text{PAH}^{+/-} + {}^2\text{Quencher}^{-/+}$$

where the superscript "2" denotes a doublet state. As argued by the authors, reduction potentials of nonalternant PAHs are generally 0.4 eV more positive than those of alternant PAHs. Examination of the experimental quenching data lead us to believe that this particular subclass of PAHs, the acenaphthylene derivatives, have HOMO–LUMO energies similar to the alternant PAHs. Their peculiar behavior might be attributed to the fixed double bond in the cyclopenta ring, which is unlike previously examined nonalternant PAH subclasses, e.g., fluorenoids and fluoranthenoids. The fixed double bond will significantly decrease the number of possible resonance structures. Trimethoxybenzene quenched the fluorescence emission intensity of aceanthrylene and acenaphtho[1,2*a*]acenaphthylene, but not that of cyclopenta[*cd*]pyrene or benz[*e*]aceanthrylene. The other solutes could not be examined as one pasteur pipet drop of trimethoxybenzene gave appreciable absorbances at their excitation wavelengths around 300 nm.

This work is supported in part by grants from the National Science Foundation (Grant No. CTS-8922485), by the University of North Texas Research Council, and by a National Science Foundation Doctoral Research Fellowship awarded to S.A. Tucker. The authors also acknowledge support from the National Institute of Environmental Health Sciences (Grant No. ES-04266).

REFERENCES

1 R. Waris, M.A. Rembert, D.M. Sellers, W.E. Acree, Jr., K.W. Street, Jr., C.F. Poole, P.H. Shetty and J.C. Fetzer, Appl. Spectrosc., 42 (1988) 1525.
2 R. Waris, M.A. Rembert, D.M. Sellers, W.E. Acree, Jr., K.W. Street, Jr. and J.C. Fetzer, Analyst, 114 (1989) 195.
3 R. Waris, W.E. Acree, Jr., K.W. Street, Jr. and J.C. Fetzer, Appl. Spectrosc., 43 (1989) 845.

4 W.E. Acree, Jr., S.A. Tucker, A.I. Zvaigzne, K.W. Street, Jr., J.C. Fetzer and H.-F. Grutzmacher, Appl. Spectrosc., 44 (1990) 477.
5 W.E. Acree, Jr., S.A. Tucker, L.E. Cretella, A.I. Zvaigzne, K.W. Street, Jr., J.C. Fetzer, K. Nakasuji and I. Murata, Appl. Spectrosc., 44 (1990) 951.
6 S.A. Tucker, A.I. Zvaigzne, W.E. Acree, Jr., J.C. Fetzer and M. Zander, Appl. Spectrosc., 45 (1991) 424.
7 S.A. Tucker, I.-L. Teng, W.E. Acree, Jr. and J.C. Fetzer, Appl. Spectrosc., 45 (1991) 186.
8 W.E. Acree, Jr., S.A. Tucker and J.C. Fetzer, Polycyclic Aromatic Compounds, 2 (1991) 75.
9 S.A. Tucker, W.E. Acree, Jr. and M.J. Tanga, Appl. Spectrosc., 45 (1991) 57.
10 S.A. Tucker, W.E. Acree, Jr. and M.J. Tanga, Appl. Spectrosc., 45 (1991) 911.
11 S.A. Tucker, W.E. Acree, Jr., M.J. Tanga, M. Zander, J.C. Fetzer, S. Tokita, K. Hiruta, K. Kitahara and H. Nishi, Appl. Spectrosc., 45 (1991) 1188.
12 S.A. Tucker, W.E. Acree, Jr., B.P. Cho, R.G. Harvey and J.C. Fetzer, Appl. Spectrosc., 45 (1991) 1699.
13 T.L. Cecil and S.C. Rutan, Anal. Chem., 62 (1990) 1998.
14 J.R. Lakowicz, Principles of Fluorescence Spectroscopy, Plenum Press, New York, 1983.
15 R.E. Kalman, J. Basic Eng., 82 (1964) 34.
16 S.C. Rutan, J. Chemom., 1 (1987) 7.
17 S.D. Brown, Anal. Chim. Acta, 181 (1986) 1.
18 S.C. Rutan, D.D. Gerow and G. Hartmann, Intell. Lab. Sys., 3 (1988) 61.
19 H. Gampp, M. Maeder, C.J. Meyer and A.D. Zuberbühler, Talanta, 32 (1985) 1133.
20 M. Maeder, Anal. Chem., 59 (1987) 527.
21 D.W. Millican and L.B. McGown, Appl. Spectrosc., 46 (1992) 28.
22 D.W. Millican and L.B. McGown, Anal. Chem., 61 (1989) 580.
23 D.W. Millican and L.B. McGown, Anal. Chem., 62 (1990) 2242.
24 T. Vo-Dinh, in L. Wehry (Ed.), Modern Fluorescence Spectroscopy, Vol. 4, Plenum Press, New York, 1981, pp. 167–192.
25 T. Vo-Dinh and P.R. Martinex, Anal. Chim. Acta, 125 (1981) 13.
26 T. Vo-Dinh, R.B. Gammage, A.R. Hawthorne and J.H. Thorngate, Environ. Sci. Technol., 12 (1978) 1297.
27 G.-P. Blümer and M. Zander, Fresenius' Z. Anal. Chem., 296 (1979) 409.
28 H.E. Zimmerman, Quantum Mechanics for Organic Chemists, Academic Press, New York, 1975, pp. 145–146.
29 J. March, Advanced Organic Chemistry: Reactions, Mechanisms and Structure, McGraw-Hill, New York, 1968, pp. 46–48.
30 V.L. Amszi, Y. Cordero, B. Smith, S.A. Tucker, W.E. Acree, Jr., C. Yang, E. Abu-Shaqara and R.G. Harvey, Appl. Spectrosc., 46 (1992) 1156.
31 S.A. Tucker, H. Darmodjo, W.E. Acree, Jr., J.C. Fetzer and M. Zander, Appl. Spectrosc., 46 (1992) 1260.
32 H. Dreeskamp, E. Koch and M. Zander, Z. Naturforsch., 30A (1975) 1311.
33 U. Breymann, H. Dreeskamp, E. Koch and M. Zander, Chem. Phys. Lett., 59 (1978) 68.
34 S.H. Chen, C.E. Evans and V.L. McGuffin, Anal. Chim. Acta, 246 (1991) 65.
35 C.K. Ingold, Structure and Mechanism in Organic Chemistry, Cornell University Press, London, 1969, p. 195.
36 H. Lee and R.G. Harvey, J. Org. Chem., 55 (1990) 3787.
37 M. Konieczny and R.G. Harvey, J. Org. Chem., 44 (1979) 2158.
38 P. Di Raddo, J.-T. Hahn and R.G. Harvey, Polycyclic Aromatic Compounds, 2 (1991) 1.
39 G. Dyker, Tetrahedron Lett., 32 (1991) 7241.
40 S. Amin, G. Balanikas, K. Huie, N. Hussain, J.E. Geddie, and S.S. Hecht, J. Org. Chem., 50 (1985) 4642.
41 B.F. Plummer, Z.Y. Ac-Saigh and M. Arfan, Chem. Phys. Lett., 104 (1984) 389.
42 N. de Kruijf and R. Verspoor, Fluorescence Spectra of 25 Polycyclic Aromatic Compounds, TNO CIVO-Institutes, Zeist, 1983.
43 S.A. Tucker, W.E. Acree, Jr., J.C. Fetzer and J. Jacob, Polycyclic Aromatic Compounds, 3 (1992) 1.
44 S.A. Tucker, V.L. Amszi and W.E. Acree, Jr., J. Chem. Educ., 69 (1992) A8.
45 D.C. Dong and M.A. Winnik, Can. J. Chem., 62 (1984) 2560.
46 S.A. Tucker, H. Darmodjo, W.E. Acree, Jr., M. Zander, E.C. Meister, M.J. Tanga and S. Tokita, Appl. Spectrosc., 46 (1992) 1630.

Analytica Chimica Acta, 278 (1993) 275–278
Elsevier Science Publishers B.V., Amsterdam

Chemiluminescence method for the determination of adenine after reaction with phenylglyoxal

Naotaka Kuroda, Kenichiro Nakashima and Shuzo Akiyama

School of Pharmaceutical Sciences, Nagasaki University, Bunkyo-machi, Nagasaki 852 (Japan)

(Received 22nd December 1992)

Abstract

A chemiluminescence (CL) method is described for the determination of adenine. Treatment of adenine with phenylglyoxal in acidic propan-2-ol gave products that produced CL in the presence of hydrogen peroxide, 2-mercaptoethanol and sodium hydroxide. The proposed method is highly sensitive and selective to adenine and adenosine. Adenine can be determined in the range 1.5×10^{-4}–5.0×10^{-7} M. The detection limit for adenine is 1.9×10^{-7} M (19 pmol per assay).

Keywords: Chemiluminescence; Adenine; Adenosine; Nucleic acid bases

In recent years, chemiluminescence (CL) methods have been developed as useful analytical techniques because of their high sensitivity, simplicity and wide dynamic range. Several methods have been reported for CL determinations of biologically and chemically important compounds [1–4]; high sensitivities (femtomole detection limits) could be attained with these methods.

It has been found that phenylglyoxal reacts selectively with adenine and adenosine in acidic propan-2-ol solution to give highly chemiluminescent compounds. Adenine-containing compounds play important roles in biological systems as nucleic acid components, coenzymes, sources of energy, metabolic regulators, etc. Therefore, a highly sensitive and selective method for detecting adenine compounds is required in biochemical and clinical studies.

The reaction of adenine derivatives with glyoxal has already been studied [5,6]. However, CL of the adduct with glyoxal has not been discussed. On the other hand, heterocyclic compounds such as 2-aminopyrazine and 2-aminopyridine are known to react with glyoxal compounds to yield bicyclic CL products [7–9]. The structure of the product with 2-aminopyrazine is closely related to a bioluminescent compound, *Cypridina* luciferin [10].

In this paper, suitable conditions for CL derivatization and CL measurement are described for determining adenine with phenylglyoxal. CL derived from other nucleic acid bases, nucleosides and biologically important 2-amino-substituted heterocyclic compounds were also examined.

EXPERIMENTAL

Reagents and apparatus

All chemicals and solvents were of analytical-reagent grade, unless stated otherwise. Deionized, distilled water was used throughout. Organic solvents were used as received. Phenylgly-

Correspondence to: N. Kuroda, School of Pharmaceutical Sciences, Nagasaki University, Bunkyo-machi, Nagasaki 852 (Japan).

oxal hydrate and other glyoxal compounds were purchased from Sigma (St. Louis, MO). Nucleic acid bases and their nucleosides, thiamine hydrochloride and folic acid were obtained from Wako (Osaka).

A TD-4000 lumiphotometer (Laboscience, Tokyo) was used for measurement of CL with a small glass test-tube (50 × 5 mm i.d.).

Assay procedure

A mixture of test solution (100 μl) in propan-2-ol and 50 μl each of 0.4 M phenylglyoxal solution and 1. 2 M hydrochloric acid in propan-2-ol were placed in a screw-capped reaction vial (amber-coloured glass, 3.5 ml; Pierce, Rockford, IL) and heated at 100°C for 2 h.

After cooling to room temperature, a 20-μl aliquot of the reaction mixture was placed in the glass tube for CL measurement and to it were added 400 μl of *N,N*-dimethylformamide (DMF) solution containing 50 mM hydrogen peroxide and 5 mM 2-mercaptoethanol. After vortex mixing, 100 μl of 0.15 M sodium hydroxide solution were added and the CL produced was measured immediately for 60 s. The total CL intensity was defined as the area under the CL decay curve.

For the reagent blank, the same procedure was used except that the test solution was replaced with propan-2-ol.

RESULTS AND DISCUSSION

Conditions for CL derivatization

The solvent effect on the reaction yields of CL products was examined by comparison of the CL intensities (Table 1). Propan-2-ol gave the most intense CL with a relatively lower CL of the reagent blank. The ratio of the CL intensity of adenine to that of the reagent blank (S/B ratio) obtained in propan-2-ol was also the largest among the solvents tested. Acetonitrile and DMF caused larger background signals. Therefore, propan-2-ol was selected for use in the procedure. As shown in Table 1, CL hardly occurred in water. The content of water in the reaction mixture also affected the CL reaction. Almost maximum and constant CL was observed in the presence of less than 1.5% water, but it decreased at higher water contents. For the preparation of test solutions, adenine was dissolved in propan-2-ol at concentrations up to 1×10^{-3} M, and water was not used in this experiment.

TABLE 1

Solvent effects on yields of chemiluminescent products

Solvent	RCI [a]		S/B ratio
	Sample [b,c]	Blank [c]	
Water	0.1	0.1	1
Methanol	0.1	0.1	1
Ethanol	9.8	0.1	98
Propan-2-ol	100	0.1	1000
Acetonitrile	9.2	3.1	3
DMF	0.8	0.6	1
Dimethyl sulphoxide	0.3	0.1	3

[a] RCI = relative CL intensity. [b] Adenine (1×10^{-3} M) in propan-2-ol solution was diluted tenfold with each solvent and then treated as in the recommended procedure. [c] The intensity of adenine in propan-2-ol was arbitrarily taken as 100.

Hydrochloric acid gave the maximum and constant CL intensity at 0.3–0.6 M in the reaction mixture; 0.3 M was chosen for further experiments.

In a preliminary experiment, phenylglyoxal, methylglyoxal and glyoxal were investigated as reagents. Among these, phenylglyoxal gave the most intense CL and was selected for the procedure. The CL intensity for adenine increased linearly with increasing phenylglyoxal concentration from 0 to 0.2 M in the reaction mixture. However, the background CL also increased with increasing phenylglyoxal concentration, and the S/B ratio was almost constant at phenylglyoxal concentrations higher than 0.075 M; 0.1 M was selected in this CL system.

The CL intensity from adenine reached a maximum after heating for 2 h at 100°C and then decreased slightly with time (Fig. 1). At lower temperatures (70 and 85°C), maximum and constant CL intensities could not be attained even after 3.5 h, although the maximum CL intensity attained at 85°C was higher than at 100°C. Heating at 100°C for 2 h, which gave reproducible results, was employed. The CL product formed was stable for at least 5 h in the reaction vial at room temperature.

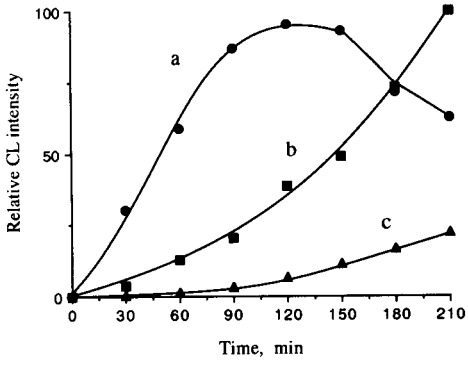

Fig. 1. Effects of reaction temperature and time on yields of chemiluminescent products. A portion (100 μl) of adenine solution (2×10^{-5} M) was treated according to the recommended procedure but for various reaction times at different reaction temperatures. Temperature: (a) 100; (b) 85; (c) 70°C.

Conditions for CL measurement

Solvent effects on the CL intensities were examined (Table 2). The solvents tested were acetonitrile, propan-2-ol, DMF, dimethyl sulphoxide, diglyme and dioxane, all of which contained hydrogen peroxide and 2-mercaptoethanol. DMF and diglyme gave relatively higher CL intensities. DMF gave the largest S/B ratio, and was therefore selected for use in this study.

Hydrogen peroxide concentrations in DMF solution in the range of 0.03–0.3 M gave the most intense CL; 0.05 M was chosen for the proposed method.

TABLE 2

Solvent effects on CL intensities

Solvent	RCI [a]		S/B ratio
	Sample [b,c]	Blank [c]	
Acetonitrile	19.0	0.6	32
Propan-2-ol	17.8	0.04	440
DMF	100	0.1	1000
Dimethyl sulphoxide	14.0	0.05	280
Diglyme	113	0.5	226
Dioxane	39.5	0.1	395

[a] RCI = relative CL intensity. [b] A portion (100 μl) of adenine solution (1×10^{-4} M) was treated according to the recommended procedure but with various solvents for CL measurement. [c] The intensity of adenine in DMF was arbitrarily taken as 100.

The presence of 2-mercaptoethanol in DMF solution affected the rate of decay of the CL emission (Fig. 2A). As the concentration of 2-mercaptoethanol increased, the time required to reach the maximum CL intensity was prolonged. The CL intensity obtained with adenine was most intense in the presence of 5–10 mM 2-mercapoethanol in DMF solution (Fig. 2B); 5 mM was adopted to obtain reproducible results.

The most intense CL occurred with addition of aqueous sodium hydroxide solution at concentrations of 0.1–0.2 M; 0.15 M was adopted for the procedure.

Detection limit and precision

A linear relationship between adenine concentration and CL intensity was obtained over the range 1.5×10^{-4}–5.0×10^{-7} M ($r = 0.994$; $n = 17$). This dynamic range for the determination was over two orders of magnitude. The detection limit of adenine was 1.9×10^{-7} M (19 pmol per assay) at an S/B ratio of 3. The precision of the method was established by repeated assay ($n = 10$) using 2×10^{-5} and 5×10^{-6} M solutions of adenine. The relative standard deviations were 6.1 and 6.7%, respectively.

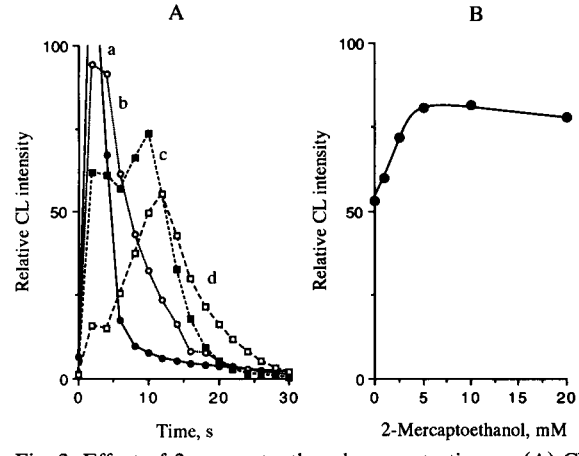

Fig. 2. Effect of 2-mercaptoethanol concentration on (A) CL decay curve and (B) CL intensity. A portion (100 μl) of adenine solution (1×10^{-4} M) was treated according to the recommended procedure but with various concentrations of 2-mercaptoethanol. 2-Mercaptoethanol concentration: (a) 0; (b) 3; (c) 10; (d) 30 mM.

TABLE 3

Relative CL intensities from nucleic acid bases, nucleosides and 2-amino-substituted heterocyclic compounds and their detection limits

Compound [a]	RCI [b]	Detection limit (M) [c]
Adenine	100	1.9×10^{-7}
Guanine [d]	0	–
Cytosine	0	–
Thymine	0	–
Uracil [e]	0	–
Adenosine [f]	98	1.8×10^{-7}
Guanosine [f]	0	–
Cytidine [f]	0	–
Thymidine [f]	0	–
Uridine [f]	0	–
Thiamine [d]	0	–
Folic acid [f]	1.0	1.6×10^{-5}
2-Aminopyrazine [f]	3.1	5.7×10^{-6}

[a] A portion (100 μl) of a 5×10^{-5} M solution of each compound was treated as in the procedure. [b] The intensity of adenine was arbitrarily taken as 100. [c] Concentration which gives an S/B ratio = 3. [d–f] These compounds were first dissolved in water, and then diluted with propan-2-ol. The contents of water in the reaction mixture were (d) 0.5%, (e) 0.6% and (f) 0.25%.

CL from nucleic acid bases, nucleosides and other 2-amino-substituted heterocyclic compounds

CL intensities and detection limits of nucleic acid bases, nucleosides and other biologically important 2-amino-substituted heterocyclic compounds obtained by this method are given in Table 3. Compounds with lower solubility in propan-2-ol were first dissolved in water and then diluted with propan-2-ol for the preparation of sample solution. Among the nucleosides tested, adenosine showed a strong CL with almost the same intensity as that of adenine. All the other nucleic acid bases and nucleosides examined showed no CL at concentrations of 5×10^{-5} M in the reaction mixture. Folic acid showed weak CL, but the intensity was only 1% of that for adenine. As reported elsewhere [8], 2-aminopyrazine is known to react with phenylglyoxal under acidic conditions to yield a chemiluminescent compound. However, the intensity was low under the conditions described under Experimental. These results suggested that the proposed method was selective for adenine or adenosine.

In conclusion, the proposed CL method for the selective determination of adenine is also sensitive, and therefore should be applicable to the detection of adenine or adenine derivatives in biological materials by combination with liquid chromatography. Elucidation of the structure of the CL product and the mechanism of the CL reaction is in progress.

REFERENCES

1 K. Nakashima, K. Suetsugu, S. Akiyama and M. Yoshida, J. Chromatogr., 530 (1990) 154.
2 H. Yuki, Y. Azuma, N. Maeda and H. Kawasaki, Chem. Pharm. Bull., 36 (1988) 1905.
3 T. Nakahara, J. Ishida, M. Yamaguchi and M. Nakamura, Anal. Biochem., 190 (1990) 309.
4 G. Zomer, R.H.V.D. Berg and E.H.J.H. Jansen, Anal. Chim. Acta, 205 (1988) 267.
5 R. Shapiro, Ann. N.Y. Acad. Sci., 163 (1969) 624.
6 N.E. Broude and E.I. Budousky, Biochim. Biophys. Acta, 254 (1971) 380.
7 T. Goto, S. Inoue and S. Sugiura, Tetrahedron Lett., (1968) 3873.
8 S. Sugiura, H. Kakoi, S. Inoue and T. Goto, Yakugaku Zasshi, 90 (1970) 436.
9 B. Alcaide, R. Pērez-Ossorio, J. Plumet and M.A. Sierra, Tetrahedron Lett., 27 (1986) 1627.
10 Y. Kishi, T. Goto, Y. Hirata, O. Shimomura and F.H. Johnson, Tetrahedron Lett., (1966) 3427.

Analytica Chimica Acta, 278 (1993) 279–285
Elsevier Science Publishers B.V., Amsterdam

Application of hydride generation to the determination of trace concentrations of arsenic by capacitively coupled microwave plasma

Dennis M. Hueber, Wellington R.L. Masamba [1], Bill M. Spencer and James D. Winefordner

University of Florida, Chemistry Department, Gainesville, FL 32611 (USA)

(Received 26th September 1992; revised manuscript received 12th January 1993)

Abstract

Studies are presented describing an application of the $NaBH_4$ reduction of soluble arsenite to form arsine for ultra-trace level arsenic determination by capacitively coupled microwave plasma atomic emission spectrometry. The arsine was condensed in a liquid nitrogen cooled trap, and introduced into the plasma after the elimination of reaction by-products that would reduce the excitation efficiency of the plasma. Use of a photodiode array detector provided a means of background correction. The procedure resulted in a limit of detection of 110 pg and a linear dynamic range of 10^4 for arsenic.

Keywords: Atomic emission spectrometry; Hydride generation; Arsenic; Microwave plasma; Plasma

The hydrides of As, Bi, Ge, Pb, Sb, Se, Sn, and Te are of importance for the determination of these elements because their hydrides are all volatile [1]. They can therefore be generated as gases suitable for effective sample introduction into an atom reservoir or excitation source suitable for determination by atomic absorption spectrometry, atomic fluorescence spectrometry, atomic emission spectrometry (AES) or mass spectrometry (only AES is specifically discussed here). The application of hydride generation to AES has been a subject of several recent reviews [2–4].

In this technique, aqueous sample solutions containing the analyte are acidified and treated with a reducing agent (usually $NaBH_4$) to generate the hydride of the analyte. The hydride is then swept out of the reaction vessel into the plasma where it is decomposed to gaseous metal atoms, excited and detected. Since all hydride forming elements have poor limits of detection when determined directly by solution nebulization, generation of the corresponding hydrides allows determinations at lower concentrations.

The advantages of utilizing this technique in AES are: (1) The introduction of gases into plasmas is highly efficient compared with pneumatic nebulization; in pneumatic nebulization, 95% of the sample solution is discarded, whereas the transport efficiency of gases to the plasma can approach 100%. Therefore, more analyte reaches the plasma, resulting in better limits of detection. (2) The generated gas is separated from solution, minimizing matrix interferences on subsequent measurements. (3) The gases formed may be trapped in a balloon, cold trap, etc. and introduced into the plasma as a plug, thereby preconcentrating the sample. Finally (4), since the sample is introduced as a gas, the plasma does not

Correspondence to: J.D. Winefordner, University of Florida, Chemistry Department, Gainesville, FL 32611 (USA).
[1] On study leave from University of Malawi, P.O. Box 280, Zomba (Malawi).

have to desolvate and vaporize the sample. The role of the plasma is to dissociate the hydrides and excite the atoms. Low power plasmas can therefore be used.

Very little work has been done [5–7] on the use of hydride generation with capacitively coupled microwave plasmas (CMPs) as excitation sources for atomic emission, although CMPs have the potential of sensitive determinations. The He CMP for excitation should result in more efficient excitation because of the high ionization energy of He. The CMP is a relatively simple type of plasma source, and operates at higher powers (250–900 W) than most microwave plasmas.

Of the various methods of hydride generation [8,9], the acid–sodium borohydride ($NaBH_4$) reaction is the most frequently used because it is the most effective.

Two approaches, continuous and batch, may be utilized to introduce the hydride into the plasma. In the continuous process, the reagents are continuously introduced into a mixing chamber where the reaction takes place. The gaseous products are swept into a gas-liquid separator where the liquid passes to a drain and the gas to the plasma. This has the advantage that the process can easily be automated. In the batch process, an aliquot of the acid solution containing the analyte is mixed with $NaBH_4$. The resulting hydrides (and gaseous byproducts) may be swept into the plasma directly, or the hydride can be trapped as it is generated and introduced subsequently as a plug. Introduction after condensation in a liquid N_2 cooled trap has the advantage that H_2, produced as a byproduct of the reaction used to generate the hydrides, can be vented away, minimizing plasma instability resulting from the introduction of high quantities of H_2. Large amounts of hydrogen also reduces the excitation efficiency of the plasma, so that higher power is needed to operate in the presence of excess H_2. Water vapor and CO_2 can also be separated from the hydride, further increasing the stability and excitation efficiency of the plasma. Also, preconcentration is achieved so that the limits of detection by this procedure tend to be superior. The greatest drawbacks of this technique are the greatly increased complexity and sample throughput time.

The purpose of the present work is to utilize separation and low temperature entrapment techniques that exclude undesirable reaction byproducts (e.g., H_2) and result in an excellent limit of detection in the CMP determination of arsenic by the generation of its volatile hydride. Resultant separation of the analyte from the matrix and byproducts permit use of a 500 W plasma.

EXPERIMENTAL

Instrumental set-up

The system used here was essentially the same as that described previously [10]. Briefly, the

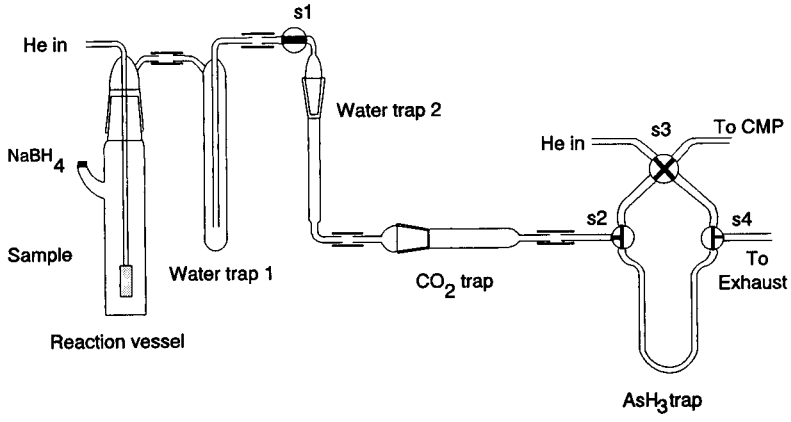

Fig. 1. Schematic diagram of AsH_3 generation system. S1 to S4 are stopcocks.

emission of the CMP was focused by a single quartz lens onto the entrance slit of a Jobin-Yvon HR 1000 spectrometer (1 m, 2400 grooves/mm, linear dispersion 0.5 nm/mm). The detector was a Princeton Instruments Model IRA-1024 photodiode array with a OSMA detector controller connected to a "286 PC-clone" computer. A combination of the ST-120 software provided by Princeton Instruments and a supplementary program written in this laboratory, was used to store and manipulate the data. Two small changes were made to this system since it was described previously [10]. (1) The graphite electrodes were replaced with titanium electrodes (Johnson Matthew, Ward Hill, MA), since graphite electrodes resulted in severe tailing of the As signals. The dimensions of the Ti electrodes were the same as those of the graphite electrodes. The final 3 mm of the Ti electrodes were tapered as this resulted in better plasma stability. (2) The current through the magnetron was regulated to minimize plasma fluctuations due to fluctuations in laboratory power.

Hydride generator / trap

The hydride generation and sample introduction apparatus, shown in Fig. 1, is similar to other designs reported in the literature [11,12]. The various components of the system were fabricated in the laboratory from borosilicate glass, and were connected by short pieces of plastic (Tygon) tubing clamped tightly over the glass tubing (5 mm o.d.) at the ends of each component. S1 to S4 represent 2 mm bore glass stopcocks greased with Corning high vacuum stopcock grease.

The reaction vessel was 15 cm long and had a capacity of 80 ml. The vessel's cap was fitted with a gas delivery tube connected to a fritted diffuser. The side arm was covered with a plastic septum. The water trap (13 cm × 2.5 cm) was immersed in a dry ice–isopropyl alcohol bath (temperature, −90°C). A second water trap (11 cm × 1.5 cm) was filled with $Mg(ClO_4)_2$ powder. The third trap (11 cm × 2.5 cm) was filled with Ascarite II (8–20 mesh); ascarite consists of NaOH on a silicate backing (Thomas Scientific, Swedesboro, NJ). This trap was used to collect CO_2 generated by carbonate impurities in the $NaBH_4$. Finally, the hydride trap was made of 5 mm o.d., 4 mm i.d. tubing. The bottom 10 cm of the tubing was filled with borosilicate glass wool, and wrapped with nicrome wire.

The two helium gas supplies were independently regulated and metered; no gas filters were used. The hydride trap was connected to the CMP torch sample tube by teflon tubing.

Reagents

Deionized water was used throughout. The arsenic standard stock solution (1000 μg/ml) was prepared by dissolving 1.320 g reagent grade arsenic trioxide (As_2O_3) in H_2O containing 4 g NaOH, and diluting to 1 l [13]. Dilute standard solutions were prepared daily from a 10 μg/ml As in 0.5% HCl standard prepared from the stock solution. The most dilute solutions (< 50 ng/ml) were prepared just before use. A 5% $NaBH_4$ in 0.11 M NaOH (for stabilizing the $NaBH_4$ [14]) solution was prepared from 99% $NaBH_4$ and 99.99% NaOH (Aldrich, Milwaukee, WI). This solution was freshly prepared every 4 h. A gas standard of 50 μl/l Arsine in He was supplied by Alphagaz, Walnut Creek, CA. Ultrapure concentrated HCl solution was supplied by Seastar Chemical (Seattle, WA). All other reagents were supplied by Fisher Scientific (Fair Lawn, NJ).

Procedure

The arsenic solution (1 to 25 ml) was added to the reaction vessel (see Fig. 1) and mixed with 25 ml of 1 M HCl. $NaBH_4$ solution (4 ml) was then added, via a septum, over a period of 2 min using a syringe pump. During the addition and the course of the reaction, He gas was passed to the sample tube of the torch through S3 at a flow-rate of 80 ml/min. Helium was also bubbled through the reaction vessel at the rate of 200 ml/min. The mixture in the reaction vessel was stirred constantly by a magnetic stirring bar. Stopcocks S1 and S2 were positioned so as to pass the hydride through the AsH_3 trap, which was immersed in a liquid nitrogen bath (6 to 8 cm deep). S4 was positioned to vent the hydrogen produced during the reaction. After 6 min (it was confirmed that 99% of the arsine was swept through

the system in 4 min or less), the helium to the reaction vessel was turned off, S2 and S3 were turned so that He passed through the AsH_3 trap, and S4 was turned so that the He was directed to the CMP. The liquid nitrogen flask was then removed and the AsH_3 trap heated using a variable transformer to apply a small voltage to the nichrome wire. The vaporized AsH_3 was then swept to the CMP and through the electrode. The arsenic atomic emission was recorded on the computer for later processing. The entire process required 10 min per sample.

Using the optimized conditions, as discussed below, the limit of detection (LOD), linear dynamic range (LDR) and relative standard deviation (RSD) for As were determined. The concentration of arsenic in dried orchard leaves (NBS SRM 1571) was also determined to check the accuracy of the technique. The orchard leaves were digested using the method described by Matsumoto et al. [12].

Optimization of the signal

The efficiency of the trap was tested by trapping a small flow (5 ml/min) of 50 μl/l arsine in helium in the cooled trap. The total area of the peak produced when the trap was warmed was used to estimate efficiency of the trap (97% with a standard deviation of 6%). The low precision of this measurement can be attributed to the uncertainty in the amount of time the hydride was allowed to flow into the trap.

A system was developed to produce a steady state arsenic signal to be used to speed the optimization of several of the experimental parameters. A flow of 5 ml/min of 50 μl/l arsine in helium was mixed with 80 ml/min of pure helium and introduced into the CMP to produce a signal at 228.8 and 235.0 nm.

Among the parameters optimized using this steady state signal were the monochromator slit widths (20 μm being optimal), the alignment, the CMP gas flow-rates, and the plasma power. The alignment of the CMP and the entrance optics were optimized each time the electrode was replaced in the CMP (the electrodes were visibly damaged by the plasma in 4–8 h). The best plasma gas mixture and flow rate for the CMP plasma gases were determined to be 98% He with 2% H_2 at 6 l/min, respectively. Larger percent-

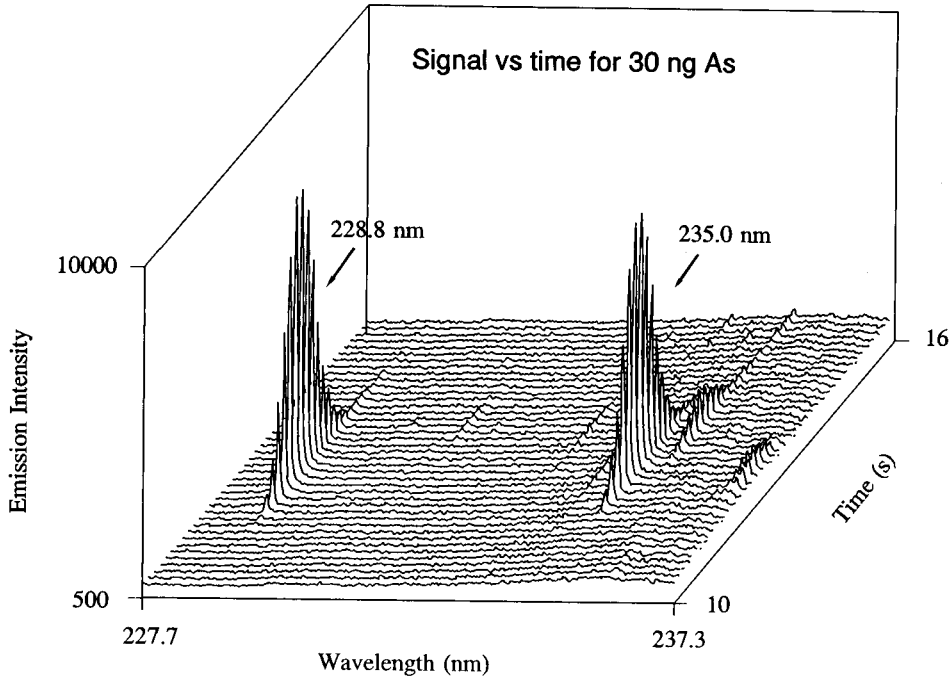

Fig. 2. A 3-dimensional plot showing the signals of 30 ng As. The CMP was operated at 500 W.

ages of hydrogen led to a greatly reduced arsenic signal, but at least 2% was necessary to maintain a stable plasma.

The heating rate of the hydride trap was optimized by measuring the signal given by a sample containing 100 ng of arsenic processed by the method outlined above.

Data reduction

A program written in the laboratory was used to convert the raw diode array data to a useful analytical signal. The average values of the five diodes nearest the peak of the signals (228.8 and 235.0 nm) were corrected for the background signal and summed over the duration of the peaks. Both results were summed, giving the total area for the signals at 228.8 and 235.0 nm. This procedure gave a lower LOD than the area at 228.8 nm alone. Attempts to use the signal height at 228.8 nm resulted in an LOD 4 times larger and a reduced linear dynamic range.

RESULTS AND DISCUSSION

Figure 2 shows the transient signals for As at 228.8 and 235.0 nm. These lines were the most sensitive seen for arsenic, the line at 193.7 was ten times less sensitive. The small emission peak at 237.1 nm is due to a weak As emission line. The emission line near 235.5 might be the result of Sn emission resulting from trace quantities of Sn in the reagents used.

Effect of power

The As signal increased as the power of the CMP was increased, but the S/N was constant at powers above 200 W (Fig. 3). As the power was increased, more energy was available to excite the As (both excitation and rotational energy increased with power); therefore, the signal increased. The noise, however, also increased with power resulting in constant S/N ratios. Thus, there was no advantage to working at power levels higher than 500 W; 500 W was used for all further studies.

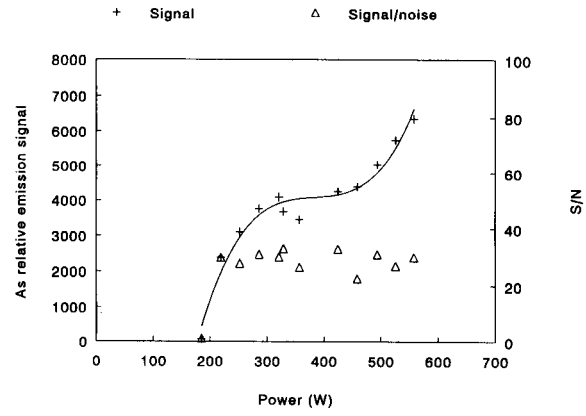

Fig. 3. Effect of power on As signal and signal-to-noise ratio.

Optimum heating rate of the AsH_3 trap

Figure 4 shows the signals obtained when the AsH_3 trap was heated at different rates. The following effects were observed: (1) The time of appearance of the signal (from the time the heating coil is turned on) decreased as the heating rate increased (Fig. 5, curve a). Increasing the heating rate reduced the time required to volatilize AsH_3. Without heating the signal appeared after 37 s, whereas with 230 W, the signal appeared after 10 s. (2) The signal duration (peak width at base, in seconds) also decreased as the heating rate increased. The signal duration when no heat was applied to the AsH_3 trap was 16 s, while the duration was 4 s for 58 W to 370 W (Fig. 5, curve b). The higher heating rates allowed

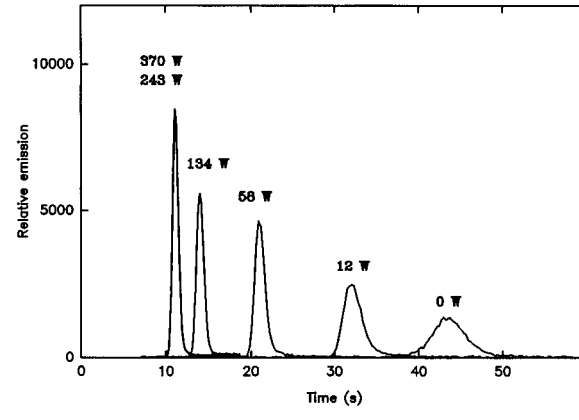

Fig. 4. Signals of As resulting from different heating rates of AsH_3 trap.

the sample to volatilize quickly from the AsH_3 trap. (3) Peak height increased rapidly as the heating rate increased (Fig. 5, curve c). Since the higher heating rates volatilized the sample quickly, the sample was introduced to the plasma as a more concentrated "plug" resulting in higher signals. The peak height for 243 W and 370 W were almost the same, indicating that the AsH_3 was being volatilized at a maximum rate. Increasing the heating rate beyond this point did not increase the signals further but could risk decomposition of the AsH_3 in the AsH_3 trap. All subsequent work was therefore carried out at 243 W.

Figures of merit

A log–log plot of signal versus mass of arsenic, over a range of 1 ng to 3 μg, was generated. Neutral density filters were used to extend the linear range of the detector for higher concentrations. The slope of the plot was 0.97 with a linear dynamic range greater than 10^4 and $R^2 = 0.998$. Using a calibration curve from 10 ng to 300 ng, a linear plot of signal versus concentration was obtained. The slope of the calibration curve was 3760 counts/ng. The limit of detection (3σ) was determined to be 60 pg based the standard deviation of the background during the evolution of the sample. This corresponded to a concentration LOD of 1.2 pg/ml for a 50 ml sample. The limiting noise source was the fluctuations in the background emission of the CMP. The LOD based on reagent blanks was slightly higher, 110 pg, probably due to the presence of some arsenic in the reagents. Table 1 shows the LODs of several related methods for comparison. A percent relative standard deviation of 4% was measured for 5 samples of 50 ng each. The analysis of five samples of orchard leaves, standardized by NBS (now NIST) as 14 ± 2 μg/g As, gave a mean concentration of 10.9 μg/g with a standard deviation of 0.7 μg/g. Although the measured concentration is significantly low (the theoretical value of t is smaller than the calculated value of t), it is not unreasonable so considering the range given for standard value, and the approximately 95% recovery efficiency of the digestion procedure.

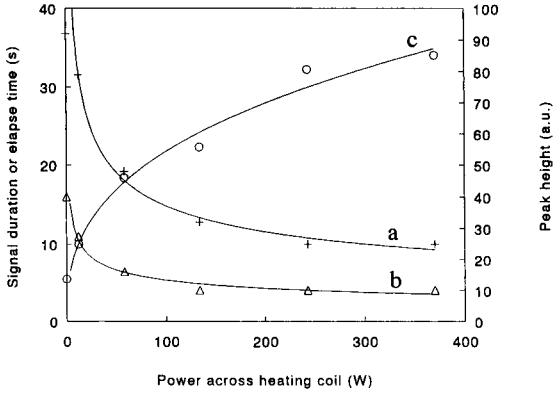

Fig. 5. Effect of power across heating coil on (a) time of appearance of signal (elapse time) (b) signal duration and (c) peak height.

TABLE 1

Reported limits of detection for arsenic by ICP and CMP–AES (ng/ml)

Plasma type	Solution nebulization	Continuous hydride generation	Hydride gereration–condensation trap
ICP	53 [2]	0.1 [15]	0.02 [2]
CMP	8000 [a]	0.25 [6]	0.002 [b]

[a] Unpublished results. [b] Present method.

Conclusions

Arsenic was determined with an absolute LOD of 60 pg corresponding to concentration LOD of 1.2 pg/ml for a 50 ml sample volume. The LDR was found to be greater than 10^4 which is typical of atomic emission techniques. This work also shows the importance of optimizing the AsH_3 heating rate in order to obtain high sensitivity and reproducible peak heights.

Hydride generation has proved to be a viable approach to obtaining an excellent LOD for arsenic which has a poor LOD by solution nebulization. The LOD for arsenic determinations with a CMP is further improved when H_2, H_2O, and CO_2 are removed. The method of CO_2 elimination employed in this study would preclude exploitation of H_2Se and H_2Te [11]. Use of a He carrier gas permitted the use of liquid N_2 as the AsH_3 cold trap.

This work was supported by a grant from the Environmental Protection Agency (EPA - CR 8188 48-01-0). Although the research described in this article has been supported by the United States Environmental Protection Agency (through CR818848 to the University of Florida), it has not been subjected to Agency review and therefore does not necessarily reflect the views of the Agency and no official endorsement should be inferred.

REFERENCES

1 J.C. Bailar Jr., H.J. Emelens, R. Nyholm and A.F. Trotman-Dickenson, Comprehensive Inorganic Chemistry, Vol. 1, Pergamon Press, Oxford, 1973.
2 T. Nakahara, Spectrochim. Acta Rev., 14 (1991) 95.
3 J.W. Hershey and P.N. Keliher, Appl. Spectrosc. Rev., 25 (1989–90) 213.
4 A.D. Campbell, Pure Appl. Chem., 64 (1992) 227.
5 R.R. Nakashima, Bunseki Kagaku, 25 (1976) 869.
6 I. Atsuya and K. Akatsuka, Spectrochim. Acta, 36B (1981) 747.
7 H. Uchida, P.A. Johnson and J.D. Winefordner, J. Anal. At. Spectrom., 5 (1990) 81.
8 T. Nakahara, Prog. Anal. Atom. Spectrosc., 6 (1983) 163.
9 W.B. Robbins and J.A. Caruso, Anal. Chem., 51 (1979) 889A.
10 W.R.L. Masamba, A.H. Ali and J.D. Winefordner, Spectrochim. Acta, 47B (1992) 481.
11 R.C. Fry, M.B. Denton, D.L. Windsor and S.J. Northway, Appl. Spectrosc., 33 (1979) 399.
12 K. Matsumoto, T. Ishiwatari and K. Fuwa, Anal. Chem., 56 (1984) 1545.
13 A.E. Greenberg, R. Trussel and L.S. Clesceri (Eds.), Selected Physical and Chemical Standard Methods for Students, Port City Press, Baltimore, 1986.
14 R. Bye, Talanta, 29 (1982) 797.
15 T. Nakahara, Anal. Chim. Acta, 131 (1981) 73.

Analytica Chimica Acta, 278 (1993) 287–292
Elsevier Science Publishers B.V., Amsterdam

Determination of bismuth(III) by graphite furnace atomic absorption spectrometry combined with liquid–liquid extraction with trioctylmethylammonium nitrate

Asako Minagawa

Laboratory of Analytical Chemistry, Faculty of Science, Niigata University, Niigata 950-21 (Japan)

Kiyoshi Sawada

Coordination Chemistry Laboratories, Institute for Molecular Science, Myodaiji, Okazaki 444 (Japan)

Toshio Suzuki

Laboratory of Analytical Chemistry, Faculty of Science, Niigata University, Niigata 950-21 (Japan)

(Received 16th November 1992; revised manuscript received 15th January 1993)

Abstract

A method for determining traces of bismuth(III) in environmental samples by graphite furnace atomic absorption spectrometry (GFAAS) after extractive separation with trioctylmethylammonium nitrate (TOMA · NO_3) is described. Bismuth(III) was quantitatively extracted and concentrated with 6% (w/v) TOMA · NO_3 in xylene from 0.1 M hydrobromic acid–0.5 M nitric acid solution. The organic phase was then washed with 1.0 M nitric acid to remove other co-extracted metal ions, bismuth(III) remaining quantitatively in xylene solution. Bismuth(III) in the organic phase was directly determined by GFAAS. The method was applied to standard reference materials and the results obtained agreed well with the certified values.

Keywords: Atomic absorption spectrometry; Sample preparation; Bismuth; Extraction; Preconcentration

Bismuth(III) is widely used in cosmetics and medicines. It is also utilized industrially as a constituent of many kinds of alloys and semiconductors and as a coolant in atomic reactors. Recently, the content of Bi(III) in the environment has become regarded as one of the indicators of industrial pollution. The concentration of Bi(III) in nature, however, is generally low and the exact determination of Bi(III) is still difficult.

Correspondence to: K. Sawada, Coordination Chemistry Laboratory, Institute for Molecular Science, Myodaiji, Okazaki 444 (Japan).

Spectrophotometry and neutron activation analysis combined with liquid–liquid extraction of chelate complexes of Bi(III) with dithizone [1], xanthates [2], amidines [3] and xylenol orange [4,5] have been studied for the determination of Bi(III) at $\mu g\ g^{-1}$ levels and below. Flow-injection analysis with liquid–liquid extraction and spectrophotometry has also been reported [6–8]. In these methods, however, the procedures are complicated because pH adjustment or addition of masking agents are required. Hydride generation atomic absorption spectrometry or anodic stripping voltammetry combined with ion-exchange

and precipitation methods have also been applied to the determination of Bi(III) in natural waters [9–12]. In these methods interferences caused by contamination are significant, so the procedures require skill.

Trioctylmethylammonium chloride (TOMA · Cl) has been used as an extracting reagent for the separation of metal ions [13–15]. Its cationic part, $TOMA^+$, extracts the anionic complex of metal ions formed in a hydrogen halide or pseudohalide aqueous solution. In this work, it was found that bismuth(III) was extracted with $TOMA \cdot NO_3$ from nitric acid solution, where nitrate ion usually obstructs the extraction of metal ions with $TOMA^+$. By combining this peculiar behaviour of bismuth(III) ion with the nitrate ion with graphite furnace atomic absorption spectrometry (GFAAS), a simple and specific method for the determination of Bi(III) was established. The method was applied to some geological standard samples.

EXPERIMENTAL

Reagents

A standard bismuth(III) solution (100 mg l^{-1}) was prepared by dilution of 1000 mg l^{-1} atomic absorption standard (Wako) with 3.0 M nitric acid. This solution was appropriately diluted prior to each determination. Hydrobromic acid solution was freshly prepared for each experiment. Stock solutions of other metal ions (100 mg l^{-1}) were prepared by dissolving the metal nitrates in 1.0 M nitric acid. Trioctylmethylammonium chloride (TOMA · Cl; Capriquat, Dojin Pure Chemicals) was weighed and dissolved in xylene. Then the xylene solution of TOMA · Cl was shaken with 2.0 M nitric acid for 15 min and the aqueous phase was discarded. Three repetitions of this procedure completed the substitution of chloride ion with nitrate ion. The xylene solution of $TOMA \cdot NO_3$ thus obtained was used. All reagents used were of analytical-reagent grade.

Apparatus

A Shimadzu Model AA-640-01S flame atomic absorption spectrometer was used for determination of bismuth(III) in fundamental extraction experiments. The same spectrometer equipped with a Model GFA-2 graphite furnace atomiser was used in analytical experiments.

The optimum GFAAS measurement conditions were determined by preliminary experiments as drying at 210°C for 30 s, ashing at 860°C for 40 s and atomizing at 2350°C for 10 s. The analytical line at 222.9 was used.

Procedure

In order to study the extraction behaviour of bismuth(III), 20 ml of aqueous solution containing 10 mg l^{-1} of Bi(III) was shaken for 10 min with 20 ml of 1% or 6% (w/v) $TOMA \cdot NO_3$ solution in xylene. This shaking time is sufficient to reach the equilibrium state. The bismuth(III) concentration in the xylene phase was determined by a flame AAS after back-extraction of Bi(III) from 10 ml of xylene solution into 10 ml of 0.2 M perchloric acid solution. In order to lower the detection limit of Bi(III) and to simplify the procedure, GFAAS was used for the determination of bismuth(III) in natural samples. A 10-μl volume of organic phase was pipetted into a graphite furnace and the content of Bi(III) in the organic phase was directly determined.

Decomposition of sample

Amounts of 500 mg of standard reference rock samples [JG-1 (granodiorite) and JR-1 (rhyolite), Geological Survey of Japan] were decomposed with a mixture of hydrochloric acid (1.5 ml), nitric acid (0.5 ml) and hydrofluoric acid (4 ml) in a sealed PTFE container at 130°C for 16 h. A 300-mg amount of a standard reference sediment sample (NIES-No 2, National Institute for Environmental Study, Japan) was decomposed with a mixture of nitric acid (3 ml), hydrofluoric acid (5 ml), hydrogen peroxide (31%, 5 ml), and two drops of sulphuric acid at 130°C for 4 h. After the solution had been evaporated to dryness, the residue was dissolved in hydrochloric acid. The solution was diluted to 50 ml with 0.5 M HNO_3–0.1 M HBr. The reagent blank determined by GFAAS was negligible.

RESULTS AND DISCUSSION

Extraction of bismuth(III)

Many heavy metal ions are extracted by TOMA · Cl from HCl or HBr solution [13–15]. In general, the extraction of metal ions is suppressed by the addition of nitric acid, which is usually used for stripping of metal ions. The effect of nitric acid on the extraction of some metal ions from 0.1 M HBr into 1% TOMA · NO_3 solution in xylene is shown in Fig. 1. As represented by zinc(II), most of the metal ions are not extracted in the presence of 0.5 M HNO_3, although Pb(II) and Cd(II) are extracted even in the presence of relatively high concentrations of HNO_3. On the other hand, Bi(III) is quantitatively extracted even with 2.0 M nitric acid.

Figure 2 shows the extraction of Bi(III) with 1% (w/v) TOMA · NO_3 solution in xylene as a function of hydrobromic acid concentration with and without the addition of 1.5 M nitric acid. Although nitric acid usually interferes with the extraction of metal ions, the extractability of Bi(III) was significantly enhanced by the presence of nitric acid. Thus, in the absence of HNO_3 0.1 M HBr is required for the quantitative extraction of Bi(III), whereas in the presence of 1.5 M nitric acid, bismuth(III) is quantitatively extracted with 0.03 M HBr. Moreover, Bi(III) is extracted from nitric acid even in the absence of hydrogen halide ($C_{HBr} = 0$).

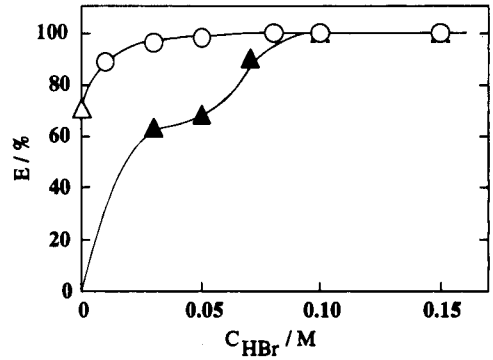

Fig. 2. Percentage extraction of bismuth(III) into 1% (w/v) TOMA·NO_3 solution in xylene at various concentrations of hydrobromic acid, (○) and (▲) without addition of 1.5 M nitric acid. △ = Extraction of bismuth from 1.5 M nitric acid in the absence of hydrobromic acid.

The effect of the concentration of nitric acid on the extraction of bismuth(III) from HCl and HBr solutions is shown in Fig. 3. In extraction from HCl, the extraction of Bi(III) is suppressed by the presence of high concentrations of HNO_3, whereas the extraction of Bi(III) from HBr solution is hardly affected by HNO_3 even very high concentrations. Consequently, it was concluded that HBr is more effective extractant of Bi(III) than is HCl.

As shown in Fig. 2, bismuth(III) is extracted from nitric acid solution even in the absence of halide. The extraction of Bi(III) as a function of nitric acid concentration (halide free) is shown in

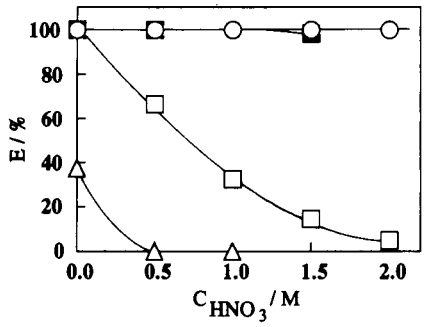

Fig. 1. Effect of concentration of nitric acid on the extraction of (○) bismuth(III), (■) cadmium(II), (□) lead(II) and (△) zinc(II) with 1% (w/v) TOMA·NO_3 solution in xylene from 0.1 M hydrobromic acid.

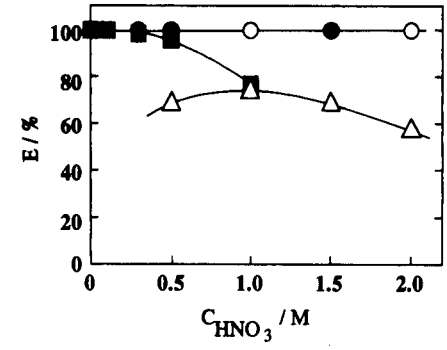

Fig. 3. Percentage extraction of bismuth(III) into 1% (w/v) TOMA·NO_3 solution in xylene at various concentrations of nitric acid from (○) 0.1 M and (●) 0.5 M hydrobromic acid, (■) 0.5 M hydrochloric acid and (△) nitric acid (halide free).

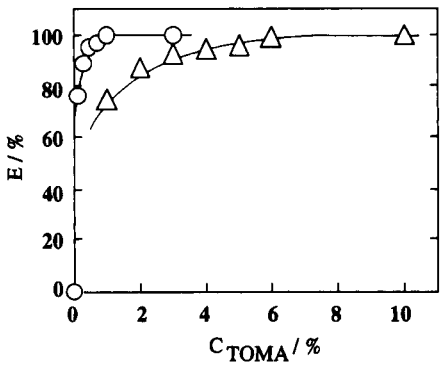

Fig. 4. Effect of TOMA·NO_3 concentration in xylene on the extraction of bismuth(III) from (○) 0.1 M hydrobromic acid–0.5 M nitric acid and (△) 1.0 M nitric acid.

Fig. 3. As can be seen, the extraction of Bi(III) shows a maximum at 1.0 M nitric acid, but the extraction was not quantitative. The effect of the TOMA · NO_3 concentration in the xylene phase was studied. As shown in Fig. 4, Bi(III) is almost quantitatively extracted at $C_{TOMA \cdot NO_3} = 6\%$ from 1 M HNO_3 (halide free), whereas it shows quantitative extraction at 1% TOMA · NO_3 in xylene in the presence of 0.1 M HBr ($C_{HNO_3} = 0.5$ M).

Preconcentration of bismuth(III) and separation from co-existing metals

As the concentration of bismuth(III) in the environment is very low, preconcentration is required for its precise determination. The possibility of preconcentration was examined with the HBr–HNO_3 and HNO_3 systems. By taking into consideration the results obtained so far, the concentration of TOMA · NO_3 in the xylene phase was chosen as 6% (w/v). The concentrations of HBr and HNO_3 in aqueous solution were $C_{HNO_3} = 0.5$ M and $C_{HBr} = 0.1$ M for the HBr–HNO_3 extraction system. The concentration of HNO_3 in the aqueous phase for the HNO_3 system (HBr free) was $C_{HNO_3} = 1.0$ M. The extraction of Bi(III) at various volume ratios of the aqueous phase to the organic phase (V_{aq}/V_{org}) is shown in Table 1. With the HBr–HNO_3 system, Bi(III) was quantitatively extracted even at $V_{aq}/V_{org} = 200$. On the other hand, with the HNO_3 extraction system, the percentage extraction of Bi(III) significantly decreased with increase in V_{aq}/V_{org}. These results indicate that the HBr–HNO_3 system is much more favourable than the HNO_3 system for the preconcentration of Bi(III).

TABLE 1

Extraction of bismuth(III) with 6% (w/v) TOMA·NO_3 at various volume ratios of aqueous to organic phase

System [a]	Volume ratio (V_{aq} / V_{org})	Extraction (%)
HNO_3–HBr	1	100
	10	100
	20	100
	100	100
	150	100
	200	100
HNO_3	1	97
	2	94
	5	86
	8	79
	10	74

[a] The concentrations of acids in aqueous solution were: 0.5 M HNO_3 and 0.1 M HBr for the HNO_3–HBr system and 1.0 M HNO_3 for the HNO_3 system.

The extraction of other metal ions was examined with the HBr–HNO_3 system and HNO_3 systems. Table 2 shows the extraction of bismuth(III) and other metal ions at a volume ratio of aqueous to organic phase of 1 : 1. With the HBr–HNO_3 system, although Fe(III), Cu(II), Ni(II), and Co(II) are not extracted, some metal ions, which form stable anionic complexes with bromide ion, such as Zn(II), Pb(II) and Cd(II), are co-extracted with Bi(III). In particular, cadmium is extracted quantitatively in this system.

TABLE 2

Extraction of bismuth and diverse metal ions into 6% (w/v) TOMA·NO_3 solution in xylene

Metal ion	Extraction (%)	
	0.5 M HNO_3–0.1 M HBr	1.0 M HNO_3
Bi^{3+}	100	97
Fe^{3+}	0	0
Cu^{2+}	0	0
Ni^{2+}	0	0
Co^{2+}	0	0
Zn^{2+}	58	0
Pb^{2+}	96	8.9
Cd^{2+}	100	0

On the other hand, most metal ions were not extracted in the HNO_3 system, although a small amount of lead was extracted. It is concluded that the HNO_3 system is superior to the HBr–HNO_3 system for the separation of bismuth(III) from other metal ions.

Analytical scheme

By taking into consideration the results in the preceding section, an analytical scheme for natural samples was established, i.e., preconcentration of Bi(III) with the HBr–HNO_3 extraction system followed by the stripping of other metal ions from the organic phase containing Bi(III) with the HNO_3 extraction system. These extractions were followed by the direct determination of Bi(III) in the organic phase by GFAAS (Scheme 1).

Bismuth(III) in the sample solution is quantitatively preconcentrated in the TOMA · NO_3 xylene solution (Org. 1) in the first extraction step by using the HBr–HNO_3 system. Then the Org. 1 phase is washed with 0.1 M HNO_3 solution in the second step. In the second step, most of other metal ions are stripped into the aqueous phase and Bi(III) remains quantitatively in the organic phase (Org. 2). The concentration of bismuth(III) in the Org. 2 phase is directly determined by GFAAS. The detection limit was determined as 0.08 $\mu g\ l^{-1}$ (signal-to-noise ratio = 3) for bismuth(III) with 200-fold preconcentration.

TABLE 3

Influence of diverse anions on the extraction of bismuth from 0.1 M HBr–0.5 M HNO_3 with 6% (w/v) TOMA·NO_3

Anion	Extraction (%)	
	0.5 M	1.0 M
Chloride	96	90
Sulphate	100	100
Perchlorate	24	3

The effects of diverse ions were investigated prior to applying this scheme to natural samples. The co-existing metal ions listed in Table 2 were not extracted from HBr–HNO_3 solution (Org. 1), except for Zn(II), Pb(II) and Cd(II). Thus, at least 100 mg l^{-1} levels of these metal ions have no effect on the determination of 0.1 mg l^{-1} of Bi(III). Cd(II) and Zn(II) ions are completely stripped out by the washing step and did not interfere even at 100 mg l^{-1}. The determination of bismuth(III) in the organic phase before the stripping (Org. 1) was subject to interference by lead above 50 mg Pb(II) l^{-1}, but by the washing with HNO_3 the influence of lead was completely eliminated, at least upto 100 mg l^{-1}.

The effects of various anions on the extraction of bismuth(III) was examined. The results are given in Table 3. Chloride and sulphate ions did not interfere the extraction of bismuth(III) up to

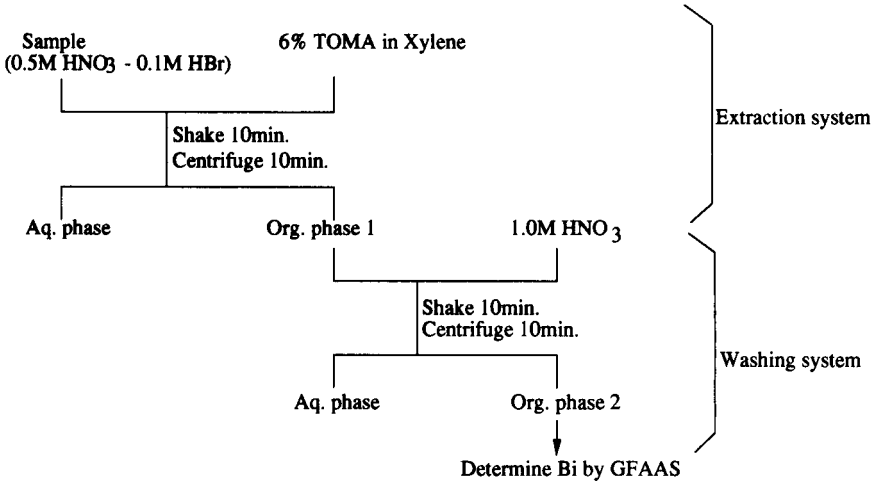

Scheme 1.

TABLE 4

Analytical results for standard reference materials

Sample	Bi concentration ($\mu g\ g^{-1}$)	
	This method	Certified value
JG-1	0.51	0.52
JR-1	0.56	0.51
NIES-No. 2	0.83	(0.45) [a]

[a] Reference value.

0.5 M. Perchlorate ion showed a significant interference at 0.05 M $HClO_4$. However, if perchloric acid is not used for the decomposition of a sample, the effect of perchlorate ion at the level of natural abundance is negligible.

Application to the natural materials

Bismuth(III) in standard reference materials was determined according to the procedure shown in Scheme 1. The results are given in Table 4 and show that the values obtained for the standard rock samples (JG-1 and JR-1) are in good agreement with the certified values. These results confirm the accuracy of the proposed method. The concentration of bismuth(III) in a standard sample of pond sediment (NIES-No. 2) was also determined. Although a concentration of 0.45 μg Bi(III) g^{-1} has been reported for this sample [16], the certified value has not been established. In this work the concentration of Bi(III) was determined as 0.83 $\mu g\ g^{-1}$.

REFERENCES

1 H.A. Mottola and E.B. Sandell, Anal. Chim. Acta, 25 (1961) 520.
2 M. Aihara and M. Kiboku, Bunseki Kagaku, 29 (1980) 243.
3 A. Ghosh, K.S. Patel and R.K. Mishra, Bull. Chem. Soc. Jpn., 62 (1989) 3675.
4 Z. Nan, Talanta, 26 (1989) 733.
5 H. Onishi and N. Ishiwatari, Bull. Chem. Soc. Jpn., 33 (1960) 1581.
6 J.S. Lobiñska, Anal. Chim. Acta, 251 (1991) 275.
7 K. Yoshimura, Bunseki Kagaku, 36 (1987) 656.
8 J.M. Calatayud, Anal. Lett., 20 (1987) 1379.
9 Y. Kanai, Bull. Geol. Surv. Jpn., 33 (1982) 619.
10 D.S. Lee, Anal. Chem., 54 (1982) 1682.
11 A. Haruta, K. Matsumoto and K. Terada, Anal. Sci., 5 (1989) 319.
12 H. Narita, K. Harada and W. Burnett, Talanta, 36 (1989) 925.
13 T. Suzuki and T. Sotobayashi, Nippon Kagaku Kaishi, 87 (1966) 587.
14 T. Suzuki, K. Kobayashi and K. Sawada, Nippon Kagaku Kaishi, 7 (1982) 1167.
15 T. Suzuki, H. Ozaki and K. Sawada, Anal. Sci., 2 (1986) 25.
16 J. Ohyama, F. Maruyama and Y. Dokiya, Anal. Sci., 3 (1987) 413.

Analytica Chimica Acta, 278 (1993) 293–306
Elsevier Science Publishers B.V., Amsterdam

Random walk simulation of flow injection analysis. Evaluation of dispersion profiles

Peter D. Wentzell, Michael R. Bowdridge, Elizabeth L. Taylor and Craig MacDonald

Trace Analysis Research Centre, Department of Chemistry, Dalhousie University, Halifax, Nova Scotia B3H 4J3 (Canada)

(Received 3rd July 1992; revised manuscript received 4th January 1993)

Abstract

The use of the random walk model for simulating peak shapes in flow injection analysis (FIA) is investigated. Studies are limited to the case of dispersion in straight tubes with laminar flow (no reaction), but more precise peak shape data than has previously been available is provided. Peak shapes obtained with the random walk model are compared with experimental results and predictions made by other theoretical approaches. Comparisons utilize a wide variety of conditions, including those treated by other authors. Favourable agreement is obtained in all cases, although some differences with experimental results are observed. The computational aspects of the random walk algorithm are considered and guidelines for its implementation are provided. The versatility of the algorithm is demonstrated through the presentation of simulation results for modified laminar flow profiles, asymmetric flow profiles, and conditions of infinite radial diffusion.

Keywords: Flow injection; Dispersion profiles; Random walk simulation

In recent years, considerable effort has been directed towards obtaining a better understanding of peak shapes in flow injection analysis (FIA). Because of the interaction of diffusion, convection and chemical kinetics, the problem is non-trivial and is made more complex by the wide variety of geometries, manifolds and flow strategies that continue to appear. Achieving a better appreciation of factors that affect the shape of flow injection profiles is important because FIA has become a widely used tool for automated analysis. Furthermore, the of use modified FIA methods such as merging zones [1,2], flow reversals [3], and sinusoidal flow [4] underscore the need to be able to theoretically predict concentration distributions in a flowing stream.

A variety of methods for modeling concentration profiles in open tubes have been developed. These have been reviewed by several authors [5–8] and an extensive discussion will not be given here. Methods include single parameter descriptions of the dispersion of the sample plug [9], solution of the convection–diffusion equations [10–13] or tanks-in-series model [14,15], and discrete simulation [16,17]. Models have considered both the case of dispersion only and dispersion with chemical reaction. Descriptions based on the calculation of a single parameter are often useful in assessing the performance of a particular experimental system, but are of limited utility for more comprehensive studies that require an accurate description of concentration profiles. Numerical solution of the differential equations associated with the convection–diffusion or tanks-in-series models have produced results that are in good agreement with experimentally observed profiles, but these approaches are computationally intensive and often limited in terms of

Correspondence to: P.D. Wentzell, Trace Analysis Research Centre, Department of Chemistry, Dalhousie University, Halifax, Nova Scotia B3H 4J3 (Canada).

the experimental geometries for which they are valid. In the work presented here, discrete simulations based on the random walk model developed by Betteridge et al. [16] are used. Although this method is also computationally intensive, it has several advantages which have been pointed out by the authors. Most notably, certain changes in the experimental parameters that are difficult to incorporate into other models are easily accommodated by the random walk model since the simulation treats individual molecules. Moreover, tentative physical models that explain the observed effects of changing system parameters (e.g. coiling, flow, injection profile, connections) may be more easily tested with the random walk model. Since the ultimate objective of these studies is to obtain a better understanding of the physical and chemical processes occurring within the FIA system, the ability to develop and test models for a variety of configurations is of critical importance.

In their original work [16], Betteridge et al. demonstrated that trends in peak height for the simulated results were in general agreement with experimental observations, but did not provide detailed comparisons of predicted concentration profiles with experimental measurements or the results of other models. This was due the limited computational capabilities which prevented the simulation of more than a few thousand molecules in a reasonable time period. This resulted in concentration profiles with large amounts of stochastic noise, making them unsatisfactory for detailed comparisons. Such comparisons are important for evaluating the potential of the random walk approach to modeling FIA profiles, however.

In the work presented here, a comparison of peak profiles obtained by the random walk model with experimental and other theoretical results is provided. To keep the scope of the study reasonable, comparisons are limited to the case of dispersion of the sample plug in a straight tube with laminar flow (no reaction). Future studies will consider different flow geometries and chemical kinetics. In the comparisons presented, experiments conducted in our laboratory as well as those carried out by Korenaga et al. [6] and Wada et al. [13] are used to evaluate the random walk approach. In addition, theoretical peak and bolus shapes predicted by solution of the convection–diffusion equation by Wada et al. [13] and Vanderslice et al. [10,12] are considered. The effect of changing the flow profile and mixing characteristics of the flow system using the random walk model are considered. Finally, some observations on implementing the random walk model are discussed.

THEORETICAL CONSIDERATIONS

The random walk model, originally used by Einstein to treat Brownian motion [18], has been widely applied to the physical sciences. The principles of this method have been discussed elsewhere [19] and will not be treated in detail here. The procedure used in this work is essentially the same as that employed by Betteridge et al. [16] with modifications made for some studies. The basic algorithm is summarized as follows. Initially, a predetermined number of molecules (typically 5000) are randomly distributed in a tube of radius R and length L. This represents the sample plug. It may be argued that a more uniform distribution of x, y, and z coordinates would be more logical, but a random distribution in a cylindrical volume is more easily implemented and avoids bias that may be introduced by regular spacing, especially on repetitive runs. Once the initial molecular coordinates have been established, the molecules are moved in discrete time intervals of Δt. Steps corresponding to molecular diffusion are taken in the x, y, and z directions. The average value of the steps is $\Delta l = (2D\Delta t)^{1/2}$, where D is the diffusion coefficient. Therefore, the step in each direction is calculated as $Q\Delta l$, where Q is a random number drawn from a uniform distribution between -2 and $+2$. In the axial (z) direction, both diffusion and convection contribute to a molecule's motion, so an extra term must be included for the latter effect. In the original simulation, a parabolic flow profile was assumed such that,

$$U = U_{max}(1 - r^2/R^2) \quad (1)$$

where U is the flow velocity at a distance r from the center of the tube, and U_{max} is the maximum flow velocity (equal to twice the average flow velocity, U_{avg}). Therefore the motion of the molecule in the z direction uses a step of $Q\Delta l + U\Delta t$, where the latter term is calculated at the x and y values after the step. To obtain detector profiles, the number of molecules which have passed the detector (a distance l from the injection point) after each one second interval is recorded. This continues for a specified period of time. To provide data for contour plots of flow profiles (bolus shapes), the simulation is stopped after a predetermined period and the number of molecules within smaller sections of the tube are counted. In both cases, simulations are repeated a sufficient number of times to provide good averaging.

Obviously, two of the factors that will affect the quality of simulation results are the total number of steps taken as the molecules move down the tube and the average size of each step. Assuming that the step size is sufficiently small, an insufficient number of iterations would be expected to lead to significant variations in the peak profiles obtained between runs. Generally this is not a problem because typical FIA conditions usually ensure an adequate number of steps and the large number of molecules employed averages out differences. The problem of insufficient step size is more critical since it can lead to systematic errors in two ways. First, axial movement of the molecule by convection is calculated from the new x and y coordinates rather than from the average flow velocity between the new and old positions. This is intended to reduce computation time and assumes that velocity differences will be small and average out. It would be useful to know what the magnitude of this effect is and if it becomes significant for larger step sizes. To this end, some of the simulations employed in this work computed an average axial velocity between points x_1, y_1 and x_2, y_2. For a symmetric laminar flow, it can be shown that this is given by:

$$U_{12} = \frac{U_{max}}{R^2\Delta^1 x}[A\Delta^1 x - B\Delta^2 x - C\Delta^3 x] \qquad (2)$$

where U_{12} is the average flow velocity between points 1 and 2, $\Delta^n x = (x_2^n - x_1^n)$; $A = R^2 - b^2$; $B = bm$; $C = (1 + m^2)/3$; $m = (y_2 - y_1)/(x_2 - x_1)$; $b = y_1 - mx_1$.

Another factor that relates to step size is the interaction of molecules with the walls of the tubing. Because the random walk simulation is based on Cartesian coordinates, it is possible to take steps in the x and y directions which can put the molecule outside the radius of the tubing. If this happened in the original simulation of Betteridge et al. [16], the x and y coordinates of the molecule were left at their previous value and movement in the axial direction due to convection was taken to be half of the value it would have been if the molecule really had remained at the same xy coordinates. This seems like a reasonable approximation to the more logical approach of "bouncing" the molecule off the wall and is much less computationally demanding. Nevertheless, it is likely to affect the results as the step size becomes larger, as the region to which the approximation must be applied becomes more significant. We have attempted to determine the maximum permissible step size to obtain reliable results and also which of the two factors (mean velocity or wall interaction) is more critical in causing deviations as the step size becomes larger.

Several other modifications were also made to the simulations in order to examine their effect on peak shapes. One of these was variation of the usual laminar flow profile by changing the power term in Eqn. 1. The modified equation was,

$$U = U_{max}(1 - r^P/R^P) \qquad (3)$$

where P was varied between 1 and 4. It can be shown that, for the modified profile,

$$U_{max} = \frac{U_{avg}(P + 2)}{P} \qquad (4)$$

The effect of changing the symmetry of the flow profile was also investigated. Non-radially symmetric velocity profiles are known to arise when FIA tubes are coiled or otherwise deformed. To examine the role of this asymmetry with minimal computational burden, an approximation to Søberg's model [20, Fig. 3.9, p. 111] was used.

The equation applied was:

$$U = N[1 - e^{-k(1-r')}] \times [1 - (x')^2 - (y')^2 + 2a(1+y')] \quad (5)$$

where U is the flow velocity at x', y'; N is a constant obtained by numerical integration to provide the correct U_{avg}; k is an adjustable constant set to 10 in this work; r' is the reduced radial position of the molecule $= r/R$; x', y' are the reduced x and y coordinates of the molecule $= x/R$, y/R; a is an asymmetry factor between 0 and 1. The second term in square brackets is a quadratic function which gives a maximum flow velocity centered at $x' = 0$, $y' = a$ and a minimum value of zero (within the confines of the tube) at $x' = 0$, $y' = -1$. The first term in square brackets forces the flow velocity to zero at the walls of the tube.

Another change that was made for some studies was the introduction of infinite radial diffusion. This was done to examine the amount of dispersion in the limiting case. To simulate an infinite rate of radial mass transfer, increments in x and y were no longer used, but rather the xy position itself was totally randomized within the cylinder. This avoids the problem of collisions with the walls as the steps become larger.

EXPERIMENTAL

Apparatus

The apparatus used to obtain the experimental flow profiles in this work is shown in Fig. 1. A very simple arrangement consisting of a pump, injection valve, tubing, and detector was used. Two types of pumps were employed to examine possible differences in profiles due to pulsations: an eight-roller peristaltic pump (Ismatec model SA, Cole-Parmer, Chicago, IL) and a stepper motor driven syringe pump (Sage Instruments model 341A, Cambridge, MA). Both pumps were calibrated before each run. For sample injection, a manually operated six-port, two-way valve (Rheodyne model 5020, Cotati, CA) fitted with a polytetrafluoroethylene (PTFE) sample loop was employed. Other workers have used special injection methods to avoid the changes in flow dynamics introduced by valve fittings and sample loop coiling [21], but we wished to obtain experimental results from a more standard FIA system. The volume of the sample loop was precisely measured by mass difference to be 232 μl. It was later determined that, for the geometry used, minor changes in the plug volume had relatively little effect on the simulation.

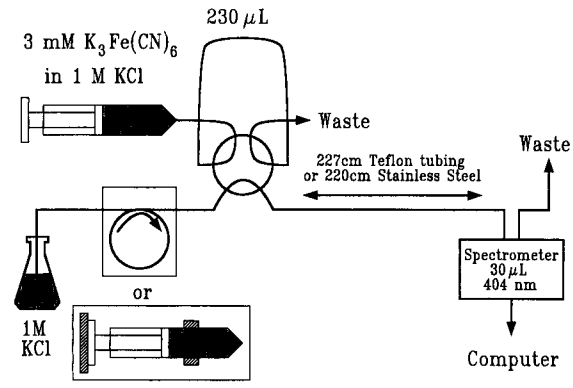

Fig. 1. Experimental apparatus for dispersion studies.

Both stainless steel (SS) (Supelco, Oakville, Ont.) and PTFE tubing (Chromatographic Specialties, Brockville, Ont.) were used in these experiments. Both were nominally 0.8 mm i.d. × 1.6 mm o.d., but internal diameters were more precisely measured as 0.801 mm (SS) and 0.875 mm (PTFE) by mass difference. In each case, the length of tubing was approximately 2 m and it was kept as straight as possible to avoid secondary flow which will increase radial mass transfer. Some bends at the injector and detector were unavoidable, but were kept to a minimum. Flanged fittings were used at the injector and detector for the PTFE tubing, while connection via short pieces of Tygon tubing was used for the stainless steel. The total length (exit of injector to entrance of detector) was 227.0 cm in the case of the PTFE and 219.4 cm in the case of the stainless steel.

The detector employed was a Hewlett-Packard 8452A diode array spectrophotometer (Hewlett-Packard, Palo Alto, CA) equipped with a 30-μl, 1-cm flow cell (Hellma, Jamaica, NY). Absorbance measurements at the wavelength of

maximum absorbance for the sample (404 nm) were acquired at 2-s intervals with an integration period of 1 s. These detector conditions introduce minimal broadening to the profiles obtained here. Because of the difficulties involved in thermostatting the long reactor, all measurements were made at room temperature. Although changes in temperature will affect dispersion [22], the variations observed in this work were not significant enough to affect comparisons with simulation results.

Reagents

All solutions were prepared in distilled water from materials of ACS reagent grade or better. The carrier used was 1 M KCl and all samples were 3 mM potassium hexacyanoferrate(III) in 1 M KCl. The diffusion coefficient for $K_3Fe(CN)_6$ under these conditions was taken as 7.6×10^{-6} cm^2 s^{-1} at 25°C [23].

Computational aspects

Simulations were run on a 16 MHz IBM PC/AT compatible computer (Tristar Computers, Tempe, AZ) with a math coprocessor. The random walk program was written in Turbo C + + (Borland Corp., Scott's Valley, CA). This allowed the use of linked lists for molecular coordinates and decreased computation time significantly by permitting molecules which had passed the detector to be eliminated from the simulation. Normally, the program displayed the detector response at 1-s intervals by counting the number of molecules which had z coordinates beyond the detector. In some cases, the axial and radial distributions at a fixed time were recorded by stopping the simulation. A single run typically contained 5000 molecules, but 10 to 200 repetitions (equivalent to 5×10^4 to 10^6 molecules) were normally averaged to obtain smooth profiles. The replicate runs with smaller arrays maximized computational efficiency and minimized the amount of data lost in the event of inadvertent program termination. A run with 5000 molecules and one step per second, with a simulated flow-rate of 1 ml/min and a tube length of 2 m, typically took about 5 min if no special calculations were added to the algorithm, an improvement of several orders of magnitude over the original work [16]. The program obtained variable simulation parameters from a data file, allowing the it to be run in batch mode overnight. Contour maps and three-dimensional displays were generated with the program SURFER (v 4.0, Golden Software, Golden, CO).

RESULTS AND DISCUSSION

Comparison of experimental and simulated profiles

Initial evaluation of the random walk simulation utilized experimental results from the flow injection system described above. Since this experimental apparatus exhibited non-idealities with respect to the model, deviations in the results were anticipated, but it was hoped that these would be minimal and might be accommodated by adjustments to the model to illustrate the versatility of the random walk approach. Results for the peristaltic pump for both the PTFE and stainless steel tubing are shown in Fig. 2. The experimental results appear as smooth curves while the simulated profiles (250 000 molecules) are somewhat jagged due to the stochastic nature of the simulation. For all of the results presented here, the simulated profiles have been normalized to the same area as the experimental profiles for comparison. Figure 2 shows that there is good general agreement between the experimental peak shapes and those obtained by the random walk simulation, although some discrepancies are apparent. Both types of tubing give similar results and the best agreement is obtained for the intermediate flow-rate. At the low flow-rate, the experimental dispersion is somewhat greater, while the opposite is true at the high flow-rate. The theoretically predicted double-peak at the high flow-rate is not observed experimentally, but this is not surprising since it has been previously shown that even a small amount of turbulence can eliminate this from experimental results [10]. Finally, the simulated profile typically starts earlier than the experimental peak in all cases.

It was thought that discrepancies between experimental and simulated results in Fig. 2 might arise from pump pulsations in the case of the

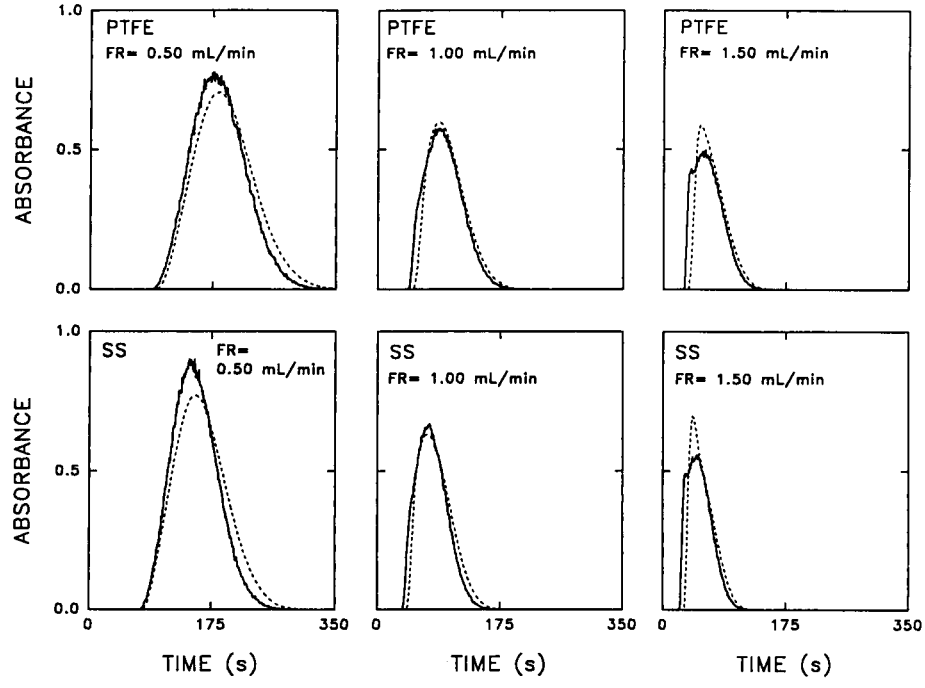

Fig. 2. Comparison of simulated and experimental dispersion profiles obtained with a peristaltic pump for PTFE and stainless steel (SS) tubing at different flow-rates (FR). Experimental results are represented by the dashed lines. See text for further details.

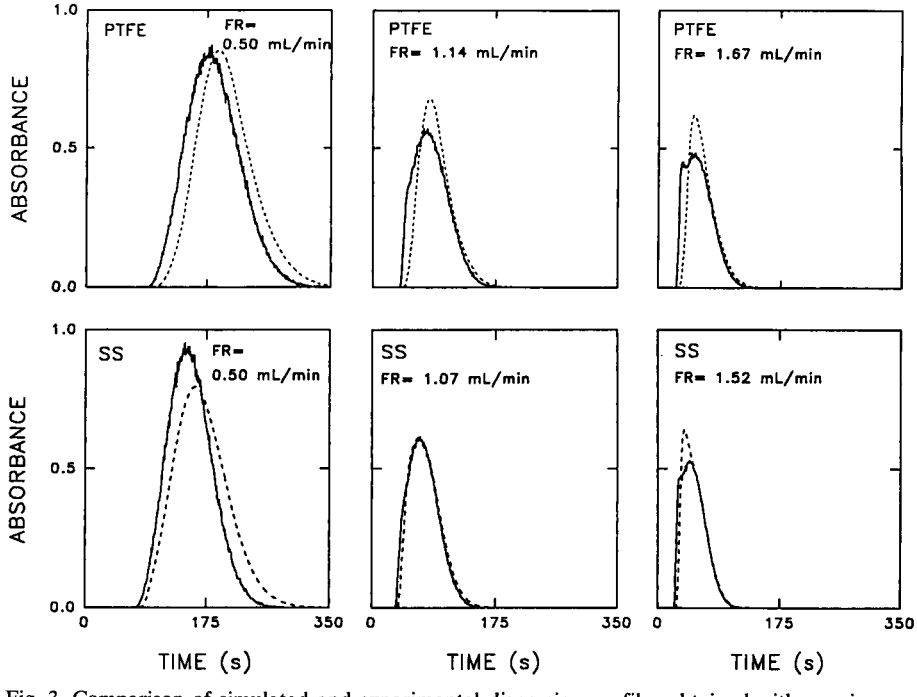

Fig. 3. Comparison of simulated and experimental dispersion profiles obtained with a syringe pump for PTFE and stainless steel (SS) tubing at different flow-rates. Experimental results are represented by the dashed lines. See text for further details.

peristaltic pump, so a syringe pump was also employed. The results in Fig. 3 show that larger deviations are generally observed with the syringe pump for both types of tubing. The time shifts are also more apparent, with simulation results leading the experimental results in all cases. The trends in dispersion are the same in this case as for the peristaltic pump. The reason for the greater discrepancies in this case are not clear, but could result from stepper motor pulsations for the syringe pump (about 170 pulses/min at 0.5 ml/min) which would cause a more turbulent flow, or a larger pressure surge on injection. The type of tubing seems to be more important in this case than for the peristaltic pump, indicating that factors such as elasticity or wettability may be important.

These results indicate a reasonably good qualitative agreement between experimental and simulated peak shapes, but suggest that some non-idealities in the experimental system may be responsible for discrepancies observed. The discrepancies are larger than what is expected on the basis of small variations in temperature or

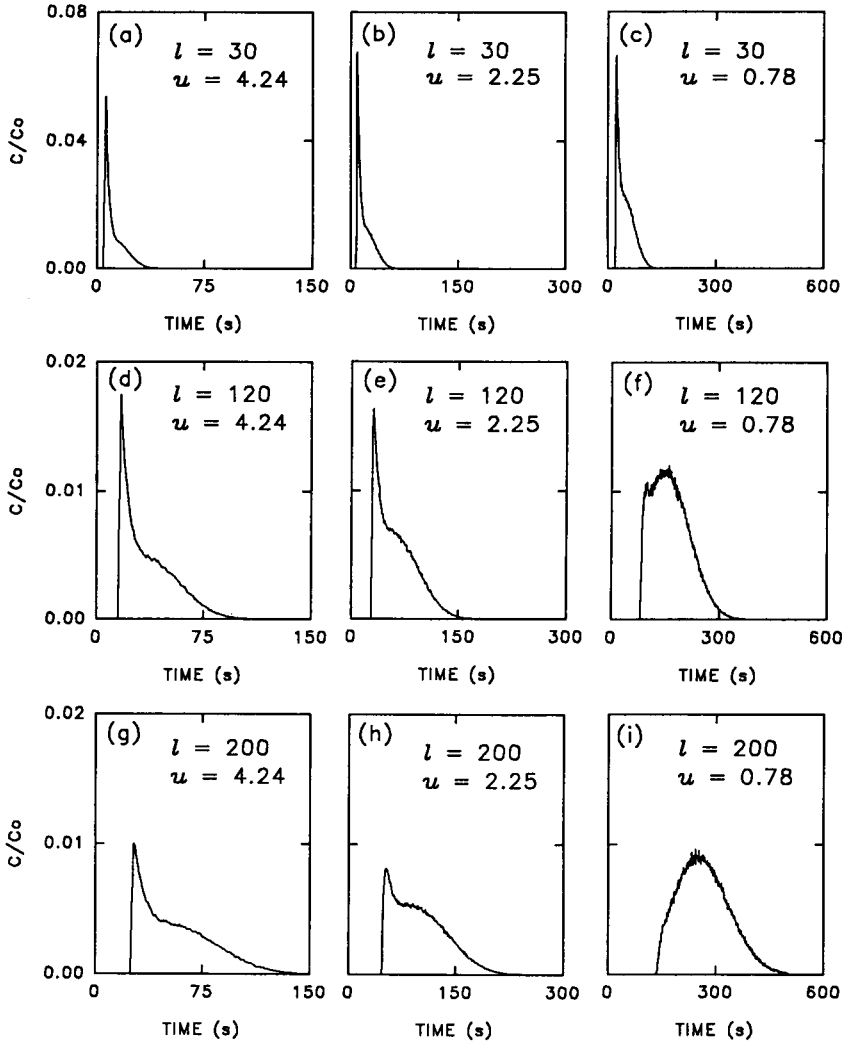

Fig. 4. Effects of simulated tube length (l, cm) and mean flow velocity (u, cm s^{-1}) on simulation results; for comparison with experimental results given in Ref. 6, Fig. 4. Other conditions given in text.

viscosity and it is believed that the assumption of a parabolic flow profile may not be valid for certain time periods (e.g. immediately following injection) or in certain regions of the tube (e.g. at connections). Valve switching on injection temporarily interrupts the flow and can result in a surge of pressure. Although this can be avoided by using stopped-flow or hydrodynamic injection techniques, these methods introduce new problems arising from the need to bring the flow rate from zero to its desired value. Connections were minimized, but non-idealities such as reduced or enlarged diameters through flanged unions may contribute to variations in the flow. Deviations from a linear geometry at the injector and detector will also contribute to secondary flow. These contributions could be minimized by employing valves or detectors of a different design, but these were not used in this work. It is expected that modified flow patterns near the injector will have the greatest effect, since they are amplified as the sample plug moves to the detector. In most cases, changes in the flow profile should increase radial mass transfer. This would be consistent with the delayed appearance times and reduced dispersion observed for the experimental peaks. The discrepancies observed in these studies are consistent with results obtained by Wada et al. [13] who used an alternative method to generate the theoretical curves.

To provide further evidence that the random walk model provides results consistent with experimental profiles under a variety of conditions, experimental results obtained by other authors were considered. One fairly extensive study was carried out by Korenaga et al. [6] under carefully controlled conditions. These authors examined the effect of flow velocity, tube length, tube diameter and diffusion coefficient on sample dispersion in straight tubes. We have used the conditions employed in the flow velocity/tube length study ($D = 3.8 \times 10^{-6}$ cm^2 s^{-1}, i.d. = 1 mm, sample volume = 10 μl) (see Ref. 6, Fig. 4) to generate corresponding profiles from the simulation. These results are presented in Fig. 4 with the same format as the original reference for easy comparison. Very good agreement was obtained between experimental peak shapes given in the reference and the simulation results presented here, although some of the experimental peaks are substantially broader. Also, the values of the concentration ratio, C/C_0, were more than an order of magnitude lower for the simulation results. Closer scrutiny of the experimental results through area calculations indicates that the values reported by Korenaga et al. are in error by a scaling factor which would place the magnitude of their measurements in agreement with ours. The effects of tube diameter and diffusion coefficient (see Ref. 6, Figs. 5 and 6) were also examined with the random walk simulation and are shown in Figs. 5 and 6, respectively. For Fig. 5, conditions used were as in Fig. 4 but with $l = 120$ cm, flow velocity = 2.3 cm s^{-1}, and tube diameters as given in the figure. Again, there is good qualitative agreement between the simulation

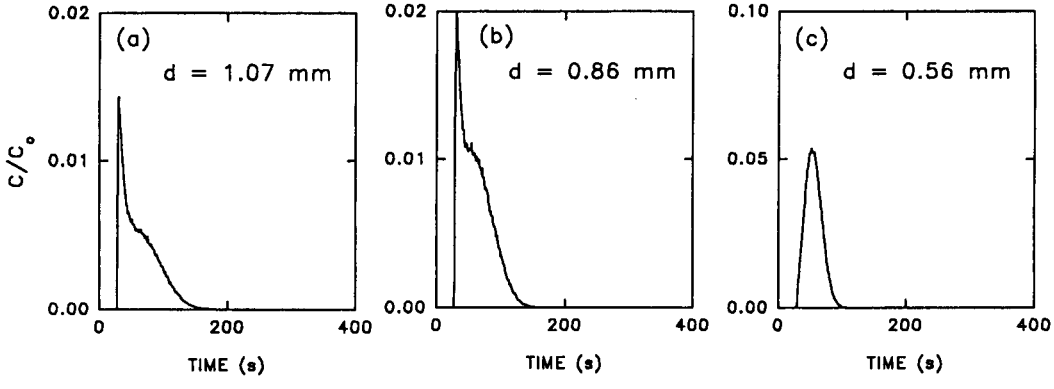

Fig. 5. Effect of simulated tube diameter (d) on simulation results; for comparison with Ref. 6, Fig. 5.

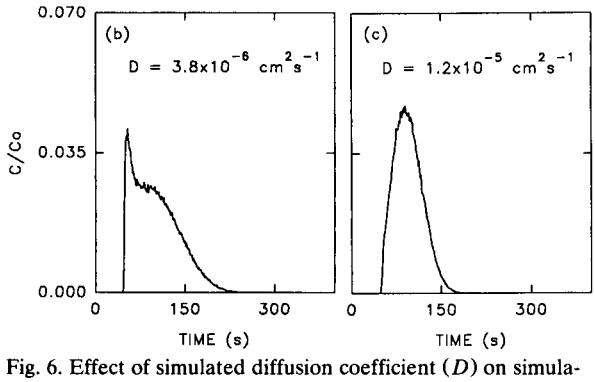

Fig. 6. Effect of simulated diffusion coefficient (D) on simulation results. For comparison with Ref. 6, Fig. 6.

peak shapes and the experimental profiles given in Ref. 6, but the experimental peaks are generally broader. For Fig. 6, only two sets of results are reported rather than the three in the original reference, as no diffusion coefficient was estimated for the sub-micron pigment ink used by the authors. Conditions used here were: sample volume = 10 μl, $l = 40$ cm, $d = 1$ mm, and flow velocity = 0.45 cm s^{-1} (diffusion coefficients given in the figure). Agreement with experimental results is not as good for the smaller diffusion coefficient, but double peaks are indicated for both experimental and simulated results. It is likely that the short tube length contributes to disagreement in this case, since this will enhance errors arising from non-ideal connections.

Comparison with other theoretical results

Previous studies have demonstrated good agreement between experimental FIA profiles and theoretical results obtained through numerical solution of the convection–diffusion equation. It was therefore of interest to determine whether the discrepancies observed for the random walk approach were due experimental limitations or fundamental differences with the convection-diffusion model. To this end, profiles obtained with the random walk model were compared with those reported by Wada et al. [13] and Vanderslice et al. [10]. Figure 7 shows results for comparison with the former (see Ref. 13, Fig. 4b). The random walk simulations employed 250 000 molecules with the following conditions: $D = 5.4 \times 10^{-6}$ cm^2 s^{-1}, i.d. = 0.50 mm, tube length (not including sample loop) = 50 cm. The sample plug lengths and flow rates are given in the figure. As before, results are presented in the same format as the original reference with the reduced time, t^*, plotted on the abscissa ($t^* = tU_{max}/L$ where t is the time, U_{max} is the maximum flow velocity, and L is the initial length of the sample plug). Comparison of Fig. 7 with the original reference produces excellent agreement in peak shape and height under all conditions. Further comparisons were made with Vanderslice et al. [10] under different conditions. The results of the random walk simulation (10^6 molecules) are shown in Fig. 8 and correspond to Figs. 8 and 9 of Ref. 10. Note that in this case the reduced time and reduced distance are given by the more usual definitions $\tau = Dt/a^2$ and $X = Dx/a^2U_{max}$, respectively. Conditions used for the simulation are given in the figure caption. Once again excellent agreement was obtained between the random walk model and solution of convection–diffusion equation, including details of the predicted "double-hump" (profiles with double maxima are predicted to occur under certain conditions, but are rarely observed in practice for dispersion only because of experimental limitations). This indicates that the two methods are consistent with

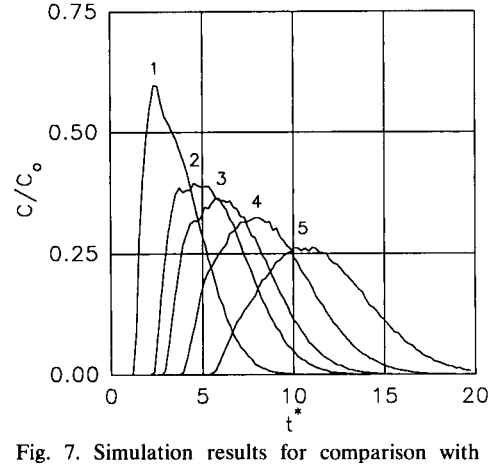

Fig. 7. Simulation results for comparison with theoretical results in Ref. 13, Fig. 4b. Values of sample plug lengths (cm) and flow-rates (ml min^{-1}): (1) 50, 0.58; (2) 100, 0.29; (3) 125, 0.23; (4) 165, 0.17; (5) 250, 0.12. Other conditions given in text.

one another and suggest that equally valid results can be obtained by alternative routes.

As an alternative to the usual comparison of peak profiles, it was decided that a direct examination of bolus shapes would be useful. This was accomplished by stopping the simulation after a predetermined solute residence time and counting molecules in defined volume elements. For this purpose, the tube was divided into 20 concentric radial elements of equal width and 20 axial elements of equal length. Concentrations were calculated as a function of radial and axial position and contour maps were generated using the program SURFER. To ensure an accurate representation, 10^6 molecules were used for each set of results. The results are shown in Fig. 9 for different values of the reduced time and are intended to be compared to Figs. 4 and 5 of Vanderslice et al. [12]. Note that the scale for $\tau = 0.01$ is expanded by a factor of 10 as in the reference. The bolus shapes produced by the simulation are in very good agreement with those obtained in reference 12 except that there appears to be a considerably larger concentration near the walls of the tube. This discrepancy is curious since the peak shapes obtained in Fig. 8 are in excellent agreement with earlier work by the same authors [10]. The bolus shapes obtained here more closely resemble those provided by Wada et al. [13], but a direct comparison has not been made to those results since reaction kinetics were also considered by the authors.

Effect of step size and wall approximations

As already noted, the effect of the mean molecular step size ($\Delta l = (2D\Delta t)^{1/2}$) is expected to influence the validity of the original algorithm used by Betteridge et al. [16] because of errors in the calculation of the mean velocity of a molecule in traversing two points and because of approximations made at the walls of the tube. The mean step size can be decreased by reducing the time interval between iterations, Δt. This was accomplished in the present work by specifying the number of iterations per second, n, such that $\Delta t = 1/n$. Increasing n improves the validity of the simulation, but also increases computation time proportionately, so it was of interest to determine the maximum permissible mean step size for consistent results. To this end, simulations were run under the conditions used for the PTFE tubing at 1 ml/min, but with $D = 1 \times 10^{-4}$ cm^2 s^{-1} to make the step size artificially large. The results for 50 000 molecules are shown in Fig. 10 for $n = 1$, 5, 10, and 100. The percentage of steps encountering the walls ranged from 31% when $n = 1$ to 3% when $n = 100$. The figure shows that the results asymptotically approach the limiting profile as n becomes larger. From these results, it appears that reasonably good

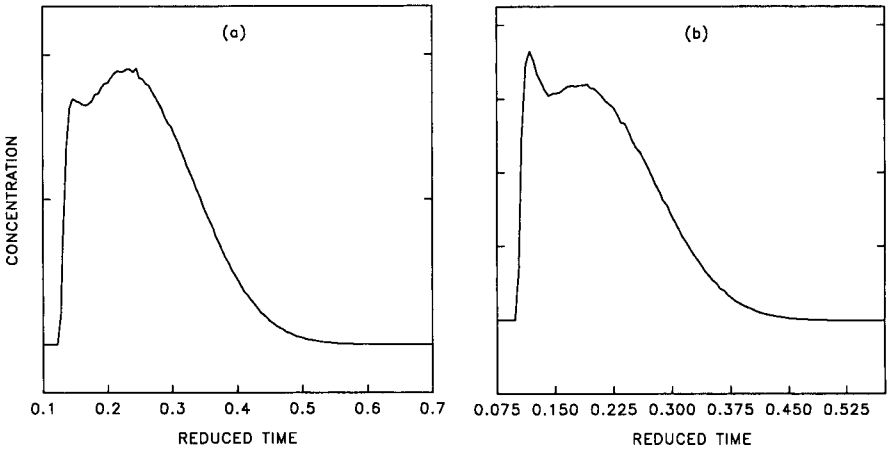

Fig. 8. Simulation results for comparison with Ref. 10, Figs. 8 and 9. Conditions used: (a) sample volume = 2 μl, i.d. = 0.23 mm, $D = 2.48 \times 10^{-6}$ cm^2 s^{-1}, $l = 30$ cm, flow-rate = 0.0615 ml min^{-1}; (b) same, except flow-rate = 0.0771 ml min^{-1}.

approximations of the true simulated profile require the mean step size to be no more than about 5 to 10% of the tube radius.

Since two factors (mean velocity and wall interactions) can affect the validity of the simulation, we wished to determine which had the greater effect. Compensating calculations to determine the true mean velocity and to allow molecules to "bounce" off of the wall were added to different versions of the program. In actual fact, it was computationally simpler to reflect the molecule backwards along its original trajectory than truly bounce it off of the wall. This is mathematically equivalent, since it leaves the molecule at the same radial position, and produces results identical to those that would be obtained if the true trajectory were used. Results in Fig. 11 show the profiles obtained with $n = 1$ for the same conditions as in Fig. 10, but with various combinations of compensating factors. It was observed

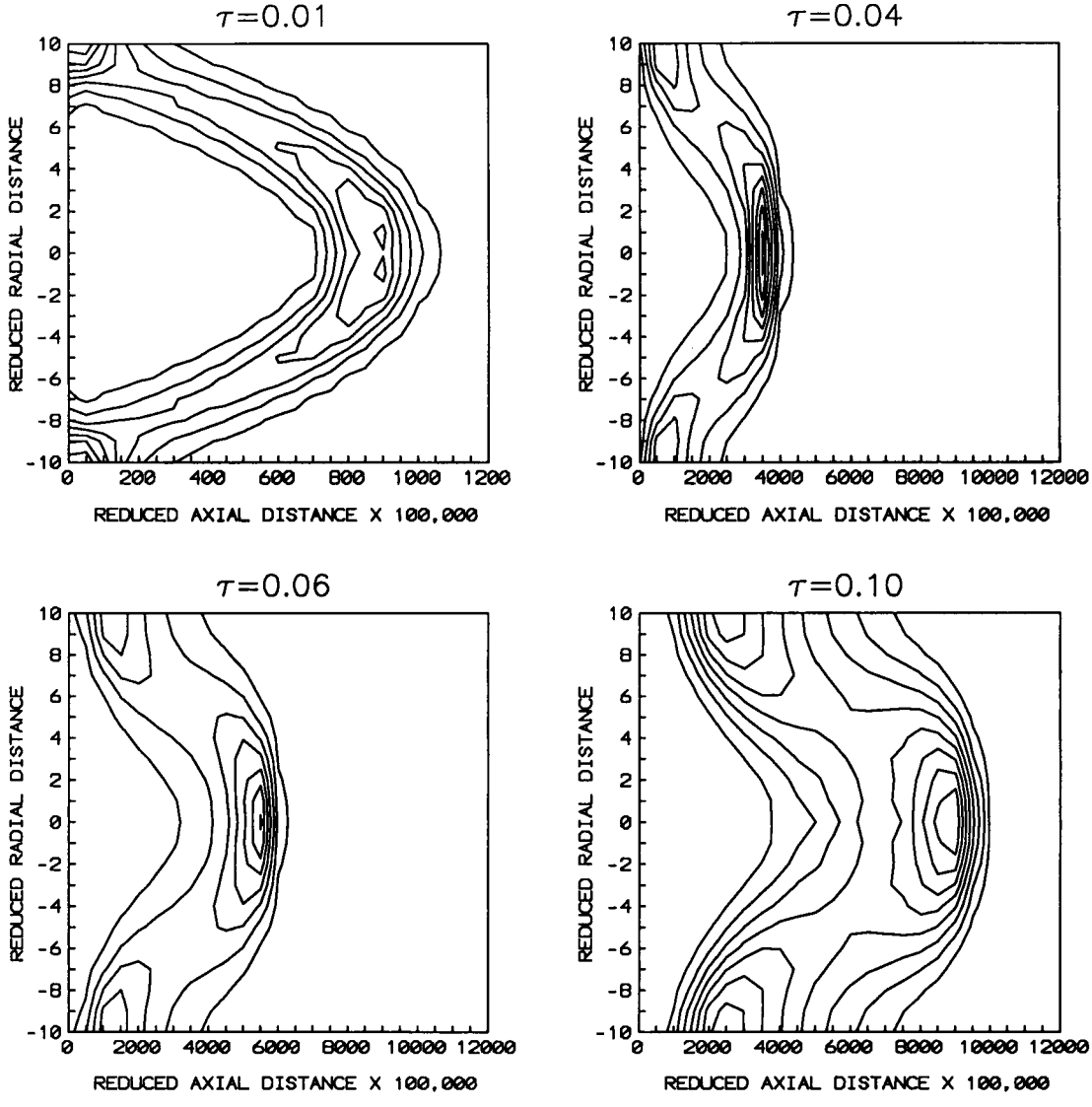

Fig. 9. Contour maps showing bolus shapes as a function of reduced time (τ), reduced radial position, and reduced axial position. For comparison with Figs. 4 and 5 of Ref. 12.

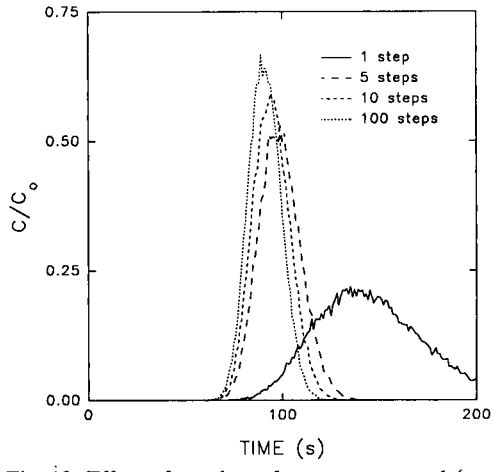

Fig. 10. Effect of number of steps per second (step size) on simulation results. An artificially large diffusion constant ($D = 1 \times 10^{-4}$ cm^2 s^{-1}) was simulated to generate these results. See text for other conditions.

that approximations made at the wall had the largest effect when the step size was very large. However, the mean velocity calculation plays a very important role as the peak shape begins to approach its limiting value. The inclusion of both compensating calculations produced results very similar to those obtained when the step size was very small.

The inclusion of corrections for the mean velocity and wall interactions may or may not be more computationally efficient than decreasing the step size, since the calculations are quite involved. In practice, decreasing the step size tends to be more straightforward when adding modifications to the algorithm such as asymmetric flow profiles, since these make the corrections more difficult. It should be noted that, for the other simulations presented here, the step size was kept small enough to ensure valid results from the simulation.

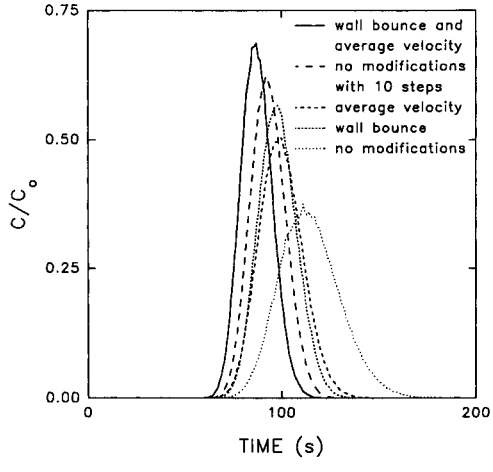

Fig. 11. Effect of wall and mean velocity approximations on simulation results. Conditions were as in Fig. 10.

Effect of flow velocity profile

One of the advantages of the random walk approach is that it is readily adapted to modifications in flow characteristics and other experimental parameters. Since even straight tubing can give rise to flow profiles that are not precisely laminar, the random walk simulation was used to evaluate the contribution that this might have to the peak shapes obtained. The first study investigated modifications to the exponent, P, in the normal laminar flow case as discussed in an earlier section. Conditions used were those for the PTFE tubing and the results for a flow-rate of 1 ml/min are shown in Fig. 12. The radial velocity profile appears as an inset. It was found that there was virtually no change in the peak position under these conditions, but dispersion was substantially affected. In all cases, the leading edge of the peak moved to slightly longer times and

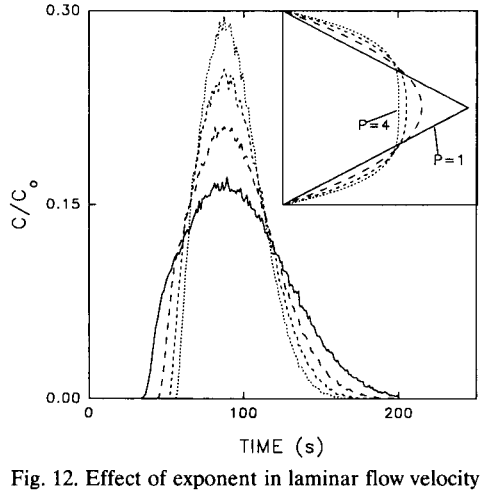

Fig. 12. Effect of exponent in laminar flow velocity profile (P) on peak shape. Velocity profiles are inset. Conditions given in text.

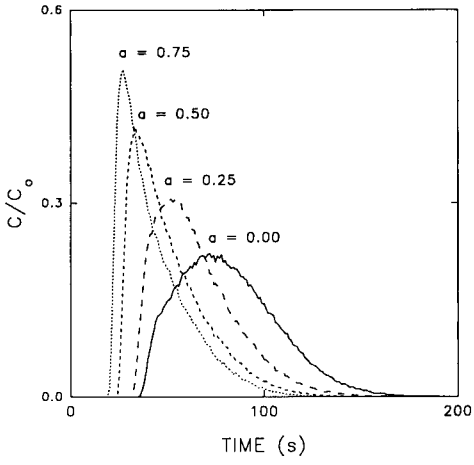

Fig. 13. Effect of flow symmetry on peak shape. Asymmetry factors (a) are given next to the corresponding peak.

became steeper as P was increased, and the peaks became narrower. In the case of the 1.5 ml/min flow-rate (not shown), the spike on the leading edge of the profile became more prominent with increasing P. It is also interesting to note the presence of an isoresponse point on the trailing edges of the peaks. In some instances, agreement between theoretical and experimental results could be improved by adjusting P, suggesting that the nature of the flow profile may change with experimental conditions. Other factors will also affect this agreement, however.

The effect of the symmetry of the flow was also investigated with a view towards possibly explaining reduced dispersion in coiled tubes. Equation 5 was used to generate laminar-type profiles with an asymmetric distribution. Results are shown in Fig. 13 for PTFE tubing conditions (1 ml/min) and asymmetry factors of 0 (normal laminar flow), 0.25, 0.5 and 0.75. The addition of the asymmetric flow did not sufficiently explain the effects of coiling. Although dispersion did decrease with increases in the asymmetry factor, changes in peak shape and position are not consistent with experimental observations for coiled tubing. More detailed studies are being carried out to try to more accurately model coiled geometries.

Effect of diffusion coefficient

Figure 14 shows the effect of varying the diffusion coefficient over a limited range on the simulation results. The conditions used were those for the PTFE tubing at 1 ml/min. The diffusion coefficient was multiplied by factors ranging from 0.6 to 1.4 and the simulation included 250000 molecules. As expected, an increase in the diffusion coefficient leads to sharper peaks due to increased radial mass transfer. It is also interesting to note what appears to be an isoresponse point on the tail of the peaks. This behaviour is consistent with changes in peak shape that have been observed by other workers [20, p. 136].

The random walk algorithm can also be used to investigate limiting dispersion for a given set of conditions. Because it is a discrete simulation, the radial component of diffusion can be separated from the axial component. The case of infinite radial diffusion can be achieved by making the x and y coordinates of each molecule completely random (within the confines of the tube) at each step. This should give the smallest dispersion possible for the flow conditions imposed. Figure 15 compares normal and infinite radial diffusion results for the stainless steel experimental conditions at 1 ml/min. The tall peak defines the limit to which dispersion can be reduced by coiling,

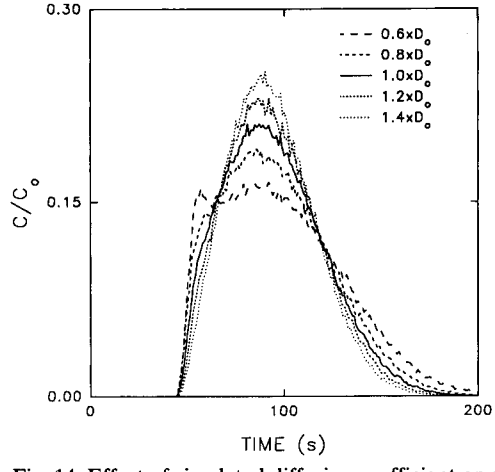

Fig. 14. Effect of simulated diffusion coefficient on simulation results. Factors by which the nominal diffusion coefficient (7.6×10^{-6} cm^2 s^{-1}) is multiplied are given next to the corresponding curve.

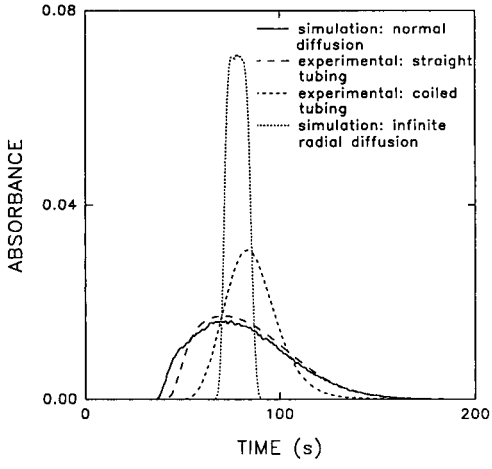

Fig. 15. Effect of infinite radial diffusion on peak shape. Comparisons are made with other experimental and simulated results. See text for conditions.

knitting or other means. The next highest peak is the experimentally observed profile when the tubing is coiled to a diameter of about 2 cm. The final two curves show simulated and experimental results when uncoiled tubing is used. It is apparent that the reduction in dispersion obtained by coiling is not at the theoretical limit, although further reduction may be limited in practice. It is unlikely that other models could be used to make this type of prediction. Further work needs to be done to determine how the random walk model may be adapted to the case of coiled tubing.

Conclusions

From the results presented here, it is evident that the random walk model can be used as effectively as other approaches for modeling peak shapes in FIA. It has been shown that modifications to flow parameters can be easily incorporated to test physical models. Agreement with experimental flow profiles is reasonably good. Differences probably arise from invalid assumptions regarding the true flow characteristics which will be affected by factors related to injection, connections, pump pulsations, tube wettability, and so on. Further work with the random walk algorithm may permit a better understanding of how these non-ideal conditions affect the flow dynamics.

The authors gratefully acknowledge helpful comments by A.P. Wade and suggestions and equipment contributed by R.D. Guy.

REFERENCES

1 H. Bergamin F°, E.A.G. Zagatto, F.J. Krug and B.F. Reis, Anal. Chim. Acta, 101 (1978) 17.
2 J. Mindegaard, Anal. Chim. Acta, 104 (1979) 185.
3 A. Rios, M.D. Luque de Castro and M. Valcarcel, Anal. Chem., 60 (1988) 1540.
4 T. Gubeli, G.D. Christian and J. Ruzicka, Anal. Chem., 63 (1991) 2407.
5 C.C. Painton and H.A. Mottola, Anal. Chim. Acta, 154 (1983) 1.
6 T. Korenaga, F.-H. Shen, H. Yoshida, T. Takahashi and K.K. Stewart, Anal. Chim. Acta, 214 (1988) 97.
7 S.R. Sumpter and M.L. Lee, J. Microcolloid. Sep., 3 (1991) 91.
8 R.D. Hull, R.E. Malick and J.G. Dorsey, Anal. Chim. Acta, 267 (1992) 1.
9 E.A.G. Zagatto, B.F. Reis and H. Bergamin F°, Anal. Chim. Acta, 226 (1989) 129.
10 J.T. Vanderslice, K.K. Stewart, A.G. Rosenfeld and D.J. Higgs, Talanta 28 (1981) 11.
11 C.C. Painton and H.A. Mottola, Anal. Chim. Acta, 158 (1984) 67.
12 J.T. Vanderslice, A.G. Rosenfeld and G.R. Beecher, Anal. Chim. Acta, 179 (1986) 119.
13 H. Wada, S. Hiraoka, A. Yuchi and G. Nakagawa, Anal. Chim. Acta, 179 (1986) 181.
14 J. Ruzicka and E.H. Hansen, Anal. Chim. Acta, 99 (1978) 37.
15 J.M. Hungerford and G.D. Christian, Anal. Chim. Acta, 200 (1987) 1.
16 D. Betteridge, C.Z. Marczewski and A.P. Wade, Anal. Chim. Acta, 165 (1984) 227.
17 C.D. Crowe, H.W. Levin, D. Betteridge and A.P. Wade, Anal. Chim. Acta, 194 (1987) 49.
18 A. Einstein, Ann. Phys., 17 (1905) 549.
19 A.G. Marshall, Biophysical Chemistry, Wiley, New York, 1978.
20 J. Ruzicka and E.H. Hansen, Flow Injection Analysis, 2nd edn., Wiley, New York, 1988.
21 S.D. Kolev and E. Pungor, Anal. Chem., 60 (1988) 1700.
22 C.L.M. Stults, A.P. Wade and S.R. Crouch, Anal. Chim. Acta, 192 (1987) 301.
23 M. von Stackelberg, M. Pilgram and V. Toome, Z. Elektrochem., 57 (1953) 342.

Analytica Chimica Acta, 278 (1993) 307–316
Elsevier Science Publishers B.V., Amsterdam

Mathematical model of flow-injection analysis. First-order chemical reaction in a straight tube

V.P. Andreev and M.I. Khidekel

Institute for Analytical Instrumentation, Russian Academy of Sciences, 26 pr. Ogorodnikova, St. Petersburg 198103 (Russian Federation)

(Received 27th October 1992)

Abstract

A mathematical model of flow-injection analysis (FIA) is developed for a pseudo-first-order chemical reaction in a straight reaction tube. Analytical expressions are derived for the first three moments of the peaks of the sample and product of the chemical reaction. A comparison with the available numerical analysis and experimental results is given. The application of the model to FIA optimization is described.

Keywords: Flow injection; Mathematical model

The flow-injection analysis (FIA) technique, introduced in 1974 [1,2], has various advantages that led to a rapid growth in its popularity [3,4]. Although this technique continues to develop rapidly, most of the publications concern the experimental and methodological aspects of FIA. Theoretical work relating to FIA, including classical papers [5,6], has been reviewed [4,7,8]. Most of the papers on the mathematical model of FIA are based on calculations of substance propagation along the reaction tube. The tube is usually assumed to be straight but the results obtained are further extended also to coiled reaction tubes.

In the largest group of studies devoted to the reaction tube process modelling, the problem is solved numerically [9–16]. The effect of chemical reaction on the characteristics of the FIA system was accounted for in [12–14,16]. The sample peak shape dependence for the pseudo-first-order reaction was investigated in [12], but the peak shape of the product of the chemical reaction was not discussed. Second-order chemical reactions were modelled in [13,14] using numerical methods (random walk model in [13] and finite-difference technique in [14]). The chemical reactions considered in [13,14] are frontal, which means that the sample and reagent are not preliminary mixed. In [16] the random walk model is used to describe the situation when sample and reagent enter into a reaction tube after passing a T-shaped mixer.

There are also studies [17–19] in which a semi-empirical approach was chosen. In particular such questions as the effects of coiled tube shape, injector and detector on the peak dispersion were discussed.

Semi-empirical studies include those in [8,20, 21], where the convective diffusion equations were reduced to the one-dimensional form and the effect of non-uniformity of the longitudinal flow profile was accounted for by introducing axial

Correspondence to: V.P. Andreev, Institute for Analytical Instrumentation, Russian Academy of Sciences, 26 pr. Ogorodnikova, St. Petersburg 198103 (Russian Federation).

dispersion coefficients whose values were mostly determined from experiments [8].

The purpose of this work was to deduce analytical expressions for the parameters of the sample and chemical reaction product concentration distribution in a straight reaction tube, which will allow one to analyse the dependence of the sample and product peak shapes on their diffusion coefficients, chemical reaction rate constant, tube dimensions and modes of FIA.

SET OF EQUATIONS AND THEIR SOLUTION

Consider a straight circular channel with an inside bore diameter $2a$. A reagent solution flows along the channel and the flow is assumed to be laminar and in a steady-state (the Poisseuille velocity profile). At a certain moment ($t = 0$) the sample is injected, and the sample concentration (C_1) is assumed to be low. The samples moves downstream, concurrently entering into reaction with the reagent, resulting in the formation of a chemical reaction product (C_2). It is assumed that sample and reagent are ab initio mixed and the reagent concentration is always much higher than that of the sample. Therefore, the chemical reaction can be considered to be first order. The reaction rate is denoted by k and the direct reaction (product formation) rate is assumed to be much greater than that of the reverse reaction (product dissociation) and, as in practice FIA is characterized by relatively short residence times, the reverse reaction will not be considered at all.

The problem is assumed to be a symmetric one with respect to the x-axis (the system of coordinates is shown in Fig. 1). The convective diffusion equations for the sample ($i = 1$) and reaction product ($i = 2$) will be

$$\frac{\partial C_i}{\partial t} + U_{\max}\left(1 - \frac{r^2}{a^2}\right)\frac{\partial C_i}{\partial x} = D_i\left[\frac{1}{r}\cdot\frac{\partial}{\partial r}\left(r\cdot\frac{\partial C_i}{\partial r}\right) + \frac{\partial^2 C_i}{\partial x^2}\right] + (-1)^i k C_1 \quad (1)$$

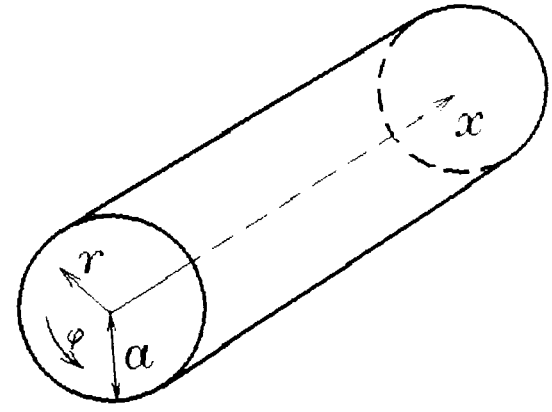

Fig. 1. FIA channel and coordinate system.

The convective diffusion equation should be supplemented with the boundary and initial conditions:

$$\partial C_i/\partial r = 0 \quad \text{at } r = a \quad (2)$$

$$C_i < \infty \quad \text{at } r = 0 \quad (3)$$

$$\partial^p C_i/\partial x^p = 0 \quad \text{at } x = \pm\infty,\ p = 0, 1, 2, \ldots \quad (4)$$

$$C_i(0, x, r) = \delta_{1,i} C_0 f(x, r) \quad (5)$$

where

$$\delta_{i,j} = \begin{cases} 0, & \text{if } i \neq j \\ 1, & \text{if } i = j \end{cases}$$

is the Kroneker delta.

We shall not seek the concentration distribution itself, but rather the distribution parameters: the amount of sample and product, centre of mass coordinate and dispersion of concentration C_i distribution. Note that these parameters are essential for FIA system optimization. The above characteristics can be found by solving the Eqns. 1–5 using the method of moments [22]. To do this we introduce the following functions:

$$\mu_{n,i}(r, t) = \int_{-\infty}^{\infty} x^n C_i(x, r, t)\, \mathrm{d}x \quad n = 0, 1, 2, \ldots \quad (6)$$

The first three moments ($n = 0, 1, 2$) have the following physical meaning: the zeroth moment ($\mu_{0,i}$) is the amount of substance (sample or product depending on the i value), the first normalized moment (centre of gravity; $\eta_i = \mu_{1,i}/\mu_{0,i}$) is the coordinate of the centre of mass of the

distribution and the second normalized central moment (variance; $\sigma^2 = \mu_{2,i}/\mu_{0,i} - \eta_i^2$) is the dispersion of the distribution.

After integration of Eqn. 1 with weight x^n and considering Eqn. 4, we obtain the following equation for moments:

$$\frac{\partial \mu_{n,i}}{\partial t} - D_i \cdot \frac{1}{r} \cdot \frac{\partial}{\partial r}\left(r \cdot \frac{\partial \mu_{n,i}}{\partial r}\right) = nU_{\max}\left(1 - \frac{r^2}{a^2}\right)\mu_{n-1,i} + n(n-1)D_i\mu_{n-2,i} + (-1)^i k\mu_{n,1} \quad (7)$$

Similarly, we can transform the boundary and initial conditions:

$$\partial \mu_{n,i}/\partial r = 0 \quad \text{at } r = a \quad (8)$$

$$\mu_{n,i} < \infty \quad \text{at } r = 0 \quad (9)$$

$$\mu_{n,i}(0, r) = \delta_{1,i} g_n(r) = \delta_{1,i} C_0 \int_{-\infty}^{\infty} x^n f(x, r)\, dx \quad (10)$$

Most FIA devices perform detection in an integral way over the entire channel cross-section. Therefore, in general we are interested in the average moments:

$$\bar{\mu}_{n,i}(t) = \frac{1}{\pi a^2}\int_0^{2\pi}\int_0^a r\mu_{n,i}(r, t)\, d\phi\, dr = \frac{2}{a^2}\int_0^a r\mu_{n,i}(r, t)\, dr \quad (11)$$

Integrating Eqn. 7 with the weight r over the channel cross-section and using conditions 8 and 9, one derives the equations for the average moments:

$$\frac{d\bar{\mu}_{n,i}}{dt} = n \cdot \frac{2U_{\max}}{a^2}\int_0^a r\left(1 - \frac{r^2}{a^2}\right)\mu_{n-1,i}\, dr + n(n-1)D_i\bar{\mu}_{n-2,i} + (-1)^i k\bar{\mu}_{n,1} \quad (12)$$

The initial condition for $\bar{\mu}_{n,i}$ will be

$$\bar{\mu}_{n,i}(0) = \delta_{1,i} q_n = \delta_{1,i} \cdot \frac{2C_0}{a^2}\int_0^a r g_n(r)\, dr = \text{constant} \quad (13)$$

Equation 12 contains an unaveraged moment $\mu_{n-1,i}$ and therefore it can be applied only for the determination of the last of the moments under consideration. All the preceding moments should be found from Eqns. 7–10, and the moments for the sample $\mu_{n,1}$ must be found first and then used to evaluate the moments $\mu_{n,2}$ of the chemical reaction product distribution.

Equation 7 for the zeroth moment of sample distribution ($n = 0$, $i = 1$) can be solved by the method of separation of variables, which gives the following expressions for the eigenvalues $\lambda_{k,1}^2$ and eigenfunctions $R_k(r)$:

$$\lambda_{k,1}^2 = (1 - \delta_{0,k})D_1\gamma_k^2/a^2 \quad k = 0, 1, 2, \ldots \quad (14)$$

$$R_k(r) = \delta_{0,k} + (1 - \delta_{0,k})J_0(\gamma_k r/a) \quad k = 0, 1, 2, \ldots \quad (15)$$

where γ_k are positive roots of the equation $J_1(z) = 0$ and J_0 and J_1 are the zeroth- and first-order Bessel functions, respectively.

The solution of Eqns. 7–9 for $n = 0$ and $i = 1$ will be

$$\mu_{0,1}(r, t) = \left[A_0 + \sum_{k=1}^{\infty} A_k J_0(\gamma_k r/a)\exp\left(-\lambda_{k,1}^2 t\right)\right] \times \exp(-kt) \quad (16)$$

The coefficients A_k ($k = 0, 1, 2, \ldots$) are chosen so that the initial condition 10 is met:

$$A_0 = C_0\int_0^a r g_0(r)\, dr/\| R_0 \|^2 \quad (17)$$

$$A_k = C_0\int_0^a r J_0(\gamma_k r/a) g_0(r)\, dr/\| R_k \|^2 \quad k = 1, 2, 3, \ldots \quad (18)$$

The norm of the eigenfunctions introduced above is defined as

$$\| R_k \|^2 = \delta_{0,k}a^2/2 + (1 - \delta_{0,k})a^2 J_0^2(\gamma_k)/2 \quad k = 0, 1, 2, \ldots \quad (19)$$

Note that if the initial distribution does not depend on the coordinate r ($g_0 =$ constant), $A_k = 0$ for $k = 1, 2, 3, \ldots$.

Because of the eigenfunction $R_k(r)$ orthogonality, the average zeroth moment of the sample distribution will always be

$$\bar{\mu}_{0,1}(t) = A_0 \exp(-kt) \tag{20}$$

From Eqn. 7 it follows that the equations for all the sample distribution moments, excluding the zeroth one, and for all the reaction product distribution moments will be inhomogeneous. They are solved by expansion in a series of the corresponding homogeneous problem eigenfunctions. Note that these eigenfunctions for the sample and the product are the same and are given in Eqn. 15, the eigenvalues for the sample distribution moments are defined in Eqn. 14 and those for the reaction product are expressed as

$$\lambda_{k,2}^2 = (1 - \delta_{0,k}) D_2 \gamma_k^2 / a^2 \quad k = 0, 1, 2, \ldots \tag{21}$$

The general form of the solution of Eqn. 7 for moments $\mu_{n,i}$ when $n + i > 1$ will be

$$\mu_{n,i}(r, t) = M_{0,n,i}(t) + \sum_{m=1}^{\infty} M_{m,n,i}(t) J_0(\gamma_m r/a) \tag{22}$$

The function $M_{m,n,i}$ is defined from the equation

$$\frac{dM_{m,n,i}}{dt} + \lambda_{m,i}^2 M_{m,n,i} = H_{m,n,i} \quad m = 0, 1, 2, \ldots \tag{23}$$

where

$$H_{m,n,i}(t) = \frac{1}{\| R_m \|^2} \left\{ n U_{\max} \int_0^a r(1 - r^2/a^2) \times R_m(r) \mu_{n-1,i}(r, t)\, dr + n(n-1) D_i \int_0^a r R_m(r) \mu_{m-2,i}(r, t)\, dr + (-1)^i k \int_0^a r R_m(r) \mu_{n,1}(r, t)\, dr \right\}$$

The initial condition for $M_{m,n,i}$ is expressed as

$$M_{m,n,i}(0) = B_{m,n,i} = \delta_{1,i} \frac{C_0}{\| R_m \|^2} \int_0^a r R_m(r) g_n(r)\, dr = \text{constant} \tag{24}$$

The solution of Eqn. 23 with the condition 24 will be

$$M_{m,n,i}(t) = \exp(-\lambda_{m,i}^2 t) \left[B_{m,n,i} + \int_0^t H_{m,n,i}(\tau) \times \exp(\lambda_{m,i}^2 \tau)\, d\tau \right] \tag{25}$$

Note that

$$\bar{\mu}_{n,i}(t) = M_{0,n,i}(t) \tag{26}$$

The details of the solution and expressions for $\mu_{0,i}$, η_i and σ_i^2 in the general case of the arbitrary initial sample distribution are given in [23]. Here the expressions for the characteristics listed in the specific case of the initial distribution in the form of the delta function are given:

$$f(x, r) = \delta(x) \tag{27}$$

For this form of the initial distribution one has

$$\bar{\mu}_{0,1}(t) = C_0 \exp(-kt) \tag{28}$$

$$\bar{\mu}_{0,2}(t) = C_0 [1 - \exp(-kt)] \tag{29}$$

The amount of sample $\bar{\mu}_{0,1}$ decreases exponentially with time, and the amount of product increases as $[1 - \exp(-kt)]$, which is natural for a first-order chemical reaction. At the given initial distribution (Eqn. 27) the coordinates of the centres of mass for the sample and the product distributions coincide. The sample and the product move along the channel at an average flow velocity

$$\bar{\eta}_1(t) = \bar{\eta}_2(t) = t U_{\max}/2 \tag{30}$$

The dispersion of the sample distribution is expressed as

$$\bar{\sigma}_1^2(t) = D_1(2 + Pe^2/96)t - a^2 Pe^2/1440 + 32 a^2 Pe^2 \sum_{m=1}^{\infty} \exp(-\lambda_{m,1}^2 t)/\gamma_m^8 \tag{31}$$

where $Pe = U_{max}a/D_1$. $Pe \geqslant 1000$ is typical for regular FIA systems with Fourier numbers $[DL/(ua^2)]$ larger than 0.7. Equation 31 reveals that the Taylor dispersion (the sample spread due to radial diffusion and radial gradient of velocity profile) affects the substance dispersion at least 10^4 times more than axial molecular diffusion.

The product peak dispersion is described by a more complicated expression:

$$\bar{\sigma}_2^2(t) = 2D_1(1 - D_2/D_1)/k + \frac{1}{1 - \exp(-kt)} \times \left\{ D_2\left[2 + \frac{D_1^2}{D_2^2} \cdot \frac{Pe^2}{96} - \frac{D_1}{D_2}\left[2 + \frac{Pe^2}{96}\right]\right] \times \exp(-kt)\right]t + \frac{32D_1Pe^2}{k} \times \sum_{m=1}^{\infty} \left(\left[\gamma_m^2(1 - D_1/D_2) - \chi D_1/D_2\right] \times \left[\gamma_m^2 + \chi D_1/D_2\right]\right)\left(\gamma_m^8\left[\gamma_m^2 + \chi\right]\right)^{-1} \times \left[1 - \frac{(\gamma_m^4 - \chi^2)}{(\gamma_m^4 - \chi^2 D_1^2/D_2^2)} \exp(-kt)\right] - 32Pe^2\chi a^2 \cdot \frac{D_1^3}{D_2^3} \times \sum_{m=1}^{\infty} \left(\left[\gamma_m^2(2 - D_1/D_2) - \chi D_1/D_2\right] \times \exp(-\lambda_{m,2}^2 t)\right)\left(\left(\gamma_m^2 - \chi D_1/D_2\right)\gamma_m^8 \times \left[\gamma_m^2(1 - D_1/D_2) - \chi D_1/D_2\right]\right)^{-1} \times \left[1 + \left(D_2^3\left[\gamma_m^2 - \chi D_1/D_2\right] \times \left[\gamma_m^2(1 - 2D_1/D_2) - \chi D_1/D_2\right]\right) \times \left(D_1^3\left[\gamma_m^2 + \chi\right] \times \left[\gamma_m^2(2 - D_1/D_2) - \chi D_1/D_2\right]\right)^{-1} \times \exp\left[-t\left(k - \lambda_{m,2}^2(1 - D_1/D_2)\right)\right]\right]\right\} \quad (32)$$

where $\chi = ka^2/D_1$. As seen from Eqns. 31 and 32, if the diffusion coefficients of the sample and the product of the chemical reaction are equal ($D_1 = D_2$), then the dispersion of the sample and product distributions will be the same. Note also that the series present in Eqns. 31 and 32 converge fairly rapidly. Therefore, for approximate calculations only the first terms should be retained. The respective error would not be great and would decrease with time.

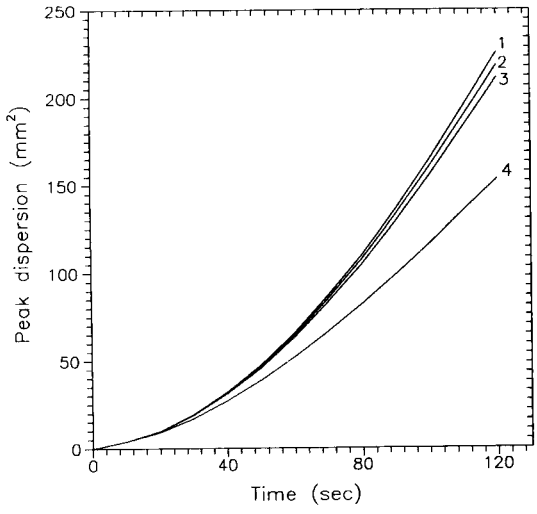

Fig. 2. Time dependences of product peak dispersion. $Pe = 1000$, $\chi = 100$. $D_1/D_2 = (1)\ 2^{1/3}$; (2) 1; (3) $0.5^{1/3}$; (4) $0.01^{1/3}$.

RESULTS AND DISCUSSION

Figure 2 shows the time dependences of the peak dispersion for the sample and chemical reaction product at $Pe = 1000$ and $\chi = 100$, with D_1/D_2 used as parameter. The following cases are included: (i) the molecular weight of the product is twice that of the sample ($D_1/D_2 = 2^{1/3}$); (ii) the product and the sample molecular weight are equal ($D_1/D_2 = 1$); (iii) the molecular weight of the product is half that of the sample ($D_1/D_2 = 0.5^{1/3}$); (iv) the molecular weight of the product is 100 times lower than that of the sample ($D_1/D_2 = 0.01^{1/3}$). As mentioned above, at $D_1/D_2 = 1$ the product and the sample peak dispersions are equal. As shown in Fig. 2, dispersion decreases with decreasing diffusion coefficient ratio D_1/D_2. Thus the dispersion for

$D_1/D_2 = 2^{1/3}$ is 1.5 times greater than that for $D_1/D_2 = 0.01^{1/3}$. This confirms the conclusion that for Fourier numbers > 0.7 with values of Pe typical for FIA the main mechanism of the distribution is Taylor dispersion.

When $kt \gg 1$, i.e., the observation time is much greater than the chemical reaction characteristic time, Eqn. 32 takes the form

$$\bar{\sigma}_2^2(t) = D_2\left[2 + \frac{D_1^2}{D_2^2}\cdot\frac{Pe^2}{96}\right]t + \text{constant}(\chi, D_1/D_2, k, t)$$

$$= 2D_2 t + \frac{a^2 U_{max}^2}{96 D_2}t + \text{constant}(\chi, D_1/D_2, k, t) \quad (33)$$

i.e., for $kt \gg 1$ the increase in dispersion with time is determined by the properties of the reaction product and the constant depends on the "history" and the sample properties.

The predictions by the present mathematical model should be compared with available experimental data. Despite the existence of many experimental studies on FIA, the choice of test experiments is limited as the required information on the sample volume, sample and product diffusion coefficients, their concentrations and chemical reaction rate constants is mostly not given.

In [14] all the necessary information is contained where, specifically, the reaction between nickel (the sample) and 2-(2-thiazolylazo)-4-methyl-5-(sulphomethylamino)benzoic acid (TAMSMB) (the reagent) was studied. In the course of a series of experiments the reaction tube length $L = 50$ cm remained constant, and the length l of the sample plug introduced into the channel and the velocity U_{max} of reagent flow were varied over a relatively wide range. The rate constant of the reaction between Ni and TAMSMB was $k^* = 0.59 \times 10^3$ l mol^{-1} s^{-1}. The reagent concentration ($C_{TAMSMB} = 1 \times 10^{-4}$ M) was an order of magnitude higher than the sample concentration ($C_1 = 1 \times 10^{-5}$ M), which made it reasonable to apply the present model constructed for pseudo-first-order reactions ($k = k^* C_{TAMSMB} = 0.59$ s^{-1}). The product concentration profile at a rectangular initial sample distribution was calculated based on the computation of the convolution of the fundamental solution in the form of a Gaussian peak with the calculated moments and the original initial distribution:

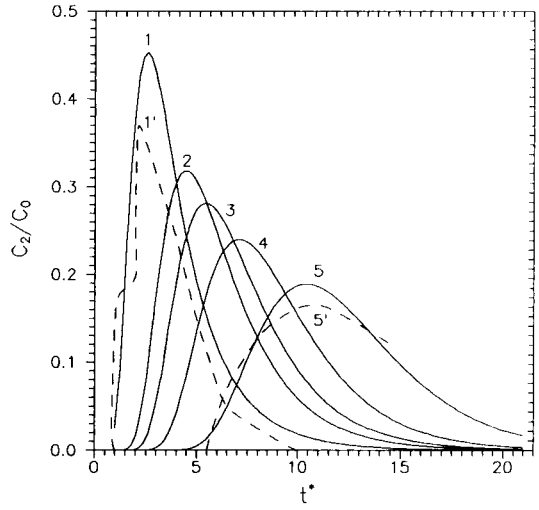

Fig. 3. Time dependences of average product concentration. Solid lines, our model; dashed lines, experimental results [14]. (1, 1') $l = 50$ cm, $U_{max} = 9.8$ cm s^{-1}; (2) 25 cm, 4.9 cm s^{-1}; (3) 20 cm, 3.9 cm s^{-1}; (4) 15 cm, 2.9 cm s^{-1}; (5) 10 cm, 2.0 cm s^{-1}, $t^* = tU_{max}/l$.

$$C_2(x, t) = \frac{\mu_{0,2}(t)}{\sqrt{2\pi}}\left\{\text{erf}\left[\frac{\eta_2(t) - x + l/2}{\sqrt{2\sigma_2^2(t)}}\right] - \text{erf}\left[\frac{\eta_2(t) - x - l/2}{\sqrt{2\sigma_2^2(t)}}\right]\right\} \quad (34)$$

Figure 3 shows time dependences of the product concentration averaged over the channel cross-section and calculated from our analytical expressions (Eqns. 29, 30, 32 and 34) as compared with those obtained from experiments [14]. It can be seen that in general our model describes the process fairly well although it does not provide exact concentration profiles since using only the first three moments of the concentration distribution is not adequate to describe very asymmetric peaks. The disparity between peak heights may be explained by the fact that in the experiment a frontal reaction takes place (the sample and the reagent are not ab initio mixed) whereas our

model deals with a volume reaction (the sample and the reagent are premixed).

The advantage of our model over the numerical analysis [14] is that analytical expressions are more suitable for FIA optimization.

Our model results were also compared with the experimental and theoretical results [12], wherein the following reaction was observed and modelled:

$$Cr_2O_7^{2-} + 3C_6H_8O_6 + 8H^+ \rightleftharpoons$$

$$2Cr^{3+} + 7H_2O + 3C_6H_6O_6 \qquad (35)$$

Only the sample concentration was measured and considered in [12]. The diffusion coefficient of the sample was not given but can be estimated based on the reduced time for the appearance of the maximum ($\tau = tD/a^2$), which may be taken from Fig. 6 in [12], and on the reaction tube length and flow-rate values. The diffusion coefficient found this way is $D_1 = 7 \times 10^{-5}$ cm^2 s^{-1}, which is higher than the expected value for Cr_2O_7. However, it is this value that was used for further calculations. Figure 4 shows the experimental curve in [12] compared with the theoretical curve in [12] for $k = 0.2$ s^{-1} and with the theoretical curve calculated from our model at the same value of k and $D_1 = 7 \times 10^{-5}$ s^{-1}. It can be seen that our model describes the experimental data better than the numerical model in [12]. The difference between theory and experiment may again be attributed to the fact that both in our model and in that in [12] the sample and the reagent are considered to be ideally mixed, whereas actually in the experiment in [12] a frontal reaction occurred.

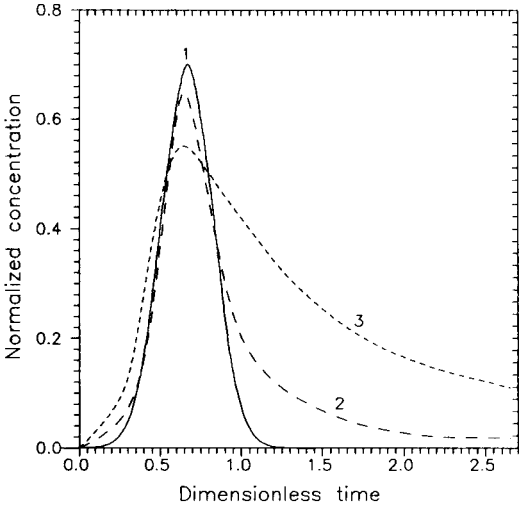

Fig. 4. Comparison of experimental and theoretical results for sample average concentration. (1) Our model; (2) experimental curve [12]; (3) theoretical curve [12].

The next test experiment was taken from [16], where the sample and the reagent were mixed in a T-shaped mixer and detection took place at six points of the reaction tube, 0, 30, 60, 90, 120 and 150 cm apart from the mixing unit. The signal maximum values measured at the six points for the reaction between Ca(II) and *o*-cresolphthalein complexone are given in Fig. 5A in [16] and the corresponding theoretical curves obtained using the random walk model are shown in Fig. 5B in [16]. Note that the results in Fig. 5 in [16] are derived for the case when the reagent concentration is 0.076, 0.148 and 0.296 times the sample concentration. As in [16] the sample and the reagent were completely interchangeable and introduced in the form of zones of comparable length and their mixing in the T-shaped mixer was considered to be ideal, the reaction can be assumed to be almost pseudo-first order and the application of our model is more or less justified. Figure 5 here shows the results of our model compared with the experimental and theoretical results in [16]. As the relationship between the detector signal and product concentration was not given in [16], for purposes of easier comparison the coefficients α_1 and α_2 relating the experimental and theoretical data in [16] and our model results are introduced so that curves 3, $3^{(1)}$ and $3^{(2)}$ in Fig. 5 coincide at the point $L = 30$ cm. It is easily seen that our model describes the experimental curve of the product peak maximum versus reaction tube length and concentration fairly satisfactorily, at least not worse than the random walk model.

The comparison with experimental data and numerical analysis results [12,14,16] shows that our model of FIA with the pseudo-first-order reaction adequately describes both the situation

when the sample and reagent are previously mixed and the case of frontal reaction between the sample and the reagent, and is inferior in accuracy only to the numerical model [14] at experimental times below the characteristic diffusion time $t_D = a^2/D$. Note, however, that even in this case (Fig. 3) the peak maximum error also is not large and is limited to about 20%.

The obtained analytical expressions (Eqns. 29, 30, 32 and 34) can be used for optimization of FIA and examples of such optimization are given below. Figure 6 shows the time dependences of the chemical reaction product peak height. As can be seen, the chemical reaction product peak-height curve has a maximum. It is clear that the ascending branch at short times corresponds to the product growth due to chemical reaction, and the descending branch at long time values to the Taylor dispersion of the product. Analysis of the two above trends shows that the time T_m when the product peak reaches its maximum must not exceed, at least substantially, the chemical reaction characteristic time $t = k^{-1}$. As in our model we restricted ourselves only to the zeroth, first and second moments of the peak product distribution, which allow one to describe a peak adequately only at $t \gg t_D$, for optimization purposes it is reasonable to use this model just for the case of a "slow" chemical reaction with $k^{-1} > t_D$. This condition is met in Fig. 6 and all subsequent figures. FIA optimization for the case of "fast" chemical reactions will be considered in a subsequent paper.

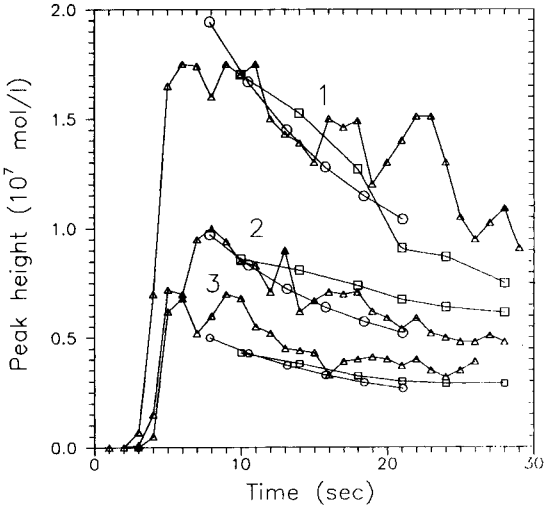

Fig. 5. Time dependences of the peak-height values for different reagent concentrations C_r: (1) $0.296C_0$; (2) $0.148C_0$; (3) $0.076C_0$, where C_0 = sample initial concentration. □ = Experiment [16]; △ = numerical analysis result [16]; ○ = our model.

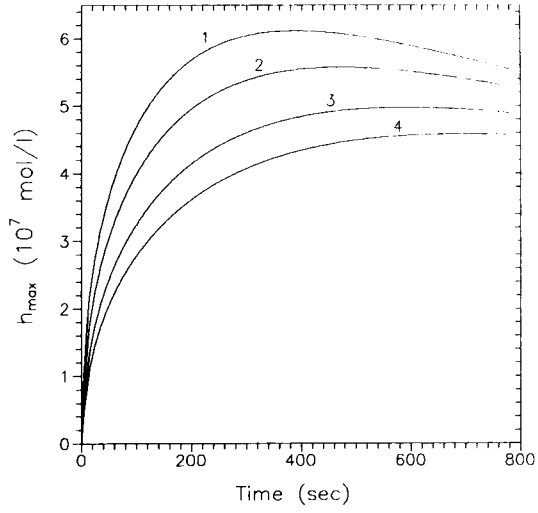

Fig. 6. Time dependences of product peak height for different values of reaction rate constant. $C_0 = 5\times10^{-5}$ M, $U_{max} = 1$ mm s^{-1}, $D_1 = 7\times10^{-6}$ cm^2 s^{-1}, $D_2 = 4.15\times10^{-6}$ cm^2 s^{-1}, $a = 0.25$ mm, initial sample length $l = 5$ mm. k: (1) 3×10^{-3}; (2) 2.5×10^{-3}; (3) 2×10^{-3}; (4) 1.7×10^{-3} s^{-1}.

The approach to the FIA optimization problem varies depending on the analysis conditions. Thus, if the signal level only slightly exceeds the instrumental noise (i.e., for low-concentration samples), the reaction tube length and flow-rate should be such that the peak enters the detector at the moment when it reaches its maximum height (T_m). Figure 7 shows plots of the optimum reaction tube length versus flow-rate. When the signal level is much higher than that of the instrumental noise, the approach to optimization should be different. In that case the selected signal level can be reached before the time T_m elapses and, hence, choosing the channel length and flow-rate such that the analysis time is equal to T_m would lead to lower throughputs of the apparatus. Therefore, in that case the optimum analysis times will not be T_m, but rather the time in which the peak height reaches the preset level defined by

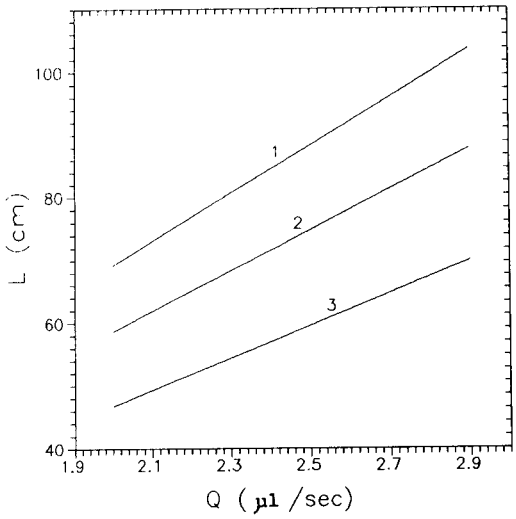

Fig. 7. Optimum (maximizing product peak-height value) reaction tube length versus flow-rate. $C_0 = 5\times10^{-5}$ M, $D_1 = 7\times10^{-6}$ cm^2 s^{-1}, $D_2 = 4.15\times10^{-6}$ cm^2 s^{-1}, $a = 0.25$ mm, $l = 5$ mm. k: (1) 1.7×10^{-3}; (2) 2.5×10^{-3}; (3) 3×10^{-3} s^{-1}.

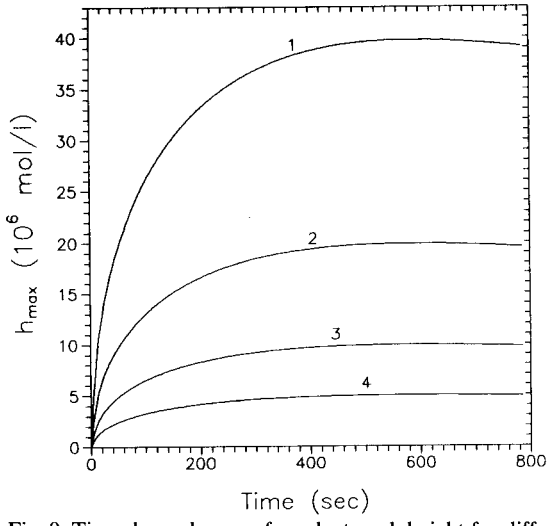

Fig. 9. Time dependences of product peak height for different values of flow-rate. $C_0 = 2\times10^{-5}$ M, $D_1 = 7\times10^{-6}$ cm^2 s^{-1}, $D_1 = 4.15\times10^{-6}$ cm^2 s^{-1}, $a = 0.25$ mm, $l = 5$ mm, $k = 2\times10^{-3}$ s^{-1}. U_{max}: (1) 0.5; (2) 1; (3) 2; (4) 4 mm s^{-1}.

the detector sensitivity. Figure 8 shows the plots of the optimum channel length in terms of reaching the preset signal level versus flow-rate. The tube lengths optimized with respect to the preset level are substantially less than those optimized in terms of the peak maximum.

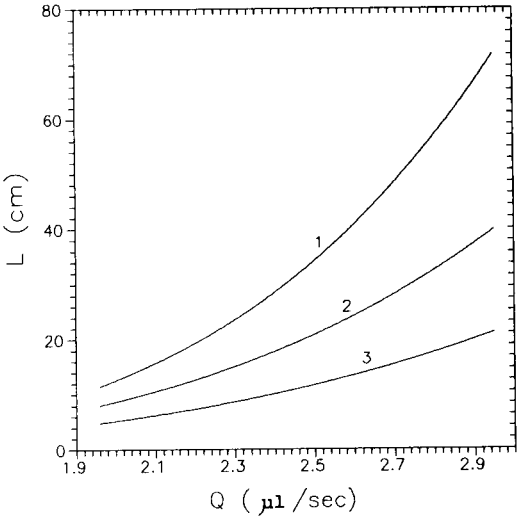

Fig. 8. Optimum reaction tube length versus flow-rate. Here optimum means the value for which a preset level of product peak height $C = 6\times10^{-7}$ M is reached. $C_0 = 2\times10^{-5}$ M, $D_1 = 7\times10^{-6}$ cm^2 s^{-1}, $D_2 = 4.15\times10^{-6}$ cm^2 s^{-1}, $a = 0.25$ mm, $l = 5$ mm.

It is interesting to compare the approaches to FIA optimization used in our work with those in [24] based on the tanks-in-series model. As in our model, the product peak in [24] was considered to be Gaussian, i.e., the approach used in [24] was applicable in the same time interval $t \gg t_D$. However, in contrast to our approach the analysis time in [24] was assumed to be entirely dependent on the reaction rate and the specified degree of the sample to product conversion and was not amenable to optimization. To increase the FIA throughput the product peak width was reduced in [24] by optimizing such parameters as the reaction tube length and diameter and also the pressure difference and detector cell volume. It seems to us that our approach to optimization allows one to take account of an important effect disregarded in [24]. Figure 9 shows the chemical reaction product peak height versus time for various flow-rates. At excessive flow-rates the specified level may never be attained as the Taylor dispersion will spread the peak before its height can adequately rise due to chemical reaction. Hence, if the analysis time is chosen so that it

exceeds the optimum value (with respect to peak maximum or specified level), which may be the case with the approach in [24], this can lead to lower sensitivity and throughput of FIA owing to excessive spreading of the product peak.

REFERENCES

1 J. Ruzicka and E.H. Hansen, Anal. Chim. Acta, 78 (1975) 17; Dan. Pat. Appl., 846/84 (1974); US Pat., 4022575 (1975).
2 K.K. Stewart, G.R. Beecher and P.S. Hare, Fed. Proc. Fed. Am. Soc. Exp. Biol., 33 (1974) 1439; US Pat., 4013413 (1975).
3 D. Betteridge, Anal. Chem., 50 (1978) 232A.
4 J. Ruzicka and E.H. Hansen, Flow Injection Analysis, Wiley, New York, 2nd edn., 1988.
5 G. Taylor, Proc. R. Soc. London, Ser. A, 219 (1953) 186.
6 G. Taylor, Proc. R. Soc. London, Ser. A, 225 (1954) 473.
7 S.H. Brooks, D.V. Leff, M.A. Hernandes Torres and J.G. Dorsey, Anal. Chem., 60 (1988) 2737.
8 J.L. Montesinos, J. Bartroli, M. Poch and M. Delvalle, Anal. Chim. Acta, 234 (1990) 67.
9 J.T. Vanderslice, K.K. Stewart, A.G. Rosenfeld and D.J. Higgs, Talanta, 28 (1981) 11.
10 M.A. Gomez-Nieto, M. Luque de Castro, M. Martin and M. Valcarcel, Talanta, 32 (1985) 319.
11 J.T. Vanderslice and G.R. Beecher, Talanta, 32 (1985) 334.
12 C.C. Painton and H.A. Mottola, Anal. Chim. Acta, 158 (1984) 67.
13 D. Betteridge, C.Z. Marczewski and A.P. Wade, Anal. Chim. Acta, 165 (1984) 227.
14 H. Wada, S. Hiraoka, A. Yuchi and G. Nakagawa, Anal. Chim. Acta, 179 (1986) 181.
15 J.T. Vanderslice, A.G. Rosenfeld and G.R. Beecher, Anal. Chim. Acta, 179 (1986) 119.
16 C.D. Crowe, H.W. Levin, D. Betteridge and A.P. Wade, Anal. Chim. Acta, 194 (1987) 49.
17 J.H.M. Van der Berg, R.S. Deelder and H.G.M. Egberink, Anal. Chim. Acta, 114 (1980) 91.
18 J.M. Reijn, W.E. Van der Linden and H. Poppe, Anal. Chim. Acta, 123 (1981) 229.
19 J.M. Reijn, W.E. Van der Linden and H. Poppe, Anal. Chim. Acta, 126 (1981) 1.
20 S.D. Kolev and E. Pungor, Anal. Chim. Acta, 185 (1986) 315.
21 S.D. Kolev, G. Nagy and E. Pungor, Anal. Chim. Acta, 241 (1990) 43.
22 R. Aris, Proc. R. Soc. London, Sci. A, 235 (1956) 67.
23 V.P. Andreev and M. Khidekel, Mathematical Model of Flow Injection Analysis in Presence of a Chemical Reaction with Excessive Amount of Reagent, All Union Science and Technol Information Institute, 1988, No. 2025-B88.
24 J.M. Reijn, H. Poppe and W.E. Van der Linden, Anal. Chim. Acta, 145 (1983) 59.

Analytica Chimica Acta, 278 (1993) 317–320
Elsevier Science Publishers B.V., Amsterdam

Liquid–solid extraction system based on mixed polymers of polyethylene glycol 2000 and Triton X-100 without organic solvents

Buhai Li, Xiaomei Sun, Guihong Wei and Zizhuan Ma

Department of Chemistry, South-Central College for Nationalities, Wuhan, Hubei 430074 (China)

(Received 10th June 1992; revised manuscript received 18th January 1993)

Abstract

On mixing of aqueous solutions of polyethylene glycol 2000 and Triton X-100 (polyoxyethylene alkylphenol) and addition of ammonium sulphate, a polymeric solid phase and an aqueous phase are formed. Suitable phase separation conditions were studied in addition to the distribution of the Arsenazo III complexes of U(VI), Sc(III), Bi(III), Zr(IV), Fe(III) and Pb(II) between the two phases. The separation of Zr(IV) from Fe(III) and the determination of the former was achieved by properly adjusting the acidity of the solution.

Keywords: Sample preparation; UV–Visible spectrophotometry; Metal ions; Polymer extractants; Zirconium

Liquid–solid extraction systems of some water-soluble polymers, e.g., polyvinylpyrrolidone (PVP) [1,2], Tween 40 [3] and Tween 80 [4], have been reported. These systems have an advantage over the two-phase aqueous system of polyethylene glycol (PEG) 2000 [5], and have been applied to the separation of various metals by using water-soluble chromgenic reagents as extractants.

Aqueous solutions of mixed polymers give rise to liquid and solid phases after addition of ammonium sulphate. Under suitable conditions some metal ions can be selectively transferred into the polymeric solid phase, while others remain in the aqueous phase. Because the salt effect, which decreases the stability of the complexes of some metal ions, is lower than in a system with a single polymer, extraction in a system of mixed polymers is more convenient.

Correspondence to: Buhai Li, Department of Chemistry, South-Central College for Nationalities, Wuhan, Hubei 430074 (China).

In this paper, a liquid–solid extraction system based on mixed polymers of PEG 2000 and Triton X-100 (polyoxyethylene alkylphenol) is reported.

EXPERIMENTAL

Apparatus and reagents

A Shanghai Model 721 spectrophotometer was used for spectrophotometric measurements.

Aqueous 32% (w/v) solutions of PEG 2000 and Triton X-100 were used.

A 1.29×10^{-3} mol l^{-1} Arsenazo III chromogenic reagent solution was prepared by dissolving the appropriate amount in water. Standard 1.0 mg ml^{-1} solutions of U(VI), Fe(III) and Pb(II) in 0.15 mol l^{-1} nitric acid, Bi(III) in 0.75 mol l^{-1} nitric acid, Zr(IV) in 10% hydrochloric acid and Sc(III) in 0.1 mol l^{-1} hydrochloric acid were prepared from $UO_2(NO_3)_2 \cdot 6H_2O$, pure lead, pure bismuth, $ZrOCl_2 \cdot 8H_2O$ and scandium

oxide, respectively. More dilute solutions were obtained by appropriate dilution.

Chloroacetic acid buffers (pH 1.5–3.0) and acetic acid buffers (pH 3.5–6.5) were prepared by adding 40% sodium hydroxide to 0.7 mol l^{-1} chloroacetic acid and 0.7 mol l^{-1} acetic acid, respectively.

All other reagents were of analytical-reagent grade.

Procedure

A 2.0-ml volume of 32% PEG 2000 solution, 3.0 ml of 32% Triton X-100 solution, a given volume of chromogenic reagent and metal ion solution were placed in a 25-ml test-tube with a stopper. The pH of the solution was adjusted from 1.5 to 6.5 with chloroacetic or acetic acid buffers, and the acidity of the strong acid solution was adjusted with HCl. A given amount ammonium sulphate was added, then the solution was diluted to 10.0 ml with distilled water and shaken for 3 min. Five minutes later, a liquid and a solid phase were formed. The liquid phase was carefully decanted directly from the tube. The polymeric solid was washed two or three times with a saturated solution of ammonium sulphate. The separated liquid was combined with the wash solution. The solid polymeric phase was dissolved in distilled water. The concentration of the extracted species in the dissolved solid or the separated liquid was determined spectrophotometrically. The percentage extraction (E) was calculated as the ratio of the amount of species extracted by the solid phase to the total amount of the species.

The conditions used for determination of the metal ions with Arsenazo III as chromogenic reagent are given in Table 1.

RESULTS AND DISCUSSION

Phase separation conditions for polymer solution

At fixed acidity (pH 4.5) and total concentration of the polymers (16%), the concentration of ammonium sulphate necessary for phase separation decreases with increasing the PEG 2000/Triton X-100 ratio. When this ratio was fixed at 2:3, the necessary salt concentration decreases with increase in the total concentration of the polymers from 5 to 10%, and then remains constant.

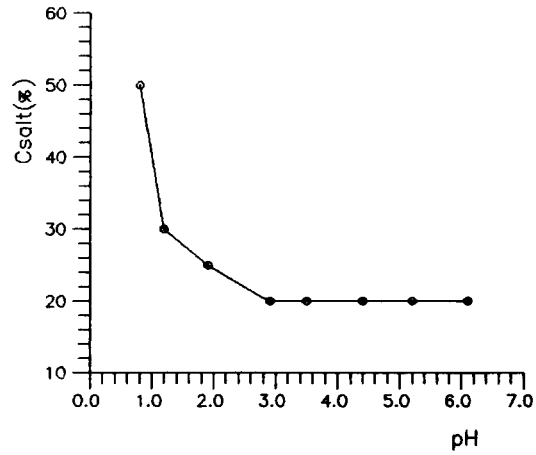

Fig. 1. Relationship between pH and ammonium sulphate concentration necessary for phase separation. Polymer concentration, 16%; PEG 2000 to Triton X-100 ratio = 2:3.

Figure 1 shows that the necessary salt concentration also depends on the pH. In the pH range 0.8–2.9 it decreases with an increase in pH and remains unchanged at higher pH. The reason is that at low pH the sulphate ion is protonated to HSO_4^- and the salting-out ability is reduced.

Distribution of chromogenic reagents

The distribution of some water-soluble reagents between the polymeric solid phase and aqueous phase was determined in the pH range 1.1–6.2. The reagents examined containing different chelating groups, were Arsenazo III, Chromazurol S, Xylenol Orange and Bromopyrogallol Red. The E values for these reagents, as shown in Fig. 2, depended on the pH of the solution. The E values of Arsenazo III were the highest (90–96%), so this reagent was chosen as the extractant. Because of the dependence of E for Arsenazo III on pH, it is necessary that the polymeric phase that contains Arsenazo III at the same pH is used as the reference when determining spectrophotometrically the E values of metal ions with Arsenazo III as extractant.

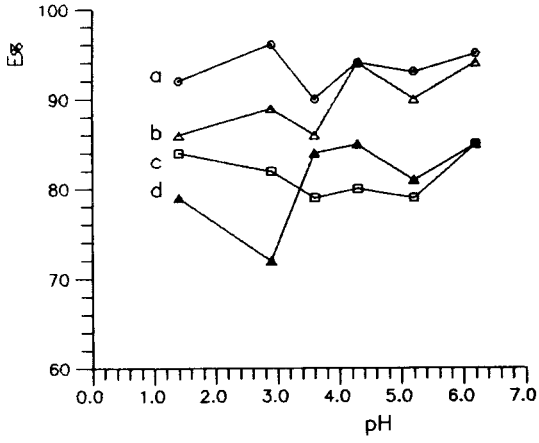

Fig. 2. Extraction acidity curves for various chromogenic reagents. Extraction conditions as in Fig. 1. (a) Arsenazo III; (b) Chromazurol S; (c) Xylenol Orange; (d) Bromopyrogallol Red. Concentration of ammonium sulphate in the various acidity as in Fig. 1.

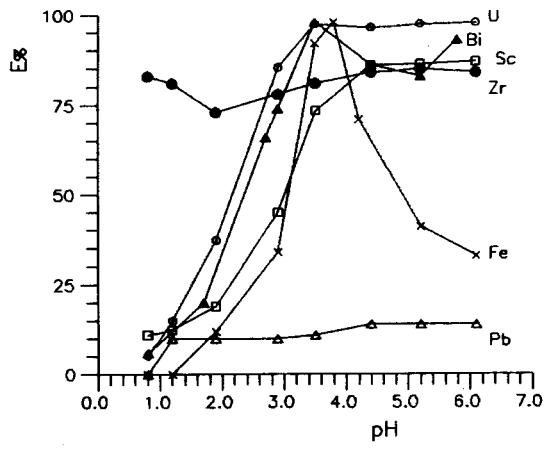

Fig. 3. Extraction acidity curve for the metals. Added amount of each metal, 50 μg; Arsenazo III concentration, 1.29×10^{-4} mol l^{-1}. Other conditions as in Fig. 1.

Extraction of metals by using Arsenazo III as extractant

Effect of pH. Figure 3 shows the dependence of E for U(VI), Sc(III), Bi(III), Zr(IV), Fe(III) and Pb(II) on pH in the presence of Arsenazo III. The stability of the complexes of U(VI) and Sc(III) can be increased by raising the pH from 0.8 to 3.5 and 4.4, respectively, so E is correspondingly increased. The maximum E value for U(VI) is at pH 3.5 and for Sc(III) at pH 4.4, but then remains unchanged on further increase in pH. The E values for Bi(III) and Fe(III) increase with increasing pH from 1.6 to 3.6 and 3.8 respectively, and then decrease with a further increase in pH, probably owing to hydrolysis and other side-reactions of the metals at high pH. In contrast to U(VI), Sc(III), Bi(III) and Fe(III), the effect of pH on E for Zr(IV) is less.

Because Pb(II) and SO_4^{2-} form an insoluble compound, Pb(II) can hardly be extracted into the polymeric phase, and the E values are lower.

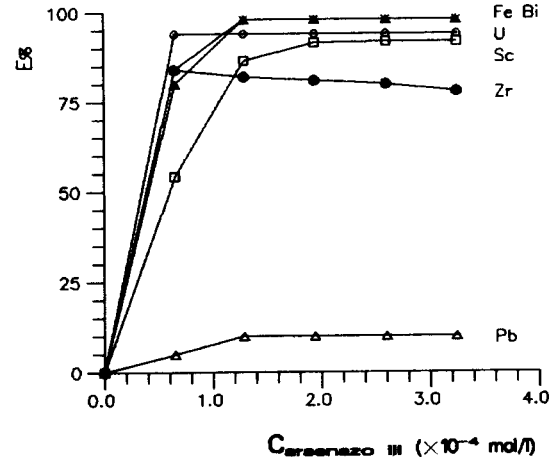

Fig. 4. Effect of Arsenazo III concentration on extraction of the metals. (E) Extraction acidity, U(VI), Bi(III), Fe(III) and Pb(II) pH 3.5; Sc(III) and Zr(IV) pH 4.5. Other conditions as in Fig. 3.

Effect of Arsenazo III concentration. At fixed pH the stability of the complexes of U(VI), Sc(III), Zr(IV) and Fe(III), and the corresponding E

TABLE 1

Spectrophotometric determination of metals

Parameter	U(VI)	Sc(III)	Pb(II)	Zr(IV)	Bi(III)	Fe(III)
Wavelength (nm)	650	660	655	665	620	622
Acidity	pH 2.0	pH 3.0	pH 5.0	0.1 M HCl	pH 2.0	pH 3.5

TABLE 2

Recovery results for extractive separation between Zr(IV) and Fe(III)

Added (μg)		Found (μg)			Recovery (%)	
Zr(IV)	Fe(III)	Zr(IV)	Fe(III)		Zr(IV)	Fe(III)
50.0	5.0	49.1	5.0		98.1	100.0
50.0	10.0	48.1	10.0		96.3	100.0
20.0	20.0	18.9	19.1		94.5	95.5
10.0	50.0	10.5	47.7		105.0	95.4
10.0	100.0	9.5	94.5		95.0	94.5
10.0	1000.0	10.2	945.0		102.0	94.5
5.0	1000.0	5.0	954.0		100.0	95.4
5.0	5000.0	4.8	4659.0		96.0	93.2
				Average	98.4	96.5
				S.D.	3.7	2.4
				R.S.D.	3.8%	2.5%

values, can be increased when the concentration of Arsenazo III is increased up to 6.45×10^{-5} or 1.29×10^{-4} mol l^{-1}, and then E remains constant with further increase in arsenazo III concentration, as shown in Fig. 4. For the same reason as indicated above, the E value for Pb(II) is small.

Figure 4 also indicates that without Arsenazo III all the E values for the studied metals are zero. This is the same as for a single polymer system, which mean that the uncomplexed metal ions cannot be extracted into the mixed polymer phase.

Recovery tests for quantitative separation of Zr(IV) and Fe(III)

Figure 3 shows that in the lower pH range (0.8–1.2), the E value for Zr(IV) is higher than 80%, but that for Fe(III) is zero. After a first extraction with Arsenazo III as extractant, we can put the mixed polymer and the Arsenazo III solutions into the extracted solution, which is shaken for 3 min. The mixed polymer solid is salted out again, and the complex of Zr(IV) with Arsenazo III quantitatively enters the mixed polymer solid, but Fe(III) remains in the solution. The separation results are also satisfactory (see Table 2).

The data in Table 2 show that this mixed polymer–$(NH_4)_2SO_4$–H_2O system can be applied to the extractive separation of various metals. The experiments also show that the reproducibility of the separation and determination of the metals is excellent. For example, for the same sample the relative standard deviation is less than 4.4% ($n = 3$). The sensitivity and linear dynamic range for the determination of the metals after separation are similar to those for the direct determination of the metal ions with Arsenazo III as chromogenic reagent.

This study was supported by the National Natural Science Fund of China.

REFERENCES

1 B.-H. Li and K.-F. Wang, Gaodeng Xuexiao, Huaxue Xuebao, 11 (1990) 336.
2 X.-M. Sun, B.-H. Li and K.-J. Fu, Mikrochim. Acta, III (1990) 101.
3 B.-H. Li and R.-G. Meng, Talanta, 37 (1990) 885.
4 B.-H. Li and B. Yang, Kexue Tongbao, 3 (1990) 192.
5 T.I. Zvarova, V.M. Shkinnev, G.A. Vorobeva, B.Ya. Spivakov and Yu.A. Zolotov, Mikrochim. Acta, III (1984) 449.

Analytica Chimica Acta, 278 (1993) 321–333
Elsevier Science Publishers B.V., Amsterdam

Equilibria among condensed phases and a multi-component solution using the concept of generalized species

Part I. Systems with mixed complexes

Alberto Rojas-Hernández, M. Teresa Ramírez and Ignacio González

Universidad Autónoma Metropolitana–Iztapalapa, Departamento de Química, Apartado Postal 55-534, 09340 México D.F. (Mexico)

(Received 1st June 1992; revised manuscript received 8th December 1992)

Abstract

A method for the construction of predominance–existence diagrams (PED) in saturated multi-component solutions is discussed. The utilization of generalized species and equilibria, both in the solution and in the condensed phases, allows for the analysis of the saturation conditions from an intrinsic solubility generalized equilibrium $[M_{(c)}^{\{\tau\}} \rightleftharpoons M^{(\tau)}]$. Likewise, an algorithm is proposed for the selection of the most insoluble condensed phase $M_{(c)}^{\{\tau\}}$, from a condensed-phases diagram (CPD) dependent upon the parameters of the saturated solution. The CPD is constructed utilizing generalized phase interconversion equilibria, where the multi-conditional constants are dependent only on the buffering conditions; it is also necessary to consider the maximum number of phases that can coexist in the system (phase rule), the electroneutrality conditions for the condensed phases and the number of variables involved in the solubility equations. The consideration of mixed complexes in all phases with the proposed algorithm is simple as it is an extension of the concept of generalized species used previously.

In order to exemplify the proposed method, graphical representations of the following systems are discussed: Zn(II)–H_2O–H, Zn(II)–$H_2C_2O_4$–H_2O–H and Ca(II)–$H_2C_2O_4$–H_2SO_4–H_2O–H, where $H_2C_2O_4$ is oxalic acid.

Keywords: Condensed-phase equilibria; Equilibria; Generalized species; Mixed complexes

In physico-chemical studies of multi-component and multi-reacting systems, one of the main problems is the prediction of the conditions for the saturation of a condensed phase, because under specific conditions several condensed phases may be in equilibrium with the solution. In the mass action law algorithm and also in that of free energy minimization, this problem is solved by exhaustively analysing either the solubility [1–5] or the free energy minimization [6–9] for each and every phase that could coexist with the solution and selecting that with the minimum solubility or else with the minimum free energy when equilibrium is attained.

A method was reported previously [10–13] for the study of multi-component and multi-reacting systems in non-saturated solutions using the definitions of generalized species and equilibria related through complexation coefficients and multi-conditional equilibrium constants dependent only on the buffering conditions; here, the concept of dismutation or disproportionation plays a key role. This method permits the consideration of mixed complexes and polynuclear

Correspondence to: A. Rojas-Hernández, Universidad Autónoma Metropolitana–Iztapalapa, Departamento de Química, Apartado Postal 55-534, 03940 México D.F. (Mexico).

species in a systematic way by combining Charlot's [10,14] and Ringbom's [15] methods. This paper discusses the algorithm that permits the study of the saturation conditions of a multi-component and multi-reacting system using the concepts of generalized species and equilibria and the phase rule.

This work is divided into two parts. In this first part, the equilibria involved in a solution with condensed phases are discussed taking into account the mixed complexes in all phases; in the following paper (Part II), the presence of polynuclear species is also analysed.

THEORY

Systems of the type M–Z, where Z is an inert solvent, at constant temperature (T) and pressure (P)

In this type of system the only species that can exist in solution is M, as Z is inert. If the solution becomes saturated and a condensed phase, $M_{(c)}$, exists, the following solubility equilibrium exists:

$$M_{(c)} \rightleftharpoons M \quad \text{with } K_M^{M_{(c)}} = [M]_{sat} = s_{M_{(c)}} \tag{1}$$

where $K_M^{M_{(c)}}$ is the intrinsic or molecular solubility equilibrium constant and $s_{M_{(c)}}$ is the solubility of pure $M_{(c)}$ in solvent Z. The subscript sat indicates that the solution is saturated in equilibrium conditions.

According to the phase rule,

$$F = C - P + 2 \tag{2}$$

where F is the number of degrees of freedom, C the number of components and P the number of phases. The maximum number of phases (P_{max}) that may coexist in the system is found where $F = 0$; then, $P_{max} = C + 2 = 4$. It is then possible to have a system (at constant T and P) where two phases coexist, i.e., the solution and the pure phase $M_{(c)}$. The graphical representation of such a system in a pM scale is

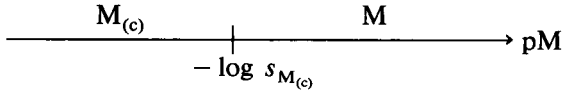

This is an existence diagram, because if $-\log s_{M_{(c)}} < pM$ the solution is not saturated and $M_{(c)}$ cannot coexist with it. This case is trivial and virtually hypothetical but gives a convenient starting point for the discussion of the cases that follow.

Systems of the type M–HZ–H, where HZ is an amphiprotic solvent, at constant T and P

Here, the concentrations of H and Z are interdependent through the self-protolysis equilibrium. The species MZ_i, where $i \in \{0,1,\ldots,n\}$, can exist in the solution whereas species of the type $MH_{j(c)}$ cannot (charges are omitted for simplicity). On the other hand, of all the condensed phases that could be formed only one will be the most stable $MZ_{a(c)}$ as it is the most insoluble. Then, if the solution becomes saturated, MZ_i can coexist with $MZ_{a(c)}$ and the following equilibria appear:

$$(i-a)HZ + MZ_{a(c)} \rightleftharpoons MZ_i + (i-a)H$$

with

$$K_{MZ_i}^{MZ_{a(c)}} = [MZ_i]_{sat}[H]_{sat}^{(i-a)} \tag{3}$$

In these systems the solubility of $MZ_{a(c)}$ ($s_{MZ_{a(c)}}$) is

$$s_{MZ_{a(c)}} = \sum_{i=0}^{n} [MZ_i]_{sat} = \sum_{i=0}^{n} \left(K_{MZ_i}^{MZ_{a(c)}} / [H]_{sat}^{(i-a)} \right) \tag{4}$$

where the subscript sat indicates concentrations in a saturated solution. Equation 4 shows that $s_{MZ_{a(c)}}$ is only a function of pH.

Systems with buffered pH. The generalized species M′ in solution (with buffered pH) can be defined as [10,12]

$$[M'] = \sum_{i=0}^{n} [MZ_i] = [M]\alpha_{M(Z)} = [M]\alpha_{M(H)} \tag{5}$$

where $\alpha_{M(Z)}$ and $\alpha_{M(H)}$ are the complexation coefficients of M, which depend on the concentrations of Z and H, respectively, and $\alpha_{M(Z)} = \alpha_{M(H)}$ because pH and pZ are interdependent.

Likewise, it is possible to define a generalized species, $M'_{(c)}$, for the condensed phase:

$$M'_{(c)} \equiv MZ_{a(c)} \tag{6}$$

where the prime refers to the buffered component (in this case Z), implicitly considered. If the solution is saturated, the generalized first-order solubility equilibrium can also be defined:

$$M'_{(c)} \rightleftharpoons M' \text{ with } K_{M'}^{M'_{(c)}} = [M']_{sat} \quad (7)$$

Comparing Eqns. 3, 4 and 5, we obtain

$$K_{M'}^{M'_{(c)}} = [M']_{sat} = \sum_{i=0}^{m} [MZ_i]_{sat} = [M]_{sat}\alpha_{M(H)} = s_{MZ_{a(c)}} = \sum_{i=0}^{n} \left(K_{MZ_i}^{MZ_{a(c)}}/[H]_{sat}^{(i-a)}\right) = s_{M'_{(c)}(H)} \quad (8)$$

where $s_{M'_{(c)}(H)}$ is the solubility of the generalized species $M'_{(c)}$, which depends on H. From Eqn. 8 it is possible to identify the solubility of $MZ_{a(c)}$ as the conditional constant of the generalized solubility equilibrium in Eqn. 7. On the other hand, from Eqn. 8,

$$pM'_{sat} = pK_{M'}^{M'_{(c)}} = -\log s_{MZ_{a(c)}} = -\log s_{M'_{(c)}(H)}$$

Then, it is possible to construct a predominance–existence diagram (PED) in the plane pM′/pH as shown in Fig. 1.

In Fig. 1, the points above the saturation line

$$pM' > -\log s_{MZ_{a(c)}}$$

correspond to unsaturated solutions, where the phase $MZ_{a(c)}$ does not exist in the system; then, according to the phase rule, the system is bivariant (at constant T and P). On the other hand, for those points below the saturation line

$$pM' < -\log s_{MZ_{a(c)}}$$

the solutions are supersaturated and $MZ_{a(c)}$ will be formed as needed to reach equilibrium; at $pM' = -\log s_{MZ_{a(c)}}$ both phases coexist. Then, according to the phase rule, if T, P and pH are constant and two phases coexist, the system is invariant ($F = 0$). The fact that the saturation line is one-dimensional reflects the dependence of $s_{MZ_{a(c)}}$ on pH, at constant T and P.

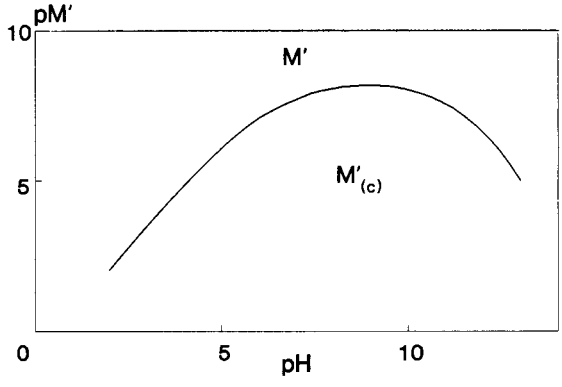

Fig. 1. Predominance–existence diagram of the system M–HZ–H. The continuous line corresponds to saturation, i.e., $pM' = -\log s_{MZ_{a(c)}} = -\log s_{M'_{(c)}}$.

Systems of the type M–L–HZ–H, where HZ is an amphiprotic solvent

Here, the following substances can exist in solution: MZ_iL_j where $i \in \{0, 1, \ldots, m(j)\}$, $j \in \{0, 1, \ldots, n\}$ and H_kL where $k \in \{0, 1, \ldots, l\}$.

However, in this case several condensed phases (all of which obey the electroneutrality principle) can appear.The chemical formulae for these phases could be represented by $MZ_{a(c)}$, $ML_{b(c)}$ and $MZ_cL_{d(c)}$.

In this case, since $C = 4$, the phase rule gives the maximum number of phases that may coexist in the system (when $F = 0$):

$$P_{max} = C + 2 = 4 + 2 = 6$$

At constant T and P up to four phases may coexist with zero degrees of freedom.

As the solubility expressions depend on two variables only, for this system the maximum number of condensed phases in equilibrium with the solution is also two.

pH buffered systems, at constant T and P. For chemical species in solution the generalized-species ML'_j under pH buffering are defined as follows [10,12]:

$$[ML'_j] \equiv \sum_{i=0}^{m(j)} [MZ_iL_j] = [ML_j]\alpha_{ML_j(Z)} = [ML_j]\alpha_{ML_j(H)}$$

$$[L'] \equiv \sum_{k=0}^{l} [H_kL] = [L]\alpha_{L(H)}$$

On the other hand, it is also possible to define generalized species for the condensed phases: $M'_{(c)}$, $ML'_{b(c)}$ and $ML'_{d(c)}$, with

$M'_{(c)} \equiv MZ_{a(c)}$, $ML'_{b(c)} \equiv ML_{b(c)}$ and

$ML'_{d(c)} \equiv MZ_cL_{d(c)}$

According to these definitions, the solubility equilibria can be written as generalized first-order solubility equilibria with their associated first-order conditional solubility constants:

$$jL' + M'_{(c)} \rightleftharpoons ML'_j \quad \text{with } K^{M'_{(c)}}_{ML'_j} = \frac{[ML'_j]}{[L']^j} \tag{9}$$

$$(j-b)L' + ML'_{b(c)} \rightleftharpoons ML'_j \quad \text{with}$$

$$K^{ML'_{b(c)}}_{ML'_j} = \frac{[ML'_j]}{[L']^{(j-b)}} \tag{10}$$

$$(j-d)L' + ML'_{d(c)} \rightleftharpoons ML'_j \quad \text{with}$$

$$K^{ML'_{d(c)}}_{ML'_j} = \frac{[ML'_j]}{[L']^{(j-d)}} \tag{11}$$

From these definitions, the first-order solubility of each of the insoluble generalized species is

$$s_{M'_{(c)}(L',H)} = \sum_{j=0}^{n} [ML'_j]_{sat} = \sum_{j=0}^{n} K^{M'_{(c)}}_{ML'_j}[L']^j \tag{12}$$

$$s_{ML'_{b(c)}(L',H)} = \sum_{j=0}^{n} [ML'_j]_{sat} = \sum_{j=0}^{n} K^{ML'_{b(c)}}_{ML'_j}[L']^{(j-b)} \tag{13}$$

$$s_{ML'_{d(c)}(L',H)} = \sum_{j=0}^{n} [ML'_j]_{sat} = \sum_{j=0}^{n} K^{ML'_{d(c)}}_{ML'_j}[L']^{(j-d)} \tag{14}$$

System buffered in H and L', at constant T and P. It was shown previously [12] that in this case a generalized second-order species [M″] can be defined as

$$[M''] = \sum_{j=0}^{n} [ML'_j] = \sum_{j=0}^{n} \left[\sum_{i=0}^{m(j)} [MZ_iL_j] \right]$$
$$= [M']\alpha_{M'(L')} = [M]\alpha_{M(Z)}\alpha_{M'(L')}$$
$$= [M]\alpha_{M(H)}\alpha_{M'(L')} = [M]\alpha_{M(H,L')} \tag{15}$$

The multiplicative structure of the complexation coefficient $\alpha_{M(H,L')}$ permits the mixed complexes $[MZ_iL_j]$ to be taken into account and conditional constants to be defined that depend only on buffering in pH and pL′ [11,12].

In a similar way, a second-order insoluble generalized species can also be defined, $M''_{(c)}$, as

$M''_{(c)} \equiv ML'_{y(c)}$ most insoluble;

$ML'_{y(c)} \in \{M'_{(c)}, ML'_{b(c)}, ML'_{d(c)}\}$

or

$$M''_{(c)} \equiv \delta_0 M'_{(c)} + \delta_b ML'_{b(c)} + \delta_d ML'_{d(c)}$$
$$= \delta_{a0} MZ_{a(c)} + \delta_{0b} ML_{b(c)} + \delta_{cd} MZ_cL_{d(c)}$$

where δ_k and δ_{kl} are Krœnecker deltas for the different insoluble species (then $\delta_{k\neq j} = 0$ and $\delta_j = 1$, or $\delta_{kl\neq ij} = 0$ and $\delta_{ij} = 1$, for the most insoluble species). This definition implies that the solution is saturated since condensed phases cannot coexist with it otherwise.

Then, the generalized second-order solubility equilibrium can be defined

$$M''_{(c)} \rightleftharpoons M'' \quad \text{with } K^{M''_{(c)}}_{M''} = [M'']_{sat} \tag{16}$$

From the definitions of $M''_{(c)}$, M″ and the solubility of each condensed phase, Eqn. 16 can be identified with the minimum solubility of the set of Eqns. 12–14. For example, under a certain imposed pH and pL′, the most insoluble species may be $MZ_{a(c)}$, whereas under different imposed pH and pL′ the most insoluble species may be $MZ_cL_{d(c)}$; then,

$$K^{M''_{(c)}}_{M''} = [M'']_{sat} \equiv s_{MZ_xL_{y(c)minimum}} = s_{M''_{(c)}(H,L')} \tag{17}$$

where

$s_{MZ_xL_{y(c)}} \in \{s_{MZ_{a(c)}}, s_{ML_{b(c)}}, s_{MZ_cL_{d(c)}}\}$

Graphical representations of M″ parameterized by pL′ and pH.

We have shown earlier that it is possible to construct two-dimensional predominance zone diagrams (PZD), pL′/pH, for the soluble species M″, where the predominance trajectories are given by equations of the type $pL' = 1/(j-i)\log K^{(j-i)L'}_{ML'_j}$ and where the stability of the ampholites is analysed by generalized first-order dismutation equilibria [12].

On the other hand, with respect to the insoluble part $M''_{(c)}$, the following considerations can be made.

According to the previous discussion, only up to two condensed phases can coexist here with the solution; this can be written as interconversion phase equilibria:

$$ML'_{x(c)} + (y-x)L' \rightleftharpoons ML'_{y(c)}$$

with

$$K^{ML'_{x(c)}}_{ML'_{y(c)}} = \frac{[ML'_{y(c)}]}{[ML'_{x(c)}][L']^{y-x}} \qquad (18)$$

As the activities of $ML'_{x(c)}$ and $ML'_{y(c)}$ can be considered as unity when they coexist with the solution (having the same solubility), then

$$pL'_{int} = \frac{1}{(y-x)} \log K^{ML'_{x(c)}}_{ML'_{y(c)}} \qquad (19)$$

where pL'_{int} is the concentration of L′ at which $ML'_{x(c)}$ and $ML'_{y(c)}$ coexist with the solution and interconvert into one other. Then, at constant T, P and pH (or T, P and pL′) and owing to the coexistence of the three phases, there are zero degrees of freedom in the system; this means that the chemical composition of the solution is invariant.

The interconversion trajectories of condensed phases described by the equation set 18 (triple trajectories) can be represented on a pL′/pH plane (Fig. 2), which constitutes a condensed-phase diagram (CPD). It can be seen here that for the system M–L–HZ–H these trajectories must be parallel for the reasons discussed earlier.

Outside of the interconversion trajectories, only one condensed phase could coexist with the solution. For example, at pH_1 and $pL'_1 < pL' < pL'_2$, the insoluble species $ML'_{d(c)}$ could coexist with the solution as it is the most insoluble species.

On the other hand, when the solution and a condensed phase coexist (at constant T, P and $pH = pH_1$), there is one degree of freedom (this could be represented by pL′). Then, under these conditions and at $pL' > pL'_2$, the solution coexists with $M'_{(c)}$; when the concentration of L′ is increased, the system reaches new equilibria by following a vertical trajectory (Fig. 2) until it reaches $pL' = pL'_2$. From that point on, an increase in the amount of L′ does not mean a decrease in pL′ but a transformation of $M'_{(c)}$ into $ML'_{d(c)}$ until $M'_{(c)}$ is exhausted. Any addition of L′ will again mean a decrease in pL′, as only one phase, $ML'_{d(c)}$ coexists with the solution.

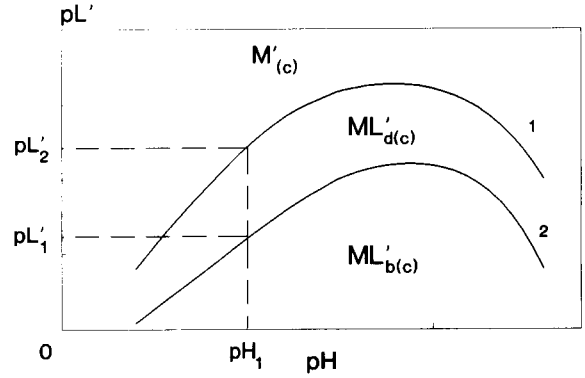

Fig. 2. Condensed phases diagram for the system M–L–HZ–H. The continuous lines correspond to the interconversion trajectories (Eqn. 18) of the phases: (1) $M'_{(c)}$ with $ML'_{d(c)}$, (2) $ML'_{d(c)}$ with $ML'_{b(c)}$. pL'_2 corresponds to the interconversion of $M'_{(c)}$ and $ML'_{d(c)}$ at pH_1, and pL'_1 corresponds to the interconversion of $ML'_{d(c)}$ and $ML'_{b(c)}$.

In the same way as in the PZD for soluble species [12], the interconversion equilibria and their trajectories must be considered for increasing L′/M′ ratio. Owing to the electroneutrality of the condensed phases, it is not possible to define arbitrarily a given L′/M′ stoichiometry.

In a different way to that for soluble species, dismutation equilibria of condensed phases cannot be established here as this would imply the coexistence of the solution with three condensed phases. However, it could happen that the interconversion trajectory (2) (Fig. 2) could be located above trajectory (1); this would mean that phase $ML'_{d(c)}$ is unstable; for this reason, only the interconversion trajectory from $M'_{(c)}$ to $ML'_{b(c)}$ would be represented.

Graphical representation of pM″/pL′/pH: the PED. Up to now, we have discussed the PZD of the chemical species in solution (which is the same regardless of whether the solution is saturated or not) and the condensed phases diagram built on the hypothesis that the solution be saturated (although it permits one to establish which

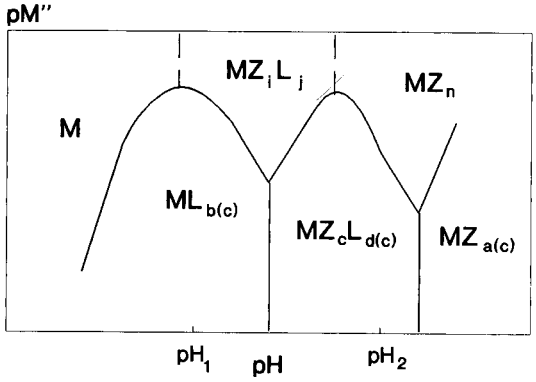

Fig. 3. Slice cut of pM″/pH at constant pL′ in the three-dimensional predominance–existence diagram of a hypothetical system of the type M–L–HZ–H. The points at (pH_1, pM''_1) and (pH_2, pM''_2) correspond to triple points where two condensed phases coexist with the solution.

is the most insoluble phase for certain known conditions).

Then, according to equilibrium 16 and Eqn. 17, it is possible to construct a PED pM″/pL′/pH in an analogous way to that described for systems of the type M–HZ–H by plotting the saturation trajectory described by

$$pK^{M''_{(c)}}_{M''} = -\log s_{MZ_xL_{y(c)minimum}} = pM''_{sat} \qquad (20)$$

The pL′ and pH intervals where a particular species MZ_xL_y is the most insoluble are selected from the CPD. Then, the corresponding function of Eqn. 20 is plotted only within these intervals.

Equation 20 corresponds to a surface in the three-dimensional pM″/pL′/pH predominance–existence diagram. Figure 3 shows a slice cut of pM″/pH at constant pL′.

In the diagram shown in Fig. 3, the continuous lines correspond to the trajectory $pK^{M''_{(c)}}_{M''} = -\log s_{MZ_xL_{y(c)minimum}} = pM''_{sat}$. Note that for pH < pH_1, $pK^{M''_{(c)}}_{M''} = -\log s_{ML_{b(c)}}$; for pH_1 < pH < pH_2, $pK^{M''_{(c)}}_{M''} = -\log s_{MZ_cL_{d(c)}}$; and for pH > pH_2, $pK^{M''_{(c)}}_{M''} = -\log s_{MZ_{a(c)}}$.

If $pM'' > pK^{M''_{(c)}}_{M''}$, no condensed phases can coexist in the solution and the diagram shows the zones of predominance of the different species of M″. The zone at MZ_iL_j corresponds to the predominance zones of different chemical species with different i and j values.

If $pM'' > pK^{M''_{(c)}}_{M''}$, the solution is supersaturated and the most insoluble phase will be formed until the saturation line is reached

$$pM''_{sat} = pK^{M''_{(c)}}_{M''}$$

Systems of the type $\underbrace{M\text{–}L\text{–}\ldots\text{–}X\text{–}HZ\text{–}H}_{\tau+2}$ *with buffering in* $\underbrace{L^{(\tau)},\ldots,X',\ H}_{\tau+1}$ *at constant T and P*

By using a generalization of the method discussed above, it is possible to define the $(\tau+1)$-order generalized species under these conditions:

In solution,

$$[M^{(\tau+1)}] = [M]\alpha_{M[H,\,X',\ldots,L^{(\tau)}]} \qquad (21)$$

where

$$\alpha_{M[H,\,X',\ldots,L^{(\tau)}]} = \alpha_{M(H)}\alpha_{M'(X')}\cdots\alpha_{M^{(\tau)}[L^{(\tau)}]} \qquad (22)$$

Equations 21 and 22 have been discussed previously in more detail [11,12].

For the condensed phases,

$$M^{(\tau)}_{(c)} = ML_i\ldots X_jZ_{k(c)}\ \text{(most insoluble)} \qquad (23)$$

selected from the set of condensed phases that could co-exist with the solution.

The $(\tau+1)$-order species, $M^{(\tau+1)}$ and $M^{(\tau+1)}_{(c)}$, can be represented in a multi-dimensional $pL^{(\tau)}/\ldots/pX'/pH$ PZD and in a CPD, respectively. In the construction of the CPD, it is important to consider the maximum number of phases that can coexist in the system (phase rule), and also the electroneutrality conditions of the condensed phases and the number of variables involved in the solubility expressions. In this case, the interconversion trajectories of condensed phases are not necessarily parallel; then, phase-dismutation equilibria could be defined to study the stability of the intermediate stoichiometry species, in a particular component.

It is then possible to establish a $(\tau+1)$-order solubility equilibrium:

$$M^{(\tau+1)}_{(c)} \rightleftharpoons M^{(\tau+1)} \quad \text{with}$$

$$K^{M^{(\tau+1)}_{(c)}}_{M^{(\tau+1)}} = [M^{(\tau+1)}]_{sat} = s_{M^{(\tau+1)}_{(c)}} \qquad (24)$$

where $s_{M^{(\tau+1)}_{(c)}} = s_{ML_i\ldots X_jZ_{k(c)}minimum}$.

Finally, it is possible to construct the PED $pM^{(\tau+1)}/pL^{(\tau)}/\ldots pX'/pH$ by plotting the saturation trajectory defined by Eqn. 24.

This analysis demonstrates that the mathematical structure of the intrinsic solubility equilibrium [16] is generalizable to multi-component systems under multiple buffering conditions and that it includes mixed species both in the solution as well as in the condensed phases, as shown in Eqn. 24. Likewise, this equation gives a more direct interpretation of the systems that reach saturation conditions as it allows for the construction of diagrams where the most important species, both in the solution and in the condensed phases, are made evident.

In general, the solubility trajectory described by Eqn. 24 is found graphically by superimposing all the solubility trajectories of the condensed phases associated with the system [17]. In this work, an alternative method is proposed that consists of the initial construction of the CPD where the intervals of composition where a phase is more insoluble than the others are established. Then, the solubility of each condensed phase is evaluated only in the composition interval where it is the most insoluble.

EXAMPLES

Three examples are now presented to exemplify the most important aspects of the methods just discussed, namely the systems Zn(II)–H_2O–H, Zn(II)–$H_2C_2O_4$–H_2O–H and Ca(II)–$H_2C_2O_4$–H_2SO_4–H_2O–H (where $H_2C_2O_4$ is oxalic acid). The chemical species considered here, and the equilibrium constants that regulate the relationships among them come from various sources [15,18–20].

Table 1 summarizes the data used to construct the diagrams for Zn(II) systems. These data consider an ionic strength lower than 0.5 M and the logarithmic values of the related equilibrium constants can vary in the range ± 0.2. For these species the data reported by Ringbom [15] were used in order to compare the diagrams presented in this paper with those reported previously [10].

As can be seen, the three systems permit the thermodynamic prediction of the solubilities, because they have a wide application in analytical chemistry in gravimetric methods.

Zn(II)–H_2O–H system

Generalized first-order species present in the system. The predominance–existence diagram pZn'/pH can be constructed by defining the generalized first-order species:

$$Zn(II)' = Zn' = Zn^{2+} + Zn(OH)^{+} + Zn(OH)_3^{-} + Zn(OH)_4^{2-}$$

$$Zn(II)'_{(s)} = Zn'_{(s)} = Zn(OH)_{2(s)}$$

Graphical representations. With the data reported by Ringbom [15], the generalized first-order solubility equilibrium is then

$$Zn'_{(s)} \rightleftharpoons Zn' \quad \text{with } K_{Zn'}^{Zn'_{(s)}} = [Zn']_{sat} = s_{Zn(OH)_{2(s)}}$$

TABLE 1

Data used to construct the diagrams for the Zn(II)–H_2O–H and Zn(II)–$H_2C_2O_4$–H_2O–H systems [15]

Equilibrium	Log K
$Zn + 2OH \rightleftharpoons Zn(OH)_{2(s)}$	15.68
$Zn + C_2O_4 \rightleftharpoons ZnC_2O_{4(s)}$	8.89
$H + C_2O_4 \rightleftharpoons HC_2O_4$	4.00
$2H + C_2O_4 \rightleftharpoons H_2C_2O_4$	5.10
$Zn + C_2O_4 \rightleftharpoons ZnC_2O_4$	3.70
$Zn + 2C_2O_4 \rightleftharpoons Zn(C_2O_4)_2$	6.00
$Zn + OH \rightleftharpoons ZnOH$	4.40
$Zn + 3OH \rightleftharpoons ZnOH_3$	14.40
$Zn + 4OH \rightleftharpoons ZnOH_4$	15.50
$Zn + H + C_2O_4 \rightleftharpoons ZnHC_2O_4$	5.60
$Zn + 2H + 2C_2O_4 \rightleftharpoons Zn(HC_2O_4)_2$	10.80

and as $[Zn']_{sat} = [Zn^{2+}]_{sat}\alpha_{Zn(OH)}$, one obtains $[Zn^{2+}]_{sat}$ from the ionic equilibrium product.

The PED pZn'/pH is presented in Fig. 4, where the continuous line represents $-\log s_{Zn(OH)_{2(s)}}$ thus calculated. For this well known case, the treatment is trivial. Figure 4 is similar to those reported earlier [15], except that here the ordinate scale is given by pZn' (as Kragten does [17]) and not $-\log s_{Zn(OH)_{2(s)}}$.

Zn(II)–$H_2C_2O_4$–H_2O–H system

Generalized species involved in the system. The different graphical representations of this system can be constructed on the basis of the definition of the generalized second order species Zn″ and $Zn''_{(s)}$.

The partition of generalized species is as follows:

(a) with respect to C_2O_4':

$Zn(II)'' = Zn'' = Zn' + Zn(C_2O_4)' + Zn(C_2O_4)_2'$.

$Zn(II)''_{(s)} = Zn''_{(s)}$ = the most insoluble between $Zn'_{(s)}$ and $ZnC_2O_{4(s)}'$

(b) with respect to H and OH:

$C_2O_4' = H_2C_2O_4 + HC_2O_4^- + C_2O_4^{2-}$

$Zn' = Zn^{2+} + Zn(OH)^+ + Zn(OH)_3^- + Zn(OH)_4^-$

$ZnC_2O_4' = ZnC_2O_4 + ZnHC_2O_4^+$

$Zn(C_2O_4)_2' = Zn(C_2O_4)_2^{2-} + ZnH_2(C_2O_4)_2$

$Zn'_{(s)} = Zn(OH)_{2(s)}$

$ZnC_2O_{4(s)}' = ZnC_2O_{4(s)}$

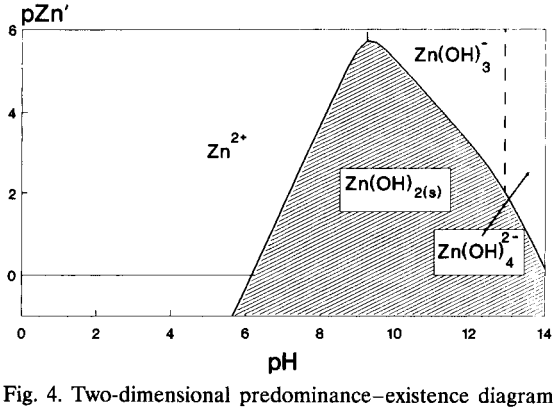

Fig. 4. Two-dimensional predominance–existence diagram of the system Zn–H_2O–H as a function of first-order generalized species of Zn(II) (Zn') and pH. Solid line corresponds to saturation condition.

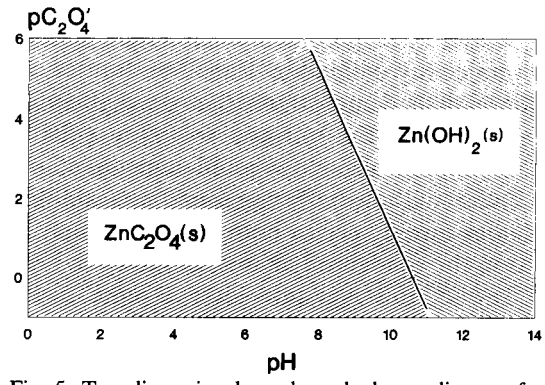

Fig. 5. Two-dimensional condensed phases diagram for the system Zn(II)–$H_2C_2O_4$–H_2O–H. The solid line corresponds to first-order generalized interconversion trajectories of the solid phases and invariant conditions in the system.

The chemical equilibrium constants that correlate the species proposed here are those reported by Ringbom [15]; in this way, the resulting diagrams can be compared with those in previous work [10].

Graphical representations on the pC_2O_4'/pH plane. The PZD pC_2O_4'/pH has been reported and discussed previously [10].

Figure 5 represents the CPD of this system on the plane pC_2O_4'/pH. The trajectory shown corresponds to the generalized first-order interconversion equilibrium

$$Zn'_{(s)} + C_2O_4' \rightleftharpoons ZnC_2O_{4(s)}'$$

As for this equilibrium

$$K^{Zn'_{(s)},\,C_2O_4'}_{ZnC_2O_{4(s)}'} = \frac{[ZnC_2O_{4(s)}']}{[Zn'_{(s)}][C_2O_4']_{int}}$$

then

$$pC_2O_{4int}' = \log K^{Zn'_{(s)},\,C_2O_4'}_{ZnC_2O_{4(s)}'}$$

In the interconversion trajectory, both $Zn(OH)_{2(s)}$ and $ZnC_2O_{4(s)}$ coexist with the solution. Outside it, only the most insoluble phase can coexist: $Zn(OH)_{2(s)}$

if $pC_2O_4' > -\log K^{Zn'_{(s)},\,C_2O_4'}_{ZnC_2O_{4(s)}'}$

or $ZnC_2O_{4(s)}$

if $pC_2O_4' < -\log K^{Zn'_{(s)},\,C_2O_4'}_{ZnC_2O_{4(s)}'}$

Graphical representation in the pZn″/pC$_2$O$_4'$/pH space. The three-dimensional diagram can be obtained by using the generalized second order equilibrium

$$Zn''_{(s)} \rightleftharpoons Zn'' \quad \text{with } K^{Zn''_{(s)}}_{Zn''} = [Zn'']_{sat}$$

as $pK^{Zn''_{(s)}}_{Zn''}$ represents the saturation surface in the three-dimensional space pZn″/pC$_2$O$_4'$/pH (Fig. 6a).

According to Eqn. 17,

$$K^{Zn''_{(s)}}_{Zn''} = [Zn''_{sat}] = [Zn^{2+}]_{sat}\alpha_{Zn'(C_2O_4')}\alpha_{Zn(H)}$$

in Fig. 6a the solution is not saturated above the saturation surface

$$pZn''_{sat} > -\log K^{Zn''_{(s)}}_{Zn''}$$

and the PZD of species Zn″ could be represented [10]. The predominance boundaries (not shown in the diagram) would be surfaces obtained by the projection of the lines of the PZD [10] above the saturation surface.

The projection of the interconversion trajectory of $ZnC_2O_{4(s)}'$ into $Zn'_{(s)}$ (Fig. 5) generates the interconversion surface projected down the saturation surface

$$pZn''_{sat} < -\log K^{Zn''_{(s)}}_{Zn''},$$

the black surface in Fig. 6a.

Then, below the saturation surface and when $pC_2O_4' > -\log K^{Zn'_{(s)},\,C_2O_4'}_{Zn(C_2O_4)'_{(s)}}$, the phase that coexists with the solution is $Zn(OH)_{2(s)}$, whereas if $pC_2O_4' < -\log K^{Zn'_{(s)},\,C_2O_4'}_{Zn(C_2O_4)'_{2(s)}}$, the coexisting phase is $ZnC_2O_{4(s)}$. In Fig. 6a the dark grey surface represents $-\log s_{Zn(OH)_{2(s)}}$ and the light grey surface represents $-\log s_{ZnC_2O_{4(s)}}$.

This rationale can also be visualized in the slice cut pZn″/pH at $pC_2O_4' = 1.0$ for this system (Fig. 6b). The continuous line in Fig. 6b corresponds to the saturation trajectory of $Zn''_{(s)}$ (corresponding to the most insoluble phase). The point at (10.105, 3.89) is the triple point of this system (where pC_2O_4' is buffered at 1.0). If pH > 10.105, the most insoluble species is $Zn(OH)_{2(s)}$ and pZn''_{sat} (Fig. 6b) is identical with pZn'_{sat} in Fig. 5.

If pH < 10.105 the most insoluble species in the system (at $pC_2O_4' = 1.0$) is $ZnC_2O_{4(s)}$. In this system, if $pZn'' > pZn''_{sat}$ the solution is not saturated and the diagram shows a PZD identical with the slice cut of the PZD at $pC_2O_4' = 1.0$ [10].

In the region where $pZn'' < pZn''_{sat}$, the diagram corresponds to a slice cut at the point $pC_2O_4' = 1.0$ of the phase diagram in Fig. 5.

Figure 6 can be applied to understand, qualitatively, the gravimetric methods for determination of Zn with oxalic acid as precipitation reagent [21]. A detailed thermodynamic study of these methods, with the aid of graphical representations, should consider the specific conditions of the medium (such as ionic force and concentration of buffers). For the precipitation of zinc oxalate it is recommended that 85% acetic acid

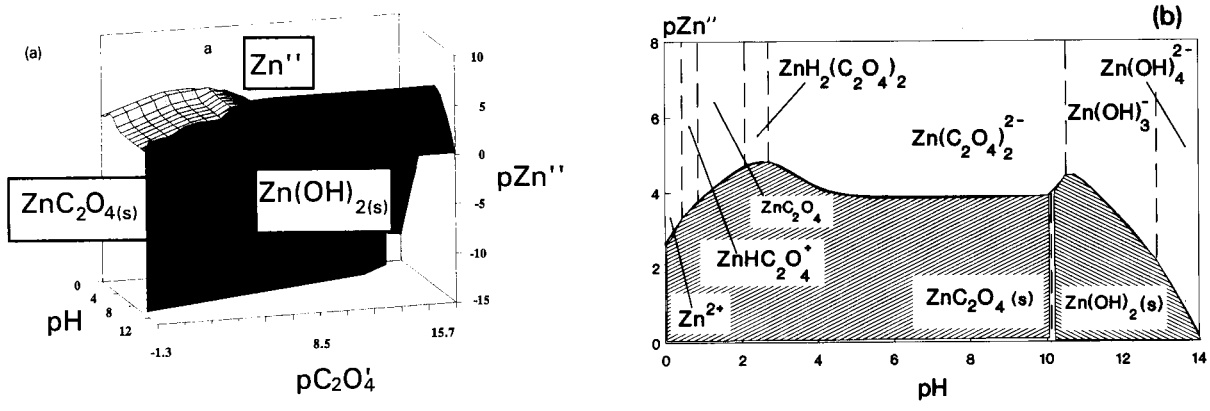

Fig. 6. (a) Three-dimensional predominance–existence diagram of the system Zn(II)–$H_2C_2O_4$–H_2O–H as a function of second-order generalized species of Zn(II) (Zn″) and pH. The saturation conditions are represented by a surface. (b) Slice cut pZn″/pH at $pC_2O_4' = 1.0$ from the three-dimensional predominance-existence diagram.

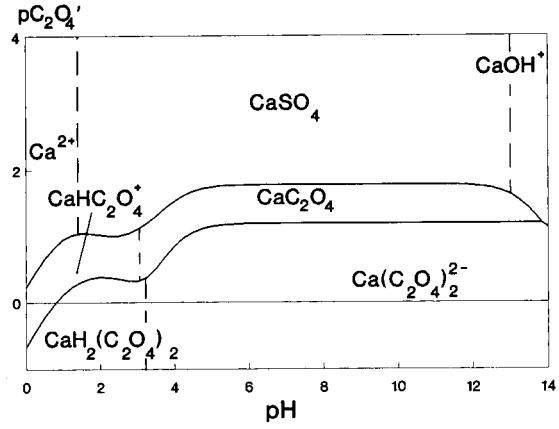

Fig. 7. Two-dimensional predominance zone diagram for the soluble chemical species involved in the third-order generalized species of Ca(II) (Ca''') as a function of second-order generalized oxalate activity (C_2O_4'') and pH. This diagram corresponds to a slice cut at $pSO_4'' = 2.0$ from the related $pC_2O_4''/pSO_4'/pH$ diagram.

be added; for this reason, the values of the equilibrium constants are different and the precipitation of zinc oxalate is favoured by the change in the dielectric constant of the solvent.

Ca(II)–$H_2C_2O_4$–H_2SO_4–H_2O–H

Generalized third order species present in the system. (a) With respect to C_2O_4'':

$$Ca(II)''' = Ca''' = Ca'' + CaC_2O_4'' + Ca(C_2O_4)_2''$$

TABLE 2

Data used to construct the diagrams for the Ca(II)–$H_2C_2O_4$–H_2SO_4–H_2O–H system [18–20]

Equilibrium	Log K
$H + C_2O_4 \rightleftharpoons HC_2O_4$	4.00
$2H + C_2O_4 \rightleftharpoons H_2C_2O_4$	5.10
$H + SO_4 \rightleftharpoons HSO_4$	1.99
$Ca + C_2O_4 \rightleftharpoons CaC_2O_{4(s)}$	7.90
$Ca + 2OH \rightleftharpoons Ca(OH)_{2(s)}$	5.26
$Ca + SO_4 \rightleftharpoons CaSO_{4(s)}$	4.37
$Ca + SO_4 \rightleftharpoons CaSO_4$	2.37
$Ca + C_2O_4 \rightleftharpoons CaC_2O_4$	2.30
$Ca + 2C_2O_4 \rightleftharpoons Ca(C_2O_4)_2$	3.49
$Ca + HC_2O_4 \rightleftharpoons CaHC_2O_4$	1.38
$Ca + 2HC_2O_4 \rightleftharpoons Ca(HC_2O_4)_2$	1.85
$Ca + H_2O \rightleftharpoons CaOH + H$	12.85

$Ca(II)''_{(s)} = Ca'''_{(s)}$ = the most insoluble between $Ca''_{(s)}$ and $CaC_2O''_{4(s)}$.

(b) With respect to SO_4':

$$C_2O_4'' = C_2O_4'$$

$$Ca'' = Ca' + CaSO_4'$$

$$CaC_2O_4'' = CaC_2O_4'$$

$$Ca(C_2O_4)_2'' = Ca(C_2O_4)_2'$$

$Ca''_{(s)}$ = the most insoluble between $Ca'_{(s)}$ and $CaSO'_{4(s)}$

$$CaC_2O''_{4(s)} = CaC_2O'_{4(s)}$$

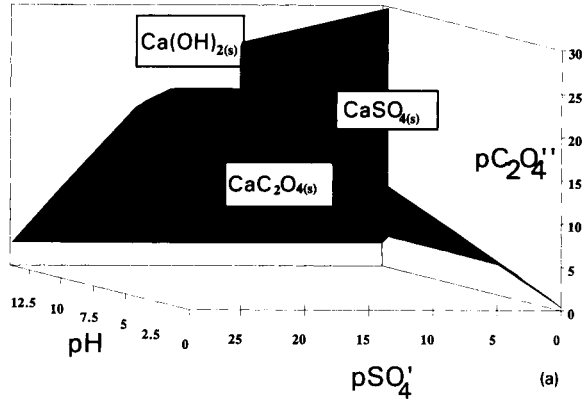

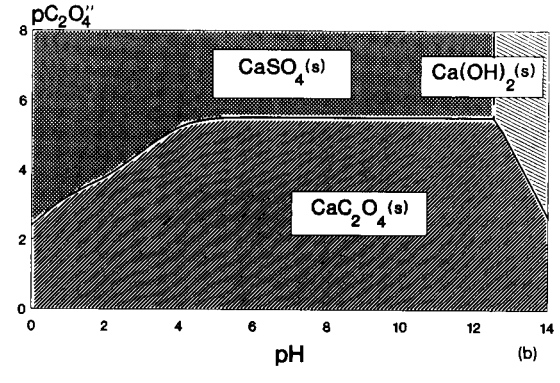

Fig. 8. (a) Three-dimensional condensed phases diagram for the chemical species involved in the third-order condensed generalized species of Ca(II) [$Ca'''_{(c)}$] as a function of second-order generalized oxalate activity (C_2O_4''), first-order generalized sulphate activity (SO_4') and pH. (b) Slice cut pC_2O_4''/pH at $pSO_4' = 2.0$ from the diagram in (a).

(c) With respect to H and OH:

$$SO_4' = HSO_4^- + SO_4^{2-}$$

$$C_2O_4' = H_2C_2O_4 + HC_2O_4^- + C_2O_4^{2-}$$

$$Ca' = Ca^{2+} + Ca(OH)^+$$

$$CaSO_4' = CaSO_4$$

$$CaC_2O_4' = CaHC_2O_4^+ + CaC_2O_4$$

$$Ca(C_2O_4)_2' = CaH_2(C_2O_4)_2 + Ca(C_2O_4)_2^{2-}$$

$$Ca'_{(s)} = Ca(OH)_{2(s)}$$

$$CaSO'_{4(c)} = CaSO_{4(s)}$$

$$CaC_2O'_{4(s)} = CaC_2O_{4(s)}$$

The chemical equilibrium constants that correlate the species proposed above are those reported by Baes and Mesmer [18], Högfeldt [19] and Sillén [20].

Table 2 summarizes the data used to construct the diagrams presented in this example. These data consider an ionic strength lower than 0.1 M.

Graphical representations. The graphical representation of Ca''' is represented in a three-dimensional PZD $pC_2O_4''/pSO_4'/pH$ constructed according to the method reported previously [11,12]. Here, only a two-dimensional slice cut of that diagram is presented (pC_2O_4''/pH at $pSO_4' = 2.0$; Fig. 7). The continuous lines represent the trajectories of the type $pC_2O_4' = [1/(j-i)]\log K^{(j-i)C_2O_4''}_{Ca(C_2O_4)_j''}$ (at $pSO_4' = 2.0$). For a more detailed discussion of the interpretation of this diagram, see [11,12].

The phase diagram of $Ca'''_{(s)}$ is represented in Fig. 8a in the space $pC_2O_4''/pSO_4'/pH$. In this space, the black and dark grey surfaces correspond to the logarithm of the two-conditional constant

$$\log K^{Ca''_{(s)}}_{CaC_2O''_{4(s)}}$$

of the second-order generalized interconversion equilibrium $Ca''_{(s)} + C_2O_4'' \rightleftharpoons CaC_2O''_{4(s)}$. The black surface appears when $Ca''_{(s)} = CaSO_{4(s)}$ ($CaSO_{4(s)}$ more insoluble than $Ca(OH)_{2(s)}$). The dark grey surface appears when $Ca''_{(s)} = Ca(OH)_{2(s)}$. $CaC_2O''_{4(s)} = CaC_2O_{4(s)}$ appears below the black and dark grey surfaces.

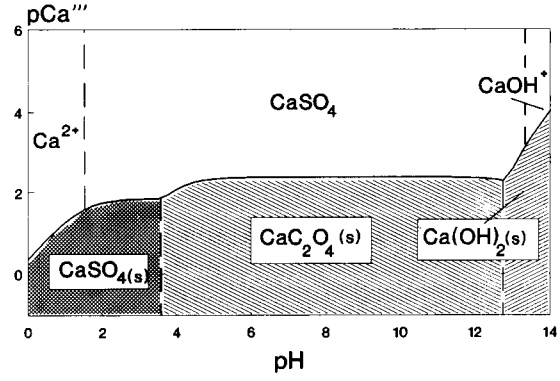

Fig. 9. Two-dimensional predominance–existence zone diagram for the system Ca(II)–$H_2C_2O_4$–H_2SO_4–H_2O–H as a function of generalized third-order species of Ca(II) (Ca''') and pH. This diagram corresponds to a slice cut at $pC_2O_4'' = 5.0$ and $pSO_4' = 2.0$ from the $pCa'''/pC_2O_4''/pSO_4'/pH$ predominance–existence diagram.

The light grey surface corresponds to the logarithm of the conditional constant of the first-order generalized interconversion equilibrium

$$Ca'_{(s)} + SO_4' \rightleftharpoons CaSO'_{4(s)}$$

The intersection of the three surfaces defines the quadruple trajectory for this system (i.e., four phases coexist).

Figure 8b represents a two-dimensional slice cut pC_2O_4''/pH at $pSO_4' = 2.0$ of the diagram in Fig. 8a.

The point ($pH = 12.55$, $pC_2O_4'' = 5.53$), at $pSO_4' = 2.0$, corresponds to the quadruple point; this point does not have any degrees of freedom since T, P and pSO_4' are fixed and four phases coexist.

The third-order generalized equilibrium $Ca'''_{(s)} \rightleftharpoons Ca'''$ with $K^{Ca'''_{(s)}}_{Ca'''} = s_{Ca'''_{(s)}}$ can be represented in a four-dimensional space $pCa'''/pC_2O_4''/pSO_4'/pH$.

Figure 9 represents a two-dimensional slice cut pCa'''/pH at $pC_2O_4'' = 5.0$ and $pSO_4' = 2.0$ of this diagram.

The interpretation of this PED is similar to those presented above.

Below the saturation line (Fig. 9), the coexistence of the phases $CaSO_{4(s)}$, $CaC_2O_{4(s)}$ and $Ca(OH)_{2(s)}$ with solution can be observed. The interconversion boundaries were obtained by slice cut of Fig. 8b for $pC_2O_4'' = 5.0$.

It should be noted that $CaC_2O_{4(s)}$ has a wide existence zone for these conditions, despite the small equilibrium concentration of C_2O_4'' and non-predominance soluble complexes of Ca''/C_2O_4''.

Slice cuts of a four-dimensional diagram $pCa'''/pC_2O_4''/pNH_3'/pH$ can be constructed to discuss the operating conditions of the qualitative [22] and quantitative [23] analytical methods for calcium determination, using oxalate as precipitation reagent. Likewise, the diagrams presented in this paper explain that H_2SO_4 cannot be used to acidify the media in these techniques.

Conclusions

An extension of the concept of generalized species for condensed phases permits generalized equilibria to be proposed for the interconversion of condensed phases. With this, it is possible to construct phase diagrams using a method similar to that for the construction of PZD. Likewise, it is possible to propose generalized solubility equilibria by using a basic scheme of intrinsic solubility [16].

On the other hand, the generalization of a mathematical structure of an ionic product equilibrium

$$ML_{b(c)} \rightleftharpoons M + bL$$

proposed by Ringbom [15] is not so evident; this is because even for a system with a small number of components (i.e., three or four) the complexity of the system grows owing to the number of solubility equilibria, the number of condensed phases that can coexist in the solution and the appearance of mixed species in both the soluble and in the condensed phases.

The generalized solubility equilibria proposed here permit PED to be constructed with a saturation trajectory defined by $pM^{(\tau+1)}$ [for a system of $(\tau+2)$ components and $(\tau+1)$ of it buffered]; this happens to be the same as that defined by Kragten [17] because for the systems studied here $pM^{(\tau+1)} = -\log C_{Mtotal}$, as polynuclear species are not considered, either in solution or in the condensed phases. The inclusion of this type of species will be discussed in Part II [24].

It is clear that the method proposed in this paper has the same limitations of any other thermodynamic study. It cannot take in account the kinetic effects (especially coprecipitation phenomena) and unstable condensed phases. It only can predict correctly the saturation conditions for systems that attain thermodynamic equilibrium rapidly or that can remain in a metastable state for a long time.

It should be noted that the precise trajectories of condensed phase interconversion predicted by thermodynamics do not correspond exactly with the experimental behaviour. These interconversion phenomena occur in a vicinity, more or less wide, of the corresponding trajectories.

The data used for the construction of the diagrams presented in this paper were selected for low values of ionic force. For systems with high values of ionic force, it is necessary to consider the variation of activity coefficients or to use data reported for medium specific conditions. For these reasons, it is necessary to undertake a very careful and detailed bibliographic revision concerning the thermodynamic data for the systems under study.

The authors thank Dr. Jorge Ibáñez for the English translation of this paper and PROIDES-SEP and CONACYT for financial support.

REFERENCES

1 N. Ingri, W. Kakolowicz, L.G. Sillén and B. Warnqvist, Talanta, 14 (1967) 1261.
2 F.J. Zelegnik and S. Gordon, Ind. Eng. Chem., 60 (1968) 29.
3 H.F. Felman, W.H. Simons and D. Bienstock, U.S. Bur. Mines. Rep. Invest., No. 7257 (1969) 22.
4 F. Morel and S. Morgan, Environ. Sci. Technol., 6 (1972) 58.
5 A.H. Truesdell and B.F. Jones, J. Res. U.S. Geol. Surv., 2 (1974) 233.
6 I.K. Karpov and L.A. Kazmin, Geochim. Int., 9 (1972) 252.
7 R. Gautman and W.D. Seider, AIChE J., 25 (1979) 991.
8 G. Eriksson, Anal. Chim. Acta, 112 (1979) 375.
9 W.R. Smith, Ind. Eng. Chem. Fundam., 19 (1980) 1.
10 A. Rojas and I. González, Anal. Chim. Acta, 187 (1986) 279.
11 A. Rojas-Hernández, M.T. Ramírez, J.G. Ibáñez and I. González, J. Electrochem. Soc., 138 (1991) 365.

12 A. Rojas-Hernández, M.T. Ramírez, J.G. Ibáñez and I. González, Anal. Chim. Acta, 246 (1991) 435.
13 A. Rojas-Hernández, M.T. Ramírez, I. González and J.G. Ibáñez, Anal. Chim. Acta, 259 (1992) 95.
14 G. Charlot, Cours de Chimie Analytique Générale, Masson, Paris, 1967.
15 A. Ringbom, Complexation in Analytical Chemistry, Wiley-Interscience, New York, 1963.
16 H.A. Laitinen and W.E. Harris, Chemical Analysis, McGraw-Hill, New York, 2nd edn., 1975.
17 J. Kragten, Talanta, 24 (1977) 483.
18 C.F. Baes, Jr., and R.E. Mesmer, The Hydrolysis of Cations, Wiley, New York, 1976.
19 E. Högfeldt, Stability Constants of Metal-Ion Complexes: Part A: Inorganic Ligands (IUPAC Chemical Data Series, No. 21), Pergamon, New York, 1979.
20 L.G. Sillén, Stability Constants of Metal-Ion Complexes (Special Publication No. 17), Chemical Society, London, 1971.
21 F.J. Welcher (Ed.), Standard Methods of Chemical Analysis, Vol. 2, Part A, Van Nostrand, New York, 6th edn., 1963.
22 United States Pharmacopeial Convention, The United States Pharmacopeia, 19th revision, Mack, Easton, PA, 1975.
23 G.H. Jeffery, J. Bassett, J. Menham and R.C. Demrey, Vogel's Textbook of Quantitative Chemical Analysis, Longman–Wiley, New York, 1989.
24 A. Rojas-Hernández, M.T. Ramírez and I. González, Anal. Chim. Acta, 278 (1993) 335.

Analytica Chimica Acta, 278 (1993) 335–347
Elsevier Science Publishers B.V., Amsterdam

Equilibria among condensed phases and a multi-component solution using the concept of generalized species

Part II. Systems with polynuclear species

Alberto Rojas-Hernández, M. Teresa Ramírez and Ignacio González

Universidad Autónoma Metropolitana–Iztapalapa, Departamento de Química, Apartado Postal 55-534, 09340 México D.F. (Mexico)

(Received 5th August 1992; revised manuscript received 8th December 1992)

Abstract

In this second part a general algorithm is presented which is based on the definition of total generalized species and equilibria and the combination of Charlot and Ringbom's approaches; this leads to the establishment of the relative importance of the chemical species present in a multi-component–multi-reacting system that includes complexation, polynucleation and phase-formation phenomena. The definition of total generalized species [$^{\dagger}M^{(\tau)}$ and $^{\dagger}M_{(c)}^{\{\tau\}}$] permits an expression to be obtained for the total generalized intrinsic solubility equilibria for the calculation of the saturation conditions in a solution in spite of the presence of polynuclear species both in the solution and in the condensed phases. The symbol used for the total generalized species implies that the subscripts for the polynucleation of M are included in the superscript dagger (†). The procedure used to select the most insoluble phase from the condensed-phases diagram of this system was described in Part I. In order to exemplify the scope of the proposed algorithm, graphical representations of the following systems are discussed: Be(II)–H_2O–H, Be(II)–H_4PDTA–H_2O–H, Ca(II)–H_3PO_4–H_2O–H and Mg(II)–H_3PO_4–NH_3–H_2O–H, where, H_4PDTA is 1,3-diaminopropylene-*N*,*N*,*N*′,*N*′-tetraacetic acid.

Keywords: Condensed-phase equilibria; Equilibria; Generalized species; Polynuclear species

In Part I [1] the equilibria between a solution and condensed phases in multi-component and multi-reacting systems were discussed, using the concepts of generalized species and equilibria. It was shown that the definition of generalized interconversion equilibria allows for the construction of condensed-phases diagrams (CPD). From these diagrams, the most insoluble phase (or the one that minimizes the free energy of the system) can be selected in order to predict the saturation conditions of the solution. In addition, this information was shown to lead to the definition of generalized solubility equilibria that include several condensed phases dependent only on the buffering conditions; this, in turn, permits these saturation conditions to be represented graphically on a predominance–existence diagram (PED). In this second part, the algorithm that allows for the inclusion of polynuclear species both in the solution and in the condensed phases is discussed.

Correspondence to: A. Rojas-Hernández, Universidad Autónoma Metropolitana–Iztapalapa, Departamento de Química, Apartado Postal 55-534, 09340 México D.F. (Mexico).

THEORY

The following discussion has, for comparison, the same structure as that in Part I [1].

Systems of the type M–Z, where Z is an inert solvent

As Z is inert, the only polynucleation and dismutation equilibria that may exist in the solution are those that relate the polynuclear species M_i ($i \in \{1, 2, \ldots, m\}$).

According to the phase rule, the number of degrees of freedom (F) in the system is

$$F = C - P + 2 \quad (1)$$

where C and P are the number of components and the number of phases in the system, respectively.

When $F = 0$ [at constant temperature (T) and pressure (P)], two phases coexist [2]. These are the solution and a pure substance of the type $M_{x(c)}$ ($x \in \{1, 2, \ldots, r\}$), where the subscript (c) indicates that M_x exists as a pure substance in the form of a condensed phase. Of all the many phases that could coexist with the solution, only the most stable allotropic form, which is also the most insoluble form, must be taken into consideration. This phase will be called $M_{a(c)}$.

Then, the solubility equilibria to be considered in the system are

$$iM_{a(c)} \rightleftharpoons aM_i \text{ with } K_{aM_i}^{iM_{a(c)}} = [M_i]_{sat}^a \quad (2)$$

where $i \in \{1, 2, \ldots, m\}$.

It may be recalled that these equilibria are meaningful only when both phases can coexist. In this case, the properties of the system are completely defined. Then, the solution is saturated and the total concentration of M in the system ($C_{M\,TOTAL}$) is the solubility of $M_{a(c)}$ (s_{M_a}) in solvent Z. Then,

$$s_{M_a} = C_{M\,TOTAL} = \sum_{i=1}^{m} i[M_i]_{sat} = \sum_{i=1}^{m} i\left[K_{aM_i}^{iM_{a(c)}}\right]^{1/a} \quad (3)$$

An equivalent route for the derivation of Eqn. 3 can be found by defining the **total generalized species**:

$$[^{\dagger}M] \equiv \sum_{i=1}^{m} i[M_i] = C_{M\,TOTAL} \quad (5)$$

and

$$^{\dagger}M_{(c)} \equiv M_{a(c)}$$

where the superscript dagger (†) indicates that all the polynuclear species involved in that phase have been considered.

Then, from Eqn. 4, the total generalized solubility equilibria can be defined as follows:

$$^{\dagger}M_{(c)} \rightleftharpoons {}^{\dagger}M \text{ with } K_{^{\dagger}M}^{^{\dagger}M_{(c)}} = [^{\dagger}M]_{sat} \quad (5)$$

and $a_{^{\dagger}M_{(c)}} = 1$. Here $K_{^{\dagger}M}^{^{\dagger}M_{(c)}}$ is a generalized constant which, according to Eqns. 3 and 4, is precisely the solubility of $M_{a(c)}$:

$$s_{M_{a(c)}} = K_{^{\dagger}M}^{^{\dagger}M_{(c)}} \quad (6)$$

As we have shown previously [3], it is possible to represent the predominance of soluble species in the system on a $-\log C_{M\,TOTAL}$ scale (or, using the nomenclature defined in the present paper, a $p^{\dagger}M$ scale). Then, if $m = 3$ in a system where the ampholyte may predominate [3],

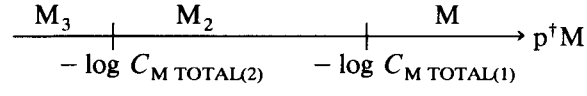

where

$$C_{M\,TOTAL(1)} = 3C_1 + 3K_{M_3}^{3M} C_1^3$$

$$C_{M\,TOTAL(2)} = \frac{C_2}{K_{M_2}^{2M}} + 5C_2$$

$C_1 = [M] = [M_2]$ and $C_2 = [M_2] = [M_3]$. However, according to Eqns. 4–6, it is also possible to include in this $p^{\dagger}M$ scale the saturation condition of $M_{a(c)}$ in the system ($p^{\dagger}M_{sat}$), since

$$p^{\dagger}M_{sat} = -\log s_{M_a} = pK_{^{\dagger}M}^{^{\dagger}M_{(c)}} = -\log \sum_{i=1}^{m} i\left[K_{aM_i}^{iM_{a(c)}}\right]^{1/a} \quad (7)$$

In unsaturated conditions ($p^{\dagger}M > -\log s_{M_a}$), Fig. 1 shows the predominance of the soluble species M_i [here $M_{a(c)}$ does not exist]. When the solution becomes saturated (at $p^{\dagger}M = -\log s_{M_a}$), its composition becomes invariant and the species that have not been predominant up to that point cannot be predominant. As is well known, the supersaturated conditions ($p^{\dagger}M < -\log s_M$) can-

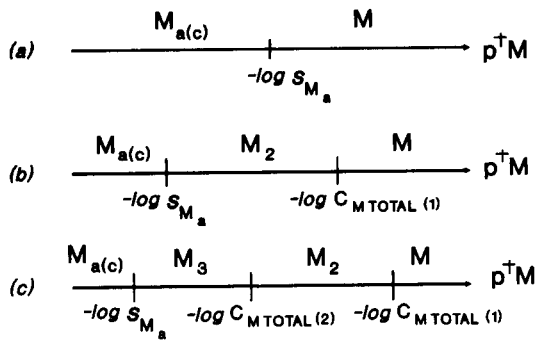

Fig. 1. Possible predominance–existence diagrams (PED) for the system $M_{a(c)}/M_3/M_2/M$ in the inert solvent Z, at constant temperature. (a) $-\log s_{M_a} > -\log C_{M\,TOTAL(1)}$; (b) $-\log C_{M\,TOTAL(2)} < -\log s_{M_a} < -\log C_{M\,TOTAL(1)}$; (c) $-\log s_{M_a} < -\log C_{M\,TOTAL(2)}$. Here $[{}^{\dagger}M'] \equiv C_{M\,TOTAL}$.

not be reached under thermodynamic equilibrium conditions; if it were reached with the initial conditions, this would mean that $M_{a(c)}$ would appear. For this reason, the existence of $M_{a(c)}$ is associated with the third region.

Systems of the type M–HZ–H, where HZ is an amphiprotic solvent at constant T and P

In this type of system, the following species can be formed in solution: M_iZ_j, $i \in \{0, 1, 2, \ldots, m\}$, $j \in \{0, 1, 2, \ldots, n(i)\}$. (It is assumed that species of the type M_iH_h can not be formed and charges are omitted for simplicity.)

According to Eqn. 1 and considering $C = 3$, the maximum number of phases that can coexist in the system is $F_{max} = 5$ (when $F = 0$).

Coexistence of the solution with a condensed phase at constant T and P. In the same manner as for the M–Z system, of the many condensed phases that may coexist with the solution, only the most stable allotropic form must be taken in account; this is, of course, the most insoluble form owing to the electroneutrality principle in each phase and the charge on each species. Here, the most insoluble phase will be called $M_aZ_{b(c)}$.

pH buffered system. Given the buffering in pH, the value of pZ is also buffered; then, the first-order generalized species [1], M_i' and $M'_{a(c)}$, are defined as

$$[M_i'] = \sum_{j=0}^{n(i)} i[M_iZ_j] = [M_i]\alpha_{M_i(H)} \qquad (8)$$

and

$$M'_{a(c)} = M_aZ_{b(c)} \qquad (9)$$

As was demonstrated previously [3], the predominance of species M_i' can be represented on a $-\log C_{M\,TOTAL}/pH$ diagram by defining the first-order generalized polynucleation equilibria.

Likewise, according to the proposal discussed in Part I [1], it is possible to define the total generalized species ${}^{\dagger}M'$ and ${}^{\dagger}M'_{(c)}$ as

$$[{}^{\dagger}M'] = C_{M\,TOTAL} = \sum_{i=1}^{m} i[M_i'] = \sum_{i=1}^{m} i[M_i]\alpha_{M_i(H)} \qquad (10)$$

and

$${}^{\dagger}M'_{a(c)} \equiv M'_{a(c)} \equiv M_aZ_{b(c)} \qquad (11)$$

where the superscript prime means that a given component (in this case Z) is included, whereas the superscript dagger indicates the implicit writing of the subscripts of a given component (in this case M).

Then, it is also possible to define the total generalized solubility equilibrium

$${}^{\dagger}M'_{(c)} \rightleftharpoons {}^{\dagger}M' \text{ with } K_{{}^{\dagger}M'}^{{}^{\dagger}M'_{(c)}} = [{}^{\dagger}M']_{sat} \qquad (12)$$

From Eqns. 10–12, the saturation function $pK_{{}^{\dagger}M'}^{{}^{\dagger}M'_{(c)}} = -\log s_{MZ} = p^{\dagger}M'_{sat}$ can be plotted on the $p^{\dagger}M'/pH$ plane to give a PED, such as those shown in Fig. 2.

The lower trajectory in Fig. 2 corresponds to the saturation of $M_aZ_{b(c)}$, according to Eqn. 12. Any point below this trajectory corresponds to supersaturated solutions that will reach the equilibrium with the $M_aZ_{b(c)}$ phase, up to a point in the saturation line. (If the system is pH buffered, the trajectory towards the saturation line will be vertical.)

Likewise, the points above the saturation trajectory correspond to unsaturated solutions. Here, different predominance zones of the first-order generalized species (M_i') can be established by the use of an algorithm similar to that described in the previous section, but this time utilizing first-order generalized polynucleation equilibria [3]. The presence of polynuclear species in the solution makes the predominance-zone diagrams

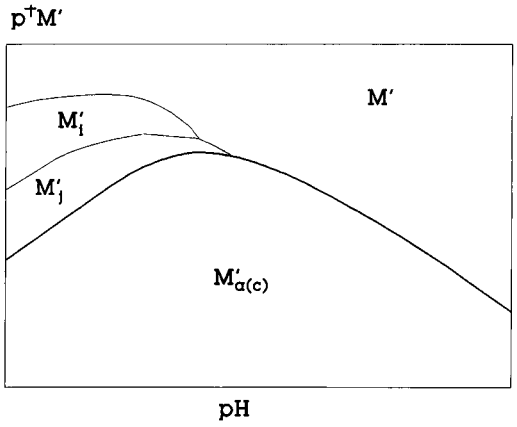

Fig. 2. Different predominance–existence diagrams (PED) on the $p^{\dagger}M'/pH$ plane. The thick line represents the saturation conditions of the solution [where $p^{\dagger}M' = pK^{\dagger}_{M'}{}^{M_{(c)}} = -\log s_{M_aZ_{b(H)}}$]. The region below the saturation trajectory corresponds to supersaturated solutions, where $M'_{a(c)} = M_aZ_{b(c)}$ must be formed until the thermodynamic equilibrium is reached. Here $[^{\dagger}M'] \equiv C_{M\,TOTAL}$.

(PZD) of the soluble species to be represented on the $p^{\dagger}M'/pH$ plane, and the PED may be constructed on the same plane by including the saturation trajectory of the most insoluble phase as noted before.

When there are no polynuclear species in the system, the PZD of the soluble species is represented in a one-dimensional pH space, whereas the PED is represented in the $p^{\dagger}M'/pH$ plane.

In addition for the present case, in order to construct only one generalized solubility equilibrium, it has been necessary to consider the implicit writing of the stoichiometric coefficients of component M in the total generalized equilibrium in Eqn. 12, by use of the superscript dagger, owing to the presence of polynuclear species.

Systems of the type M–L–HZ–H, where HZ is an amphiprotic solvent at constant T and P

In this type of system the following species can be formed in the solution: $M_iL_jZ_k$ ($i \in \{0, 1, \ldots, m\}$, $j \in \{0, 1, \ldots, n(i)\}$, $k \in \{0, 1, \ldots, o(i, j)\}$.

According to Eqn. 1 and considering $C = 4$, the maximum number of phases that can coexist in the system is: $P_{max} = 6$ (when F = 0).

Coexistence of the solution with condensed phases at constant T and P. In this case, as opposed to the previous ones, it is possible to have systems where the solution can coexist with more than one condensed phase without violating the phase rule [for example, $M_aL_bZ_{c(c)}$, $M_dL_eZ_{f(c)}$, $M_gL_hZ_{q(c)}$] or the electroneutrality principle for each of them; however, as discussed previously [1], only up to two condensed phases can coexist with the solution.

Systems buffered in H and L′ at constant T and P. In this case it is possible to define the second-order generalized species M''_i and $M''_{x(c)}$, where $i \in \{1, 2, \ldots, m\}$ and $x \in \{1, 2, \ldots, r\}$; then, it is possible to define the generalized solubility equilibria

$$iM''_{a(c)} \rightleftharpoons aM''_i \text{ with } K^{iM''_{a(c)}}_{aM''_i} \tag{13}$$

$$iM''_{d(c)} \rightleftharpoons dM''_i \text{ with } K^{iM''_{d(c)}}_{dM''_i} \tag{14}$$

$$iM''_{g(c)} \rightleftharpoons gM''_i \text{ with } K^{iM''_{g(c)}}_{gM''_i} \tag{15}$$

It is also possible to combine the total generalized equilibria by using the definition of the total second-order generalized species:

$$[^{\dagger}M''] = \sum_{i=1}^{m} i[M''_i] \tag{16}$$

and

$$^{\dagger}M''_{(c)} = \text{the most insoluble among } M''_{a(c)},\ M''_{d(c)} \text{ and } M''_{g(c)} \tag{17}$$

Then, it is possible to construct the generalized solubility equilibrium

$$^{\dagger}M''_{(c)} \rightleftharpoons {}^{\dagger}M'' \text{ with } K^{\dagger M''_{(c)}}_{\dagger M''} = [^{\dagger}M'']_{sat} \tag{18}$$

where

$$K^{\dagger M''_{(c)}}_{\dagger M''} = \begin{cases} \sum_{i=1}^{m} i\left(K^{iM''_{a(c)}}_{aM''_i}\right)^{1/a} & \text{if } M''_{a(c)} \text{ is the most insoluble phase} \\ \sum_{i=1}^{m} i\left(K^{iM''_{d(c)}}_{dM''_i}\right)^{1/a} & \text{if } M''_{d(c)} \text{ is the most insoluble phase} \\ \sum_{i=1}^{m} i\left(K^{iM''_{g(c)}}_{gM''_i}\right)^{1/a} & \text{if } M''_{g(c)} \text{ is the most insoluble phase} \end{cases} \tag{19}$$

It can be seen that $K^{\dagger M''_{(c)}}_{\dagger M''}$ is the solubility of the most insoluble phase for a given set of conditions. Then,

$$s_{\dagger M''_{(c)}} = K^{\dagger M''_{(c)}}_{\dagger M''} = [\dagger M'']_{sat} \quad (20)$$

As the total second-order generalized solubility constants, represented by Eqn. 19, are dependent only on pH and pL′ (at constant T and P), then the graphical representation of Eqn. 20 must be done in the $p^{\dagger}M''/pL'/pH$ space. According to the previous discussion [3], it is in this same space that the PZD of the soluble species (represented by $^{\dagger}M''$) can be constructed.

To construct the PED, it is necessary to establish which is the most insoluble phase among all the possible condensed phases $[^{\dagger}M''_{(c)}]$ for a given set of conditions. As proposed in Part I [1], such information can be obtained by previously constructing the condensed phases diagram (CPD). These diagrams are constructed with the knowledge of first-order generalized interconversion equilibria

$$(ae - db)L' + dM_aL'_{b(c)} \rightleftharpoons aM_dL'_{e(c)} \quad (21)$$

and

$$(hd - eg)L' + gM_dL'_{e(c)} \rightleftharpoons dM_gL'_{h(c)} \quad (22)$$

where the interconversion conditional constants are

$$K^{dM_aL'_{b(c)}}_{aM_dL'_{e(c)}} = \frac{1}{[L']^{(ae-db)}_{int}} \quad (21a)$$

and

$$K^{gM_dL'_{e(c)}}_{dM_gL'_{h(c)}} = \frac{1}{[L']^{(hd-eg)}_{int}} \quad (22a)$$

where $[L']_{int}$ corresponds to the generalized concentration of L′ for which the solution coexists with two condensed phases.

It can be noted that in Eqns. 21a and 22a pL'_{int} is dependent only on pH for both cases (at constant T and P); for this reason, the CPD for this system is represented on the pL′/pH plane. The type of diagrams that can be constructed for this system is presented in Fig. 3.

It is important to point out that even though polynuclear species are considered in the condensed phases $[^{\dagger}M''_{(c)}]$, the CPD is not dependent on the concentration of M. In the same manner as for the case where no polynuclear species are considered [1], the interconversion trajectories of the CPD (Eqns. 21a and 22a) are parallel to each other and then the diagram is similar to that shown in Fig. 2 in Part I [1], and so is its interpretation.

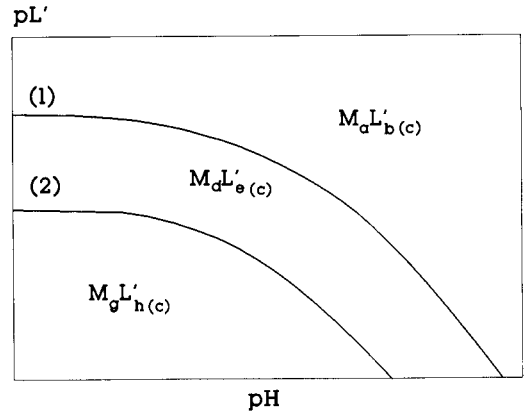

Fig. 3. Representation of a condensed-phases diagram (CPD) for the system M–L–HZ–H. The solid lines (1) and (2) represent the triple trajectories (coexistence of two condensed phases with solution) and are related to the interconversion conditional constants for the condensed phases. In this case, $(b/a) < (e/d) < (h/g)$ and $i < j$.

In order to construct the CPD with the same method as that used for the two-dimensional PZD of soluble species [4], analysis of the interconversion equilibria in ascending order with respect to the relationship y/x [in $M_xL_yZ_{z(c)}$] is proposed. In this way, the most insoluble condensed phase that coexists with the solution (Fig. 3), when pL′ larger than those of the triple trajectory (1), corresponds to the smallest y/x relationship.

The ratio y/x could give a non-integral value (owing to polynucleation of M). In the same manner as in the case analysed previously [1], if the trajectory (2) is located above the trajectory (1) in Fig. 3, the species $M_dL_eZ_{f(c)}$ is unstable and then must be taken into account only in the diagram for the interconversion equilibrium between $M_aL_bZ_{c(c)}$ and $M_gL_hZ_{q(c)}$.

With the CPD constructed as described above, it is possible to find the pL′ and pH intervals that

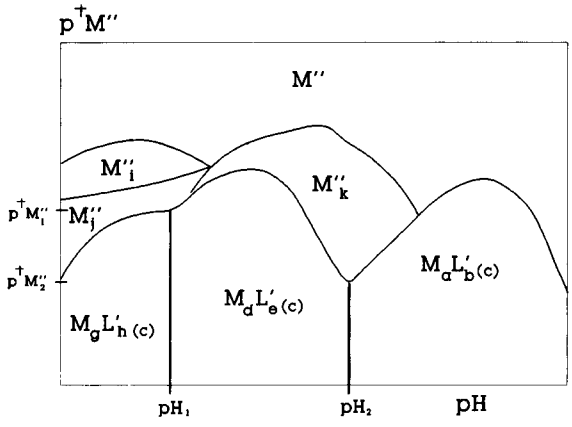

Fig. 4. Example of a two-dimensional slice cut of the PED $p^{\dagger}M''/pL'/pH$ at constant pL′ for the system M–L–HZ–H. The thick line represents the saturation conditions of the solution [where $p^{\dagger}M'' = pK^{\dagger M''_{(c)}}_{\dagger M''} = -\log s_{\dagger M''}$). The region below the saturation trajectory corresponds to supersaturated solutions, where the most insoluble phases of $^{\dagger}M''_{(c)}$ [$M_aL'_{b(c)} \equiv M_aL_bZ_{c(c)}$, $M_dL'_{e(c)} \equiv M_dL_eZ_{f(c)}$ or $M_gL'_{h(c)} \equiv M_gL_hZ_{q(c)}$] must be formed until the thermodynamic equilibrium is reached. The points at (pH_1, $p^{\dagger}M''_1$) and (pH_2, $p^{\dagger}M''_2$) are triple points and vertical lines represent the interconversion of the different phases that can be formed. Here [$^{\dagger}M'$] $\equiv C_{M\,TOTAL}$, $(b/a) < (e/d) < (h/g)$ and $i < j < k$.

define the domain ranges for the function $K^{\dagger M''_{(c)}}_{\dagger M''}$, shown in Eqn. 19.

Figure 4 shows a slice cut at constant pL′ in the PED $p^{\dagger}M''/pL'/pH$ for this system.

The thick solid lines represent the saturation condition of the system for the most insoluble phase [$p^{\dagger}M''_{sat} = -\log K^{\dagger M''_{(c)}}_{\dagger M''}$ at constant pL′]. At $p^{\dagger}M'' > p^{\dagger}M''_{sat}$, the solution is not saturated and this condition represents the predominance of the species $^{\dagger}M''$. Below the saturation line, the solution becomes saturated in the most insoluble phase; the vertical solid lines define the interconversion of condensed phases.

With the solution under invariant conditions (pL′, T and P) and with three coexisting phases, the degrees of freedom are zero, according to the phase rule. In these cases, the points (pH_1, $p^{\dagger}M''_1$) and (pH_2, $p^{\dagger}M''_2$) at constant pL′ are triple points of the system. The triple points are obtained from the slice cut at constant pL′ in the interconversion diagram in Fig. 3.

Systems of the type $\underbrace{M\text{–}L\text{–}\ldots\text{–}X\text{–}Z\text{–}H}_{\tau+2}$ *with*

buffering in $\underbrace{L^{(\tau)},\ldots,X',H}_{\tau+1}$ *at constant T and P*

For a generalization of the method discussed above, it can be demonstrated that under these conditions [3], the τ-order generalized species can be defined in solution:

$$[M_i^{(\tau)}] = [M_i]\alpha_{M_i[H,X',\ldots,L^{(\tau)}]} \tag{23}$$

where

$$\alpha_{M_i[H,X',\ldots,L^{(\tau)}]} = \alpha_{M_i(H)}\alpha_{M_i'(X')}\cdots\alpha^{(\tau)}_{M_i[L^{(\tau)}]} \tag{24}$$

and for the condensed phases [1]

$$M^{(\tau+1)}_{x(c)} = M_xL_y\ldots Z_{z(c)}\ \text{(most insoluble)} \tag{25}$$

selected from the set of phases that could coexist with solution.

As discussed earlier, the generalized species $M_i^{(\tau+1)}$ and $M^{(\tau+1)}_{x(c)}$ can be represented in multidimensional PZD and CPD, respectively.

The PZD can be represented in a $-\log C_{M\,TOTAL}/pL^{(\tau)}/\ldots/pX'/pH$ space, as discussed previously [3]. The CPD can be represented in a $pL^{(\tau)}/\ldots/pX'/pH$ space, by generalizing the method described above for the construction of such diagrams and taking into account the considerations discussed before for similar cases [1].

It is possible to define the total $(\tau+1)$-order generalized species

$$[^{\dagger}M^{(\tau+1)}] = \sum_{i=1}^{m} i[M_i^{(\tau+1)}] = C_{M\,TOTAL} \tag{26}$$

$$^{\dagger}M^{(\tau+1)}_{(c)} = M^{(\tau+1)}_{x(c)}\ \text{most insoluble} \tag{27}$$

In this way, a total $(\tau+1)$-order generalized solubility equilibrium can be proposed:

$$^{\dagger}M^{(\tau+1)}_{(c)} \rightleftharpoons {}^{\dagger}M^{(\tau+1)}\ \text{with}$$

$$K^{\dagger M^{(\tau+1)}_{(c)}}_{\dagger M^{(\tau+1)}} = [^{\dagger}M^{(\tau+1)}]_{sat} = s_{\dagger M^{(\tau+1)}_{(c)}} \tag{28}$$

Then, the PED of the system can be constructed in the same space as the PZD and the intervals for the existence of the most insoluble phases can be selected from the corresponding CPD.

The previous study showed that in the systems with polynuclear species of M, it is necessary to keep implicit the writing of the subscripts for the polynucleation of M (through the definition of total generalized species $^{\dagger}M$) in order to recover the mathematical structure of an intrinsic solubility equilibrium [$M_{(c)} \rightleftharpoons M$], and also to consider (also implicitly) the buffering imposed on the system [by the use of the generalized species $M', \ldots, M^{(\tau)}, M^{(\tau+1)}$], in each phase that could be present in the system.

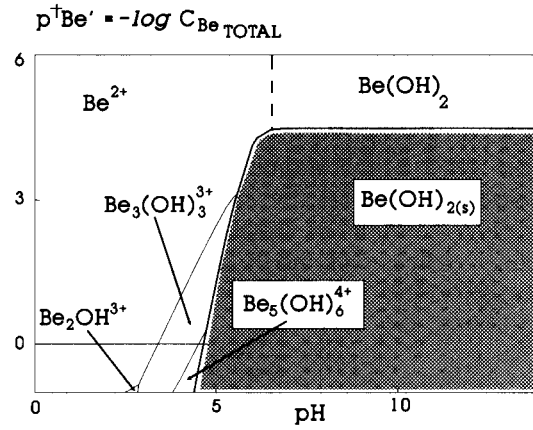

Fig. 5. Predominance–existence diagram (PED) for the Be(II)–H_2O—H system in the space $p^{\dagger}Be'/pH$.

EXAMPLES

In order to demonstrate the most important aspects derived from the theoretical section, four examples (with increasing complexity) are discussed: Be(II)–H_2O–H, Be(II)–PDTA–H_2O–H, Ca(II)–H_3PO_4–H_2O–H and Mg(II)–H_3PO_4–NH_3–H_2O–H (where $H_4PDTA \equiv$ 1,3-diaminopropylene-*N*,*N*,*N*′,*N*′-tetraacetic acid and PDTA ≡ PDTA′ = H_4PDTA, H_3PDTA^-, H_2PDTA^{2-}, $HPDTA^{3-}$, $PDTA^{4-}$).

The systems involving Be(II) are developed in order to discuss the experimental results reported previously [5,6]. The Mg(II) system corresponds to the chemical conditions of the classical gravimetric method for magnesium determination [7].

Be(II)–H_2O–H system

In this system it is possible to define the total first-order generalized species $^{\dagger}Be'$ and $^{\dagger}Be'_{(s)}$:

$$[^{\dagger}Be'] = [Be'] + 2[Be'_2] + 3[Be'_3] + 5[Be'_5] + 6[Be'_6]$$

and

$$^{\dagger}Be'_{(s)} = Be'_{(s)} = Be(OH)_{2(s)}$$

The partition of the first-order generalized species in solution (Be'_i) as a function of pH, and also the PZD $p^{\dagger}Be'/pH$ (where $p^{\dagger}Be' = -\log C_{M\,TOTAL}$) has been presented and discussed elsewhere [3].

It is then possible to define the total first-order generalized solubility equilibrium

$$^{\dagger}Be'_{(s)} \rightleftharpoons {}^{\dagger}Be' \text{ with } K^{\dagger Be'_{(s)}}_{\dagger Be'} = [^{\dagger}Be']_{sat} = s_{Be(OH)_2}$$

The data utilized for the construction of this diagram, concerning the soluble species, are those reported by Mederos *et al.* [5], for an ionic strength of 0.5 M. Their values were summarized in Table 1 in a previous paper [3]. The pK_s of $Be(OH)_{2(s)}$ (7.18) was taken from Baes and Mesmer [8] at the same ionic strength.

The PED on the plane $p^{\dagger}Be'/pH$ for this system is shown in Fig. 5. It can be seen that, for $p^{\dagger}Be' > p^{\dagger}Be'_{sat}$ (where $p^{\dagger}Be'_{sat}$, is the thick solid line), Fig. 5 is the same as the PZD previously reported for this system [3].

At $p^{\dagger}Be' < p^{\dagger}Be'_{sat}$ the PED shows the coexistence of $Be(OH)_{2(s)}$ with the solution.

On comparison of the PZD [3] with Fig. 5, it can be seen that the saturation of the solution with $Be(OH)_{2(s)}$ impedes the predominance of $Be_6(OH)_8^{4+}$ despite though the closeness of the saturation line with the borderline of the predominance of $Be_5(OH)_6^{4+}$ and $Be_6(OH)_8^{4+}$ (at $4 < pH < 5$). This implies a small influence of these species on the solubility; this effect is taken into account in the calculation of $p^{\dagger}Be'_{sat}$ described above.

In other studies, at $4 < pH < 5$ the fraction of $Be_6(OH)_8^{4+}$ was not insignificant when the solution was saturated or near saturation; this has been discussed by Mederos *et al.* [5] and Bruno [6] utilizing distribution diagrams. This explains the fact that the potentiometric results obtained by them have sufficient precision to calculate the equilibrium constant of $Be_6(OH)_8^{4+}$ in the system; this could not be justified if the borderline of predominance analysed above were far from the saturation line at all times.

Be(II)–PDTA–H_2O–H system

Here it is possible to define the total second-order generalized species $^{\dagger}Be''$ and $^{\dagger}Be''$ such that the partition of these generalized species is as follows:

$$[^{\dagger}Be''] = [Be''] + 2[Be_2''] + 3[Be_3''] + 5[Be_5''] + 6[Be_6'']$$

and

$$^{\dagger}Be''_{(s)} = Be''_{(s)}$$

The partition of the species with respect to PDTA′ and to H for the soluble species has been described previously [3]. On the other hand, $Be''_{(s)} = Be'_{(s)} = Be(OH)_{2(s)}$, as there are no reported data on condensed phases for PDTA.

In this way, the total second-order generalized solubility equilibrium is:

$$^{\dagger}Be''_{(s)} \rightleftharpoons {}^{\dagger}Be'' \text{ with } K_{^{\dagger}Be''}^{^{\dagger}Be''_{(s)}} = [^{\dagger}Be'']_{sat} = s_{Be(OH)_2}$$

As $s_{Be(OH)_2}$ is dependent of both pH and pPDTA′, the graphical representation of this equilibrium can be made in the space $p^{\dagger}Be''$/pPDTA′/pH, which is the same space where the PZD of the $^{\dagger}Be''$ soluble species is represented [3].

Figure 6 shows the slice cut $p^{\dagger}Be''$/pH at pPDTA′ = 1.0 for the Be(II)–PDTA–H_2O–H system considering the formation of $Be(OH)_{2(s)}$. The thick solid line shows the zone of coexistence of $Be(OH)_{2(s)}$ with solution and corresponds to $-\log K_{^{\dagger}Be''}^{^{\dagger}Be''_{(s)}}$ for pPDTA′ = 1.0.

For $p^{\dagger}Be'' > -\log K_{^{\dagger}Be''}^{^{\dagger}Be''_{(s)}}$, the diagram is the same as the two-dimensional slice cut $p^{\dagger}Be''$/pH at pPDTA′ = 1.0 for soluble species reported previously [3]. The saturation of the solution in $Be(OH)_{2(s)}$ impedes $Be_6(OH)_8^{4+}$ predominating in the solution; at the same time, the presence of PDTA′ makes the molar fraction of $Be_6(OH)_8^{4+}$ always insignificant.

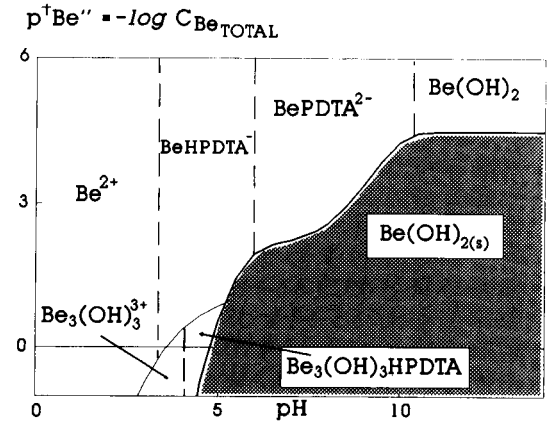

Fig. 6. Slice cut of the predominance–existence diagram (PED) for the Be(II)–PDTA–H_2O–H system in the space $p^{\dagger}Be''$/pH, at pPDTA′ = 1.0.

When comparing the saturation lines of Figs. 5 and 6, it can be seen that these trajectories are different whereas the presence of PDTA′ promotes the predominance of Be(II)–PDTA complexes. It is important to note that the method proposed here for the construction of PED allows for the inclusion of polynuclear species, mixed complexes and condensed phases, as can be seen in Figs. 5 and 6.

Ca(II)–H_3PO_4–H_2O–H system

It is possible to define here the total second-order generalized species $^{\dagger}Ca''$ and $^{\dagger}Ca''_{(s)}$. The partition of these species is as follows:

With respect to polynucleation:

$$^{\dagger}Ca'' = Ca''$$

$$^{\dagger}Ca''_{(s)} = \text{the most insoluble among } Ca''_{(s)} \text{ or } Ca''_{3(s)} \text{ or } Ca''_{4(s)} \text{ or } Ca''_{5(s)}$$

With respect to PO_4':

$$Ca'' = Ca' + CaPO_4'$$

$$Ca''_{(s)} = Ca'_{(s)} + CaPO'_{4(s)} + Ca(PO_4)'_{2(s)}$$

$$Ca''_{3(s)} = Ca_3(PO_4)'_{2(s)}$$

TABLE 1

Data used to construct the diagrams for the Ca(II)–H_3PO_4–H_2O–H system [8–11].

Equilibrium	Log K
$Ca + H_2O \rightleftharpoons CaOH + H$	12.85
$H_2PO_4 + H \rightleftharpoons H_3PO_4$	2.05
$HPO_4 + H \rightleftharpoons H_2PO_4$	7.31
$PO_4 + H \rightleftharpoons HPO_4$	12.92
$Ca + HPO_4 \rightleftharpoons CaHPO_4$	2.74
$Ca + H_2PO_4 \rightleftharpoons CaH_2PO_4$	1.41
$Ca + PO_4 \rightleftharpoons CaPO_4$	6.46
$Ca + HPO_4 \rightleftharpoons CaHPO_{4(s)}$	6.57
$Ca + 2H_2PO_4 \rightleftharpoons Ca(H_2PO_4)_{2(s)}$	3.00
$Ca + 2OH \rightleftharpoons Ca(OH)_{2(s)}$	5.26
$3Ca + 2PO_4 \rightleftharpoons Ca_3(PO_4)_{2(s)}$	28.7
$4Ca + 3HPO_4 \rightleftharpoons Ca_4H(PO_4)_{3(s)} + 2H$	−11.59
$5Ca + 3PO_4 + OH \rightleftharpoons Ca_5(PO_4)_3OH_{(s)}$	57.8

$$Ca''_{4(s)} = Ca_4(PO_4)'_{3(s)}$$

$$Ca''_{5(s)} = Ca_5(PO_4)'_{3(s)}$$

With respect to H:

$$PO'_4 = H_3PO_4 + H_2PO_4^- + HPO_4^{2-} + PO_4^{3-}$$

$$Ca' = Ca^{2+} + Ca(OH)^+$$

$$CaPO'_4 = CaH_2PO_4^+ + CaHPO_4 + CaPO_4^-$$

$$Ca'_{(s)} = Ca(OH)_{2(s)}$$

$$CaPO'_{4(s)} = CaHPO_{4(s)}$$

$$Ca(PO_4)'_{2(s)} = Ca(H_2PO_4)_{2(s)}$$

$$Ca_3(PO_4)'_{2(s)} = Ca_3(PO_4)_{2(s)}$$

$$Ca_4(PO_4)'_{3(s)} = Ca_4H(PO_4)_{3(s)}$$

$$Ca_5(PO_4)'_{3(s)} = Ca_5(PO_4)_3OH_{(s)}$$

The solubility constants for all the condensed phases considered here are those reported in [8–11], whereas the constants corresponding to the soluble species are those reported in [8,9,11].

Table 1 summarizes the data used to construct the diagrams presented in this example. The ionic strength considered was 0.0 M.

As for this system there are no polynuclear species reported in solution, the PZD for the generalized species $^{\dagger}Ca''$ can be represented on the plane pPO'_4/pH (Fig. 7). The method of construction and its interpretation have been discussed previously [4].

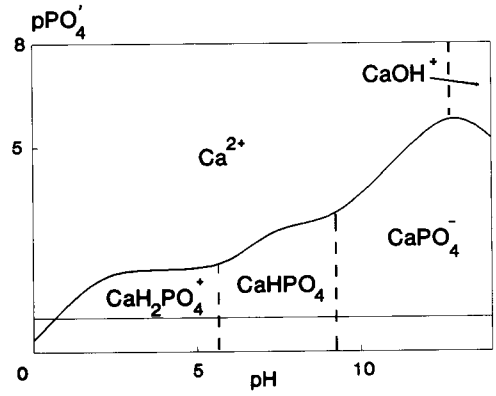

Fig. 7. Predominance-zone diagram (PZD) for the Ca(II)–H_3PO_4–H_2O–H system in the space pPO'_4/pH.

In order to select the most insoluble condensed phase for a given set of conditions, the corresponding CPD of the $^{\dagger}Ca''_{(s)}$ species is constructed on a plane pPO'_4/pH (Fig. 8). In order to construct this diagram, the first-order generalized interconversion equilibria of the type

$$(wz - xy)PO'_4 + yCa_w(PO_4)'_{x(s)} \rightleftharpoons wCa_y(PO_4)'_{z(s)}$$

with

$$K^{yCa_w(PO_4)'_{x(s)}}_{wCa_y(PO_4)'_{z(s)}} = \frac{1}{[PO'_4]^{(wz-xy)}_{int}}$$

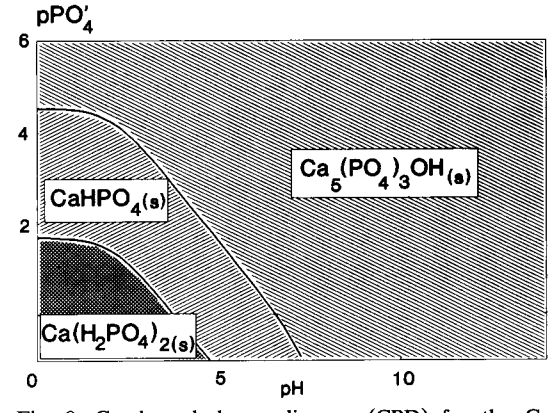

Fig. 8. Condensed-phases diagram (CPD) for the Ca(II)–H_3PO_4–H_2O–H system in the space pPO'_4/pH.

are analysed. These equilibria are analysed in a successive fashion as the stoichiometric ratio of $(PO_4')/Ca'$ increases.

The interconversion trajectories in Fig. 8 correspond to functions of the type $pPO_4' = [1/(wz - xy)] \log K_{wCa_y(PO_4)_z'(s)}^{yCa_w(PO_4)_x'(s)}$ that are dependent only on pH. Each of these trajectories indicates the coexistence of two condensed phases with the solution; they are all parallel, as discussed in the theoretical section.

The interconversion trajectory between $Ca(OH)_{2(s)}$ and $Ca_5(PO_4)_3OH_{(s)}$ is not shown in Fig. 8 as the experimental conditions required are outside the normal range ($pPO_4' \gg 6$ and $pH \gg 14$).

It can be observed that at fixed pH, the stoichiometric ratio $(PO_4')/(Ca')$ of the condensed phases that coexist with the solution changes from 3:5 to 1:1 and 2:1 as pPO_4' decreases. Note that the species $Ca_3(PO_4)_{2(s)}$ and $Ca_4H(PO_4)_{3(s)}$ are unstable for the reasons discussed in the theoretical section. In this way, the analogy for the construction and interpretation of these CPD with the PZD of the soluble species is shown.

In the same manner, it is possible to propose the total second-order generalized solubility equilibrium

$$^{\dagger}Ca''_{(s)} \rightleftharpoons {}^{\dagger}Ca'' \text{ with } K_{^{\dagger}Ca''}^{^{\dagger}Ca''_{(s)}} = [{}^{\dagger}Ca'']_{sat} = s_{^{\dagger}Ca''_{(s)}}$$

where $s_{^{\dagger}Ca''_{(s)}}$ corresponds to the solubility of the most insoluble condensed phase [$Ca_5(PO_4)_3OH_{(s)}$, $CaHPO_{4(s)}$ or $Ca(H_2PO_4)_{2(s)}$] and is dependent only on pPO_4' and pH.

Then, the saturation surface represented by the total second-order generalized equilibrium is represented in a space $p^{\dagger}Ca''/pPO_4'/pH$. In order to simplify the discussion, only a slice cut ($p^{\dagger}Ca''/pH$ at $pPO_4' = 1.0$) of this diagram is shown (Fig. 9).

The PED in Fig. 9 shows that the method proposed here permits polynuclear condensed phases and mixed complexes to be included.

Mg(II)–H_3PO_4–NH_3–H_2O–H system

In this system it is possible to define the total third-order generalized species $^{\dagger}Mg'''$ and $^{\dagger}Mg'''_{(s)}$. The partition of these species is as follows:

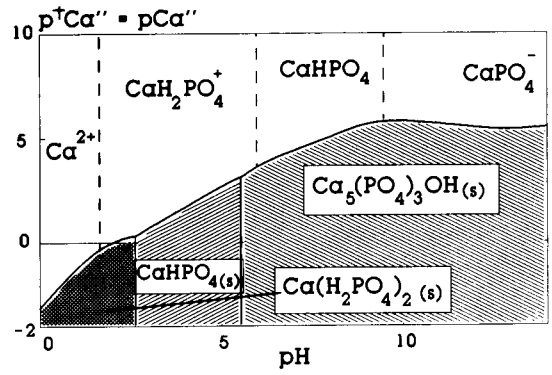

Fig. 9. Slice cut of the predominance–existence diagram (PED) for the Ca(II)–H_3PO_4–H_2O–H system in the space $p^{\dagger}Ca''$/pH, at $pPO_4' = 1.0$.

With respect to polynucleation:

$$[{}^{\dagger}Mg'''] = [Mg'''] + 2[Mg_2'''']$$

$^{\dagger}Mg'''$ = the most insoluble among $Mg'''_{(s)}$ or $Mg'''_{3(s)}$

With respect to PO_4'':

$$Mg''' = Mg'' + MgPO_4'' + Mg(PO_4)_2''$$

$$Mg_2'''' = Mg_2(PO_4)_2''$$

$Mg'''_{(s)}$ = the most insoluble among $Mg''_{(s)}$ or $MgPO''_{4(s)}$

$$Mg'''_{3(s)} = Mg_3(PO_4)_{2(s)}''$$

With respect to NH_3':

$$PO_4'' = PO_4'$$

$$Mg'' = Mg' + Mg(NH_3)' + Mg(NH_3)_2' + Mg(NH_3)_3'$$

$$MgPO_4'' = MgPO_4'$$

$$Mg(PO_4)_2'' = Mg(PO_4)_2'$$

$$Mg(PO_4)_2'' = Mg_2(PO_4)_2'$$

$$Mg''_{(s)} = Mg'_{(s)}$$

$MgPO''_{4(s)}$ = the most insoluble among $MgPO'_{4(s)}$ or $MgNH_3PO'_{4(s)}$

$$Mg_3(PO_4)_{2(s)}'' = Mg_3(PO_4)_{2(s)}'$$

With respect to H:

$$NH_3' = NH_4^+ + NH_3$$

$$PO_4' = H_3PO_4 + H_2PO_4^- + HPO_4^{2-} + PO_4^{3-}$$

$$Mg' = Mg^{2+} + Mg(OH)^+$$

$$Mg(NH_3)' = Mg(NH_3)^{2+}$$

$$Mg(NH_3)_2' = Mg(NH_3)_2^{2+}$$

$$Mg(NH_3)_3' = Mg(NH_3)_3^{2+}$$

$$MgPO_4' = MgH_2PO_4^+ + MgHPO_4 + MgPO_4^-$$

$$Mg(PO_4)_2' = MgH_3(PO_4)_2^+$$

$$Mg_2(PO_4)_2' = Mg_2H_2(PO_4)_2$$

$$Mg_{(s)}' = Mg(OH)_{2(s)}$$

$$MgPO_{4(s)}' = MgHPO_{4(s)}$$

$$MgNH_3PO_{4(s)}' = MgNH_4PO_{4(s)}$$

$$Mg_3(PO_4)_{2(s)}' = Mg_3(PO_4)_{2(s)}$$

The sources for the equilibrium constants data are [8–12]. Table 2 summarizes the data used in this example. The ionic strength considered is lower than 0.1 M.

The PZD for the $^{\dagger}Mg'''$ total generalized species can be represented in a four-dimensional space $p^{\dagger}Mg'''/pPO_4''/pNH_4'/pH$. The construction method and its interpretation have been discussed previously [3]. As an example, Fig. 10 shows only a two-dimensional slice cut $p^{\dagger}Mg'''/pH$ at $pPO_4'' = 1.0$ and $pNH_3' = -0.3$ of the PZD under discussion.

TABLE 2

Data used to construct the diagrams for the Mg(II)–H_3PO_4–NH_3–H_2O–H system [8–12].

Equilibrium	Log K
$Mg + H_2O \rightleftharpoons MgOH + H$	11.40
$Mg + NH_3 \rightleftharpoons Mg(NH_3)$	0.23
$Mg + 2NH_3 \rightleftharpoons Mg(NH_3)_2$	0.08
$Mg + 3NH_3 \rightleftharpoons Mg(NH_3)_3$	−0.30
$NH_3 + H \rightleftharpoons NH_4$	9.24
$PO_4 + H \rightleftharpoons HPO_4$	12.92
$HPO_4 + H \rightleftharpoons H_2PO_4$	7.31
$H_2PO_4 + H \rightleftharpoons H_3PO_4$	2.05
$Mg^+ PO_4 \rightleftharpoons MgPO_4$	3.40
$Mg + HPO_4 \rightleftharpoons MgHPO_4$	2.91
$Mg + H_2PO_4 \rightleftharpoons MgH_2PO_4$	0.60
$MgH_2PO_4 + HPO_4 \rightleftharpoons MgH_3(PO_4)_2$	2.50
$2MgHPO_4 \rightleftharpoons Mg2H_2(PO_4)_2$	1.40
$Mg + HPO_4 \rightleftharpoons MgHPO_{4(s)}$	5.82
$Mg + NH_4 + PO_4 \rightleftharpoons MgNH_4PO_{4(s)}$	12.6
$3Mg + 2PO_4 \rightleftharpoons Mg_3(PO_4)_{2(s)}$	25.2
$Mg + 2OH \rightleftharpoons Mg(OH)_{2(s)}$	11.15

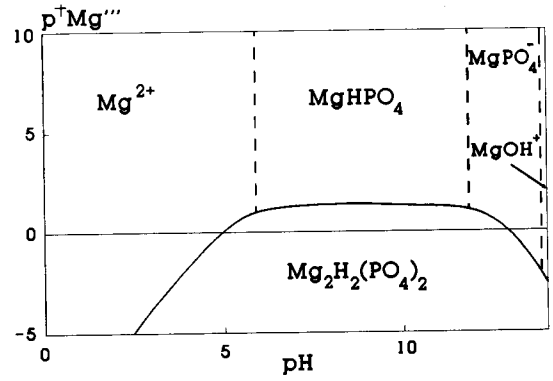

Fig. 10. Slice cut of the predominance-zone diagram (PZD) for the Mg(II)–H_3PO_4–NH_3–H_2O–H system in the space $p^{\dagger}Mg'''/pH$, at $pNH_3' = -0.3$ and $pPO_4'' = 1.0$.

Despite the ammonia concentration, Mg–NH_3 complexes cannot predominate under the chemical conditions analysed by this diagram.

In order to select the most insoluble condensed phase for a given set of conditions, the corresponding CPD is constructed in a space $pPO_4''/pNH_3'/pH$ utilizing the second-order generalized interconversion equilibria

$$3Mg_{(s)}'' + 2PO_4'' \rightleftharpoons Mg_3(PO_4)_{2(s)}''$$

$$Mg_3(PO_4)_{2(s)}'' + 4PO_4'' \rightleftharpoons 3Mg(PO_4)_{2(s)}''$$

These interconversion equilibria correspond to surfaces in the three-dimensional space. The interpretation of this kind of diagram is similar to that for the examples discussed earlier. The difference in this instance is that as this is a five-component system, if the interconversion trajectories cross, it is possible to define (on the crossing trajectory) the phase dismutation equilibrium

$$3Mg_3(PO_4)_{2(s)}'' \rightleftharpoons 6Mg_{(s)}'' + 3Mg(PO_4)_{2(s)}''$$

The pNH_3' and pH values that describe the interconversion trajectory make the two-conditional dismutation constant become unity.

This equilibrium shows the coexistence of three condensed phases with the solution; at constant T and P, this equilibrium appears when the system is one-variant according to the phase rule; this implies that the dismutation equilibrium is present in a one-dimensional trajectory in the three-dimensional space $pPO_4''/pNH_3'/pH$.

Figure 11 shows the slice cut pPO_4''/pH at $pNH_3' = -0.3$ of the three-dimensional CPD. The point at ($pPO_4'' = 8.60$, $pNH_3' = -0.30$ and $pH = 9.62$) corresponds to the dismutation point of the phase $Mg_3(PO_4)''_{2(s)}$ [or $Mg_3(PO_4)_{2(s)}$]; for this reason from the dismutation point on, only the interconversion trajectory of the second-order generalized interconversion equilibrium appears:

$$Mg''_{(s)} + PO_4'' \rightleftharpoons MgPO''_{4(s)}$$

At pH lower than 9.62, the diagram shows two successive interconversion trajectories [with respect to the $(PO_4'')/(Mg'')$ ratio], as $Mg_3(PO_4)''_{2(s)}$ might coexist with the solution. At $pH < 5.84$ the interconversion trajectories are parallel because, although NH_3' is present in the system, it is not involved in any condensed phase. At $5.84 < pH < 9.62$, the successive trajectories are not parallel because under these conditions the most insoluble of the two $MgPO''_{4(s)}$ generalized species [$MgHPO_{4(s)}$ and $MgNH_4PO_{4(s)}$] is $MgNH_4PO_{4(s)}$.

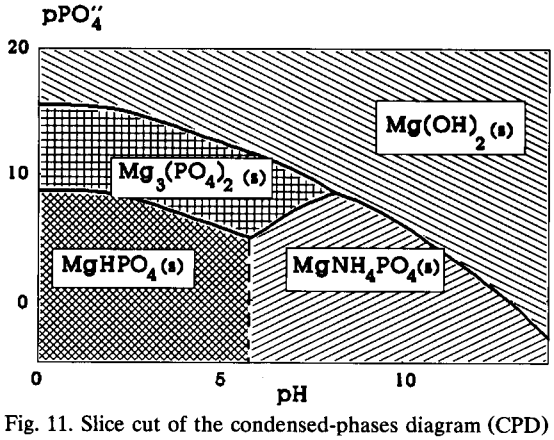

Fig. 11. Slice cut of the condensed-phases diagram (CPD) for the Mg(II)–H_3PO_4–NH_3–H_2O–H system in the space pPO_4''/pH, at $pNH_3' = -0.3$.

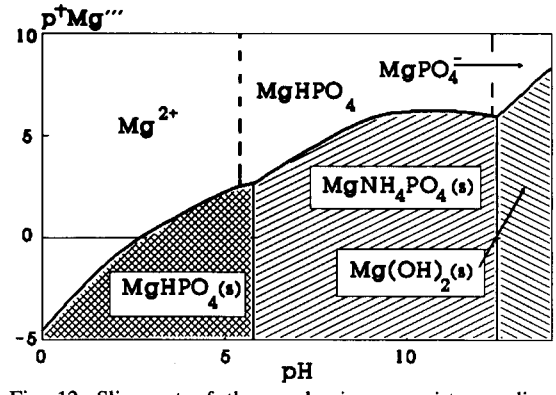

Fig. 12. Slice cut of the predominance–existence diagram (PED) for the Mg(II)–H_3PO_4–NH_3–H_2O–H system in the space $p^{\dagger}Mg'''/pH$, at $pNH_3' = -0.3$ and $pPO_4'' = 1.0$.

In this way, it is possible to propose the total third-order generalized solubility equilibrium

$$^{\dagger}Mg'''_{(s)} \rightleftharpoons {}^{\dagger}Mg''' \text{ with } K^{\dagger Mg'''_{(s)}}_{\dagger Mg'''} = \left[{}^{\dagger}Mg'''\right]_{sat} = s_{\dagger Mg'''_{(s)}}$$

where $s_{\dagger Mg'''_{(s)}}$ corresponds to the solubility of the most insoluble phase that is selected from the three-dimensional CPD $pPO_4''/pNH_3'/pH$.

The total third-order solubility equilibrium is represented in the same four-dimensional space $p^{\dagger}Mg'''/pPO_4''/pNH_3'/pH$, in which the PZD of the $^{\dagger}Mg'''$ species is represented.

In order to simplify the discussion and to make a comparison with the PZD of Fig. 10, the same two-dimensional slice cut ($p^{\dagger}Mg'''/pH$ at $pPO_4'' = 1.0$ and $pNH_3' = -0.3$) is presented for the case discussed here (Fig. 12).

The thick solid line corresponds to the saturation trajectory of the most insoluble species in the system; this species was selected by making a horizontal slice cut at $pPO_4'' = 1.0$ in the CPD of Fig. 11. This trajectory was calculated with the three-conditional constant of solubility equilibrium mentioned above and has been superimposed on the diagram in Fig. 10.

The points at ($pH = 5.84$, $p^{\dagger}Mg''' = 2.69$) and ($pH = 13.25$, $p^{\dagger}Mg''' = 5.27$) correspond to triple points (at $pNH_3' = -0.3$ and $pPO_4'' = 1.0$, constant T and P) of the coexistence of three phases.

The comparison between Figs. 10 and 12 shows that the saturation line is always located above the trajectory where Mg''' and Mg_2''' are equal; for

this reason, saturation is achieved before Mg_2''' can predominate (at $pNH_3' = -0.3$ and $pPO_4'' = 1.0$).

The closeness of the equal concentrations line of Mg''' and Mg_2''' (Fig. 10) with the saturation line (Fig. 12), for $pH < 5.84$, indicates that the fraction of Mg_2''' in the saturated solutions is not negligible; nevertheless, its value can be determined experimentally.

The system discussed here corresponds to the chemical condition for the classical gravimetric method for magnesium determination [7]. The diagrams presented here can justify the operating conditions of this method.

Conclusions

In this second part, it has been demonstrated that the definition of total generalized species [$^{\dagger}M^{(\tau)}$ and $^{\dagger}M_{(c)}^{(\tau)}$] permits the structure of an intrinsic solubility equilibrium to be maintained in a system under multiple buffering in spite of the presence of polynuclear species both in solution and in the condensed phases.

In order to select the most insoluble phase in the systems with polynuclear species present, a CPD is constructed in a space with one less dimension than the corresponding space for the PZD and PED; this is a result of the fact that the CPD consider only saturated solutions. For this reason, the generalized interconversion equilibria do not depend on [$^{\dagger}M^{(\tau)}$], but only on the τ buffering conditions.

Likewise, it is demonstrated that it is possible to construct diagrams for condensed phases in equilibrium with multi-component solutions by using the same algorithm as used for the construction of the PZD diagrams of soluble species. To do this, one has to use the successive generalized interconversion equilibria [for the ratio of the stoichiometric coefficients $(L^{(\tau)})/(M^{(\tau)})$] and the dismutation equilibria (when allowed by the phase rule, i.e. for five or more components including the amphiprotic solvent). The construction of PED when there are polynuclear species is achieved by including the saturation trajectory in the PZD.

In Part I [1], the limitations and several statements concerning the application of these diagrams to real systems were discussed. Obviously, they are also valid for this second part.

The equilibria involving the gas phase with these systems will be discussed in another paper.

The authors thank Dr. Jorge Ibáñez for the English translation of this paper and PROIDES-SEP and CONACYT for financial support.

REFERENCES

1 A. Rojas-Hernández, M.T. Ramírez and I. González Anal. Chim. Acta, (1993).
2 J.C. Angus and Ch.T. Angus, J. Electrochem. Soc., 132 (1985) 1014.
3 A. Rojas-Hernández, M.T. Ramírez, I. González and J.G. Ibáñez, Anal. Chim. Acta, 259 (1992) 95.
4 A. Rojas and I. González, Anal. Chim. Acta, 187 (1986) 279.
5 A. Mederos, S. Domínguez, E. Chinea and F. Brito, in A. Paz-Sandoval (Ed.), Memorias del III Congreso Iberaomericano de Química Inorgánica, México, 1991, p. 136.
6 J. Bruno, J. Chem. Soc., Dalton Trans., (1987) 2431.
7 G.H. Jeffery, J. Bassett, J. Mendham and R.C. Demrey, Vogel's Textbook of Quantitative Chemical Analysis, Longman–Wiley, New York, 1989.
8 C.F. Baes, Jr., and R.E. Mesmer, The Hydrolysis of Cations, Wiley, New York, 1976.
9 R.M. Smith and A.E. Martell, Critical Stability Constants, Vol. 2, Plenum, New York, 1975.
10 E. Högfeldt, Stability Constants of Metal-Ion Complexes: Part A: Inorganic Ligands (IUPAC Chemical Data Series, No. 21), Pergamon, New York, 1979.
11 J. Lurie, Handbook of Analytical Chemistry, Mir, Moscow, 1978.
12 L.G. Sillén, Stability Constants of Metal-Ion Complexes (Special Publication No. 17), Chemical Society, London, 1971.

ANALYTICA CHIMICA ACTA, VOL. 278 (1993)

AUTHOR INDEX

Calendar of forthcoming meetings

★ *indicates new or amended entry*

June 29-July 4, 1993
York, UK.
XXVIII Colloquium Spectroscopicum Internationale. *Contact:* Department of Chemistry (CSI Secretariat), Loughborough University of Technology, Loughborough, Leics. LE11 3TU, UK.

★ ***July 4–7, 1993***
Durham, UK
XXVIII Colloquium Spectroscopicum Internationale Post-Symposium: Graphite Atomizer Techniques in Analytical Spectroscopy. *Contact:* XXVIII Colloquium Spectroscopicum Internationale (Post-Symposium Graphite Atomizer Techniques in Analytical Spectroscopy), Department of Chemistry (CSI Secretariat), Loughborough University of Technology, Loughborough, Leics. LE11 3TU, UK.

July 7–9, 1993
York, UK.
Modern Ultraviolet Spectrometry. *Contact:* Dr. Tom Frost, Wellcome Foundations Ltd., Dartford Hill, Dartford DA1 5AH, UK. Tel: +44 322 223-488; Fax: +44 322 289-285.

July 11–14, 1993
Crete, Greece
Sixth International Symposium on Polymer Analysis and Characterization. *Contact:* Judith A. Sjoberg, Professional Association Management, 815 Don Gaspar, Sante Fe, NM 87501, USA. Tel.: (505) 989-4735; Fax: (505) 989-1073.

July 11–15, 1993
Brno, Czech Republic
Chemometrics III. Third Czechoslovak Chemometric Conference with international participation. *Contact:* RNDr. Josef Havel, Dept. of Analytical Chemistry, Masaryk University, Kotlarska 2, CS-61137 Brno. Tel.: +42 5-7129284; Telex: +42 5-740108; or RNDr. Miroslav Holik, Research Institute of Fine Chemicals, Lachema, Karasek 28, CS-62133 Brno. Tel.: +42 5-773077/270; Telex: +42 5-771121. *(Further details pubished in Vol. 272, No. 2).*

★ ***July 13–14, 1993***
Bradford, UK
Research and Development Topics in Analytical Chemistry. Meeting of the Analytical Division of the Royal Society of Chemistry. *Contact:* The Royal Society of Chemistry, Burlington House, Piccadilly, London W1V 0BN. Tel.: +44 71 437-8656.

★ ***July 13–15, 1993***
York, UK
Course: Problem Solving for Analytical Leaders. Developing Problem Solving Skills in a Technical Context. *Contact:* Dr. Terry Threlfall, Industrial Liaison Executive, Department of Chemistry, University of York, Heslington, York YO1 5DD, UK. Tel.: +44 904 432576; Telex: 57933 yorkul; Fax: +44 904 432516.

July 19–21, 1993
Guildford, UK
6th Symposium on Handling of Environmental and Biological Samples in Chromatography. *Contact:* Mrs. M. Frei-Häusler, IAEAC Secretariat, Postfach 46, CH-4123 Allschwil 2, Switzerland.

★ ***July 26–29, 1993***
Washington, DC, USA
107th Annual AOAC International Meeting and Exposition Focusing on Methods Needs for Chemical and Biological Analysis. *Contact:* Margaret Ridgell, AOAC International, Suite 400, 2200 Wilson Boulevard, Arlington, VA 22201-9077, USA. Tel.: +1 703 522-3032; Fax: +1 703 522-5468.

August 9–11, 1993
Winnipeg, Canada
3rd Soil and Sediment Residue Analysis Workshop. International Association of Environmental Analytical Chemistry. *Contact:* Dr. G.R. Barrie Webster, Pesticide Research Laboratory, Department of Soil Science, University of Manitoba, Winnipeg, MB, Canada R3T 2N2. Tel.: (204) 474-6039; Fax: (204) 272-6019. Prof. Dr. J. Tarradella, IGE-Ecole Polytechnique, Federale de Lausanne, 1015 Lausanne, Switzerland. Tel.: +41 21 6932712; Fax: +41 21 6932727.

August 9–13, 1993
Beijing, China
ASIANALYSIS II. Second Asian Conference on Analytical Chemistry. *Contact:* Prof. Erkang Wang, 109 Sitalin Street, Changchun Institute of Applied Chemistry, Chinese Academy of Sciences, Changchun, Jilin 130022, China.

August 15–20, 1993
Beijing, China
34th IUPAC Congress: Chemistry for the 21st Century. *Contact:* Prof. Xinqi Song, Secretary-General of 34th IUPAC Congress, c/o Chinese Chemical Society, P.O. Box 2709, Beijing 100080, China.

August 21–24, 1993
Bologna, Italy
CHESM-93. Chemometrics and Environmetrics Meeting. *Contact:* Prof.Daniela Cocchi, Dipartimento di Scienze Statistiche "Paolo Fortunati", Università di Bologna, Via Belle Arti 41, I-40126 Bologna, Italy. Tel.: +39 51-258234; Fax: +39 51-232153; Email: cocchi%statbo.cineca.it@icnucevm.cnuce.cnr.it.

★ ***August 23–26, 1993***
York, UK
Course: Capillary Electrophoresis. *Contact:* Dr. Terry Threlfall, Industrial Liaison Executive, Department of Chemistry, University of York, Heslington, York YO1 5DD, UK. Tel.: +44 904 432576; Telex: 57933 yorkul; Fax: +44 904 433433.

August 23–27, 1993
Budapest, Hungary
9th Danube Symposium on Chromatography. *Contact:* Prof. L. Szepesy, Symposium Secretariat, Department of Chemical Technology, Technical University of Budapest, Budafoki ut 8, H-1521 Budapest, Hungary. Tel. +36 1 186-9000; Fax +36 1 181-2755; Telex 225931 muegy h. *(Further details published in Vol. 264, No. 2).*

August 23–27, 1993
Calgary, Canada
9th International Conference on Fourier Transform Spectroscopy. *Contact:* Conference Office, The University of Calgary, 2500 University Drive NW, Calgary, Alta. T2N 1N4, Canada. Tel.: +1 403 220-5051; Fax: +1 403 289-7287.

★ ***August 29–September 3, 1993***
Bratislava, Slovak Republic
9th International Symposium on Advances of Chromatography in Industry. *Contact:* Dept. of Analytical Chemistry, Slovak Technical University, Radirského 9, 812 37 Bratislava, Slovak Republic. Tel.: +42 7 560-43; Fax: +42 7 493-198.

September 5–10, 1993
Loutraki, Greece
5th European Conference on the Spectroscopy of Biological Molecules. *Contact:* Professor Theo Theophanides, Chairman of ECSBM '93, Department of Chemical Engineering, National Technical University of Athens, Zografou Campus, Zografou 15780, Athens, Greece. Tel.: +30 1-7792438; Fax+ +30 1-7700989. *(Further details published in Vol. 268, No. 2).*

September 5–11, 1993
Edinburgh, UK.
Euroanalysis VIII. *Contact:* Miss P.E. Hutchinson, Analytical Division, The Royal Society of Chemistry, Burlington House, Piccadilly, London W1V 0BN, UK. Tel.: +44 71 437 8656; Fax: + 44 71 734 1227; Telex: 268001. *(Further details published in Vol. 252, No. 1–2).*

★ ***September 7–9, 1993***
Antwerp, Belgium
2nd European FTMS Workshop. *Contact:* Dr. Luc Van Vaeck, Department of Chemistry, University of Antwerp, Universiteitsplein 1, B 2610 Wilrijk, Belgium. Tel.: +32 3 820-2348; Fax: +32 3 820-2376.

September 7–10, 1993
Verona and Soave, Italy
Applications of HPLC and CE in the BioSciences (12th International Symposium on Biomedical Applications of Chromatography and Electrophoresis and 2nd International Symposium on the Applications of HPLC in Enzyme Chemistry). *Contact:* Dr. F. Tagliaro, Scientific Secretariat, c/o Istituto di Medicina Legale, Policlinico Borgo Roma, I-37134 Verona, Italy. Tel.: +39 45 807-4618; Fax: +39 45 505-259. *(Further details published in Vol. 268, No. 2).*

September 8–10, 1993
Prague, Czech Republic
International Association of Environmental Analytical Chemistry 4th Workshop on Chemistry and Fate of Modern Pesticides and Related Pollutants. *Contact:* Dr. J. Hajslova, Institute of Chemical Technology, Department of Food Chemistry and Analysis, Suchbatarova 5, 16628 Prague 6-Dejvice, Czechoslovakia. Fax: +42 23-114769.

★ ***September 8–11, 1993***
Tan-Tar-A, MO, USA
14th International Symposium on Polynuclear Aromatic Hydrocarbons. *Contact:* Prof. E. Cavalieri, Epply Institute, Medical Center, University of Nebraska, Omaha, NE 68198-6805, USA. Tel.: +1 402 559-4090; Fax: +1 402 559-4651.

★ ***September 12–17, 1993***
Toronto, Canada
9th International Conference on Heavy Metals in the Environment. *Contact:* Heavy Metals Secretariat, CEP Consultants Ltd., 26–28 Albany Street, Edinburgh EH1 3QH, UK. Tel.: +44 31 557-2478; Fax: +44 31 557-5749.

★ ***September 13–17, 1993***
Prague, Czech Republic
International Conference on Nuclear Analytical Methods in the Life Sciences. *Contact:* Jan Kucera, Nuclear Research Institute, 250 68 Rez near Prague, Czech Republic. Tel.: +42 2 685-7831, ext. 2268; Fax: +42 2 685-7667.

September 19–22, 1993
Research Triangle Park, NC, USA
2nd National Symposium on Planar Chromatography: Modern Thin-Layer Chromatography. *Contact:* Janet E. Cunningham, Barr Enterprises, P.O. Box 279, Walkersville, MD 21793, USA. Tel.: (301) 898-3772; Fax: (301) 898-5596.

★ ***September 20–24, 1993***
Vienna, Austria
Dioxin '93. 13th International Symposium on Chlorinated Dioxins and Related Compounds. *Contact:* Symposium Secretariat, Dioxin '93, Gesellschaft Österreichischer Chemiker, Nibelungengasse 11, A-1010 Vienna, Austria. Tel.: +43 1 587-3980 or 587-4249; Fax: +43 1 587-8966.

★ ***August 30–September 2, 1993***
Kolding, Denmark
Second European Symposium on Near Infrared (NIR) Spectroscopy. Aspects of Industrial Use. *Contact:* Lone Vejgaard, The Biotechnological Institute, Holbergsvej 10, P.O. Box 818, DK-6000 Kolding, Denmark. Tel.: +45 75 520433; Fax: +45 75 529989.

★ ***October 4–6, 1993***
Paris, France
Short Course: Sample Handling of Pesticides in the Aquatic Environment. Organized by the International Association of Environmental Analytical Chemistry and the Ecole Supérieure de Physique et de Chimie Industrielles de la Ville de Paris. *Contact:* M. Frei-Häusler, IAEAC, Postfach 46, CH-4123 Allschwil 2, Switzerland.

October 5–8, 1993
Beijing, China
4th ISEC. Fourth International Seminar on Electroanalytical Chemistry. *Contact:* Prof. Erkang Wang, 109 Sitalin Street, Changchun Institute of Applied Chemistry, Chinese Academy of Sciences, Changchun, Jilin 130022, China.

October 8–13, 1993
Beijing, China
5th BCEIA. Fifth International Beijing Conference and Exhibition on Instrumental Analysis. *Contact:* General Service Office, 5th BCEIA, Room 5412, Building No. 4, Xi Yuan Hotel, Er Li Gou, Beijing 100046, China.

November 1–4, 1993
Oslo, Norway
LAB '93, Laboratory Exhibition. *Contact:* Norges Varemesse, P.O. Box 130, Skoyen, 0212 Oslo 2, Norway. Tel.: +47 2-43 90100; Fax: +47 2-43 1914.

★ ***November 2–4 1993***
Helsinki, Finland
KEMIA 93. Finnish Chemical Congress and Exhibition. *Contact:* Ms. Anita Haatainen, tel.: +358 0 150-9207, or Mr. Seppo Niiranen, tel.: +358 0 150-9215.

★ ***December 6–8, 1993***
Stockholm, Sweden
Symposium on Purity Determination of Drugs. *Contact:* Swedish Academy of Pharmaceutical Sciences, P.O. Box 1136, S-111 81 Stockholm, Sweden. Tel.: +46 8 245085; Fax: +46 8 205511.

January 10–15, 1994
San Diego, CA, USA
1994 Winter Conference on Plasma Spectrochemistry. *Contact:* Dr. R. Barnes, ICP Information Newsletter, Department of Chemistry, GRC Towers, University of Massachusetts, Amherst, MA 01003-0035, USA. Tel.: +1 413-545-2294; Fax: +1 413-545-4490. *(Further details published in Vol. 272, No. 2).*

February 22–25, 1994
Antwerp, Belgium
HTC 3. Third International Symposium on Hyphenated Techniques in Chromatography. *Contact:* Royal Flemish Chemical Society (KVCV), Working Party on Chromatography, c/o Dr. R. Smits, BASF Anstwerpen N.V., Central Laboratory, Scheldelaan, B-2040 Antwerp, Belgium. Tel.: +32 3 568 2831; Fax: +32 3 568 3250; Telex: 31047 basant b. *(Further details published in Vol. 268, No. 2).*

February 28–March 4, 1994
Chicago, IL, USA
PITTCON '94. Pittsburgh Conference on Analytical Chemistry and Applied Spectroscopy. *Contact:* Pittsburgh Conference, Suite 332, 300 Penn Center Blvd., Pittsburgh, PA 15235-9962, USA.

★ ***March 27–30, 1994***
Galveston, TX, USA
International Federation of Automatic Control (IFAC) Symposium on Modeling and Control in Biomedical Systems. *Contact:* IFAC Biomedical Symposium, University of Texas Medical Branch, Box 55176, Galveston, TX 77555-5176, USA. Tel.: +1 409 770-6628 or 770-6605; Fax: +1 409 770-6825.

April 19–22, 1994
Munich, Germany
ANALYTICA 94. 14th International Trade Fair for Biochemical and Instrumental Analysis with International Conference. *Contact:* Bernhard Schauder, ANALYTICA Press Office, Münchener Messe- und Ausstellungs-Gesellschaft mbh, Messegelände, Postfach 12 10 09, D-8000 Munich 12, Germany. Tel.: +49 89-51070; Fax: +49 89-5107506; Telex: 5212086 ameg d.

May 8-13, 1994
Minneapolis, MN, USA
HPLC '94. 18th International Symposium on High Performance Liquid Chromatography. *Contact:* Janet E. Cunningham, Barr Enterprises, P.O. Box 279, Walkersville, MD 21793, USA. Tel.: (301) 898-3772; Fax: (301) 898-5596.

June 19–24, 1994
Bournemouth, UK
20th International Symposium on Chromatography. *Contact:* The Executive Secretary, Chromatographic Society, Suite 4, Clarendon Chambers, 32 Clarendon Street, Nottingham NG1 5JD, UK. Tel.: +44 603-500596; Fax: +44 602-500614.

July 1994
Maastricht, The Netherlands
International Chemometrics Research Meeting. *Contact:* Laboratory for Analytical Chemistry, Faculty of Science, Catholic University of Nijmegen, Toernooiveld 1, 6525 ED Nijmegen, The Netherlands.

September 11–16, 1994
Essen, Germany
EUCMOS XXII. XXII European Congress on Molecular Spectroscopy. *Contact:* Congress Secretariat, Gesellschaft Deutscher Chemiker, Abt. Tagungen, P.O. Box 900440, W-6000 Frankfurt 90, Germany. Tel.: +49 69 7917-366; Fax +49 69 7917-475; Telex 4 170 497 gdch d. *(Further details published in Vol. 272, No. 2).*

September 21–23, 1994
Stockholm, Sweden
5th International Symposium on Pharmaceutical and Biomedical Analysis: *Contact:* Swedish Academy of Pharmaceutical Sciences, P.O. Box 1136, S-111 81 Stockholm, Sweden. Tel.: +46 8 245085; Fax: +46 8 205511.

September 22–24, 1994
Constanta, Romania
12th Conference on Analytical Chemistry. *Contact:* Dr. Gabirel-Lucian Radu, Romanian Society of Analytical Chemistry, 13 Blvd. Carol I, Sector 3, 70346 Bucharest, Romania.

March 6–10, 1995
PITTCON '95. Pittsburgh Conference on Analytical Chemistry and Applied Spectroscopy. *Contact:* Pittsburgh Conference, Suite 332, 300 Penn Center Blvd., Pittsburgh, PA 15235-9962, USA.

July 9–15, 1995
Hull, UK
SAC 95. *Contact:* Analytical Division, The Royal Society of Chemistry, Burlington House, Piccadilly, London W1V 0BN, UK. Tel.: +44 71 437-8656; Fax: +44 71 734-1227.

Announcement from the Publisher

Elsevier Science Publishers encourages submission of articles on floppy disk.

All manuscripts may now be submitted on computer disk, with the eventual aim of reducing production times still further.

The preferred storage medium is a 5¼ or 3½ inch disk in MS-DOS format, although other systems are welcome, e.g. Macintosh.

After **final acceptance**, your disk plus one final, printed and exactly matching version (as a printout) should be submitted together to the editor. **It is important that the file on disk and the printout are identical.** Both will then be forwarded by the editor to Elsevier.

Illustrations should be provided in the usual manner.

Please follow the general instructions on style/arrangement and, in particular, the reference style of this journal as given in 'Instructions to Authors'.

Please label the disk with your name, the software & hardware used and the name of the file to be processed.

Contact the Publisher for further information:

Elsevier Science Publishers
Analytica Chimica Acta
P.O. Box 330
1000 AH Amsterdam, The Netherlands
Phone: (+31-20) 5862 791 Fax: (+31-20) 5862 459

ELSEVIER SCIENCE PUBLISHERS

711\414\140\079\03

PUBLICATION SCHEDULE FOR 1993

	S'92	O'92	N'92	D'92	J	F	M	A	M	J	J	A
Analytica Chimica Acta	267/1 267/2	268/1 268/2	269/1 269/2	270/1 270/2	271/1 271/2	272/1 272/2 273/1–2	274/1 274/2	275/1–2 276/1 276/2	277/1 277/2	278/1 278/2	279/1 279/2	280/1 280/2
Vibrational Spectroscopy		4/1			4/2		4/3	5/1		5/2		5/3

INFORMATION FOR AUTHORS

Manuscripts. The language of the journal is English. English linguistic improvement is provided as part of the normal editorial processing. Authors should submit three copies of the manuscript in clear double-spaced typing on one side of the paper only. *Vibrational Spectroscopy* also accepts papers in English only.

Abstract. All papers and reviews begin with an Abstract (50–250 words) which should comprise a factual account of the contents of the paper, with emphasis on new information.

Figures. Figures should be prepared in black waterproof drawing ink on drawing or tracing paper of the same size as that on which the manuscript is typed. One original (or sharp glossy print) and two photostat (or other) copies are required. Attention should be given to line thickness, lettering (which should be kept to a minimum) and spacing on axes of graphs, to ensure suitability for reduction in size on printing. Axes of a graph should be clearly labelled, along the axes, outside the graph itself. All figures should be numbered with Arabic numerals, and require descriptive legends which should be typed on a separate sheet of paper. Simple straight-line graphs are not acceptable, because they can readily be described in the text by means of an equation or a sentence. Claims of linearity should be supported by regression data that include slope, intercept, standard deviations of the slope and intercept, standard error and the number of data points; correlation coefficients are optional.

Photographs should be glossy prints and be as rich in contrast as possible; colour photographs cannot be accepted. Line diagrams are generally preferred to photographs of equipment.

Computer outputs for reproduction as figures must be good quality on blank paper, and should preferably be submitted as glossy prints.

Nomenclature, abbreviations and symbols. In general, the recommendations of the International Union of Pure and Applied Chemistry (IUPAC) should be followed, and attention should be given to the recommendations of the Analytical Chemistry Division in the journal *Pure and Applied Chemistry* (see also *IUPAC Compendium of Analytical Nomenclature, Definitive Rules*, 1987).

References. The references should be collected at the end of the paper, numbered in the order of their appearance in the text (*not* alphabetically) and typed on a separate sheet.

Reprints. Fifty reprints will be supplied free of charge. Additional reprints (minimum 100) can be ordered. An order form containing price quotations will be sent to the authors together with the proofs of their article.

Papers dealing with vibrational spectroscopy should be sent to: Dr J.G. Grasselli, 150 Greentree Road, Chagrin Falls, OH 44022, U.S.A. Telefax: (+1-216) 2473360 (Americas, Canada, Australia and New Zealand) or Dr J.H. van der Maas, Department of Analytical Molecule Spectrometry, Faculty of Chemistry, University of Utrecht, P.O. Box 80083, 3508 TB Utrecht, The Netherlands. Telefax: (+31-30) 518219 (all other countries).

0003-2670/93/$06.00

This issue is printed on acid-free paper.

PRINTED IN THE NETHERLANDS

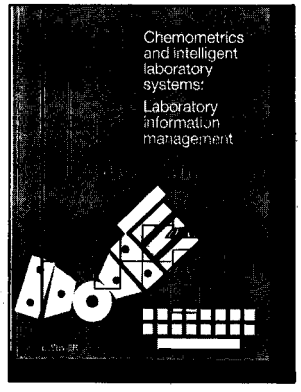

Audience

Chemists, pharmacists, computer scientists and managers working in academic, clinical, industrial and government laboratories.

LABORATORY INFORMATION MANAGEMENT

Section of CHEMOMETRICS AND INTELLIGENT LABORATORY SYSTEMS

AIMS AND SCOPE

The journal covers all aspects of information management in a laboratory environment, such as information technology, storage, processing and flow of data. The following topics are covered:

- **Laboratory Information Management Systems (LIMS):** Systems architecture, database design, novel aspects of interfacing, methods of data acquisition and integration with other computer applications and instruments.
- **Means of integrating and merging laboratory information:** Document preparation using chemical structures, spectra, results and text; corporate communication.
- **Networks:** Novel technology for the dissemination, storage and retrieval of information.
- **Regulatory Aspects:** Development and implementation of governmental guidelines and regulations and industry standards, and their effect on information management.
- **Electronic Laboratory Notebooks.**
- **Human aspects of laboratory automation:** The application of chemometrics and expert systems to handle laboratory information is within the scope of the journal. The application of robotics or dedicated automation systems is of interest where these systems form part of an integrated solution for information management. The journal aims to cover micro-, mini-, and mainframe applications and systems, both those designed in-house or available commercially.

The journal publishes five types of papers: **Original research papers, Tutorial articles, Case studies, State-of-the-art review articles, and Short communications. A Monitor Section** provides news on meetings, book and software reviews, a calendar of forthcoming events, etc.

ABSTRACTED/INDEXED IN: ASCA, Analytical Abstracts, BioSciences Information Service, Cambridge Scientific Abstracts, Chromatography Abstracts, Current Contents, Current Index to Statistics, Excerpta Medica, INSPEC, SCISEARCH

1993: SUBSCRIPTION INFORMATION
Volume 21 in 3 issues
Dfl. 448.00 / US $ 256.00 (including postage) ISSN 0925-5281

I would like ☐ a free sample copy of Laboratory Information Management.
☐ Instructions to Authors.
☐ to enter a subscription for 1993.
Please send me a Proforma Invoice

Name _____

Address _____

_____

_____

The Dutch Guilder price (Dfl.) is definitive. US$ prices are for your convenience only and are subject to exchange fluctuations. Customers in the European Community should add the appropriate VAT rate applicable in their country to the price(s).

711\414\143\0065

Elsevier Science Publishers
Attn. Carla G.C. Stokman
P.O. Box 330, 1000 AH Amsterdam
The Netherlands
Fax: (+31-20) 5862 845
In the USA & Canada
Attn. Judy Weislogel
P.O. Box 945, Madison Square Station
New York, NY 10160-0757, USA
Fax: (212) 633 3880

0003-2670(19930622)278:2;1-7